Using X-ray and neutron scattering to study the dynamics of low-dimensional systems

Andrew Colin Walters

A Thesis presented for the degree of
Doctor of Philosophy

I, Andrew Colin Walters, confirm that the work presented in this thesis is my own. Wherever information has been derived from other sources, this has been indicated in the thesis.

Abstract

The theoretical and experimental study of low-dimensional systems has dominated much of modern condensed matter physics. Such systems present a range of different phenomena which are not observed in more isotropic, three-dimensional materials. This thesis constitutes the study of the excitations of two types of low-dimensional system: the magnetic excitations in the one-dimensional $S = 1/2$ antiferromagnetic chain compound Sr_2CuO_3 as studied using inelastic neutron scattering, and the phonons in quasi-two-dimensional graphite intercalation compounds CaC_6 and BaC_6 studied using inelastic X-ray scattering. Initially an introduction to the vast field of low-dimensional systems is provided, followed by a description of the neutron and X-ray scattering technique. Spinon excitations in Sr_2CuO_3 have been measured up to ≈ 600 meV, and are found to be well-described by the Heisenberg model. A new version of the magnetic form factor for Cu^{2+} in Sr_2CuO_3 provides an explanation for the considerable reduction in the measured inelastic neutron scattering intensity, which may have significant consequences for past and future work on other related materials. The phonons in superconducting CaC_6 ($T_c = 11.5$ K) are found to be in reasonable agreement with Density Functional Perturbation Theory calculations, but the measured dispersions in non-superconducting BaC_6 are significantly different to those predicted. No direct evidence for electron-phonon coupling is found in either compound. It is concluded that the X-ray data supports the validity of the theoretical description of CaC_6, but the use of significantly inaccurate lattice parameters for BaC_6 in the calculation may provide an explanation of the poor agreement in this case.

For Mum, Dad and David

Acknowledgements

Over the course of four years, many people give invaluable help at different times, and human nature dictates that sometimes some of these moments slip the memory. In an experimental physics PhD, there are countless instances when people help enormously by just making some equipment work, or simply by providing much-needed sympathy when something goes badly wrong. Here I would like to thank the people to whom I am especially grateful.

My PhD supervisors, Des McMorrow and Toby Perring, have provided me with a great deal of help in a variety of ways and some excellent advice, which I have tried to follow as often as possible. My introduction to the life of a PhD student began at the ISIS pulsed neutron source in Oxfordshire, and I owe a lot to Toby's close supervision during that time, not least on the importance of paying due care and attention in experimental science. During my time at UCL, I have been very grateful for Des's support and belief in my abilities, which has provided me with the opportunity to begin to direct some of my research during the latter part of my studies.

Turning to the people who have made a dramatic difference to my thesis work, there is no doubt that a hugely influential person has been Dr Chris Howard of UCL, who I have worked with very closely on the study of phonons in graphite intercalation compounds (GICs). The main reason why many experimental measurements have not been done on CaC_6 and other similar GICs is because of the enormous challenges involved in making pure samples of these materials. Through a lot of hard work and ingenuity Chris managed to overcome these problems, which has made all the inelastic X-ray scattering measurements discussed in this thesis possible. I would also like to thank him for all the rest of the help he has provided both as a friend and scientific colleague over the last few years, as well as getting me into Stamford Bridge twice (albeit to witness two draws against those two greats of English football: Wigan and Hull).

I would also like to thank Igor Zaliznyak, of Brookhaven National Laboratory who - as well as being involved in the original experiment at the MAPS spectrometer on Sr_2CuO_3 -

provided the insight to anticipate that the Cu^{2+} magnetic form factor in this system could provide an explanation for the reduced intensity observed. This realisation constitutes the major new result of our work on Sr_2CuO_3, so his impact on my work cannot be overstated. Igor has also provided me with some no holds barred grillings during my trips to Brookhaven, which hopefully will have stood me in good stead for my viva.

There are many other people to thank for all kinds of help, and I now appreciate the inevitable urge to string seemingly random names together in an acknowledgements section. I hope the following people know how grateful I am for their considerable help at different times in my PhD: Mark Ellerby, Andrei Savici, Duc Le, Christian Rüegg, Tom Fennell, Chris Frost, Tom Weller and Mark Dean. To the many other people who have helped me in any way at all over the last few years (but arbitrarily have not been named in person), I thank all of you for your help and advice.

A big non-science thank you goes to my family, and especially my parents for managing to put up with me for four months while I wrote my thesis at their home. I should also thank all of my classmates in my French lessons in Chesterfield, Daniel Brownlow for all the intense games of squash, Chesterfield FC's flirtation with the play-offs as well as the friendly staff at the Caffè Nero's in Chesterfield and at the Chesterfield Library: they all helped me to stay as sane as possible during the writing-up experience.

Contents

List of Figures

List of Tables

Chapter 1

Introduction

The study of low-dimensional systems encompasses a tremendous amount of research in condensed matter physics today. Real low-dimensional systems display phenomena which are characteristic of theoretical models which only consider zero, one or two dimensions. Low-dimensional systems are of huge interest theoretically, as not only can the reduction of the dimensionality of a theoretical problem aid simplification, the number of dimensions itself often has huge implications on the behaviour of the system itself [1].

Reduced dimensionality has a huge impact in the study of phase transitions, where the number of dimensions is closely linked to the role of (usually thermal) fluctuations. It can be shown that the mean-field theory description of phase transitions works well in four or more dimensions, but as the number of dimensions become fewer, fluctuations have an increasing impact on the behaviour observed, limiting the applicability of the mean-field approach [2]. In fact, in a perfect example of a one-dimensional material, theory predicts that no phase transitions can exist other than at $T = 0$, where a quantum critical point (QCP) can exist. QCPs themselves have attracted a large amount of recent study, largely because the influence of quantum fluctuations near QCPs can lead to exotic states of matter [3].

Low-dimensional systems are also at the core of much of the current work on future electronical devices, as many devices employ two-dimensional thin films or etched one-

dimensional conductive channels [4]. Possibly the most famous reduced dimensional systems studied in recent years are the high-temperature superconducting cuprates, which all share two-dimensional copper and oxygen plaquettes (CuO_4 groups) [5].

A great deal of experimental research on low-dimensionality is concentrated on real systems which are analogues of well-established theoretical models. The study of these systems can provide vital evidence as to the strength of the theory. One example of such a study is the inelastic neutron scattering (INS) investigation presented in this thesis of the magnetic excitations of the one-dimensional (1D) spin-1/2 ($S = 1/2$) antiferromagnet Sr_2CuO_3. A significant property of any dynamical system is its dynamical correlation functions, which describe the spatial and temporal correlations within the system. Theoretical and experimental descriptions of the spin-spin correlation function of 1D $S = 1/2$ Heisenberg chains have been discussed for many decades [6, 7, 8, 9]. The inelastic neutron scattering technique has the unique advantage of directly measuring the spin-spin correlation function, as it is proportional to the measured differential scattering cross-section.

In our study of Sr_2CuO_3 the interest primarily lay in the role of increased electron itinerancy on the magnetic excitations. For most real systems the energy cost for electron hopping is many orders of magnitude larger than the energy scale of the magnetic excitations, and consequently the electrons can be justifiably modelled as localised to each site. However, in Sr_2CuO_3 the energy cost for electron hopping is only about eight times greater than the magnetic excitations, so does the simplified picture of isolated spins still hold? In Chapter 3 the analysis of our INS data on Sr_2CuO_3 is presented, accompanied by a discussion of the impact that our results may have on future studies. We have found that the increased mobility of the electrons does not affect the measured spin-spin correlation function from the static electron picture, but that the time-averaged position of the electrons themselves changes significantly. More specifically, the magnetic Cu electrons have a larger than anticipated probability of being near to the O site: the bonding is far more **covalent** than usually assumed in the literature [10, 11].

Another exciting area of low-dimensional systems research is the study of novel superconductors, as the nature of the superconducting mechanism for many such materials is

not fully understood [12, 13]. After the successes of the BCS theory of superconductivity [14], there was a tremendous surprise when many ceramic cuprates, which are highly insulating at room temperature, became superconducting at far higher temperatures than any previous superconductor [15] [16]. By understanding the superconducting mechanism in such systems, the possibility of being able to create future materials with even higher superconducting transition temperatures is greatly increased.

The recent discovery of superconductivity below 39 K in readily available MgB_2 [17] took the research community by surprise. The superconductivity in MgB_2 was found to conform largely to the BCS model, but has two superconducting gaps [18]: the first material ever found to exhibit this behaviour. Within the last five years, the graphite intercalation compounds (GICs) YbC_6 and CaC_6 have been found to have much higher critical temperatures that predicted (6.5 K and 11.5 K respectively) [19]. These materials are now also thought to superconduct which can be described within the BCS model [20], but there are many properties of these materials which are still not explained by the theory. In the study of any superconductor, the vibrational excitations (phonons) of the system are of special interest, as in the BCS theory, electron pairs (Cooper pairs) couple together via phonons. In Chapter 4 of this thesis, inelastic X-ray scattering (IXS) surveys of the phonons in CaC_6 and BaC_6 ($T_c < 0.080$ K [21]) are presented. Although the results are mostly consistent with theory in CaC_6, the measured phonons are dramatically different to the theoretical predictions in BaC_6. In addition, an as yet unexplained intercalant mode is observed in both GICs, in striking disagreement to the theory. This study, together with recent Angle-Resolved PhotoEmission Spectroscopy (ARPES) measurements on CaC_6, strongly suggests that the superconductivity in the GICs is far from being understood, despite some claims [22, 23].

In addition to the two projects discussed on Sr_2CuO_3 and GICs, I have also been involved in X-ray and neutron reflectivity measurements of the structure and magnetism of two-dimensional thin film manganite systems. These systems are mooted as possible prototypes for future computing devices. This work, although it does share the common theme of reduced dimensionality, is not discussed in detail in this thesis. An overview of the work involved in this project is provided in Appendix C.

In Chapter 2 an overview of the scattering technique is given, with specific detail about magnetic inelastic neutron scattering and phononic inelastic X-ray scattering. The inelastic neutron scattering investigation on Sr_2CuO_3 is presented in Chapter 3, and a description of the inelastic X-ray scattering experiments on CaC_6 and BaC_6 together with the data analysis is provided in Chapter 4. Chapter 5 comprises a summary of the current status on the projects discussed, with a brief description of our plans for future work.

Chapter 2

Inelastic X-ray and Neutron Scattering: techniques and instruments

2.1 Introduction to X-ray and neutron scattering

X-ray and neutron scattering techniques are at the very heart of condensed matter physics. The history of scattering techniques has a long history, all the way back to the work done independently by Max Laue and the Braggs (W. L. Bragg and W. H. Bragg) in 1913, who described the mathematical basis of diffraction [24]. Laue and the Braggs won the Nobel Prize for Physics in 1914 and 1915 respectively for their pioneering work. X-ray and neutron diffraction have provided the means by which we know the vast majority of the crystal structures of compounds, and has had a wide-ranging impact on a variety of different areas of science, such as the discovery of the double helix structure of DNA by Crick and Watson in 1953 [25].

A diffraction measurement is sensitive to the reciprocal space lattice of the material, which is the Fourier transform of the real space lattice. The Fourier transform describes an in-

version of the length scales which define the real crystal (small differences become large, large differences become small), resulting in the capability of extremely accurate measurement of very small distances (i.e. the lattice parameters of crystals, which have length of the order of 1 Å). A key advantage of x-ray and neutron scattering techniques is their ability to measure materials in bulk, in contrast to many surface-sensitive experimental techniques which have proved extremely popular in recent years. This helps to reduce any concerns about surface effects that are often quoted in the literature.

This chapter begins with a discussion of the advantages of X-rays and neutrons as scattering probes. That is followed by a brief description of some of the different types of X-ray and neutron sources, ranging from lab-based X-ray sources to nuclear reactors. A generalised version of the scattering cross-section is provided for both probes, highlighting the similarities of both techniques. The scattering cross-section is then described for the specific case of inelastic X-ray scattering (IXS) in the studies of phonon excitations, which includes providing a description of the IXS spectrometer located at Sector 3 at the Advanced Photon Source, USA. Finally the use of neutrons in the study of magnetic excitations is explained, with a description of the Inelastic Neutron Scattering (INS) MAPS spectrometer, which is based at ISIS, the pulsed neutron source at the Rutherford Appleton Laboratory, UK.

2.2 X-ray and neutrons: a comparison

The mathematics behind the scattering technique using X-rays and neutrons is very similar, and will be discussed in detail in Section 2.4. However the origin of the interaction between the scattering probe and the system of interest is dramatically different. This should not surprise us too much, as one is an electromagnetic wave and the other is a subatomic particle! Throughout the following I will assume knowledge of the simple expressions given in Equations 2.1 and 2.2, which underpin the fundamental basis of scattering experiments. By measuring the initial and final momenta and energies of the scattering probe, we find the momentum and energy transferred from/to the target system (Q and ΔE respectively). In the case of elastic scattering the change in energy is zero, and so

the issue is simplified into finding the particular momenta that the scattering probe preferentially gives or receives momentum from the target system. This simplification means that Bragg's Law (Equation 2.3) can be used, which relates Q to the wavevector k (now $k_i = k_f$) via the scattering angle 2θ.

$$\delta E = E_{initial} - E_{final} = E_i - E_f \tag{2.1}$$

$$\delta k = Q = \boldsymbol{k_i} - \boldsymbol{k_f} \tag{2.2}$$

$$Q = 2 \mid \boldsymbol{k} \mid \sin\theta \tag{2.3}$$

The relationship between wavevector and energy is very different when X-rays are used than when neutrons are used, and both relations are provided in Equations 2.4 and 2.5. The mass of the neutron is always defined as m. The wavevector k is proportional to the reciprocal of the probe's wavelength, and is defined as $k = \frac{2\pi}{\lambda}$.

$$E_{neutron} = \frac{\hbar^2 k^2}{2m} \tag{2.4}$$

$$E_{X-ray} = \hbar c k \tag{2.5}$$

A first step to understanding the use of X-rays and neutrons in scattering measurements is to be aware of the nature of the interaction between the probe and the scattering system. To describe the strength of the interaction, alternatively called the scattering power, it is helpful to introduce the idea of the scattering length. As a first approximation, we can assume that the interaction between the probe and a scattering body only contains s-wave components, which means that the scattering observed is isotropic and therefore can be described by a single parameter with no directionality. This single parameter is called

the scattering length. The probability of a probe being scattered into final solid angle Ω_f by a scattering body is represented by the differential cross-section $\frac{d\sigma}{d\Omega_f}$, so following the discussion above $\frac{d\sigma}{d\Omega_f} = b^2$, where b is the scattering length.

In X-ray scattering, the interaction is only with the electrons in a system, via the electromagnetic force. The details of the interaction are derived elsewhere with the use of perturbation theory on the Hamiltonian that describes the interaction of an ensemble of electrons with an incident electromagnetic wave [26, 27]. The leading term here is the elastic (Thomson) scattering term. Within the simple scattering length described previously, the scattering power of an X-ray scattering from a single electron is $\frac{d\sigma}{d\Omega_f} = {r_0}^2$, so the X-ray scattering length is r_0. Here the constant $r_0 = 2.818 \times 10^{-15}$ m is the classical electron radius, and is equal to $\frac{1}{4\pi\epsilon_0}\frac{e^2}{m_e c^2}$, where m_e is the electron mass.

For neutrons, the interaction is two-fold: the neutrons can interact directly with the nuclei, and they also have a magnetic moment which can interact with unpaired electrons in magnetic materials. The nature of the interaction between a neutron and nuclei is not completely understood, but it is known to have a very short range ($\sim$1 fm, or 1×10^{-15} m) [28], so on the length scale of a crystal lattice ($\sim$ 1 nm, or $\sim 1 \times 10^6$ fm) the interaction can be thought of as happening at a point in space. The neutron scattering length b is dependent on the nucleus being scattered from, and varies in an unpredictable way as a function of atomic number Z. However, it is usually of the order of 1 fm, which is the same magnitude as the X-ray scattering length r_0.

As the magnetic interaction in the scattering of neutrons is due to the electrons, the scattering length for magnetic neutron scattering system is very similar to that in X-ray scattering: $\frac{d\sigma}{d\Omega_f} = (\gamma r_0)^2$. Here γ is the neutron gyromagnetic ratio, which is the ratio of the neutron magnetic dipole moment and the angular momentum. It has a numerical value of approximately -1.9 [28], so the strength of magnetic neutron scattering is of the order of both the strength of nuclear neutron scattering and electron X-ray scattering.

Since neutrons are insensitive to charge directly, whether it be on the electrons or the nuclei, and also since the interaction of neutrons with nuclei and electronic moment is relatively weak, neutrons are able to probe large bulk samples ($\approx$ 10 g) in one single

measurement. This provides an extremely accurate measure of the purity of the sample. On the other hand, X-rays are almost entirely attenuated by similarly sized samples, as the photoelectric absorption process acts to absorb the incident X-ray, outputting an electron as a result. Although X-rays are not as capable as neutrons of measuring samples in bulk, in comparison to many other techniques X-ray scattering is very much a bulk measurement, with the X-ray attenuation length often in the range of 10 to 100 μm. Usually a sample in an X-ray scattering experiment will be made so that the X-rays only have to pass through approximately one attenuation length of the material, in order to best optimise the scattering cross-section [29].

An important distinction between X-ray scattering and neutron scattering is that in X-ray scattering the incoherent cross-section is so miniscule in comparison to the coherent cross-section that it can be ignored entirely. Incoherent scattering arises from small variations of the scattering potential V for a particular lattice site from the mean value of V taken over all lattice sites [30]. In neutron scattering the neutron scattering length can vary considerably from nucleus to nucleus, making the incoherent cross-section of some elements even larger than the coherent cross-section itself (vanadium and light hydrogen being good examples).

Using equations 2.4 and 2.5, if $k = 1$ Å^{-1}, the order of the reciprocal lattice spacing in many hard condensed matter studies, $E_{neutron} = 2.072$ meV whereas $E_{X-ray} = 12.41$ keV. $E_{neutron}$ is at the energy transfer appropriate for studies of magnetic and phononic excitations, but E_{X-ray} is about six orders of magnitude larger. This means that the measurement of the energy of meV excitations using neutrons is relatively straightforward, as the energy transferred by/to the neutron is likely to be a significant fraction of the incident energy. This property of the neutron, often described as a fortunate accident, is nothing of the sort. If one probes a set of nuclei with a probe which has a similar mass to nuclei, the fact that the momentum and energy scales are similar should come as no surprise. The situation is very different in IXS studies, where a change in the incident wavevector k_i of even 0.01% can result in a change of incident energy of over 1 eV. This advantage for INS has meant that until the last twenty years, INS has been the only technique that was capable of measuring meV excitations throughout the Brillouin zone.

However, the advent of extremely high-resolution monochromators at X-ray synchrotron sources has led to the monopoly of INS studies of phonons being undermined. In fact the advantages given above for INS can be turned on their head, if we take as our premise that it is possible to monochromate an incident X-ray beam of energy $\approx$ 10 keV to a sufficient standard ($\approx$ 5 meV). The fact that the energy transfer of meV excitations is of the same order of the scattering probe in INS creates its own issues, as this means that the choice of E_i is very important, as it defines which area of (Q,ΔE) space can be probed in a measurement. It also leads to the energy and momentum resolution being strongly coupled, with both resolutions approximately proportional to E_i. As a result, it can prove difficult to find the most effective area in (Q,ΔE) space to measure in. Since the energy of the incident X-ray is vast in comparison to the energy transferred to the target system, the energy resolution and momentum resolution are completely decoupled, and instead can be found by reference to the properties of the monochromator and the size of the detector aperture respectively.

We may make use of Equation 2.6, which is valid regardless of the scattering probe, as it is simply a consequence of the cosine rule in reciprocal space. By multiplying Equation 2.6 by $\frac{\hbar^2}{2m}$ we can use Equation 2.4 to give Equation 2.7, which is now only valid for neutron scattering. This equation links the energy transfer E with the momentum transfer Q, with the necessary dependence on the scattering angle 2θ. Figure 2.1 displays the trajectory in (Q,E) space that detector banks at 2θ = 5, 10, 30, 60, 90 and 120° measure on a direct geometry instrument at ISIS. The trajectory results from the final energy E_f being allowed to vary. This figure shows the strong coupling of energy and momentum for INS, which results in the corresponding coupling in the energy and momentum resolution.

$$Q^2 = k_i^2 + k_f^2 - 2k_i k_f \cos 2\theta \tag{2.6}$$

$$\frac{\hbar^2 Q^2}{2m} = E_i + E_f - 2\sqrt{E_i E_f} \cos 2\theta \tag{2.7}$$

In Figure 2.2 displays the trajectory that a detector at 2θ = 5, 10, 30, 60, 90 and 120° could

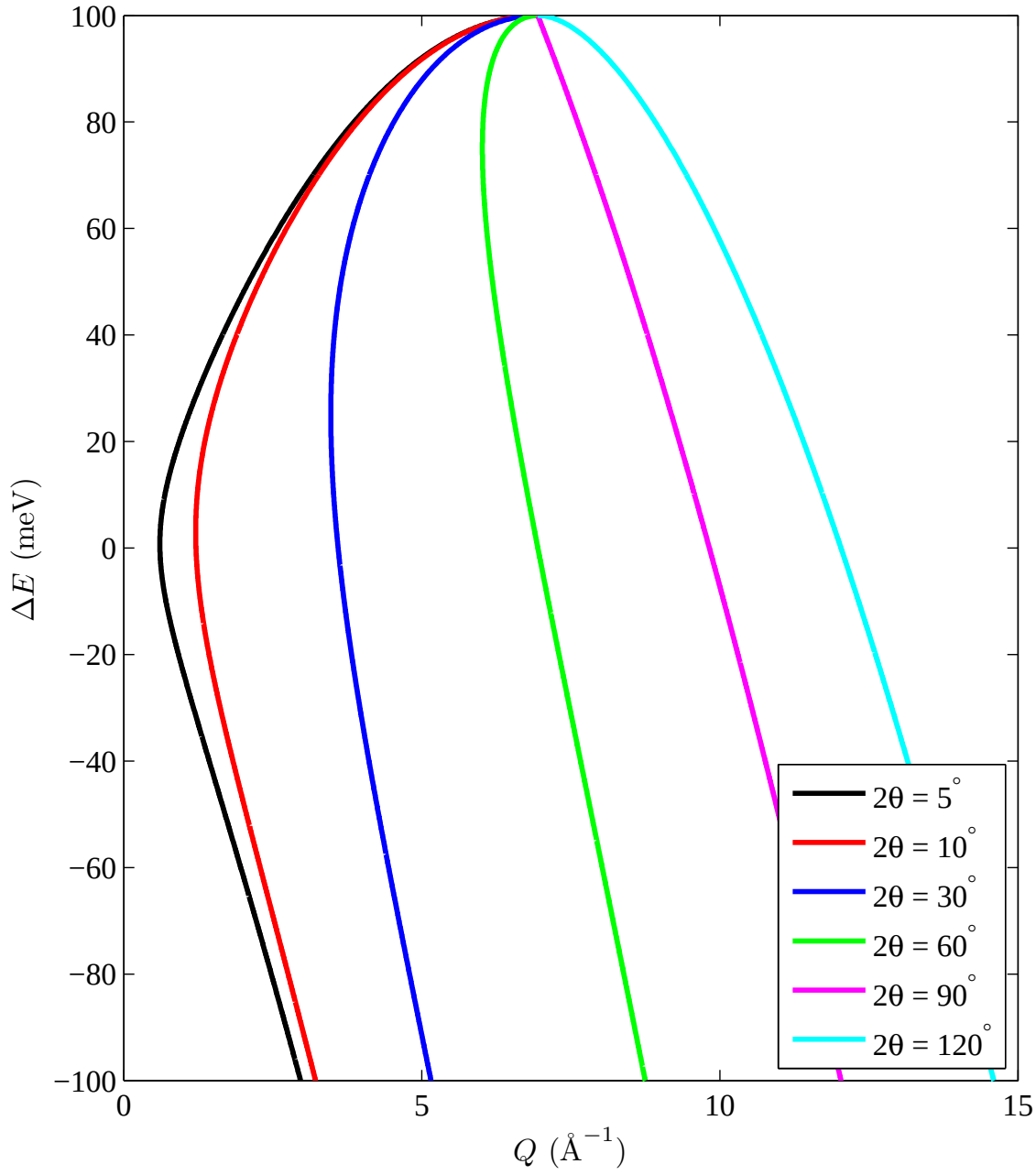

Figure 2.1: Energy transfer ΔE and corresponding momentum transfer Q measured at scattering angle 2θ = 5, 10, 30, 60, 90 and 120° on a direct geometry inelastic neutron spectrometer at a spallation neutron source. The incident energy was set at 100 meV. This figure is adapted from [31].

Source type	Brightness ($s^{-1}m^{-2}ster^{-1}$)	dE/E (%)	Divergence ($mrad^2$)	Flux ($s^{-1}m^{-2}$)
Neutron reactor source	10^{15}	2	10×10	1×10^{11}
X-ray tube	10^{20}	0.02	0.5×10	5×10^{14}
Synchrotron bending magnet	10^{27}	0.1	0.1×5	5×10^{20}
Synchrotron undulator	10^{33}	10	0.01×0.1	1×10^{24}

Table 2.1: Brightness and flux statistics for generalised X-ray and neutron sources [32]

measure at (provided there was no experimental limit in the final energy E_f that could be measured). This plot was created using Equations 2.5 and 2.6. Despite the considerable difference in the relationship between wavevector k and E in the two cases, this figure at first glance looks similar to Figure 2.1. However, the energy scale is completely different, as in Figure 2.2 the energy transfer covers a range of 20 keV. The inset is the same figure, but in an energy range more suitable to the study of phonons. The inset underlines the point that energy and momentum are barely coupled at all at the energies of interest, as the more traditional coupling between E and Q only occurs if $E_i \approx E_{phonon}$.

2.3 The production of X-rays and Neutrons

There are many different ways of producing X-rays and neutrons, but for many investigations (especially inelastic studies), large-scale facilities are necessary in order to have the necessary incident flux. The flux should be sufficient to make experiment counting times viable for experiments to take place over the timescale of a week.

In Table 2.1 a comparison of the flux and brilliance of neutron and X-ray sources is provided. It is clear that X-ray synchrotron sources provide a far higher incident integrated flux than equivalent nuclear reactor neutron sources. But as discussed in Section 2.2, the very different interaction that neutrons have with matter as compared to X-rays makes them very useful, despite this striking disparity in the flux which is currently attainable at large-scale facilities.

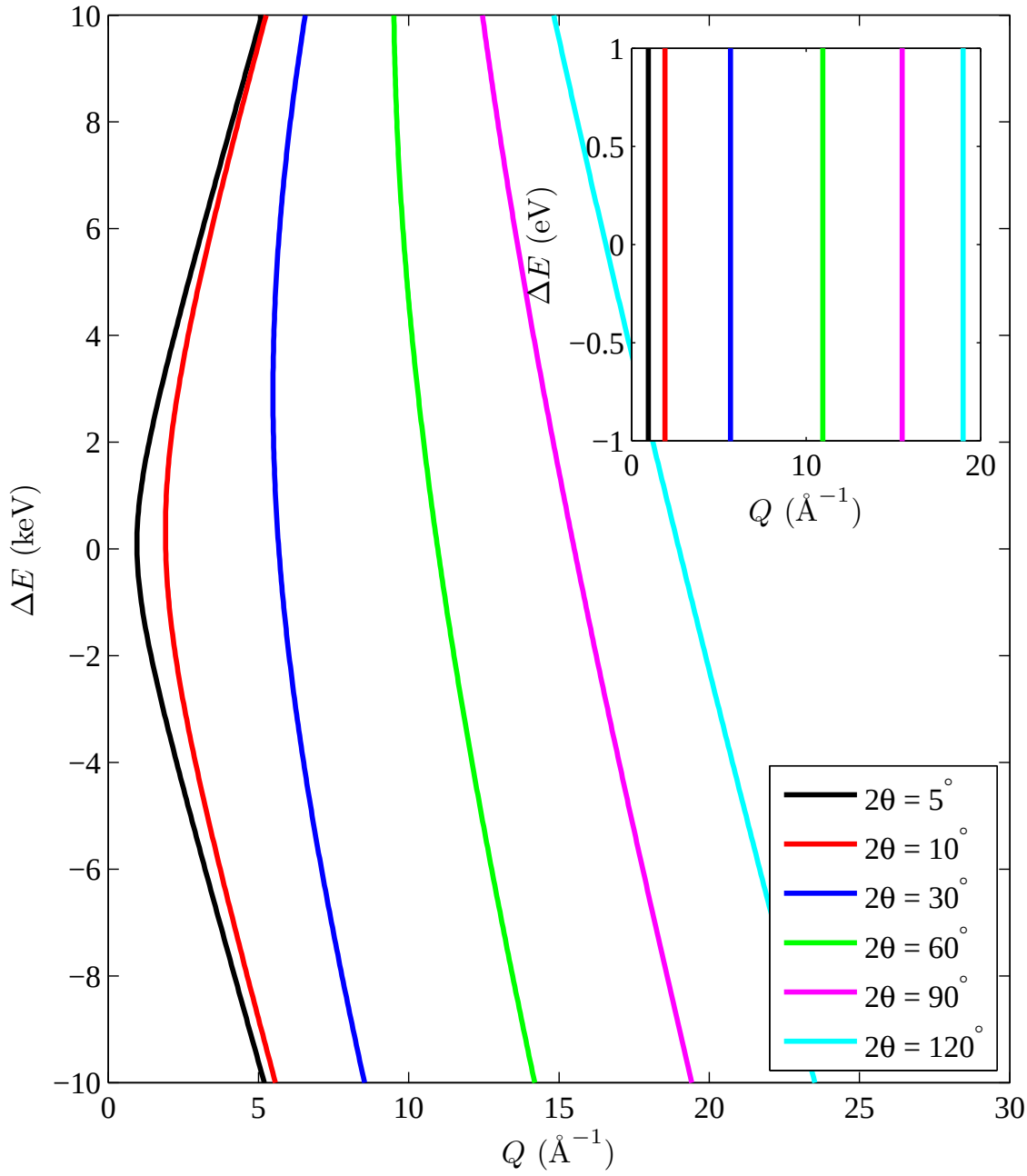

Figure 2.2: Energy transfer ΔE and corresponding momentum transfer Q measured at scattering angle $2\theta = 5$, 10, 30, 60, 90 and 120° on a inelastic X-ray spectrometer at a synchrotron. The incident energy was set at 21.658 keV, the incident energy used at Sector 3 at the Advanced Photon Source, USA.

2.3.1 X-ray sources

In modern times the most readily available source of X-rays are lab-based 'rotating anode' sources [27]. These work by heating up a metal filament to high temperatures so that electrons are excited from its surface, and then accelerating these electrons via an electric field such that they hit a positively charged metal target (the anode). The impinging electrons produce a large heating effect on the anode, and consequently the anode is rotated so that the heat is dissipated over its whole surface. The interaction of the electrons on the anode creates X-rays in two ways. The first way results directly from the sudden decrease in the speed of the electrons as they hit the anode, as to conserve energy the electrons convert their kinetic energy into emitted X-rays. This type of radiation is called Bremsstrahlung radiation, the name of which derives from the German for 'braking radiation'. The other way X-rays are produced is via emission. The incident electrons can transfer energy to the electrons in the anode, exciting them into higher electronic states. When the electrons relax back into their original state, X-rays of a very specific energy (the energy difference between the two states) is produced. This effect produces a far higher X-ray flux than the Bremsstrahlung effect, as is shown in Figure 2.3. The maximum flux from such a device is around 1×10^9 photons $s^{-1}rad^{-1}$, and is primarily limited by the quality of the heat dissipation from the rotating anode.

Far higher X-ray flux than is possible with a rotating anode can be produced at large-scale synchrotron facilities, where electrons are forced to undergo circular motion at relativistic speeds by electric and magnetic fields. Initially electrons are produced by heating a cathode to around 1000 °C, and are then accelerated to over 99% of the speed of light in a linear accelerator (linac), in an analogous way to X-ray tubes. Instead of hitting an anode, the electrons are then injected into the storage ring in which they undergo circular motion (although sometimes the electrons are put into the storage ring via a curved accelerator to increase the initial speed of the electrons even further). The resulting X-rays are produced tangentially to the circle. To increase the total X-ray flux available at a synchrotron, the electrons are passed through arrays of permanent magnets (called undulators) within the storage ring, which introduces additional accelerations. Since the energy of the electrons

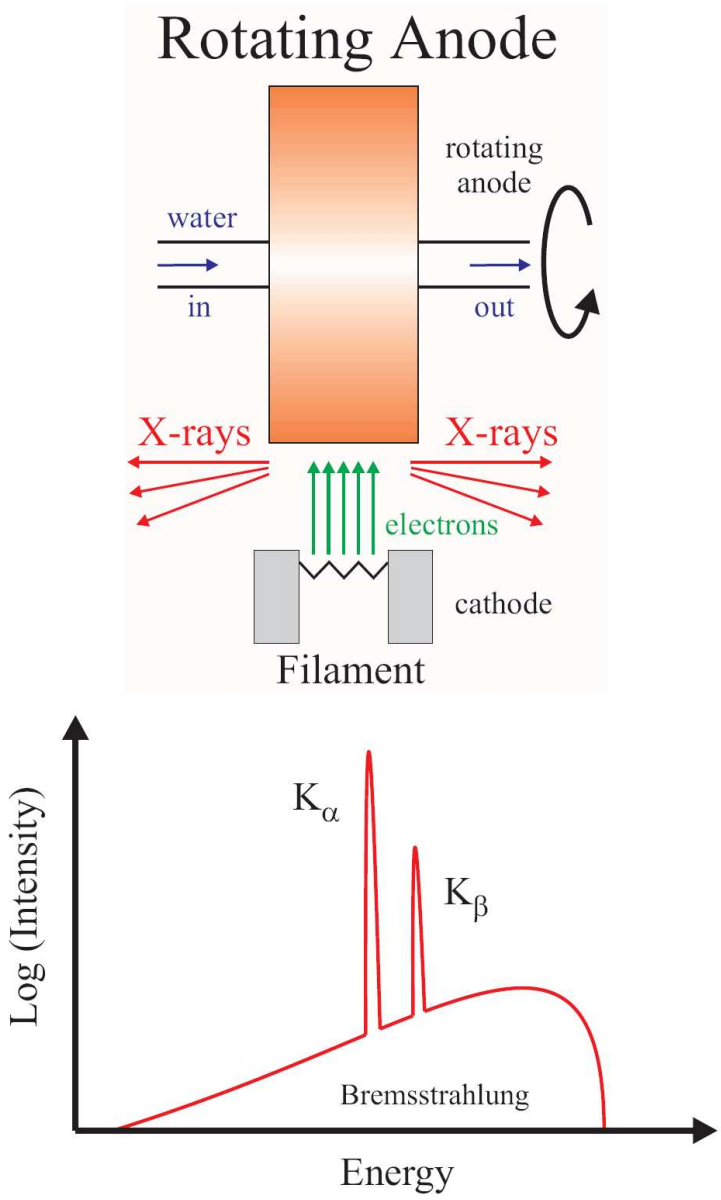

Figure 2.3: A schematic of a rotating anode (top) and a simple graph of the X-ray intensity spectrum it can produce (bottom). In the graph the discrete emission lines can be observed, superimposed on the background of the continuous bremsstrahlung radiation. The emission lines are due to two different electronic transitions. Figure slightly adapted from [27].

decreases as energy is lost as X-rays, the electrons also pass through radio-frequency accelerating cavities which replenish the electron's kinetic energy. The energy of the X-rays that are produced can be tuned via the choice of the mass of the charged particle and by the radius of the circular path the particle undergoes. For most condensed matter studies electrons are used as the charged particles, and the radius of the premier synchrotrons around the world is around 150 m.

2.3.2 Neutron sources

There are two main types of neutron sources: reactor sources and spallation sources. Neutrons are produced within nuclear reactors by the fission of uranium-235, whereas at spallation sources the neutrons are produced when high-energy protons hit a heavy target (tantalum at ISIS), which causes the target nuclei to become unstable and as a result emit neutrons in all directions. Reactor sources are usually operated continuously, so there is no time-structure in the incident neutron beam to each instrument. Spallation sources by their very nature have an obvious point in time at which the neutrons were produced (when the proton hits the heavy target), and this information can be used very effectively by producing the neutrons in pulses. Currently the usable time-averaged flux of spallation sources is approximately an order of magnitude lower than comparable reactor sources, but the maximal flux is much higher at spallation sources. This is a natural consequence of a pulsed spallation source, as between pulses no neutrons are being produced.

At both reactor and spallation sources, the neutrons produced have to be moderated (slowed down, or decreased in energy) before they can be used for condensed matter studies. Moderators consist of some material maintained at a particular temperature, resulting in the neutrons being slowed down via interaction with the atoms or molecules within the moderator. Graphite, methane and heavy water are examples of moderators used at ISIS.

All the INS data that will be discussed were measured at ISIS, the spallation neutron source at the Rutherford Lab, UK. ISIS produces high-flux pulses of neutrons at a rate of 50 Hz. Since all the neutrons are emitted within one microsecond, and the velocity of

the neutrons once they have passed through the moderator has been reduced to about 10^4 ms^{-1}, the energies of the neutrons can be determined using the time-of-flight method. The initial and final energies are found by measuring the length of time taken for the neutrons to travel from the moderator to the sample and then the time taken for the neutron to go from the sample to the detector/s.

At a reactor source, the energy of the neutrons prior to moderation is well described by a Maxwellian distribution of characteristic temperature around 350 K, equivalent to 30 meV [33]. Consequently, the number of neutrons produced with energies higher than 100 meV (often called epithermal neutrons) is relatively small. At a spallation source the number of epithermal neutrons is dramatically larger, and so INS studies which plan to look at excitations at these energies are normally better suited for spallation sources. In addition, triple-axis instruments, which are the usual inelastic instruments at a reactor source, can suffer from higher-order scattering issues, which are exacerbated at high incident energy transfers [31]. This effect does not happen with inelastic instruments which use the time-of-flight technique to find the neutron energy. However, studies which require low energy transfers (< 10 meV, often called 'cold' neutrons) are usually better suited to reactor sources, as even after moderation the incident time-averaged flux at such low incident energies is higher at reactor sources.

2.4 The scattering cross-section

The physical basis for the form of the scattering cross-section for neutrons and X-rays has been given with far more clarity and detail than can be afforded here, but a brief overview of the origins of the scattering cross-section is provided. Most derivations work from Fermi's Golden Rule, which is given in Equation 2.8. Fermi's Golden Rule itself is derived from first-order perturbation theory, so by using it we are immediately approximating the scattering process. This boils down to the viewpoint that the scattering process does not have any lasting effect on the system being studied: it does not make any changes to the possible states that the system can inhabit. Note that this does not preclude the possibility of a scattering probe (an X-ray or neutron) moving the system into an excited

state. It merely states that the scattering probe cannot create a new state of the system by virtue of the scattering process.

$$P_{\boldsymbol{k_i},\lambda_i \rightarrow \boldsymbol{k_f},\lambda_f} = \frac{2\pi}{\hbar} \mid \langle \boldsymbol{k_f}\lambda_f \mid V \mid \boldsymbol{k_i}\lambda_i \rangle \mid^2 \rho(\boldsymbol{k_f}, E_f) \tag{2.8}$$

In the case of scattering, Fermi's Golden Rule provides a means to find the probability $P_{i \rightarrow f}$ of the total system (both the target and the scattering probe) changing from its initial state λ_i to its final state λ_f. It is proportional to the matrix element of the initial and final states over the interaction V between the target and the scattering probe, and also proportional to the final density of states $\rho(\boldsymbol{k_f}, E_f)$. It assumes that the potential V due to the scattering process is weak, and therefore is far from a full description of the scattering process. However, it has proved an extremely effective method by which the scattering process can be mathematically expressed. From this, the generalised differential scattering cross-section can be derived [30, 28]:

$$\frac{d^2\sigma}{d\Omega_f dE_f} \mid_{\lambda_i \rightarrow \lambda_f} = \frac{k_f}{k_i} \mid \langle \boldsymbol{k_f}\lambda_f \mid V \mid \boldsymbol{k_i}\lambda_i \rangle \mid^2 \delta(\Delta E + E_i - E_f) \tag{2.9}$$

Here a delta function in energy is included to ensure that the conservation of energy is obeyed, as $E_f = E_i + \Delta E$ from Equation 2.1. Equation 2.9 is valid for any type of target system, but in the case of crystalline systems we can use the symmetry of the crystal lattice to simplify the expression for the differential cross-section. Now the potential V can be expressed as a sum of potentials which are centred at each lattice site, which have coordinates $\boldsymbol{r}_l$. This leads to an important simplification of the matrix element in both Equations 2.8 and 2.9, which is given in Equation 2.10:

$$\langle \boldsymbol{k_f}\lambda_f \mid V \mid \boldsymbol{k_i}\lambda_i \rangle = \int V(\boldsymbol{r}) e^{i\boldsymbol{Q}\cdot\boldsymbol{r}} d\boldsymbol{r} \langle \lambda_f \mid \sum_l e^{i\boldsymbol{Q}\cdot\boldsymbol{r}_l} \mid \lambda_i \rangle \tag{2.10}$$

Now the matrix element has become the product of the Fourier transform of the scattering potential $V(\boldsymbol{r})$, which we may call $V(\boldsymbol{Q})$, and a simpler matrix element. Note that this

simplification implicitly assumes that the final state of the neutron is a plane-wave, which seems very reasonable within the weak scattering picture that we have used. This is also consistent with the first-order perturbation theory stance that we have already taken using Fermi's Golden Rule.

The differential cross-section given in Equation 2.9 is the cross-section for the target system moving from the initial state λ_i to λ_f. In a real experiment we measure the different cross-section due to all possible initial states to all possible final states at the particular temperature and pressure being measured at. We allow for this mathematically by taking an average over all the possible initial states and then summing over the possible final states. The result of this is shown in Equation 2.11. $P(\lambda_i)$ is the probability of initially being in state λ_i.

$$\frac{d^2\sigma}{d\Omega_f dE_f} = \frac{k_f}{k_i} \sum_{\lambda_i,\lambda_f} P(\lambda_i) \mid \langle \lambda_f \mid V(\boldsymbol{Q}) \sum_l e^{i\boldsymbol{Q}\cdot\boldsymbol{r_l}} \mid \lambda_i \rangle \mid^2 \delta(\Delta E + E_i - E_f) \tag{2.11}$$

Another equivalent way of expressing the differential cross-section is in terms of the dynamic structure factor $S(\boldsymbol{Q}, \Delta E)$, which can also be expressed as the Fourier transform of a density-density correlation function [28]. The density correlation function represents a mathematical description of all of the structure and dynamics of the system. This form is given in Equation 2.12. This form neatly distinguishes between two parts of the differential cross-section: everything other than the density-density correlation function is purely a result of the properties of the individual scatterers (contained within $V(\boldsymbol{Q})$), whereas $S(\boldsymbol{Q}, \Delta E)$ contains within it all of the collective properties of the system. So almost all X-ray and neutron scattering experiments can be summarised as studies of the density-density correlation function. The only situation where this is not the case is in magnetism in neutron scattering, where instead we are measuring the spin-spin correlation function. This situation will be discussed later in this section.

$$\frac{d^2\sigma}{d\Omega_f dE_f} = N\frac{k_f}{k_i} \mid \langle V(\boldsymbol{Q}) \rangle \mid^2 S(\boldsymbol{Q}, \Delta E) \tag{2.12}$$

In the case of elastic neutron scattering, in which the neutrons scatter directly from the nuclei, we may replace $V(\boldsymbol{Q})$ with b, where b is the neutron scattering length. Since the nuclear potential is a delta function in real space, the Fourier transform means that it becomes independent of Q. However, in the case of X-ray scattering - both elastic and inelastic - scattering occurs from the electrons, which cannot be simplified to a delta function on the length scales which concern us. This means that in IXS studies of lattice vibrations (phonons), one assumes that any movement of the electrons averages itself out in the time-scale over the vibration. This assumption is called the adiabatic approximation.

A generalised form of the X-ray differential cross-section for phonons is provided in Equation 2.13. In addition, we have a term due to the polarisation of the initial and final X-rays. Note that the polarisation of the diffracted photon cannot be perpendicular to the incident polarisation, due to the appearance of the dot product of the two polarisations $\epsilon_i \cdot \epsilon_f$. Otherwise equation 2.13 is similar to Equation 2.11, except that instead of a generic $V(\boldsymbol{Q})$ within the matrix element, we have $\sum_l e^{i\boldsymbol{Q}\cdot\boldsymbol{r}_e}$, where $\boldsymbol{r}_e$ is the position of the lth electron from which the X-ray may scatter. Note the important difference between $\boldsymbol{r}_e$ and $\boldsymbol{r}_l$, the former being the coordinates of the electrons and the latter the coordinates of the nuclei.

$$\frac{d^2\sigma}{d\Omega_f dE_f} = {r_0}^2(\epsilon_i \cdot \epsilon_f)^2 \frac{k_f}{k_i} \sum_{\lambda_f,\lambda_i} P_{\lambda_i} \mid \langle \lambda_f \mid \sum_l e^{i\boldsymbol{Q}\cdot\boldsymbol{r}_e} \mid \lambda_i \rangle \mid^2 \delta(\Delta E + E_i - E_f) \qquad (2.13)$$

Although it is a thorough description, Equation 2.13 does not provide a simple means by which the experimenter can develop an intuition for the relative cross-sections of different phonon modes. The matrix element within it can be simplified, if we assume that the sample is a perfect single crystal and we assume that all vibrational excitations are harmonic (the potential energy associated with an atom moving away from its normal position with a displacement δx is proportional to δx^2). The resulting expression for one-phonon scattering is given in Equation 2.14, and $F_{in}(\boldsymbol{Q})$ is defined in Equation 2.15.

$$\frac{d^2\sigma}{d\Omega_f dE_f} = {r_0}^2(\epsilon_i \cdot \epsilon_f)^2 \frac{k_f}{k_i} \sum_j \langle n(E) + \frac{1}{2} \pm \frac{1}{2} \rangle (E_j(\boldsymbol{q})^{-1} F_{in}(\boldsymbol{Q}) \delta(\Delta E \pm E_j) \tag{2.14}$$

$$F_{in}(\boldsymbol{Q}) = \mid \sum_k M_k^{-\frac{1}{2}} f_k(Q) [\boldsymbol{e}_k^j(q) \cdot \boldsymbol{Q}] e^{i\boldsymbol{Q}\cdot\boldsymbol{r}_k} e^{-w_k} \mid^2 \tag{2.15}$$

In Equation 2.14 the sum over j is done over all the different phonon modes in the crystal. The large term in angular brackets describes the population of the phonon modes at the temperature they are measured at, and has a plus or minus sign depending on whether the phonon involved in scattering is created or destroyed. The plus or minus sign in the delta function is also dependent on whether the phonon was created or detroyed. $\boldsymbol{q}$ is the reduced momentum transfer, and is related to $\boldsymbol{Q}$ via the equation $\boldsymbol{Q} = \boldsymbol{G} + \boldsymbol{q}$, where $\boldsymbol{G}$ is a reciprocal lattice vector. The appearance of $E_j(\boldsymbol{q})$ highlights the fact that the energy of a phonon measured at a particular value of $\boldsymbol{Q}$ is dependent on where it appears in the Brillouin zone, regardless of which Brillouin zone it is measured in.

Equation 2.15 contains some of the most important information for anyone involved in inelastic phonon studies. Here k is summed over all of the atoms in the unit cell. It is immediately clear that the phonon intensity is inversely proportional to the mass of the nuclei M_k involved in the excitation. Similarly, the cross-section is proportional to the square of the Fourier transform of the electron density f_k. The e^{-w_k} term is the Debye-Waller factor, and results from variation of the atomic positions which cannot be described by a ubiquitous excitation such as a phonon.

The term in square brackets in 2.15 is perhaps most important, as it causes many issues for the experimenter. $\boldsymbol{e}_k^j(q)$ is the eigenvector of the jth phonon mode at reduced momentum $\boldsymbol{q}$ of the kth atom. The wavevectors of the phonons in a system are related in a non-trivial way to its symmetries, and as a result it can be rather difficult to intuit the phonon cross-section without recourse to a theoretical model. This means that for any particular value of Q the phonon cross-section could be zero, as the component of the eigenvectors may conspire to make the phonon unobservable. Conversely you may be able to measure a phonon in a specific Brillouin zone, but it may be far more intense in another Brillouin

zone, making it ineffective to measure the mode in the Brillouin zone in which the mode is weak. The ideal situation is to have some kind of theoretical calculation of the phonons prior to the experiment, as a guide, but clearly this is not a situation that always happens (and did not happen with the phonon studies discussed in this thesis).

The magnetic inelastic neutron cross-section is given in Equation 2.16, and is the most complicated of all of the cross-sections dealt with here. As provided earlier in the discussion of the scattering length of magnetic neutron scattering in Section 2.2, the scattering power of magnetic neutron scattering intensity is of the order of $(\gamma r_0)^2$. It also contains a Fourier transform of electronic density $F(\boldsymbol{Q})$, as seen in Equation 2.15. g is the Landé factor, and $S^{\alpha\beta}(\boldsymbol{Q},\omega)$ is the spin-spin correlation function, with α and β each defining a spatial coordinate. This equation assumes that there is no polarisation analysis of the neutrons.

$$\frac{d^2\sigma}{d\Omega_f dE_f} = \frac{N}{\hbar}\frac{k_f}{k_i}(\gamma r_0)^2 \left(\frac{g}{2}\right)^2 |F(\boldsymbol{Q})|^2 \sum_{\alpha\beta}(\delta_{\alpha\beta} - \hat{Q}_\alpha \hat{Q}_\beta) S^{\alpha\beta}(\mathbf{Q},\omega) \tag{2.16}$$

The biggest difference between Equation 2.16 and the previous expressions is the appearance of the $(\delta_{\alpha\beta} - \hat{Q}_\alpha \hat{Q}_\beta)$ term summed over α and β with the spin-spin correlation function. $\hat{Q}$ is a unit vector along the direction of Q. These so-called polarization factors directly stem from the dipolar interaction between neutrons and the electron spin. In most studies they are thought to only contribute a constant term to the overall measured differential cross-section (see Appendix B).

The aim here has been to introduce all of the necessary expressions for the differential cross-section that X-rays and neutrons are sensitive to, without attempting to reintroduce the entirety of scattering theory. An attempt has been made to provide a brief summary of the mathematical basis that allows us to express very complicated physical objects into what are (relatively) simple mathematical objects. The central message is that scattering measurements, be it with X-rays or neutrons, and either purely inelastic or elastic, measure different parts of correlation functions which describe the collective behaviour of the system under scrutiny.

2.5 A generalised inelastic X-ray or neutron instrument

As discussed previously, if one wishes to study excitations via a scattering technique, then a measurement of the initial and final momenta and energies of the scattering probe has to be accomplished. Probably the most straightforward way of accomplishing this is to fix k_i (thereby also defining E_i), k_f and the scattering angle 2θ. This can be understood with reference to Equation 2.6, together with either Equation 2.4 or Equation 2.5.

In Figure 2.4 such an instrument is presented, which fixes k_i, k_f and 2θ. This type of instrument is used routinely at neutron reactor sources to study excitations, and is called a Triple-Axis Spectrometer (TAS). The energy selection of the initial and final energies is done by use of high-quality single crystals. The energy selection is done by rotating the single crystals to particular values of 2θ, so that Bragg's law (Equation 2.3) can be used to only allow neutrons with a particular wavevector k to be diffracted. This method thereby selects a specific energy of neutrons from the neutrons incident on the single crystal. The incident neutron beam is monochromated by the first crystal (called the monochromating crystal, or just the monochromator), which is housed within the monochromator changer, and the final neutron energy is set by the second crystal (the analysing crystal, or analyser as labelled in Figure 2.4. The Q to be measured has been defined by a combination of E_i, E_f and the scattering angle 2θ (see Equation 2.6). The triple-axis spectrometer is so-called as it involves three vertical axes: one at the monochromator, one at the sample itself and another at the analyser.

2.6 IXS instruments with meV resolution: Sector 3 at the APS

Recent advances in the monochromation of X-ray beams has resulted in the capability of inelastic X-ray spectrometers boasting energy resolutions which are comparable to the energy resolutions possible on similar triple-axis spectrometer instruments at neutron reactor sources. IXS instruments capable of reaching meV resolution are based on the triple-axis

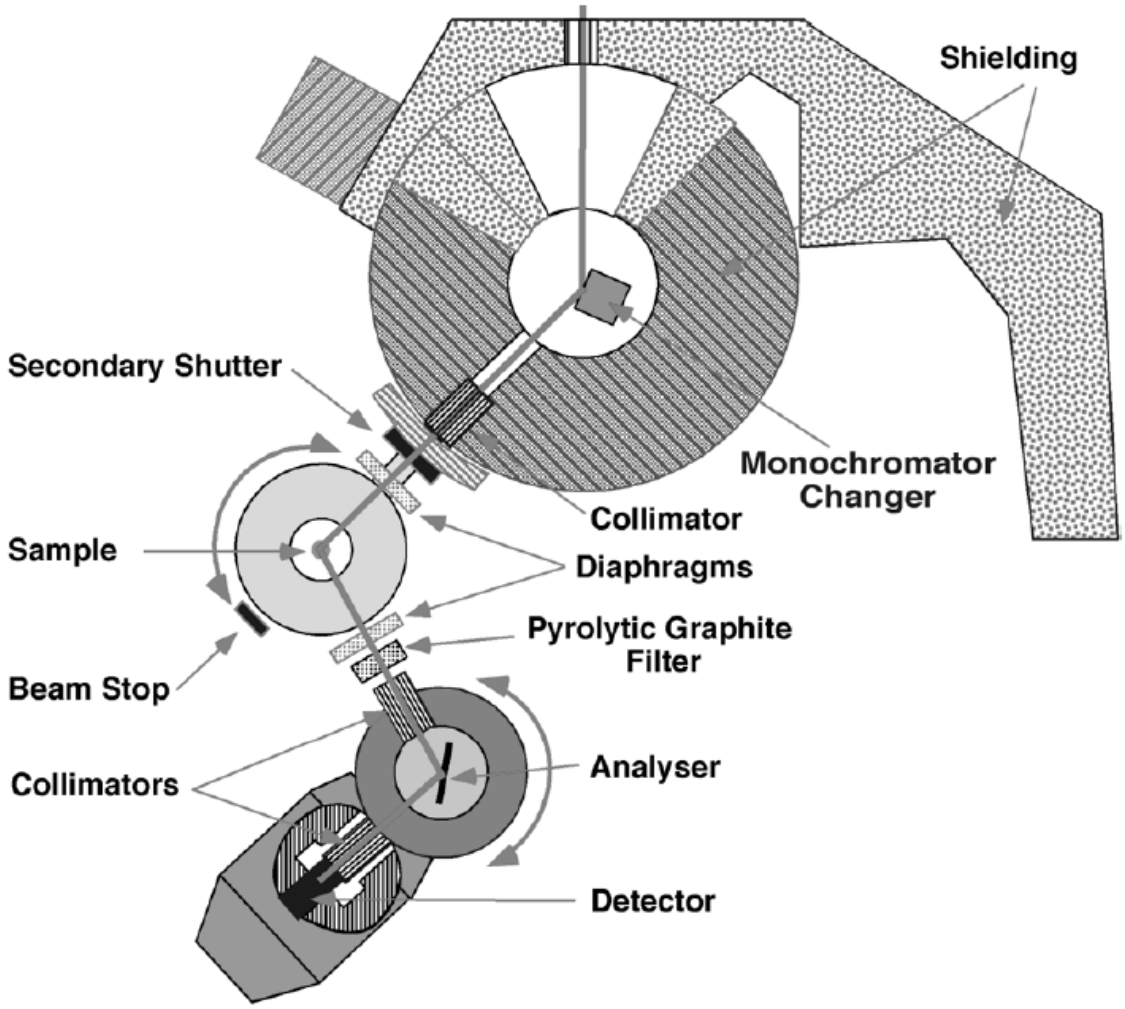

Figure 2.4: A schematic of a Triple-Axis Spectrometer (TAS) as used at neutron reactor sources [31].

spectrometer model discussed in Section 2.5. Schematics of some of these IXS instruments are provided in Figure 2.5. The initial and final energies of the X-rays are found in precisely the same manner as in a TAS, via a Bragg condition in the monochromator and analysers.

In order to attain such high energy resolution via a Bragg reflection, extremely high-quality large silicon crystals are used, as the narrow mosaic of the monochromating crystal corresponds directly to the energy resolution possible in the diffracted beam. The angular divergence of the incident crystal $\Delta\theta$ has to be considered, as $\Delta E/E_i = \cot(\theta_B)\cdot\Delta\theta$, where θ_B is the scattering angle of the Bragg peak used for monochromation. Over the majority of values of θ_B, $\cot\theta_B$ is approximately unity, so the angular divergence $\Delta\theta$ would need to be similar in size to the ratio $\Delta E/E_i$. If the incident energy is 21.658 keV and we require a resolution of 2.2 meV (as at Sector 3), the ratio $\Delta E/E_i$ is around 1×10^{-7}, but the angular divergence at a synchrotron is typically around 1×10^{-4} (see Table 2.1). At the ESRF and SPring-8 this problem is solved by ensuring that the Bragg reflections used have scattering angles very close to 90° (i.e. in backscattering geometry), as this dramatically minimises the cotangent term in the expression for the energy resolution ($\cot 90° = 0$), enabling the experimental angular divergence to be sufficient [29].

In the case of the instruments at the ESRF and at SPring-8, E_i is then changed by decreasing the temperature of the monochromating crystal, so that the d-spacing decreases and the energy selected by the Bragg condition is increased. This method requires extremely sophisticated temperature control of both the monochromator and analyser crystals, as the difference in their temperatures directly corresponds to a measurement of the energy transfer. This is seen in the relationship $\Delta E/E_i = \alpha\Delta T$, where α is the thermal expansion coefficient of silicon at room temperature and has the numerical value of 2.68×10^{-6} K^{-1}). Because of the small value of α, the temperature differentials are very small, (of the order of mK), so the temperature measurements have to be accurate to at least 0.5 mK [29].

In the experiments discussed in Chapter 4, all of the measurements were done at Sector 3 at the Advanced Photon Source, USA. The monochromator design here is somewhat different, and is dealt with in great detail elsewhere [34]. The instrument at Sector 3 is

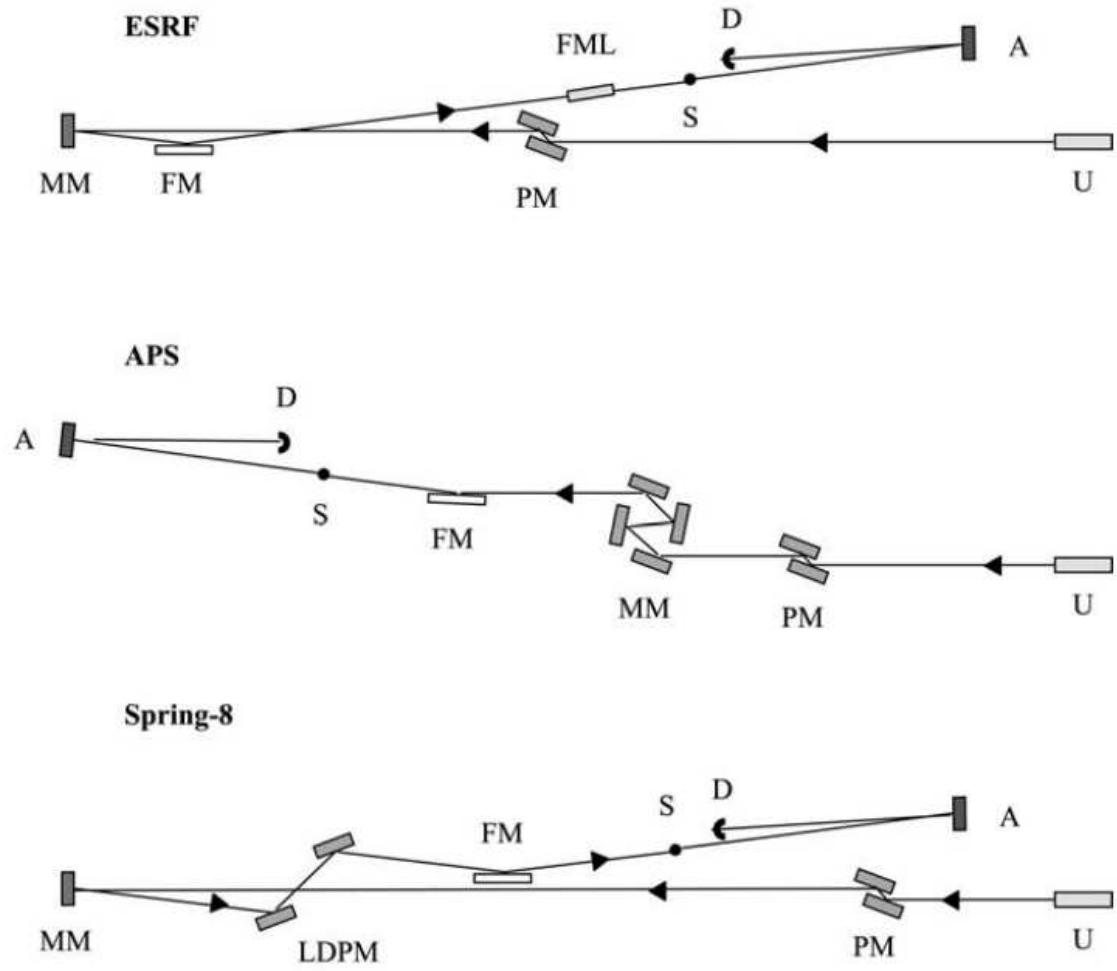

Figure 2.5: Schematics of different types of inelastic X-ray spectrometer designs used at the European Synchrotron Radiation Source (ESRF), the Advanced Photon Source (APS) and at SPring-8 (not to scale). U: undulator, PM: high heat load premonochromator, MM: high-resolution main monochromator, LDPM: large vertical deflection Si (111) monochromator, FM: focusing mirror, FML: focusing multilayer, S: sample, A: analyzer crystal(s), D: detector [29].

capable of doing inelastic nuclear resonant scattering measurements, as the incident energy can be tuned in particular energy regions depending on the choice of monochromator. With a nominal incident energy between 21.50 and 21.70 keV, the monochromator used in our studies can also be used to study resonant effects on ^{151}Eu, which has a resonance at 21.542 keV [35]. On the contrary, the incident energy used on instruments at the ESRF and SPring-8 cannot be tuned in this way, as the monochromation is accomplished by making use of Bragg reflections at Bragg angles extremely close to 90°. Any change in the incident energy results in a change in the Bragg angle, which means the energy resolution due to the angular divergence will dominate. The flexibility in incident energy at Sector 3 is achieved by finding another method to reduce the angular divergence of the incident X-rays, which allows us to relax the condition of the Bragg angle being very close to 90°, and so the energy may then be tuned without a dramatic reduction in energy resolution.

The method by which the angular divergence is reduced at Sector 3 is by making use of Bragg reflections from asymmetrically cut silicon crystals, which can dramatically improve the collimation of the X-ray beam [34, 35]. This highly collimated beam is then monochromated by a Bragg peak with a Bragg angle around 80°, so that the energy resolution due to the angular divergence is still being minimised to some extent. In the case of the monochromator used at Sector 3, the collimation is achieved using the (4 4 0) reflection in a asymmetrically cut silicon crystal, and the monochromation by making use of the (15 11 3) reflection at $\theta_B = 83.2°$.

All of this careful monochromation of the incident beam would be useless however without the corresponding energy selection by the analyser crystals. Analysers at all current IXS spectrometers use the backscattering geometry discussed ($\theta_B = 90°$) to select a particular energy, as shown in Figure 2.6. Energy scans are always achieved by changing E_i, and so the analyser crystals are fixed and unable to scan independently from each other. Please note that most IXS instruments use multiple detectors, each with its own analyser. In the case of Sector 3, four analysers are used, with analyser 1 at the largest value of 2θ and analyser 4 the lowest. This means that multiple datasets can be measured simultaneously. One issue that this raises is that the set of points in reciprocal space mapped out by the analysers maps out an arbitrary area in reciprocal space, and so if you are especially

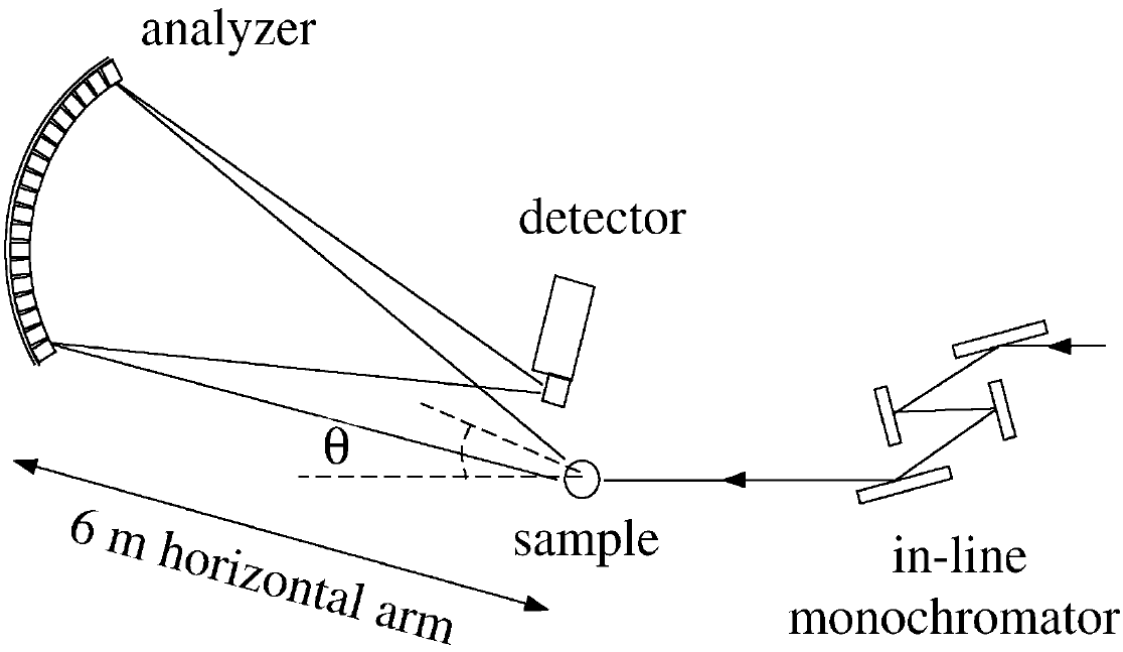

Figure 2.6: A schematic of the inelastic X-ray spectrometer at Sector 3, at the Advanced Photon Source, USA [35].

interested in a particular trajectory in the Brillouin zone, this is very likely to be impossible using all of the analysers in a single scan.

For IXS all inelastic scans are done via constant Q scans, also called energy scans. This can be done by simply changing the incident energy E_i and maintaining the final energy E_f. From Equations 2.1 and 2.2, and using either Equation 2.4 or Equation 2.5, it is clear that by changing the energy transfer ΔE the momentum transfer Q must accordingly change. In IXS this relationship is greatly simplified, since the magnitude of Q is extremely small in comparison to the magnitude of k_f, usually four of five orders of magnitude smaller. Consequently we can approximate k_i as k_f, drop the subscript and Equation 2.6 simplifies dramatically to $Q = 2k \sin\theta$, which is Bragg's Law (Equation 2.3). We can therefore calculate where we wish to measure in reciprocal space by simply moving to the relevant Q and then do an energy scan.

2.7 INS instruments at pulsed neutron sources: the MAPS instrument

MAPS is an example of a direct geometry spectrometer based at ISIS, at the Rutherford Appleton Laboratory in Oxfordshire. Direct geometry spectrometers work by fixing the incident energy E_i and using the time-of-flight method to find the energy of all the neutrons which are then scattered from the sample. The monochromation of the incident neutrons is also set using the time-of-flight method, as by only allowing neutrons to hit the sample in a narrow time interval after they are produced by spallation, monochromation of the incident neutrons is achieved. Since this requires careful timing at the micro-second scale, and needs to be done for each pulse (fifty times a second), the simplest way to implement this monochromation is to use blockers which rotate at 50 Hz. Since these blockers act to 'chop' the incident neutrons up in time, they are called choppers. This is the reason why direct geometry instruments are also often called chopper spectrometers.

At MAPS two choppers are actually used, as can be seen in Figure 2.7. The first chopper that the neutrons come into contact with is called the Nimonic chopper (also called the background chopper), so-called because of the neutron-absorbing Nimonic alloy it is made from. In reality the Nimonic chopper on MAPS is a thick sheet of material rotating about an axis at its edge, which at the moment the neutrons are produced blocks the flightpath. This means that any background from unwanted high-speed neutrons or other fast particles (Gamma rays etc.) do not reach the sample.

Subsequent to the Nimonic chopper, the second chopper (called the Fermi chopper) then sets the incident energy. The Fermi chopper is also responsible for the incident energy resolution and the incident collimation of the neutrons. The Fermi chopper is a cylinder which has apertures in it which only allow neutrons through within a very specific time interval after the neutrons were produced. Since the Fermi chopper is rotating at a high frequency, the apertures within it are slightly curved to approximate the straight path of the neutrons in the rotating frame of the chopper. The choice of incident energy is then achieved by changing the phase of the rotating chopper relative to the frequency of the

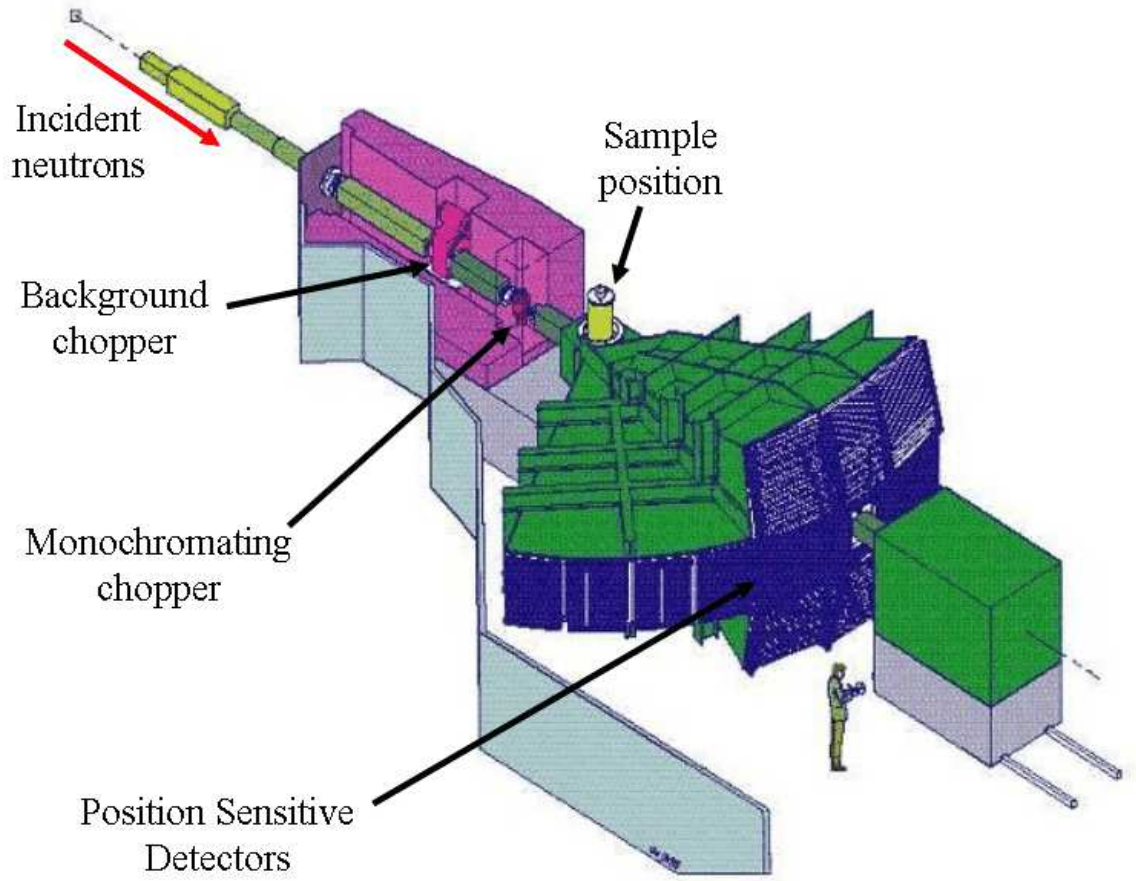

Figure 2.7: A schematic of the MAPS direct geometry inelastic neutron spectrometer, based at ISIS, UK [36].

incident neutron pulses at ISIS.

The moderator used at MAPS is a water moderator maintained at 300 K, which is the moderator at ISIS most suited for high incident energy studies such as the one I have been involved in (see Chapter 3). For instruments which are optimised for lower energies around 10 meV, such as the MARI chopper spectrometer at ISIS, a methane moderator is used at a temperature of 100 K.

In the case of MAPS and other recent chopper spectrometers and pulsed neutron sources, very large detector banks are used in combination with the choppers. In the case of MAPS a detector area of about 16 m^2 is used. Since the vast majority of the neutrons which enter MAPS have already been removed by virtue of the monochromation, we try to use as

many neutrons as possible by making the detector banks extensive. This directly results in a large area of (Q,ΔE) space being sampled in every pulse of neutrons (at MAPS, over 1×10^6 points in (Q,ΔE) space are usually measured at in any one measurement). This is where this technique of inelastic neutron scattering differs dramatically from the triple-axis technique, as the triple-axis technique only measures at a specific point in (Q,ΔE) space at each point in a scan. By measuring along multiple trajectories in (Q,ΔE) space using a triple-axis spectrometer we can produce a similar picture that a chopper spectrometer would create by default. So the use of a triple-axis or chopper spectrometer is dependent on the requirements of the experiment. If the experimenter is interested in a very specific, small area of (Q,ΔE) space, then the triple-axis route at a reactor source is probably best (provided that the excitation is not over 200 meV, as the incident flux of of high energy neutrons is comparatively reduced at a reactor source). However, if the interest lies in a larger range of (Q,ΔE) space, the chopper spectrometer route is probably best. This could be put more expressively by stating that the canvas can be painted in its entirety in large brushstrokes by a chopper spectrometer, and the fine detail in specific areas can be found using a TAS.

One important issue in the production of INS datasets from chopper spectrometers is the issue of accurate normalisation of the data, so that the data can be put on an absolute intensity scale. This is usually done by measuring the neutron cross-section of a vanadium sample of known mass, as vanadium has both a very small coherent neutron scattering cross-section and a significant incoherent neutron scattering cross-section (see Section 2.2). The incoherence of the scattering from vanadium means that the neutrons are scattered isotropically, so by comparing the expected theoretical neutron scattering cross-section for vanadium integrated over over all energy transfer and a known solid angle with an equivalent measurement of a sample of vanadium, a numerical factor can be applied to the unnormalised INS data to convert the intensity scale into the correct units (usually mbarns/meV/sr/scattering centre). The accuracy of this normalisation is around 10%, although there can be additional factors that can decrease the measured cross-section, due to the neutron absorption and attenuation of the sample of interest, but these tend to only be of the order of 5% of the total intensity.

The energy resolution at a chopper spectrometer is dependent on the energy linewidths defined by the moderator and the Fermi chopper. Different Fermi choppers can be used to improve the energy resolution, although there is a corresponding cost in incident flux. In Chapter 3 more detail is provided on the energy resolution of MAPS as a function of energy transfer for the specific E_i of interest in that INS study. The generic property of the energy resolution of a chopper spectrometer is that it scales linearly with E_i and is worst at very low energy transfer (typically approximately 5% of E_i), but at higher energy transfer the energy resolution improves significantly, dropping to just 2% of E_i. At MAPS the vast majority of studies use the so-called 'sloppy' chopper, which gives the lowest energy resolution at a particular E_i. This is because usually energy resolution is compromised slightly for increased statistical quality of the data.

The momentum resolution can be found from the geometry of the experiment: the intrinsic momentum resolution of MAPS is found by measuring the solid angle of each detector (measured from the sample position) and converting that real space uncertainty into a reciprocal space uncertainty via knowledge of the scattering angle and the initial and final neutron energies. In addition, the momentum resolution is also dependent on the solid angle subtended by the moderator measured at the sample position, and the angular extent of the sample itself as observed from the moderator and the detectors. As the incident energy is increased, reciprocal space essentially contracts in real space, as Q is approximately proportional to k_i^2, or ΔE, using Equation 2.6. This means that at higher E_i the solid angle subtended by a specific detector corresponds to a larger uncertainty in Q. This explains the reduction in the quality of the momentum resolution when the incident energy is increased.

Happily for the experimenter, the considerations of energy and momentum resolution are dealt with in full by the TobyFit program, written by Dr Toby Perring of ISIS [37]. This program is able to convolute a given INS cross-section with the details of the resolution function of a neutron chopper spectrometer at a neutron spallation source, thereby providing a realistic description of INS data at any chopper spectrometer. The software takes into account all the parameters which can influence the momentum and energy resolution, including the initial lineshape of the neutron beam provided by the moderator, as well

as the pulse shape allowed through by the chopper. It also considers less obvious factors such as the jitter associated with the high-frequency rotation of the chopper. The physical extent of the sample can also be inputted, together with its mosaic, in order to correctly simulate the total momentum resolution.

The success of MAPS has had a profound effect on the design of other similar chopper spectrometers at ISIS, such as MERLIN, and LET in the future. It also continues to influence the design of instruments at the new, higher flux spallation neutron source based at Oak Ridge National Laboratory, such as SEQUOIA and CNCS.

Chapter 3

Inelastic Neutron Scattering Study of the Spinon Excitations of the One-Dimensional $S = 1/2$ Antiferromagnet Sr_2CuO_3

3.1 Introduction to one-dimensional $S = 1/2$ antiferromagnetic chains

Spin-1/2 antiferromagnets in both one and two-dimensions are of considerable interest, particularly as archetypal test systems for understanding different models of spin systems [11, 38, 39, 40]. Quantum effects on $S = 1/2$ systems are especially enhanced as they have the lowest spin possible, with only two available spin states: $+1/2$ (up) and $-1/2$ (down). This is far from the classical picture of magnetic moments which can have any orientation in three-dimensions. The detailed study of the simplest possible magnetic systems underpins the understanding of all the remaining (by definition more complicated) systems, so the importance of the study of test systems cannot be overestimated.

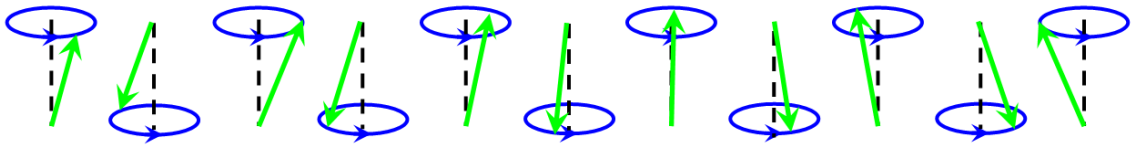

Figure 3.1: A perspective view of the time-evolution of a spin-wave excitation in a line of antiferromagnetically aligned spins.

The study of 1D spin-1/2 antiferromagnets based upon cuprate systems (such as Sr_2CuO_3) can result in greater understanding of the two-dimensional high-temperature superconducting cuprates [5]. Indeed a significant amount of the study of these materials in the last twenty years has stemmed from the interest the electron correlation effects in the superconducting cuprates: in particular, the role of the corner-sharing CuO_4 plaquettes in the doped $YBa_2Cu_3O_7$ cuprate [41] and the appearance of one-dimensional stripes in the doped $La_{2-x}Sr_xCuO$ materials [42].

3.1.1 Magnetic excitations in one-dimension

The elementary excitations of an antiferromagnet are usually described within the spin-wave theory, which was pioneered by Anderson in 1952 [43]. Spin-wave theory describes the ground state of the antiferromagnet as the famous Néel state (↑↓↑↓...), which has excitations due to canting of the spins away from their preferred position, in a wave-like pattern over multiple spin sites. The quanta of these spin-wave excitations are called magnons. This behaviour is pictorially represented in Figure 3.1. However, this viewpoint assumes the continuum approximation: i.e. that the spin on each site can be made to point in any direction, like a classical vector. In quantum spin systems, this assumption is far from valid, as there are only discrete spin states that can be attained. Despite these shortcomings, the spin-wave description works surprisingly well in two-dimensional and three-dimensional systems even for systems with low S.

The failure of the spin-wave description in 1D is spectacular, as even the Néel ground state cannot exist, as quantum fluctuations in 1D are sufficient to destroy this state [43]. In fact it is now well-established that in one-dimension the excitations of the electron are

most readily described as independent excitations of spin and charge, known as spinons and holons [44]. This phenomenon is known as spin-charge separation. This means that if a one-dimensional system is doped, the electrons or holes decay into the spin and charge degrees of freedom allowed.

A representation of how spinon excitations are produced is provided in Figure 3.2. The 1D chain is shown in an unexcited state in Figure 3.2(a). If one of the $-1/2$ (down) spins in the spin chain is then flipped into the $+1/2$ (up) state (i.e. by the interaction of a neutron), this creates the 1D analog of domain walls between adjacent electrons in the same spin state (labelled with dashed lines in Figure 3.2), which can then propagate along the chain in opposite directions. These pairs of parallel spins are the spinons: they are the quanta of excitation used to describe this phenomenon. It is clear that one single excitation (the changing of one spin state into another) creates two spinons. This means that higher order excitations only take place for even numbers of spinons (four-spinon excitations, six-spinon excitations etc.). In addition to this, since at least two independently propagating spinons are formed in each interaction with a neutron, the total momentum and energy transfer is dependent on the momentum and energy of each spinon. This results in the observation of a spinon continuum, where the measured excitations are not sharp line features in $(Q, \Delta E)$ space, but occupy two-dimensional areas in $(Q, \Delta E)$ space.

3.1.2 The 1D $S = 1/2$ Heisenberg antiferromagnet

The simplest model for spin systems is the Heisenberg model, which is capable of providing an explanation for a variety of phenomena despite its remarkable simplicity. In the Heisenberg model (Equation 3.1) the quantity J_{ij} is the magnetic exchange constant, and is a measure of the strength of magnetic interaction between spins i and j. Magnetic exchange interactions arise from electronic states with different magnetic moments having different energy due to the electrostatic Coulomb replusion of the electrons. In the case of the cuprates, the copper atoms are not adjacent, but have oxygen atoms between them. As a consequence superexchange is responsible for the magnetic exchange, resulting from the overlap of the Cu orbitals with the O orbitals [45]. Often a simplification of the Heisenberg

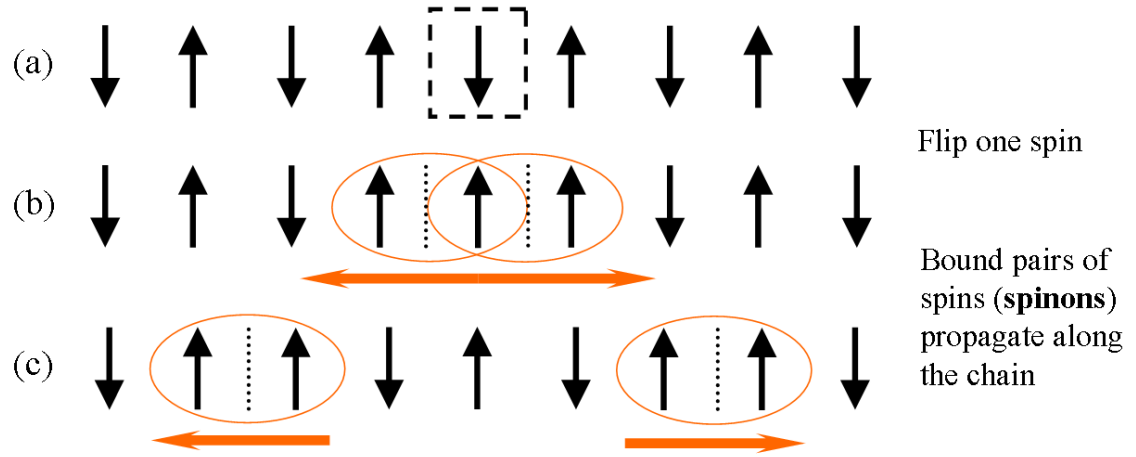

Figure 3.2: A description of the time-evolution of a two-spinon excitation in a one-dimensional $S = 1/2$ chain. Up arrows denote a spin state of $+1/2$, down arrows $-1/2$. In (a) the one-dimensional chain is an unexcited state, but then the system is excited into an excited state (b). This creates bound pairs of spins (spinons), which travel away from each other along the chain (c).

model is used, where J_{ij} is a constant value J for adjacent spins and zero otherwise. This is the form that is used throughout the remainder of this chapter.

$$H = -\sum_{ij} J_{ij} S_i \cdot S_j \tag{3.1}$$

The mathematical framework within which the correlation functions of Heisenberg systems can be found was put forward by Hans Bethe almost eighty years ago [6]. The Bethe Ansatz has been the basis of much of the theoretical work on Heisenberg systems, but the exact calculation of the spin-spin correlation function of a Heisenberg $S = 1/2$ 1D antiferromagnet has proved extremely problematic. The theoretical work done on these systems has always fascinated theorists, as it represents one of the simplest systems imaginable in 1D. In the sixties significant work was done: the lower boundary of the spinon excitation spectrum was found exactly by des Cloizeaux and Pearson [7], and is given in Equation 3.2. Then Yamada was able to show that the excitations of the first excited states (the two-spinon excitations) is a continuum of excitations given by Equations 3.2 and 3.3 [46].

$$E_L = \frac{\pi J}{2}|\sin(Q_{chain})| \tag{3.2}$$

$$E_U = \pi J|\sin(\frac{Q_{chain}}{2})| \tag{3.3}$$

Over ten years after Yamada's work, Müller et al. proposed the Müller Ansatz formulism of the spin-spin correlation function for the $S = 1/2$ 1D antiferromagnet [8], based on the previous work discussed and their own finite-chain calculations. This form of the correlation function, given in Equation 3.4, bootstraps the lower and upper boundaries defined in Equations 3.2 and 3.3 of the spinon continuum via the use of the Heaviside function θ. It also includes a square-root singularity in the intensity at the lower boundary, meaning that the vast majority of the spectral weight contained with the lower and upper boundaries is found just above the lower boundary.

$$S_{MA}(Q_{chain}, \Delta E) = \frac{A}{2\pi}\frac{\theta(\Delta E - \Delta E_L(Q_{chain}))\theta(\Delta E_U(Q_{chain}) - \Delta E)}{\sqrt{\Delta E^2 - \Delta E_L(Q_{chain})^2}} \tag{3.4}$$

Almost twenty years after Müller's work, Bougourzi et al. were able to make the first exact calculation of the two-spinon excitation spectrum [47], which accounts for 71.3% of the total spectral weight of the spinon continuum [9]. The remaining 28.7% is taken up by higher order spinon excitations (four-spinon, six-spinon etc.). So despite the exactness of this solution, it is definitely almost 30% incorrect, and therefore inappropriate to be used as an accurate representation of the spin-spin correlation function.

In the last five years there has been much theoretical progress by Caux and co-workers [48, 9]. They were able to provide the first ever exact description of the four-spinon excitations, as a result of very laborious work involving the evaluation of complex contour integrals in $(\boldsymbol{Q}, \Delta E)$ space [9]. Although their method could be generalised for all possible spinon excitations (not just four-spinon), they found that their calculation of the four-spinon contribution provided about 27(1)% of the total spectral weight, meaning that

only about 2% of the spectral weight is as a result of higher order excitations (six-spinon and above). This means that by simply adding the two exact calculations of the two-spinon and four-spinon calculations together, a version of the spin-spin correlation function for the 1D $S = 1/2$ Heisenberg antiferromagnet is found which is only 2% of the spectral weight away from a full, exact description.

3.1.3 The 1D $S = 1/2$ Hubbard antiferromagnet

In the Hubbard model (for which the Hamiltonian is given in Equation 3.5), instead of describing the magnetic interaction via the magnetic exchange constant J as in the Heisenberg model, we directly represent the competing electrostatic energy scales t and U. t is the energy associated with an electron hopping from one site to an adjacent site, and is summed over all spin states σ and all sites i. U is the Coulomb energy penalty for a site to be doubly-occupied, as this means two electrons have to be put in close proximity. Note that the Hubbard model introduces the idea of electron itinerancy into the system, as in the Heisenberg model the electrons are fixed in their specific lattice sites. It is well-known that if the energy penalty U associated with a doubly-occupied site is extremely large in comparison to t, then the Hubbard model collapses onto the Heisenberg model, and in this special case the magnetic exchange constant J equates to $4t^2/U$.

$$H = -t \sum_{i,\sigma} \hat{c}^{+}_{i,\sigma} \hat{c}_{i+1,\sigma} + U \sum_{i} \hat{n}_{i,\downarrow} \hat{n}_{i,\uparrow} \tag{3.5}$$

The extended Hubbard model is also provided in Equation 3.6, which is the same as the normal Hubbard model except that an additional term is added which includes any effects due to the Coulomb interaction between electrons on adjacent sites. The energy associated with this interaction is V. This is the form of the Hubbard model which was used to produce simulations of the spin-spin correlations function which will be discussed in Sections 3.4.5 and 3.4.6.

$$H = -t \sum_{i,\sigma} \hat{c}^{+}_{i,\sigma} \hat{c}_{i+1,\sigma} + U \sum_{i} \hat{n}_{i,\downarrow} \hat{n}_{i,\uparrow} + V \sum_{i,\sigma,\sigma'} \hat{n}_{i,\sigma} \hat{n}_{i+1,\sigma'} \tag{3.6}$$

3.1.4 The real analogs of $S = 1/2$ antiferromagnets

There are many different materials which are $S = 1/2$ antiferromagnets, but perhaps the most significant in terms of the history of the understanding of spinon excitations in one-dimension is $KCuF_3$, on which many of the early INS studies of 1D $S = 1/2$ antiferromagnets were completed (primarily because it was possible to grow very large single-crystals). In fact the very first confirmation of the spinon continuum was made using INS data from $KCuF_3$ [49], and was later clarified and expanded upon with higher quality INS data again from $KCuF_3$ [50, 40]. Organic magnets have also been studied via INS, including some early work on $CuCl_2{\cdot}2N(C_5D_5)$ (CPC) which observed the lower boundary of the spinon excitations but attributed additional intensity above the boundary to an instrumental artifact [51]. In addition there has been INS work on the two-dimensional $S = 1/2$ organic material $Cu(DCOO)_2{\cdot}4D_2O$, which shows a decrease in the measured intensity ascribed to quantum fluctuations. Perhaps the most studied examples of $S = 1/2$ antiferromagnets tend to be cuprate systems, because of the close relationship to the cuprate superconductors. La_2CuO_4 and $Sr_2CuCl_2O_2$ are good examples of two-dimensional $S = 1/2$ antiferromagnets, whereas Sr_2CuO_3 and $SrCuO_2$ are good one-dimensional examples.

The magnetism in cuprates is a direct result of unpaired electrons in the copper orbitals. Cuprates usually contain CuO_4 groups, in which the copper ion has the charge 2+. One of these holes is in the $4s$ band, and the other is removed from the $3d$ band. Due to the crystal field splitting in cuprates, the $3d$ band with most energy (and therefore the one which ionises most readily) is the $3d_{x^2-y^2}$. This hole in the $3d_{x^2-y^2}$ results in an overall spin of $S = 1/2$ for the copper electrons.

A schematic of the electronic structure of insulating cuprates is provided in Figure 3.3. The difference between the Lower Hubbard (LH) and Upper Hubbard (UH) bands shown is the

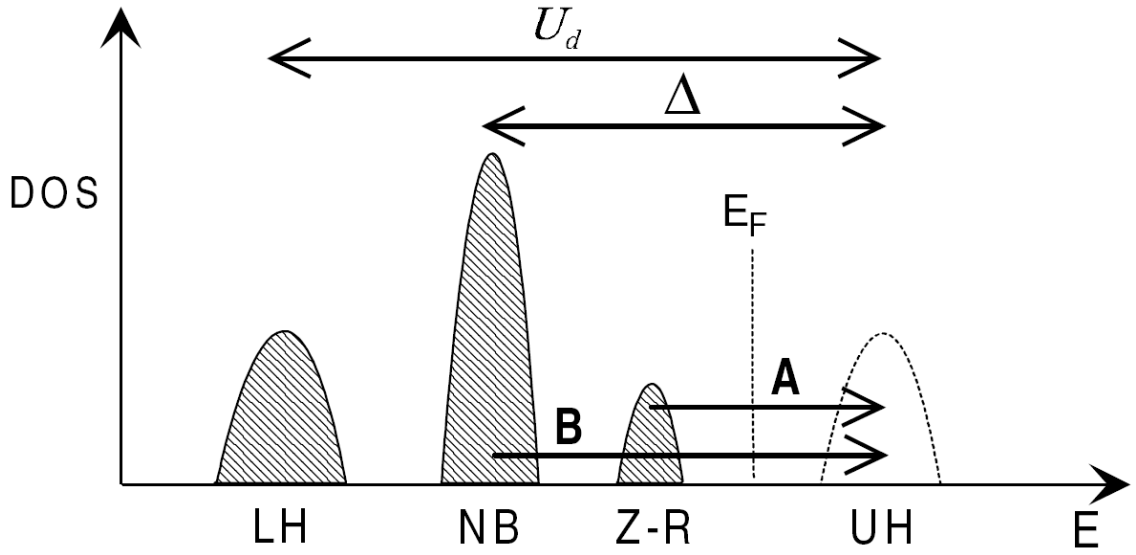

Figure 3.3: A schematic of the electronic density of states for insulating cuprates (also called Charge-Transfer (CT) insulators) such as Sr_2CuO_3. LH: lower Hubbard band. UH: upper Hubbard band. NB: non-bonding O $2p$ band. ZR: ZhangRice singlet band. E_F: Fermi energy. The energy differences UH-LH and NB-LH are of the same order as the Coulomb interaction of the Cu ions U_d and the energy seperation between the Cu $3d$ and O $2p$ orbitals Δ respectively [44].

additional energy of a Cu site if an additional electron is added to the system. The band labelled NB is due to the O $2p$ orbital which is not involved in the bonding with the copper (NB = Not Bonding). The ZR band is due to the appearance of the Zhang-Rice singlet [52], which results from the combination of the strong Coulomb interaction of the Cu ions combined with the strong hybridisation of the Cu $3d_{x^2-y^2}$ and O $2p_\sigma$ orbitals. The Zhang-Rice singlet is formed by a hole carried over the four oxygen atoms binding strongly to the Cu^{2+} ion. In a material such as Sr_2CuO_3, which is not overdoped with electrons or holes, it may seem strange that effects which appear from hole doping might be prevalent, but when the band-structure is studied experimentally (e.g by optical conductivity) the experimenter necessarily excites electrons from occupied states to unoccupied states, thereby creating holes in the system.

The key result in Figure 3.3 as far as this investigation is concerned is that the lowest charge excitation is the excitation labelled A, when an electron is excited from the Zhang-Rice singlet band into the Upper Hubbard band. Both optical conductivity and infrared

absorption are sensitive to this excitation, and in most real materials, its energy is approximately 2 eV [44]. This energy is far larger than the usual scale of the spin excitations J, which is more variable but is usually no larger than 100 meV. So in the vast majority of real systems, there is a dramatic difference in the charge and spin energy scales. This means that regardless of any consideration of the peculiarity of spin-charge separation in 1D, the difference in energy scale alone makes the charge and spin excitations independent. Unusually, in Sr_2CuO_3 (and in the related material $SrCuO_2$), these energy scales are not so different, and the question here is whether is it possible to see any influence on the magnetic excitations arising from the proximity of the charge excitations.

3.2 Introduction to Sr_2CuO_3

Sr_2CuO_3 is often described as a very good example of a 1D $S = 1/2$ antiferromagnet. Since the Néel temperature of Sr_2CuO_3 has been measured to be $T_N = 5$ K, the ratio of the intrachain magnetic coupling J to the interchain coupling J' can be calculated. J/J' is found to be over 10^5 [53]), making this material one of the best realisations of a truly one-dimensional $S = 1/2$ antiferromagnet. $KCuF_3$, another 1D antiferromagnet which has been studied extensively, has a somewhat lower value of J/J' of 10^2 [54], so Sr_2CuO_3 is a much better example of the idealised 1D model. It has been found that Sr_2CuO_3 also has interesting properties which are unconnected with its similarity to some of the superconducting cuprates, including a large increase in heat conductance in the chain direction mediated by the spinon excitations [55] and the appearance of ultrafast optical nonlinearity [56].

Sr_2CuO_3 has an orthorhombic structure, space group $Immm$, and is shown in Figure 3.4. The 1D chains are formed by corner sharing squares of CuO_4, and are in the b axis direction in the orientation of the crystallographic axes given in Figure 3.4. From neutron diffraction measurements at 11 K the lattice parameters of Sr_2CuO_3 have been found to be $a = 12.6910(7)$ Å, $b = 3.9089(2)$ Å and $c = 3.4940(2)$ Å[53] (the labelling of the axes in this thesis is different to that in the reference).

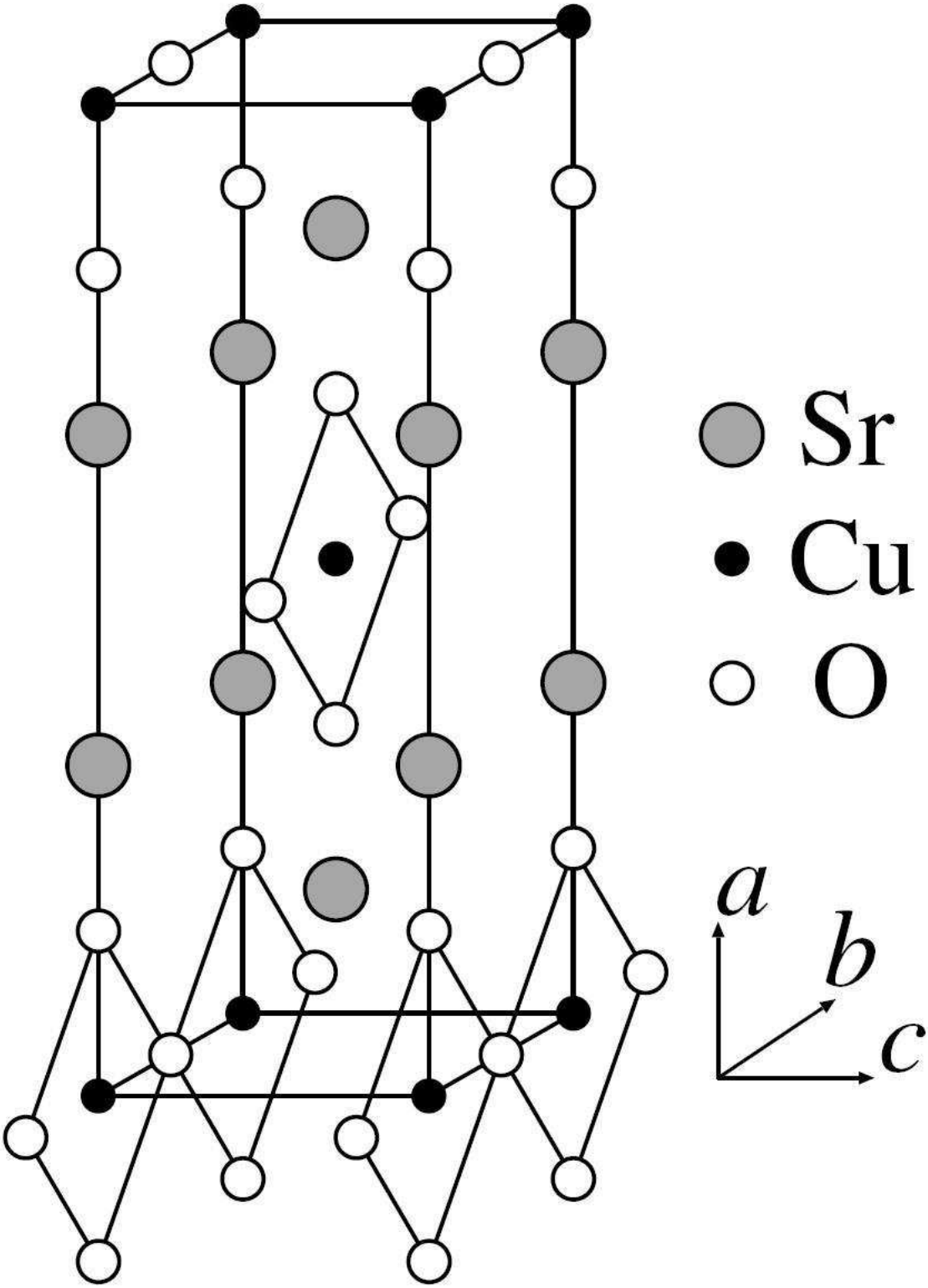

Figure 3.4: Structure of Sr_2CuO_3 [56]

There have been many different experimental investigations which have put forward different values for the intrachain coupling J for Sr_2CuO_3, including magnetic susceptibility measurements [53, 57], photoemission [58, 59]and infrared optical absorption measurements [60]. There is some inconsistency in these results, with some of the earlier studies giving a value of J which is less than half of more recent values. Prior to this study, the overall agreement in the literature was that J lay in the region 0.2 to 0.26 eV, with the most recent photoemission study estimating $J \approx 0.26$ eV [59]. It is not clear why the J in Sr_2CuO_3 (and in the related compound $SrCuO_2$, where $J = 0.226$ eV [10]) is so large in comparison to other analogous materials [61].

Since the measured optic gap Δ can be approximated as $\Delta \approx U/2$, we can find the hopping integral t from the Hubbard model provided we know J and U, as $J = 4t^2/U$ in the $U/t \rightarrow \infty$ limit (see Section 3.1.3). Taking J as 0.26 eV and U as 3.0 eV (based on measurements of the optic gap to be 1.5 eV from infrared absorption and photoemission [56, 58, 59]), t is found to be 0.44 eV. This means that for Sr_2CuO_3 the ratio U/t is just ≈ 7. In most real analogs of $S = 1/2$ 1D antiferromagnets, U/t is of the order 10^2, and therefore the phenomenon of spin-charge separation can be understood quite readily since the energy scales are so dramatically different. This means that Sr_2CuO_3 is an excellent system in which to explore itinerant effects on the spin excitations in the 1D Hubbard model.

The effects of itinerancy on the spin excitations of a 1D Hubbard chain were studied theoretically in a recent paper [62], which primarily discussed the two extreme cases where $U/t \rightarrow \infty$ and $U/t \rightarrow 0$. They concluded that (as already known [8]) in the $U/t \rightarrow \infty$ case the maximal intensity within the two-spinon boundaries is located at the lower boundary, but found that in the $U/t \rightarrow 0$ case a significant amount of intensity is located near the upper boundary. This is shown pictorally in Figure 3.5. The intensity plot for $U/t = 0.4$ in Figure 3.5(b) is somewhat misleading, as the divergence seen at the lower boundary in the $U/t \rightarrow \infty$ limit still exists in the $U/t = 0.4$ case, but is missing because of an approximation used in the calculation. Nevertheless, the observation remains that additional spectral weight shifts towards the upper boundary of the spinon continuum. Another significant result is that the energy scale in these two cases is different: in Figure 3.5(a) the continuum

reaches πJ, whereas in Figure 3.5(b) it reaches $4t$. However in the case of Sr_2CuO_3, where $U/t = 7$, such energy renormalisations of the spinon continuum boundaries are predicted to be minimal. However, the suggestion was made that in INS studies of Sr_2CuO_3 and $SrCuO_2$ there should be evidence for electron itinerancy effects, even in the region of the lower boundary of the spinon continuum [62]. This constitutes the primary motivation for our study of Sr_2CuO_3.

Prior to my PhD, my collaborators had already completed a detailed INS study of the spinon excitations in $SrCuO_2$ [10]. These measurements had shown that there was a clear discrepancy between the Müller Ansatz and reality, as the measured intensity was reduced by over a factor of two [10]. Due to the magnetic form factor of the Cu^{2+} ion in Sr_2CuO_3 (to be discussed in detail later in this chapter), the higher energy spin excitations are difficult to measure on a chopper spectrometer at a pulsed neutron source such as MAPS. This means that a transfer of spectral weight from just above the lower boundary to just below the higher boundary may manifest itself in real data as a decrease in the measured intensity.

In our Sr_2CuO_3 study we aimed to study the itinerancy effects in more detail by collecting considerably better quality INS data with far more sample than the previous $SrCuO_2$ INS study had used. This would allow us to measure the spinon excitations with much higher resolution than had ever been achieved previously at such high energy transfers (> 200 meV).

3.3 The details of the INS experiment

The Sr_2CuO_3 sample consisted of three crystals, of total mass 18.45 g, all of which were grown using the travelling solvent-floating zone method at Brookhaven National Laboratory by Genda Gu. Two of the crystals, crystals A and B, were grown in oxygen at 11 bar and had masses 5.80 g and 5.88 g respectively. The third, crystal C, was grown in air and had a mass of 6.77 g. To make single-crystal measurements of Sr_2CuO_3, these three crystals needed to be coaligned. Before the samples were shipped to the UK, an upper limit

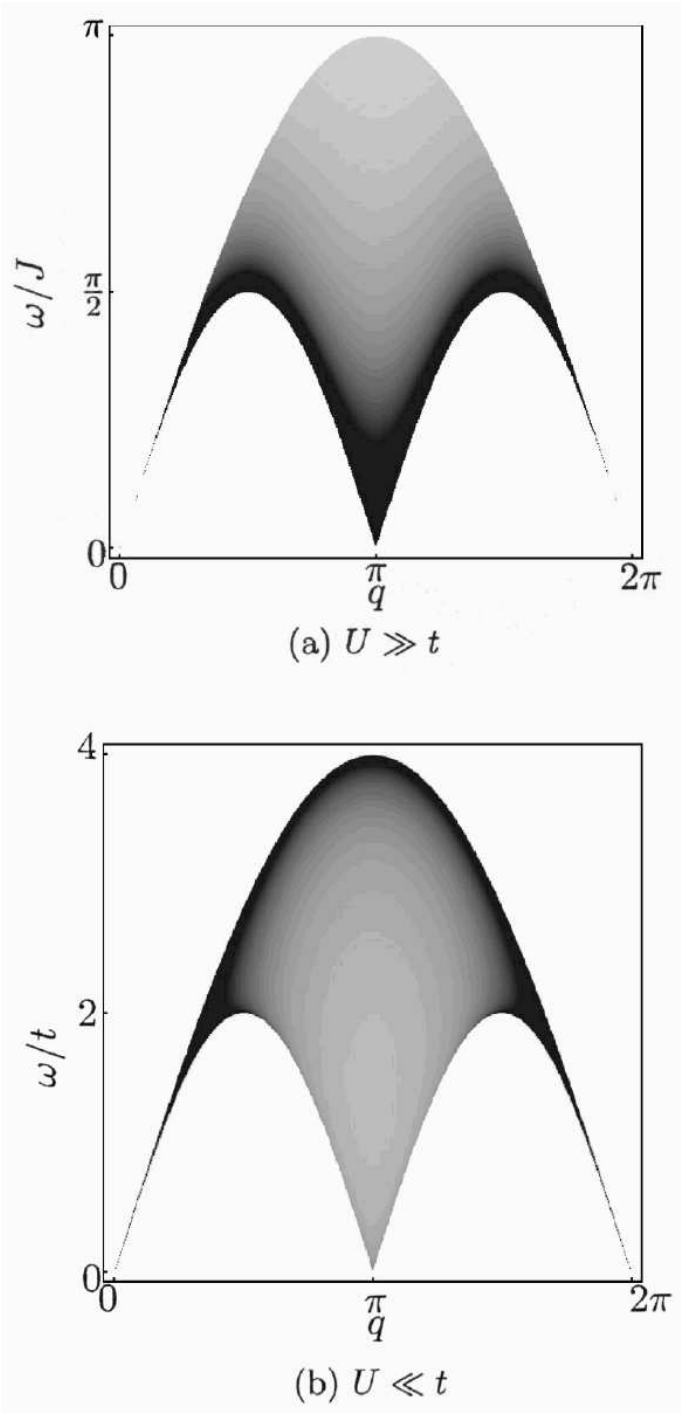

Figure 3.5: Theoretically calculated intensity plots of the spin-spin correlation function for a Hubbard $S = 1/2$ chain: (a) $U/t \to \infty$, (b) $U/t = 0.4$ [62].

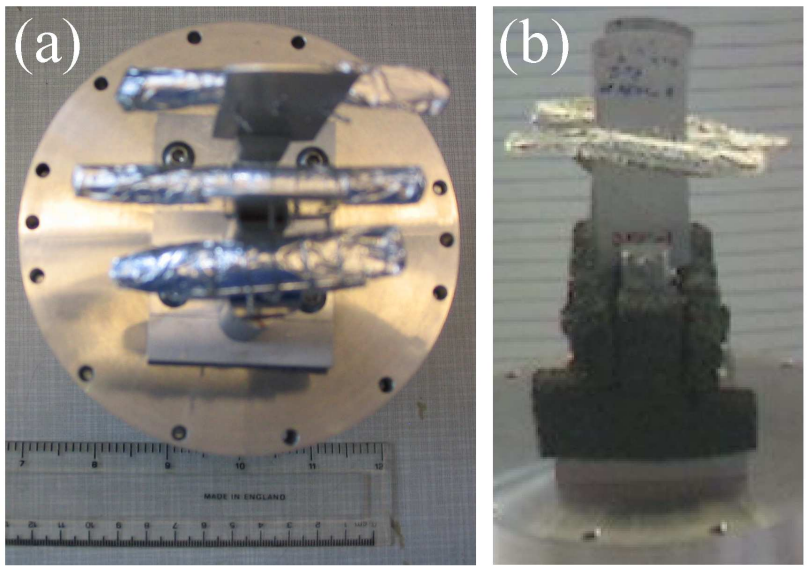

Figure 3.6: Photos of the three mounted Sr_2CuO_3 samples after coalignment on the underside of the lid of an aluminium can as discussed in the main text. Note that the samples are wrapped in aluminium foil. (a) is a top view of the samples prior to the B_4C shielding being put in place, and (b) is a side view of the samples, together with the B_4C shielding as it was positioned for the INS measurements.

to the mosaic of the samples was found using neutron diffraction. These measurements were done at the High Flux Isotope Reactor at the Oak Ridge National Laboratory, USA. Both crystals A and B had Bragg peaks of full-width half-maxima (FWHM) - also called the mosaic - of about 1/3 of a degree, and crystal C had an even smaller mosaic of about 1/4 of a degree. The samples had been wrapped in thin aluminium foil, which in turn were mounted on aluminium plates on aluminium posts via a small set screw.

An aluminium sample mount was designed for the three samples, which fixed onto the underside of a lid of a aluminium can of diameter 70 mm, as shown in Figure 3.6. This required careful measurement of all the constituent parts: the shape of each sample, the size of the aluminium plates that the samples had been mounted on, the diameter of the cylindrical aluminium posts (measured in Imperial measurements in the USA) so that it would fit inside the can. In Figure 3.6(b), the B_4C shielding made up can also be seen. This was put in place to absorb any neutrons (boron is an excellent absorber of neutrons) which would otherwise interact with the aluminium posts supporting the samples, thereby

reducing any background due to the aluminium. This shielding also acted to absorb any incoming neutrons which were not incident on the sample, and reduce any effects due to multiple scattering.

The coalignment of the three samples was done on ALF, an instrument at ISIS maintained specifically for coaligning multiple single crystal samples. We found that the individual alignment done in the US had been adversely affected in transit, changing the relative alignment of the samples by up to 5° in all directions. The morphology of the samples aided the alignment, as the chain axis b^* was along the major axis of the samples, which all had a approximately cylindrical shape. After aligning the first sample so that the a^* axis was in the vertical and the chain axis b^* was in the horizontal, that sample was then coaligned with one of the others, before finally all three samples were coaligned. Although the flexibility of the aluminium plates allowed the relative alignment of any sample to be altered about any axis, the lack of a precise goniometer for each sample did cause problems. On several occasions the attempted adjustment of the position of the sample in one direction caused the sample to relax in the opposite direction due to the elasticity of the aluminium. However, having three goniometers in the sample can would have caused its own set of problems, as it would have almost certainly added to the observed incoherent and phononic background, and would have to be very small to fit into the MAPS aluminium can. Such goniometers are also somewhat expensive.

After the samples were coaligned on ALF, the combined sample was then sealed with indium wire in an aluminium can. This was done in a helium atmosphere using a glove bag in order to eliminate any subsequent background from frozen water had the sample had been cooled to liquid helium temperatures in air. The aluminium can also provided an extra radiation shield to aid the sample cooling, and was made only 2 mm thick, so reducing any INS background from it.

Using a white (polychromatic) incident neutron beam with the slits (also called jaws) before the sample fully open (55 mm by 55 mm), the coaligned sample was aligned relative to the MAPS spectrometer such that the chain axis b^* was perpendicular to the incident neutrons. This was done in order to maximise the amount of scattering from

the chain and also maximise the sensitivity of the detector banks, as a small momentum transfer perpendicular to the incident neutron momenta results in the maximum amount of deviation in the neutron's trajectory. Other considerations also pin down whether the incident neutrons should be parallel to the a^* or the c^* axis. In any neutron scattering experiment, the magnetic form factor acts to decrease the observed magnetic intensities as the momentum transfer Q increases. In the Cu^{2+} ion, as with many other transition metal ions, the electron density is very anisotropic. This is because the magnetic electrons are in the $3d_{x^2-y^2}$ orbitals, which is very two-dimensional. Since the magnetic form factor is the Fourier transform of the electron density, this means that the magnetic form factor is also very anisotropic. As the spinon continuum of excitations extends to very high energy transfers (up to around 800 meV), we aligned the sample such that the magnetic form factor decreased slowly as a function of momentum transfer parallel to the incident beam, as this is the direction which is most directly coupled to energy transfer.

Once the coaligned samples had been aligned in MAPS with the b^* axis perpendicular to the incident beam as discussed, the physical extent of the samples in the plane perpendicular to the incident beam direction (the a^*b^* plane) was calculated in order to best optimise the position of the jaws. The smaller the incident beam, the fewer neutrons which could add to the observed background. The size of the combined sample was calculated from the measurements made of the samples during the design of the sample mount. We opted to keep the horizontal jaws as wide as possible (55 mm), whilst making the vertical separation 21.5 mm, the minimum width required to illuminate all three samples. The intensity of the Sr_2CuO_3 (020) peak did not change with the jaws fully open and with the jaws in the new position, confirming that all of the samples were still illuminated with the smaller incident neutron beam.

The FWHM of the energy resolution at MAPS scales approximately linearly with incident energy, so although the lower incident energies were only able to probe the spinon excitations below the incident energy of the neutrons, the energy resolution in the region of (Q,ΔE) space probed was much better. Since the INS cross-section for phonons approximately scales as Q^2 (as it does in the IXS phonon cross-section in Equations 2.14 and 2.15), the larger incident energies also produce higher phononic backgrounds as the

average magnitude of Q is larger. The choice of chopper frequency for each incident energy was informed by the CHOP program, written by Dr Toby Perring of ISIS. This program calculates the inelastic resolution, the elastic linewidth and the incident flux once the incident energy, choice of chopper and chopper frequency are specified. Typical CHOP output is plotted in Figure 3.7.

Firstly the lowest chosen incident energy - 240 meV - was used, as the number of neutrons which enter the MAPS spectrometer with 240 meV is much higher than at higher incident energies, and therefore we would be able to ascertain more quickly whether or not the spin excitations being measured were along the lines that we expected. We then incrementally increased the incident energy on MAPS to 516 meV and then 794 meV, with the incident flux accordingly decreasing each time, until finally spending over four days of beamtime at an incident energy of 1088 meV.

For each incident energy, multiple datasets (or runs) were added together to increase the statistical quality of the data. However, in the case of two of these runs (one at 794 meV and one at 1088 meV) the Nimonic chopper frequency was accidentally set to 50 Hz, thereby blocking some of the neutrons which could be usefully monochromated by the Fermi chopper. We corrected for this by comparing the integrated intensity over an area in (Q,ΔE) space with no magnetic scattering when the Nimonic chopper was at 50 Hz and 100 Hz. The ratio of these two integrals then provided a scale factor to multiply by the 50 Hz run so that it was put on the same absolute intensity scale as the 100 Hz run.

3.4 Analysis

3.4.1 Initial choices

Before starting to fit such a large dataset, a choice needed to be made concerning how this was to be achieved. The most obvious way would be to fit each entire dataset (at each of the four values of E_i) directly to the calculated INS intensity. However, if done as a first step, this would be very likely to be a very crude fit to the data since there is a large

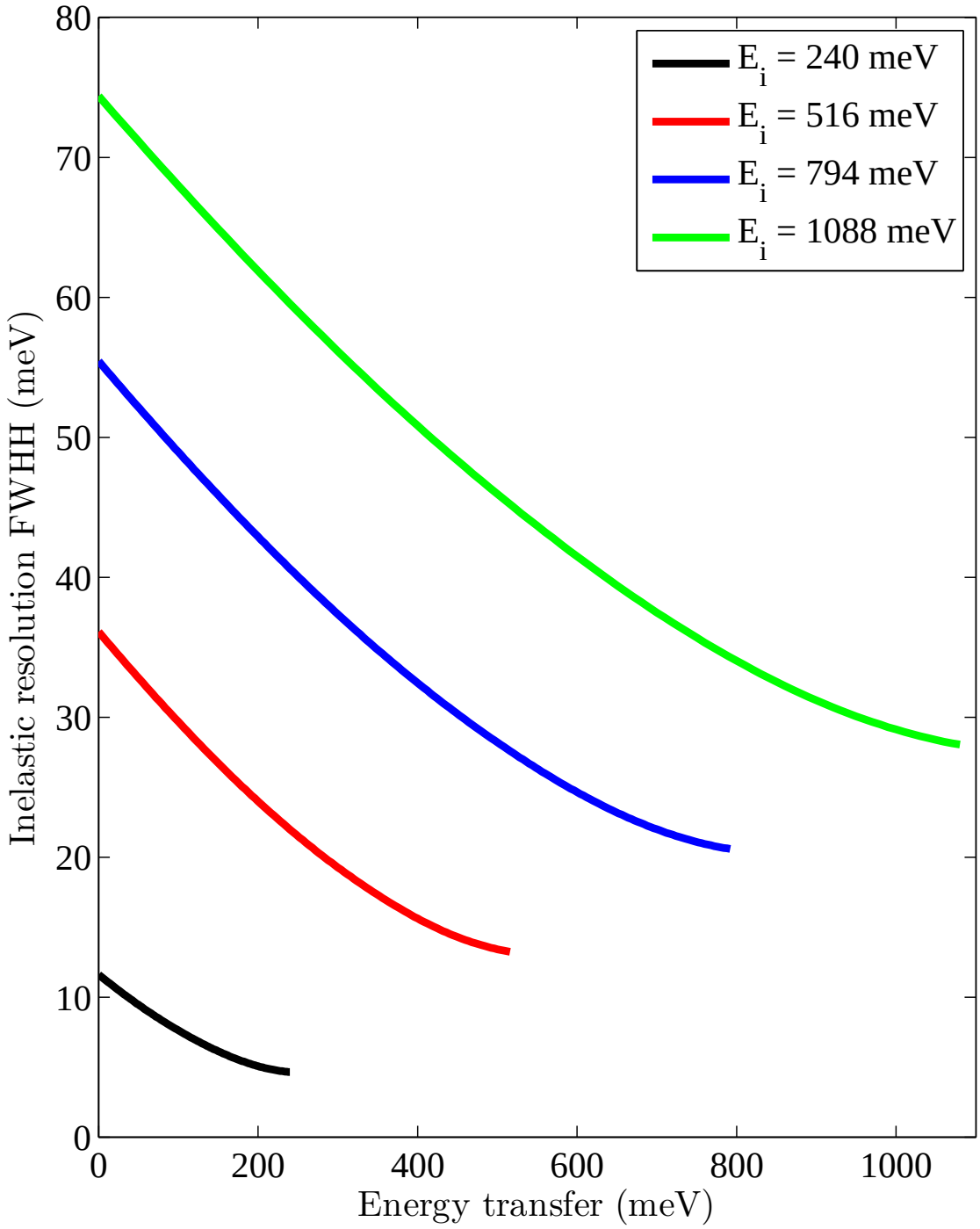

Figure 3.7: Simulated inelastic resolution for each incident energy E_i which was used at MAPS (based on output from CHOP program written by T. G. Perring).

amount of aluminium in the beam due to the sample mount. A more pragmatic approach would be to divide each dataset into smaller, more manageable parts which can be fitted separately. This approach takes advantage of the large datasets acquired using a chopper spectrometer at a pulsed neutron source such as ISIS, as we can use data from seemingly less interesting areas of (Q, E) space which provide more information about the behaviour of the background.

The datasets were fitted by fitting independent Intensity v Q_k 'cuts' through the data, integrated over short ranges in both ΔE and Q_h. Here Q_k is the momentum along the chain, and Q_h is the momentum perpendicular to the chain and perpendicular to the incident neutrons. These cuts take advantage of the sharp boundaries in the spinon excitations, allowing the magnetic signal to be easily separated from the background. If Intensity v ΔE cuts were fitted (integrated in both Q_k and Q_h) then although there would still be two sharp boundaries in the magnetic intensity, it would be very difficult within the spinon continuum to separate magnetic signal from the background. An additional - but possibly more mundane - reason to fit cuts rather than the entire dataset is due to the issue of computation time. To fit an entire summed MAPS dataset (approximately 100 Mb) to a simulated dataset would take days or weeks of computation time on a single high-specification personal computer, whereas a fit to a cut with ~ 100 Q_k positions with associated intensities and errors takes about 90 minutes (when including the time to simulate the complex resolution function of a chopper spectrometer). Finally, the choice of fitting Intensity v Q_k cuts meant that any strong energy dependence of the background could be ignored, as all the data which were summed to produce the cut are necessarily within a small range in energy transfer.

The integration width in energy transfer was chosen based on the simulated inelastic resolution calculated by the CHOP program. There is little value in the integration width in energy transfer being smaller than the inelastic energy resolution at that energy transfer, as no information is lost by increasing the integration width. However, if the integration width is made much larger than the resolution then there is a danger of averaging out any useful energy dependence in the data. Clearly a compromise has to be made between these two extremes. As can be seen in Figure 3.7, the inelastic energy resolution decreases as a

function of energy transfer, so one could imagine that the energy transfer integration width could be chosen in a similar, energy transfer dependent way. However for simplicity, one energy transfer integration width was chosen for each dataset measured using a specific E_i. The choices we made can be seen in Appendix A.

The range of the energy transfer centres of the cuts for each dataset was done with reference to the relative size of the magnetic signal to the background, and also on the quality of fit attained for each cut. The choice in the energy transfer centres is also documented in Appendix A. No cuts with an average energy transfer below 60 meV were used, as the phonons in aluminium are prominent up to 40 meV, and in chopper spectrometers multiple scattering can occur, creating INS intensity due to multi-phonon processes which can be even higher in energy transfer. On a time-of-flight chopper spectrometer like MAPS, the background also increases at the highest energy transfers at each E_i. This is because the neutrons which correspond to extremely large energy transfer are those which have an extremely low final energy E_f, so all neutrons (regardless of their scattering history) which enter the detectors at very slow speeds end up contributing to the measured background in this region.

The integration limits in Q_h, length of the Q_k cuts and the size of the Q_k bins for each cut were all relatively fluid throughout the data analysis. Once again there was a compromise to be made between fitting more data in each cut (by maximising both the integration limits for each E_i and the length of the Q_k cuts) and using fewer data over which it may be easier to describe the background. In the end, the same integration range ($-8 < Q_h < 8$) was used for all values of E_i, as it was a reasonable choice which enabled high-quality fits, but in addition highlighted in itself the arbitrariness in any choice made. At an energy transfer ΔE of 160 meV in the $E_i = 1088$ meV dataset (the lowest energy transfer fitted at this E_i) the maximum range in Q_h was ± 14.7. This can be directly seen in Figure 3.10. This limit in the integration range in Q_h could be said to be relatively conservative in this case. However the description of the background becomes much less accurate at higher Q, hence the fairly restrictive integration range.

The size of the Q_k bins was initially chosen based upon the smallest values which did

not produce any odd binning effects in the MatLab software package MSLICE [63], which adopts a simple summation approach to rebinning which can cause issues with smaller bins. These initial choices were in many cases modified based on the goodness of fit to each cut: i.e. if the reduced χ^2 was much less than one, the bins may be too large (the data may have been 'overbinned'), thereby washing out some of the detail in the data. Conversely, a large χ^2 may suggest the bins are too small - the data have been 'underbinned'. It is clear that the dialectic between data preparation and data analysis is very important in this instance.

Once the initial choices had been made about the cuts, some checks of the symmetry of the data were performed. Two such checks can be seen in Figure 3.8. Figure 3.8(a) one cut has been created by integrating over all Q_h in the positive direction (plotted in black) and the overlaid cut is a result of integrating in the negative direction (in red). If the sample was misaligned, then the magnetic peaks in these cuts would not lie on top of each other. Likewise, we can check the alignment by plotting the cut measured in the negative Q_k direction on the same axis as that measured in the positive direction (shown in Figure 3.8(b)). Within the accuracy of these measurements, the alignment looks very good.

Much of the early analysis centred on improving the understanding the four datasets by making slices and cuts through the data. This proved to be extremely important, especially in aiding the development of modelling the background. In Figure 3.9 four constant energy slices are presented for each E_i which are centred around zero energy transfer. By using these slices, MAPS can be used as a diffractometer. The information is largely the same in all the slices, although the gaps in the detectors occur at different momentum transfer since the E_i is different in each case. The huge scattering intensity from aluminium is very clearly seen in the powder rings. These primarily come from the sample mount as opposed to the sample can, since the energy selection is done via the time-of-flight method (see Section 2.7), so any neutrons elastically scattered from the can would appear at some non-zero energy transfer. Throughout the analysis we have assumed that all the incident neutrons are scattered at the sample position.

Figure 3.9 also helps to elucidate another early decision made in the analysis. When

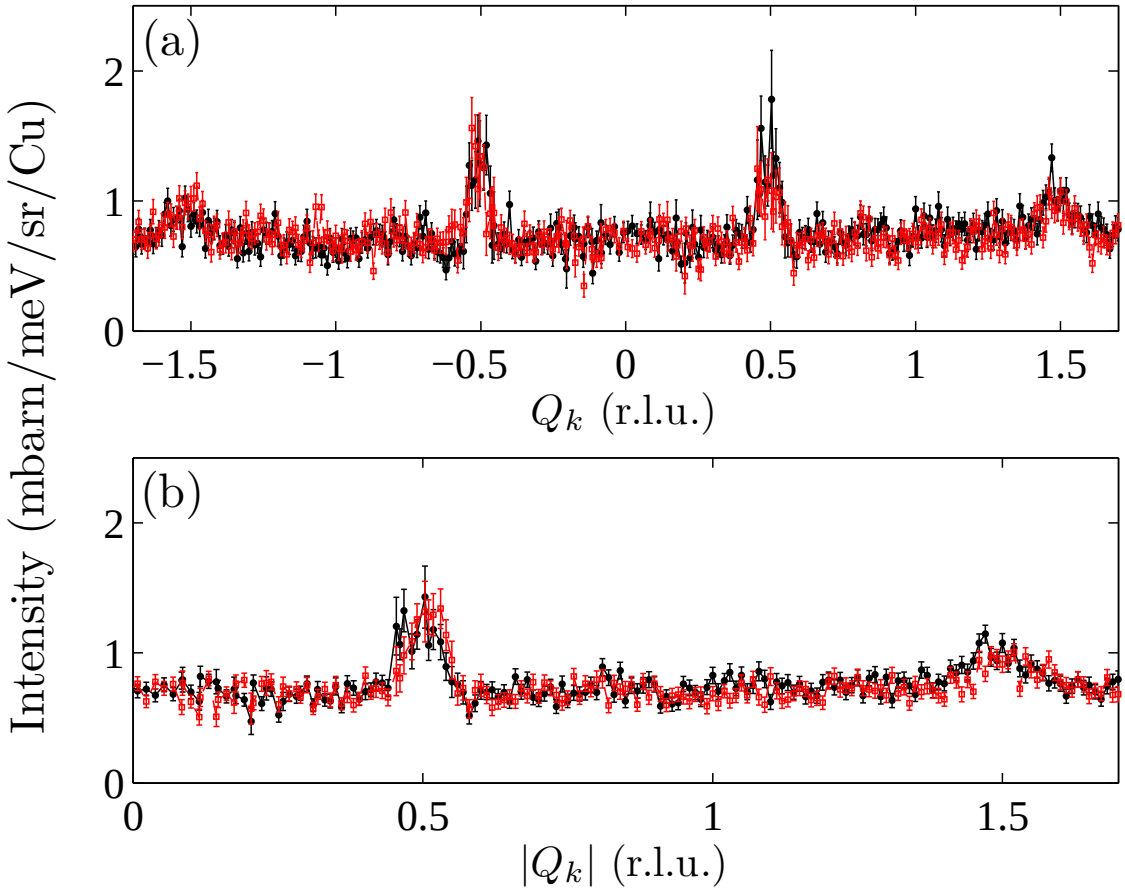

Figure 3.8: Testing the symmetry of the MAPS data: (a) Two Q_k cuts integrated between different ranges in Q_h, black was integrated between -8 and 0 (r.l.u.), and red was integrated between 0 and 8 in Q_h. (b) Two Q_k cuts, black was measured in the positive Q_k direction, red in the negative Q_k direction. Note the effect of the magnetic form factor decreasing the magnetic intensity at higher Q.

modelling the background, an increase in the background around $Q_k = 0$ was observed, especially in the lower energy cuts. This resulted from the tails of the large (020) and $(0\bar{2}0)$ peaks (seen in the smallest detector banks at low Q in Figure 3.9(a)) extending to larger energy transfer because of the relatively large energy resolution at low energy transfer. This effect proved difficult to model, not just because it was so localised in Q, but because the problem was completely different at different values of E_i. At $E_i = 1088$ meV the energy resolution is at its worst, so one would assume this problem would be maximised. However the chosen incident energy happens to place the (020) and $(0\bar{2}0)$ peaks in a gap in the detectors (see Figure 3.9(d)), thereby removing the problem. The biggest problems came at $E_i = 240$ meV and $E_i = 794$ meV (Figure 3.9(b) and (c)), as in these datasets the diffraction peaks are on the edge of the detectors. This means that any slight misalignment of the sample is intensified, as you are not integrating over the whole of the peak. Consequently the background (for constant energy cuts at low energy transfer) is extremely anisotropic in Q_h at these incident energies. Because of these difficulties, all data measured in the small detector banks were removed from the final datasets. This decision meant that the statistical quality of the data was reduced around $Q_k = 0$, but the formulation of the background was much simpler.

Initially, each cut was fitted to an equivalent cut through the Müller Ansatz [8] added to a background, once that had been convolved with both the analytic form of the Cu^{2+} ion magnetic form factor [31] and with the instrumental resolution function. This was all done within the TobyFit program (see Section 2.7). The parameters which were allowed to vary for each cut were:

- The intensity scale factor A, originally defined by Müller et al. [8] in their definition of the Müller Ansatz
- The magnetic exchange coupling constant J, from the Heisenberg model(see Section 3.1.2)
- Background parameters (dependent on the particular functional form of the background being used)

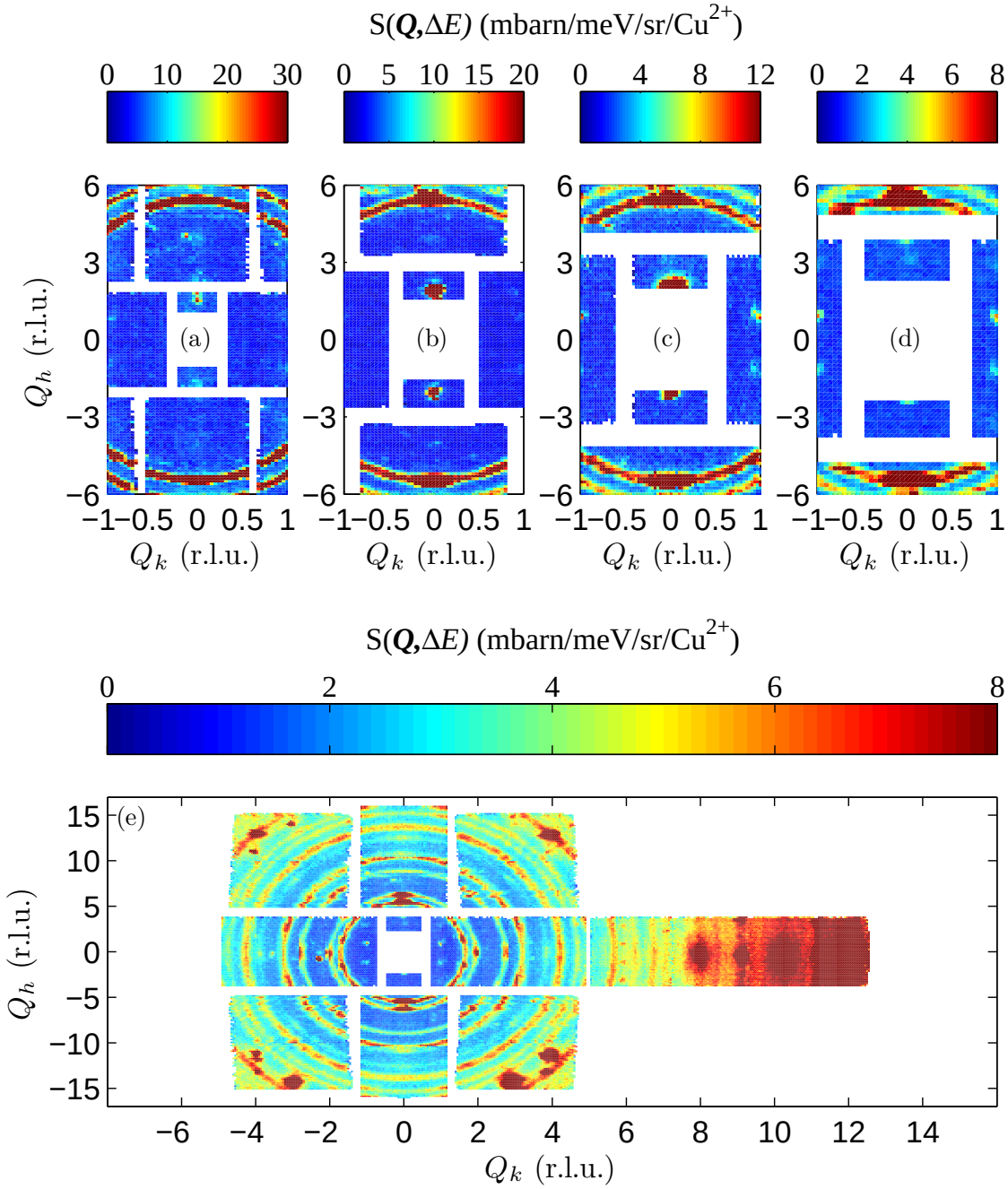

Figure 3.9: Diffraction data from MAPS at different incident energies: (a) $E_i = 240$ meV (b) $E_i = 516$ meV (c) $E_i = 794$ meV and (d) $E_i = 1088$ meV. (e) Diffraction from the entire momentum range probed in the $E_i = 1088$ meV dataset. The shape of the detector banks is plain to see, albeit slightly distorted by the transformation to $(\boldsymbol{Q}, \Delta E)$ space.

The quality of the fit to each cut was ascertained with recourse to the outputted correlation matrix and the reduced χ^2. A script was written in MatLab which reads the output fitted parameters with their associated errors and could plot them as a function of energy transfer. Plotting the fitted intensity scale factor A and magnetic exchange J in this way also gives a sense of the overall quality of fit: ideally both A and J should be completely independent of energy transfer, so these plots should give flat lines. In addition, we know that the A should have a value somewhere between 1 and 1.5 in the Müller Ansatz, from arguments due to spin sum rules [8] [64], and J should be approximately 260 meV from previous experimental studies discussed in Section 3.2. Any deviations from these known values serve to highlight issues in the quality of the fit of the data to the theoretical model.

3.4.2 Formulation of the background for each constant energy cut

The background (i.e. all of the scattering which is not inelastic magnetic scattering) constitutes the vast majority of the entire signal. It is produced via many different processes, the most prevalent being coherent scattering due to phonons and Bragg peaks and incoherent scattering, which manifests itself as a very broad feature centred at zero energy transfer at all Q. It is therefore very important that the background is well described, as otherwise it is very difficult to be certain about any conclusions drawn about the magnetic scattering.

The first stage in the analysis was to simply try a flat, one parameter background to each cut, to see how much the cuts varied from this simplistic background. This initial fitting of the data also allowed any initial problems with the fitting in TobyFit to be ironed out. This first iteration gave a surprisingly good fit to many cuts in the $E_i = 240$ meV dataset, but in other cuts failed to deal with the increase of the background as the magnitude of Q_k increased.

The simplest background which increases as the magnitude of Q_k increases is a background which is proportional to Q_k^2. However, if we study the background using constant energy slices, it is clear that the background does not just increase as a function of Q_k, but as Q_h as well. One such constant energy slice is shown in Figure 3.10. The increase in the

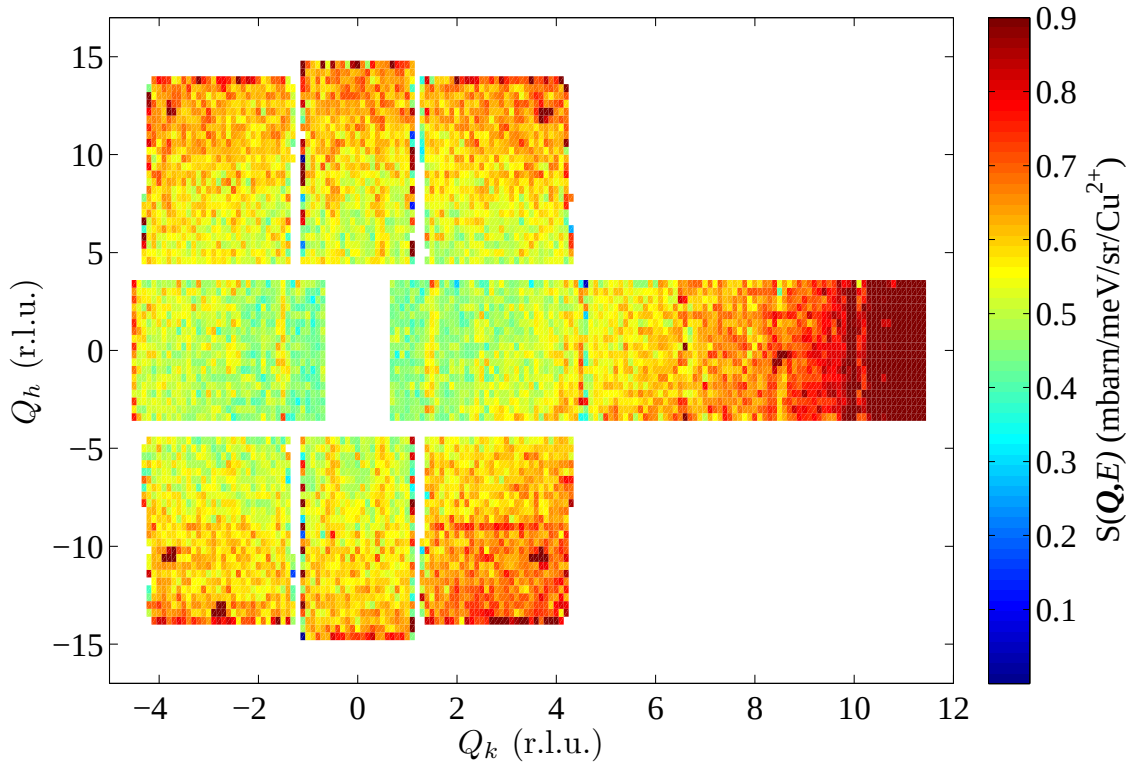

Figure 3.10: A constant energy slice through the $E_i = 1088$ meV dataset, centred at 160 meV. An increase in the background as a function of increasing Q can be observed.

background can clearly be seen as a function of Q_h and Q_k. TobyFit allows the background to be dependent on the scattering angle 2θ, so to a first approximation we can include a term in the background which is proportional to θ^2. If the additional term had been made proportional to θ, there would have been an unphysical discontinuity in the background at $\theta = 0$. This $A + B\theta^2$ background was much more successful than the flat background in its description of the data.

In Figure 3.11 a representative constant energy cut is shown, plotted with the appropriate fits done in TobyFit using different formulations of the background. In Figure 3.11(a) the fit to a constant background is shown, with the discrepancies with the data which have been discussed. Then in Figure 3.11(b) the fit to the $A+B\theta^2$ background is displayed. This background introduces sudden changes in the background to each fit, despite it only being dependent on the scattering angle 2θ. In Figure 3.12 the reason for these discontinuous

changes in the background can be understood. The constant energy slice in Figure 3.12(a) shows the data (as a function of Q_h and Q_k) which are summed together to produce the constant energy cut in Figure 3.12(b) at 160meV from the $E_i = 794$ meV dataset. Starting from $Q_k = -2$, we can see that data from three detector banks are summed together in the final cut, with a relatively large average value of θ. As Q_k goes from -2 to -1.4, the average magnitude of θ decreases continuously. Between -1.4 and -1.1 the two detector banks at higher Q no longer contribute to the cut, meaning the average value of θ is now smaller and so the background is accordingly reduced in this narrow range in Q_k. At -1.1 in Q_k, two detector banks at non-zero Q_h contribute to the cut in Figure 3.12(b), increasing the average value of θ and therefore increasing the background. As Q_k increases to about -0.6, the background becomes gradually smaller as the average value of θ is decreases. Finally, from $Q_k = -0.6$ to 0.6 there are no detectors around zero Q_h (as this would be the straight-through beam position), so the average value of θ is relatively large, resulting in a large background in this range. Since the detector banks are symmetrical in the mirror plane defined by the Q_h and Q_l axes, the background is largely symmetrical in Q_k (Q_k=$-Q_k$).

Fitting all of the constant energy cuts with the $A + B\theta^2$ background resulted in a far better fit of the data, but there were still clear discrepancies, especially at some of the higher energy transfer cuts measured using incident energies of 794 meV and 1088 meV where a linear increase in the background as a function of Q_k could be observed. This asymmetric background is likely to be due to slight differences between the positioning of the B_4C shielding on either side of the sample mount. To account for this asymmetry in the background, an extra term in the background was introduced for each cut, as defined in Equation 3.7 . This background gave reasonable agreement at all incident energies and energy transfers, but the largest remaining discrepancy was around $Q_k = 0$, where the simulation consistently underestimated the measured INS intensity. The true origin of this discrepancy is discussed later in this chapter in Section 3.5.

$$S_{\text{back}}(Q_k, \theta) = A + BQ_k + C\theta^2 \tag{3.7}$$

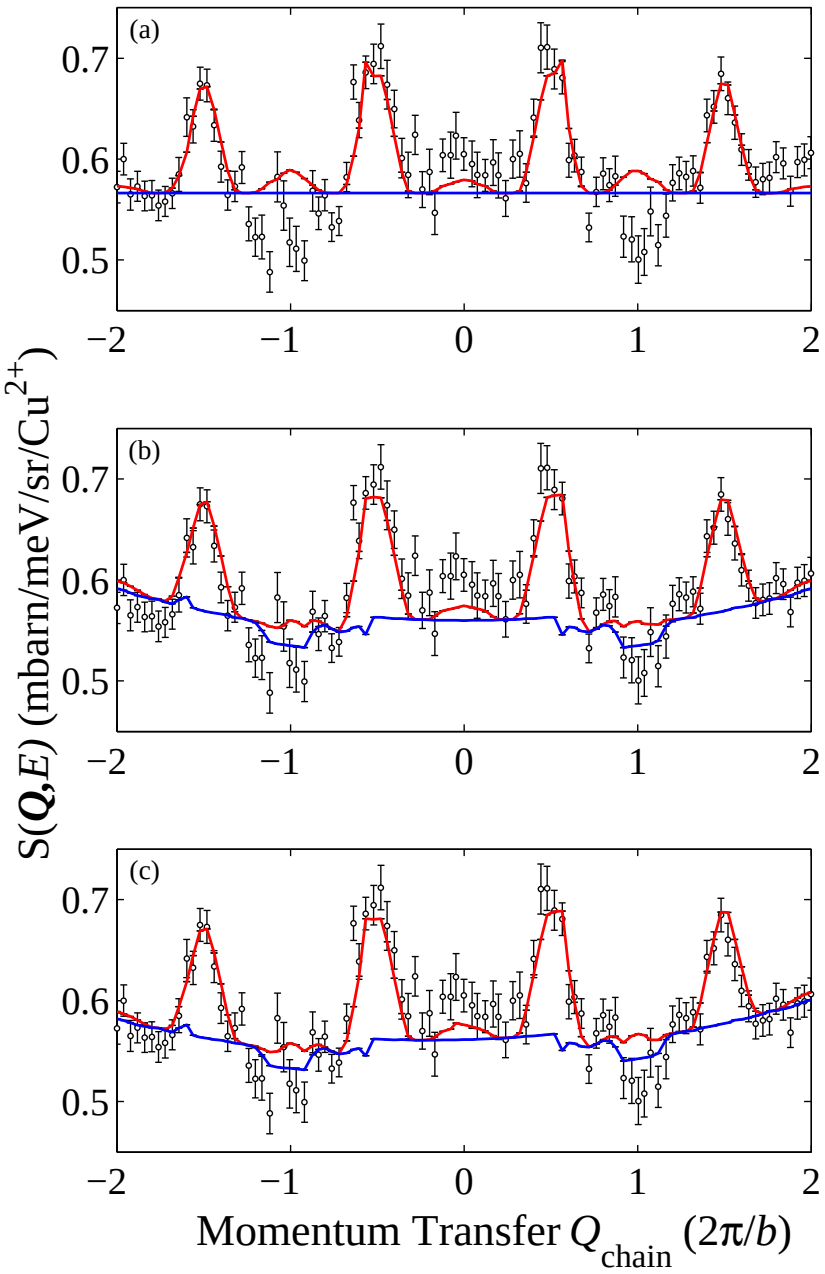

Figure 3.11: The constant energy cut at 160 meV, taken from the $E_i = 794$ meV dataset, as fitted with different forms of the background. The background was initially flat (a). A $A+B\theta^2$ background was then used (b), and finally a slight positive slope on the background as a function of Q_k was added (c). The Müller Ansatz [8] was used here to describe the spinon continuum, convoluted with the analytical ionic form of the magnetic form factor [31].

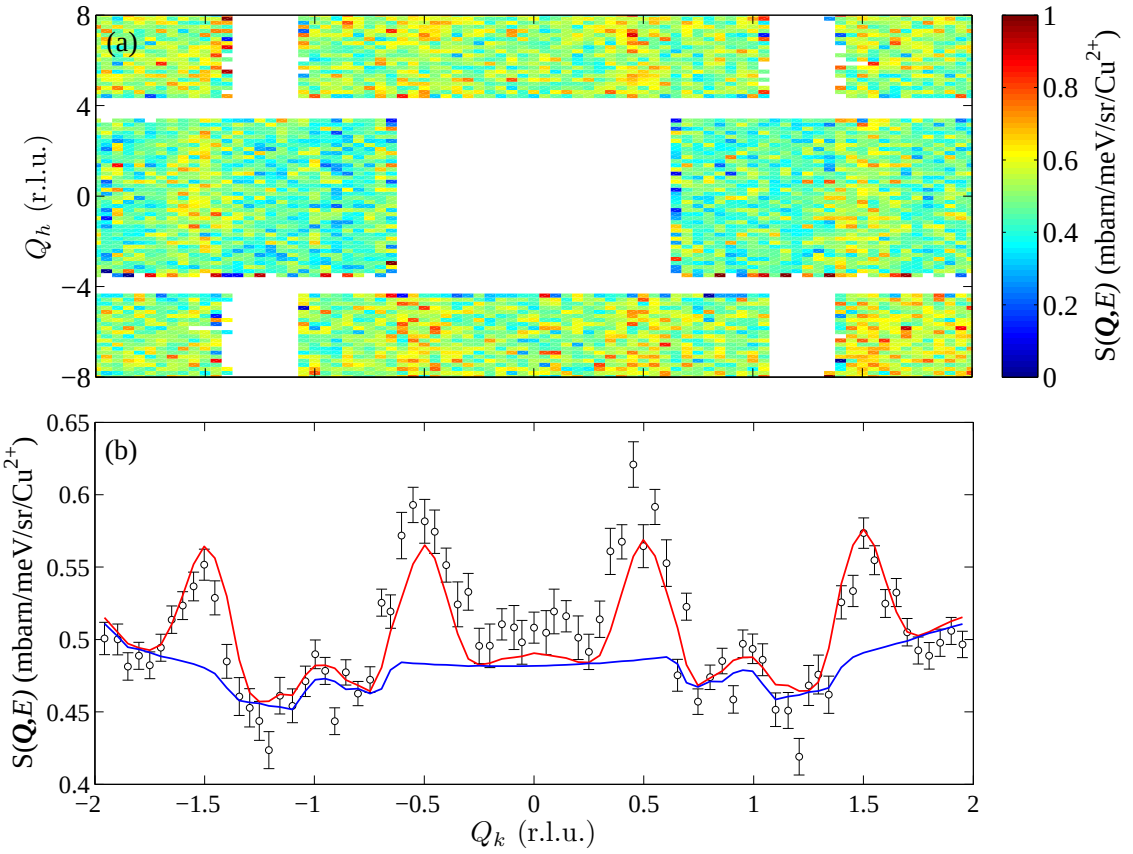

Figure 3.12: (a) A detail of Figure 3.10, but with the limits in Q_h and Q_k the same as that used in all fitted constant energy cuts. The final cut is produced by summing all the data in the Q_h direction and plotting the resulting intensity as a function of Q_k. The gaps in the detector banks produce sudden changes in the average value of θ as a function of Q_k, meaning that a background with a θ^2 dependence has - at first glance - strange behaviour when plotted against Q_k, as shown in (b).

To try to correct this discrepancy, another term was added to the background which was proportional to θ^4. This term was added as it is the simplest even function that can be added to the background (after the term proportional to θ^2). This background slightly improved the quality of fit, but this improvement was almost inevitable since another parameter can be fitted to improve the quality of fit. The coefficient of the θ^4 term was actually negative, which makes this form of the background somewhat unphysical, as at high Q the θ^4 term will dominate and the background will be large and negative. However, at the relatively low Q that we are interested in, this background is reasonable, and merely acts to decrease the rate at which the background increases as a function of θ (or Q). Since this additional term in the background made little real difference to the quality of fit, it was removed and the three parameter fit described before (see Equation 3.7) was used for each constant energy cut.

3.4.3 Formulation of the background for ΔE v Q_k slices

In order to provide images which better convey the continuum of excitations in Sr_2CuO_3, it was very important to find a way of subtracting a background from ΔE v Q_k slices. Perhaps the most obvious way would have been to fit the slices directly in TobyFit, which would necessitate the formulation of a suitable background. However, this would have taken a lot of computing power and would not have told us much more about the system: the fitting of the data via the constant energy cuts provides the robust test that the data analysis requires. The production of the ΔE v Q_k slices is more of an exercise to present the high statistical quality of the data, and does not necessarily have to represent a different way of fitting the datasets.

The initial method chosen to find a background for the ΔE v Q_k slices was to use an interpolated background: that is, a background which uses the measured INS intensity in areas in $(\boldsymbol{Q}, \Delta E)$ space which are outside the spinon continuum and then interpolates this background over the spinon continuum. This background has to be smoothed, as otherwise the background-subtracted INS intensity outside the spinon continuum will appear to be exactly zero, since that is precisely what we have used as the background. It is also

important not to use intensity too near the spinon continuum as 'background', as there are energy and momentum resolution effects from the instrument to take into account (as well as the intrinsic mosaic of the sample), which may mean that magnetic intensity is measured outside the spinon continuum.

Although the interpolated background method is capable of constructing a background which is smoothly varying in Q_k and energy transfer and provides a relatively straightforward way to produce background-subtracted slices, there are significant problems in its implementation. There are many hidden control parameters: exactly where in $(\boldsymbol{Q}_k, \Delta E)$ is considered completely non-magnetic? Over what length scale (in both Q_k and ΔE) should the interpolated background be smoothed over? What kind of function should be used for the convolution in the smoothing (gaussian, top-hat etc.)? Changes to these parameters can substantially change the resulting background, and therefore the background-subtracted data. This leads to inevitable tweaking of these parameters to make the data look as good as possible, but in my opinion severely damages the integrity of the data.

Because of the above concerns with the intepolated background, an analytical form of the background was found (i.e. one with an analytic form which can be defined with as few parameters as possible), as this reduces any qualms that one could have with background-subtracted data. Since the fitting already discussed had given rise to a well-behaved, three-parameter background for each of the constant energy cuts, the logical next step was to study the energy transfer dependence of the fitted values of these parameters. This is shown in Figure 3.13. The black lines on all the plots are fits to the fitted background parameters, done using the MatLab package, MFit. For background parameters A and B a reasonable quality of fit was found using a Gaussian centred at zero energy transfer (defined in Equation 3.8), and for parameter C a simple constant sufficed.

$$S_{Gaussian}(\Delta E) = G_1 e^{-\frac{\Delta E^2}{2G_2^2}} + G_3 \tag{3.8}$$

Upon fitting background parameters A and B with a Gaussian, it became clear that the width (G_2) was sufficiently similar in both cases that the same value could be used for

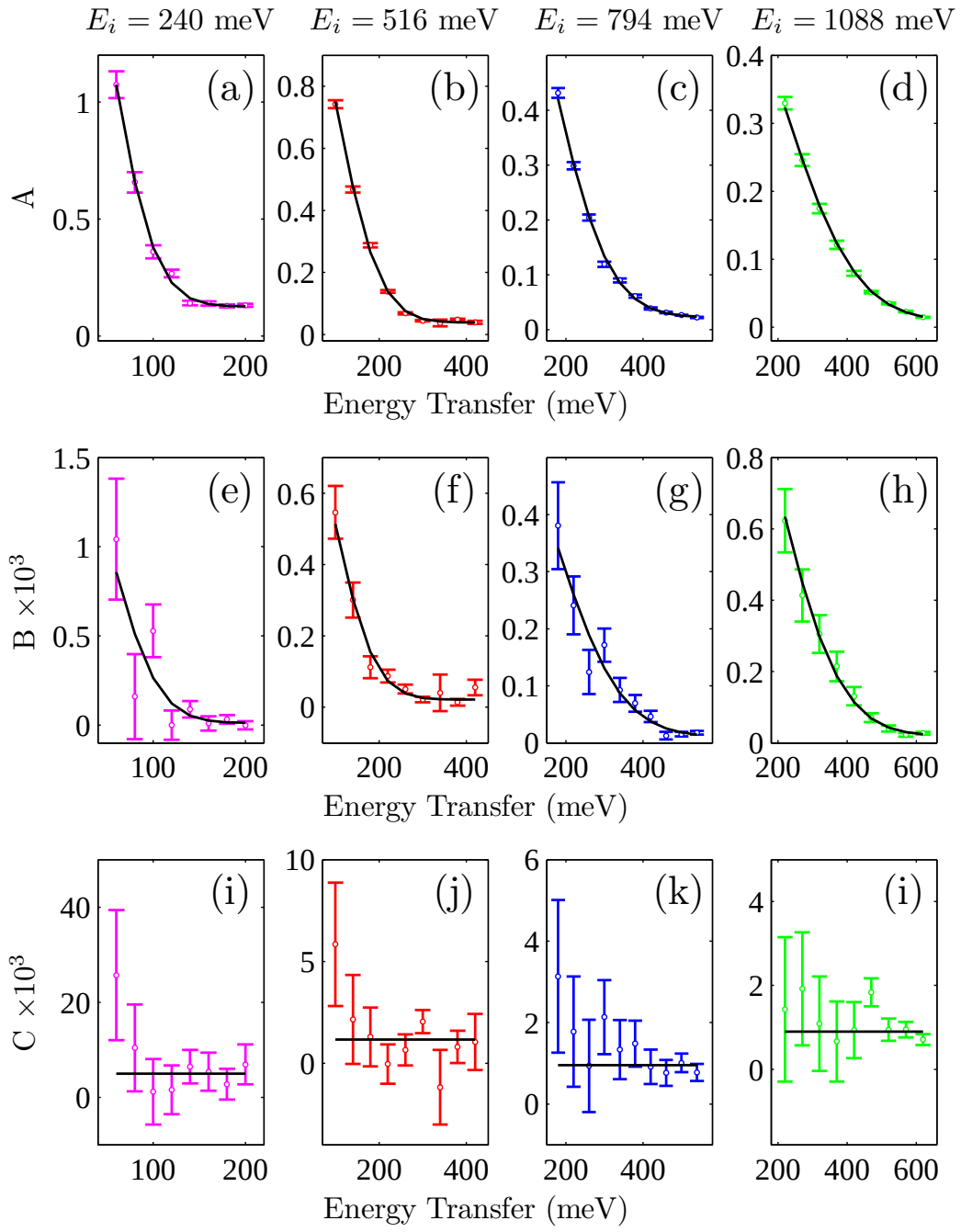

Figure 3.13: Fitted background parameters A, B and C (as defined in Equation 3.7) plotted as a function of energy transfer. Each datapoint is the result of a fit to a constant energy transfer cut, with the corresponding error on the fit plotted as an error bar. The black line on each plot in (a) - (h) is a fit to the fitted parameters using a Gaussian centred at the origin (defined in Equation 3.8). The black line in (i) - (l) is a fit to the fitted parameters using just a constant term.

		Incident Energy (meV)			
Background Parameter	Fit Parameter and χ^2	240	516	794	1088
A	G_1(arb.units.)	2.0(3)	1.19(8)	0.81(5)	0.55(2)
	G_2(meV)	49(2)	98(3)	150(3)	210(3)
	G_3(arb.units.)	0.127(8)	0.039(6)	0.023(2)	0.008(1)
	χ^2	2.21	5.38	2.76	0.85
B$\times 10^3$	G_1(arb.units.)	2(1)	0.9(2)	0.6(2)	1.2(2)
	G_2(meV)	51(14)	93(9)	168(20)	185(10)
	G_3(arb.units.)	0.01(3)	0.022(9)	0.011(6)	0.020(5)
	χ^2	1.89	1.21	1.73	0.69
C$\times 10^3$	C_1(arb.units.)	5(1)	1.2(4)	1.0(1)	0.9(1)
	χ^2	0.61	1.11	0.63	1.36

Table 3.1: The results of the fits to the energy dependence of the fitted background parameters to each constant energy cut, as plotted in Figure 3.13. All of the fitting of the energy dependence of these background parameters was done in the MatLab package MFit.

both with little decrease in the fit quality. In Table 3.1 the fitted parameters for A, B and C at each incident energy are provided.

Several different functions were tried, all centred at zero energy transfer, in MFit to fit the energy dependence of A and B, including an exponential (defined as $X_1 e^{-\frac{\Delta E}{X_2}} + X_3$) and a Lorentzian (defined as $L_1 \frac{L_2^2}{L_2^2+\Delta E^2} + L_3$). Unsurprisingly, the fit quality was improved slightly if the function was allowed to move from the zeroed position, but since the real background clearly has a maximum at zero energy transfer, the background was fixed to also have a maximum at this position. The Gaussian was used purely because the overall quality of fit was best with that functional form. Ultimately the most accurate description was sought of the energy transfer dependence of the fitted parameters: the search was not for a functional form which was necessarily based on a specific physical process, as the background is so complicated as to make that extremely difficult.

From the fitting shown in Figure 3.13 and Table 3.1, the expression given in Equation 3.9 was used as the analytical form of the background. This form of the background uses the same width of Gaussian for fit parameters B_2 and B_3), which are the terms in the background that correspond to background parameters A and B in the fits to each constant

energy cut. The slight slope in the background as a function of Q_k is accounted for in the same way as in the fitting of the constant energy cuts, as it had very little energy transfer dependence (B_5 corresponds to C for the fits to the constant energy cuts). In fact, other than the Gaussian width, the only additional fit parameter is an additional constant which is independent of energy transfer. This is to take into account the significant constant terms which appeared in the Gaussian fits to A and B (parameter G_3), but since they were simple constants, they can be absorbed into one single parameter.

$$S_{back}(Q_k, \theta, \Delta E) = e^{-\frac{\Delta E^2}{2B_1^2}}(B_2 + B_3\theta^2) + B_4 + B_5 Q_k \tag{3.9}$$

In order to get the best values for B_1 to B_5 in Equation 3.9, this form of the background was used in a simultaneous fit of multiple constant energy cuts from each dataset. The cuts that were fitted were those that were in a range of energy transfer which provided a large amount of magnetic scattering. The starting values for the fits were estimated from the results of the fits shown in Table 3.1. The results of these fits to multiple cuts was used as the background which was subtracted from the cuts presented in Figure 3.14.

3.4.4 Fitting the data to the Müller Ansatz

In Sections 3.4.2 and 3.4.3, the discussion of the background was restricted to the fitting of the Müller Ansatz form of the spin-spin correlation function for the 1D Heisenberg spin-1/2 chain. The advantage of the Müller Ansatz for the initial discussion is in its simplicity: it has a very simple functional form, as given in Equation 3.4. In Figure 3.15 the A and J plots are provided (these provide a representation of the overall quality of fit: see Section 3.4.1) for the fits to the Müller Ansatz using the constant energy cuts at the four different values of E_i. Although there is some scatter in the J plot, overall the weighted mean of the fitted values of J (plotted in black) is a good description of all of the fitting at different energy transfers. The fitted value of $J = 240(2)$ meV is in reasonable agreement with the value of 260 meV given in previous studies discussed in Section 3.2. However, the A plot clearly shows a deviation from a flat line: the fitted value of A reduces from about 0.50

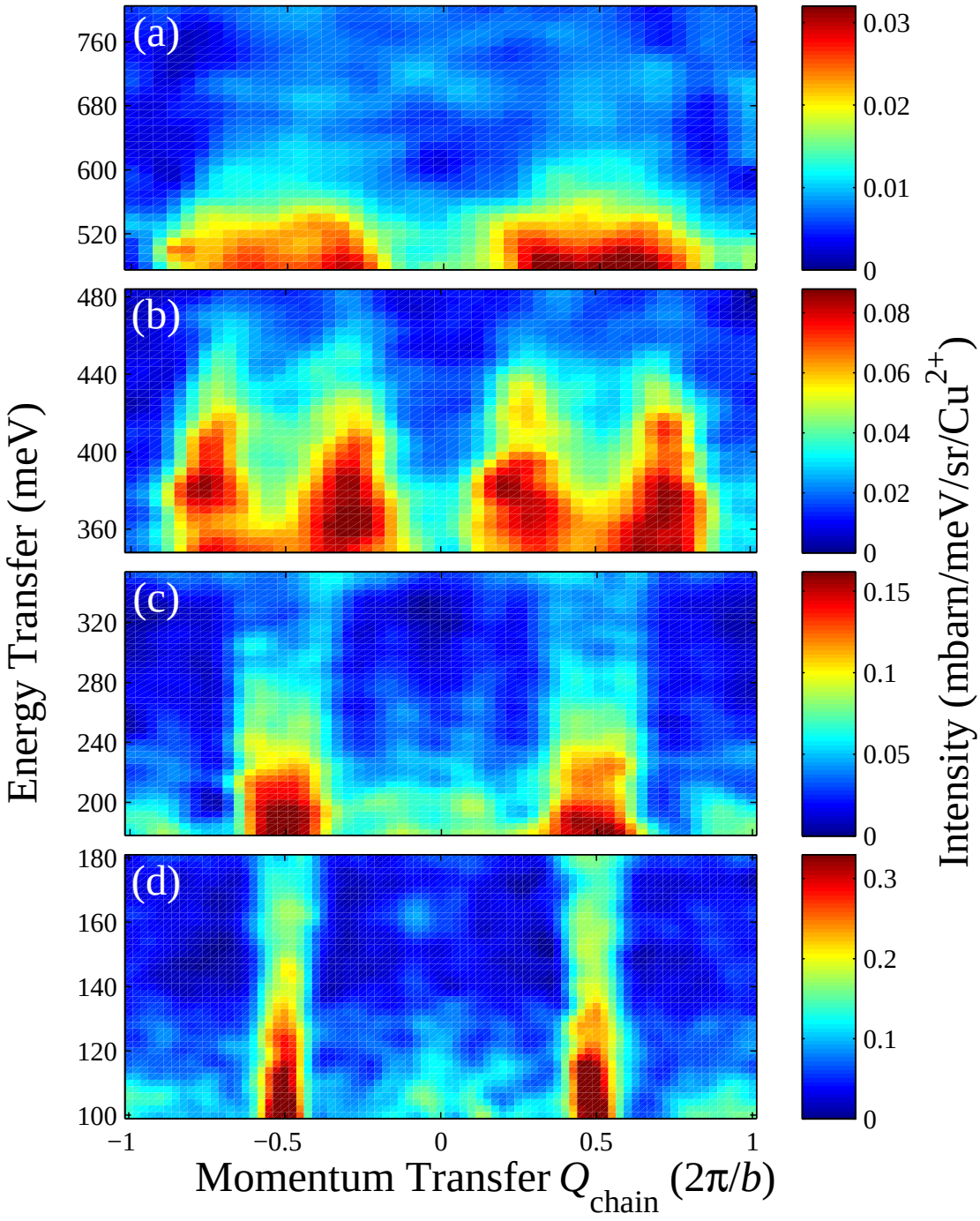

Figure 3.14: Inelastic neutron scattering data for incident energies of 240 meV, 516 meV, 794 meV and 1088 meV. An analytical form of the background has been subtracted from the data, as discussed in the text.

between 60 meV and 300 meV to 0.33 above 450 meV, meaning that in comparison to the lower energy transfers, the Müller Ansatz over-estimates the magnetic intensity at higher energy transfers. The fact that the Müller Ansatz description is incomplete may not come as a complete surprise however, since it is an ansatz: an educated guess to be tested by experiment.

This is not the whole story though, as in fact the intensity scale factor A should lie approximately somewhere between 1 and 1.5 [8], and so clearly is much reduced by around a factor of a third. This dramatic reduction in A was a big surprise, and cannot be easily explained with recourse to inaccuracies with the vanadium normalisation discussed in Section 2.7. The immediate thought was that there may be a mistake in the definition of the inelastic neutron scattering cross-section, but independent checks of the Fortran code (used within TobyFit) by myself and other collaborators have found no such mistake. In Appendix B more details are provided about the checking of the normalisation.

Regardless of the mystery of the missing intensity, datafitting continued by fitting the data to different forms of the spin-spin correlation function. It was felt that the missing intensity itself could be evidence to suggest that the Heisenberg model is somehow insufficient to describe the magnetic excitations here. The focus was to fit the INS data to calculations of the spinon continuum which were based on both the Heisenberg and Hubbard model Hamiltonians, as there was still the possibility that the Hubbard model calculations could provide a better description of the magnetic excitations than the Heisenberg model, and thereby belie the importance of electron itinerancy in Sr_2CuO_3.

3.4.5 The different versions of the spinon continuum for Sr_2CuO_3

Immediately after our MAPS experiment, we were attracted to recent work on the calculation of spin-spin correlation functions of Heisenberg chains at zero temperature [48], which used numerical summations of exact form factors to calculate multi-spinon excitations. This method inherently accounts for higher order excitations, and the intensity maps provided in $(\boldsymbol{Q}, \Delta E)$ space are shown to obey the spin sum rules up to at least 95% of the expected weighting [48]. However, due to the inexact summation, these calculations

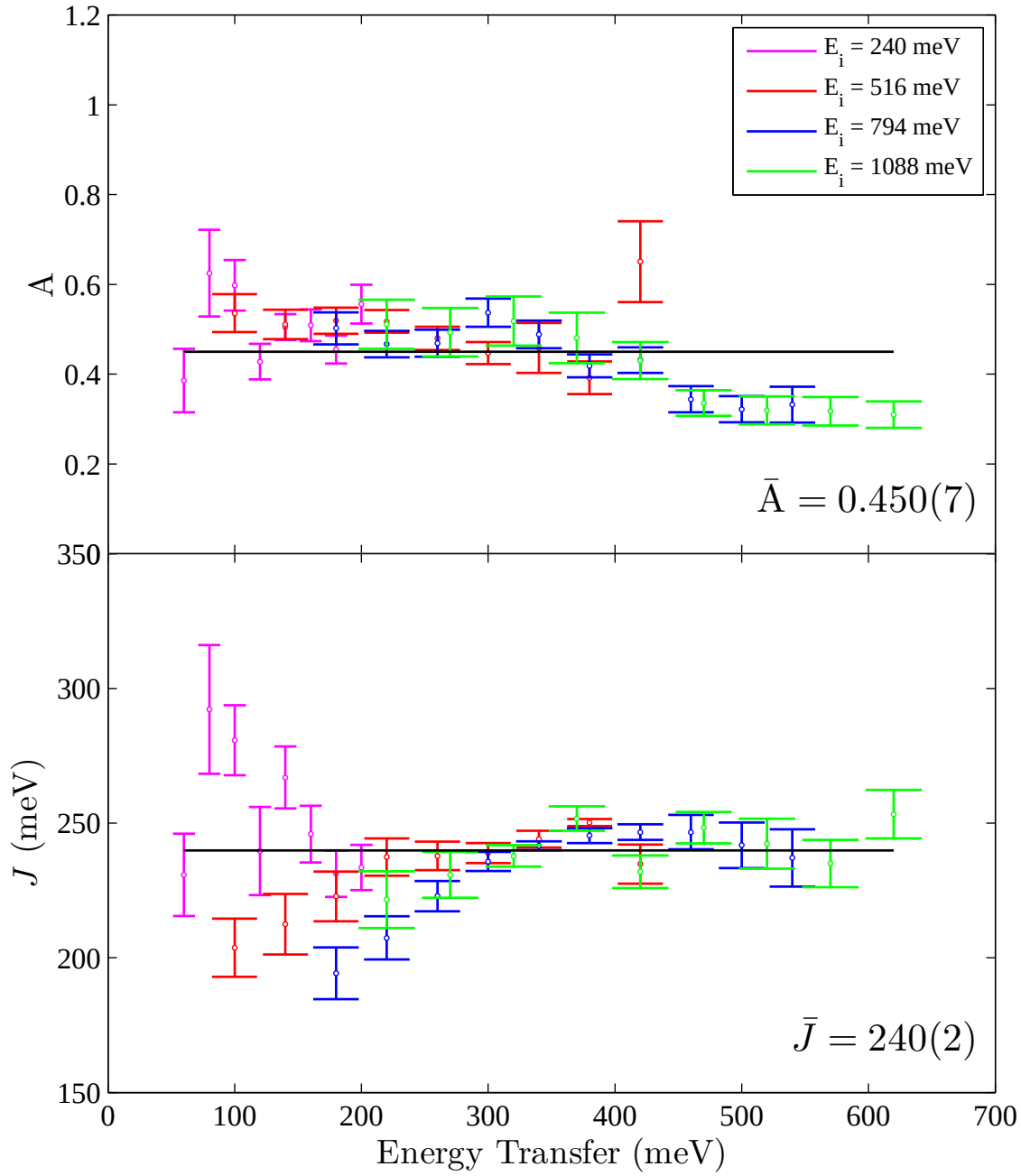

Figure 3.15: Results of fits to the Müller Ansatz (A and J plots): intensity prefactor A and magnetic coupling constant J found from fits to different energy cuts are plotted as a function of ΔE.

are then convoluted with a Gaussian in order to smooth out any unphysical artifacts of the calculation. After discussion with the first author on this work, Jean-Sebastian Caux, we attained three separate files with a version of the spin-spin correlation function using $N = 400$ sites on the chain: one file contained the array of momentum transfers at which the spin-spin correlation function had been found, another contained the energy transfers and finally another contained the 2D intensity array for the spin-spin correlation function itself. After correspondence with Caux, he sent two further versions of these calculations. These two calculations were not simply convoluted by a Gaussian, but by an asymmetric function which ensured that no magnetic intensity was moved at negative energy transfer after convolution. The second calculation once again had $N = 400$ sites on the chain, and the third had $N = 500$, which might be expected to increase the accuracy of the calculation as this is somewhat nearer to the $N \rightarrow \infty$ limit. Surprisingly though, the sum rules are satisfied slightly less well by the $N = 500$ calculation (only 99.1% compared to 99.4%), due to inaccuracies in the summation method employed.

Since our initial motivation was to look for possible effects on the spin excitations due to itinerancy effects, we also scoured the literature for theoretical work done on 1D $S = 1/2$ systems which are initially described by the Hubbard model. We found the work of Holger Benthien especially relevant, as he had recently provided simulations of resonant inelastic X-ray scattering spectra and optical conductivity for a recent study of the similar material $SrCuO_2$ [65]. After contacting Benthien, he sent us a dataset created for $SrCuO_2$, calculated with the extended Hubbard model parameters set to $U/t = 7.8$, $V/t = 1.3$ and $t = 0.435eV$, as defined in Equation 3.6. This 2D intensity map was arranged in an entirely different manner to Caux's dataset, requiring considerably different subroutines to be written in Fortran to read the data.

In order to fit these different calculations to the data, a routine in Fortran was written which was capable of doing linear interpolation (and extrapolation) in two-dimensions. TobyFit is written such that the simulated INS intensity (background + spin-spin correlation function) is calculated for each point in $(\boldsymbol{Q}, \Delta E)$ independently, so the interpolation code was simply written to do linear interpolation for one point at a time. The difficulty in writing any interpolation code lies not in getting the correct weighting for each of the four

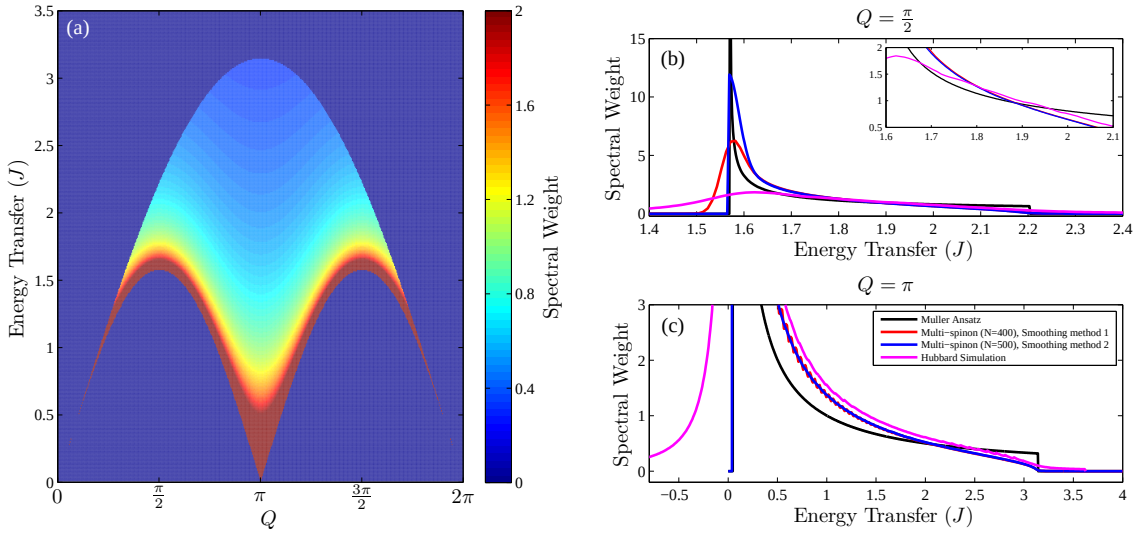

Figure 3.16: Comparison of different calculations for the spin-spin correlation function for a 1D spin-1/2 antiferromagnet. The intensity map as a function of Q and ΔE as calculated by the Müller Ansatz [8] is plotted in (a), alongside constant Q cuts plotted at $Q = \frac{\pi}{2}$ (b) and $Q = \pi$ (c) for the Müller Ansatz [8], for two different calculations of the Heisenberg multi-spinon excitations [48, 66] and for the extended Hubbard model [67].

points on the grid which surrounds the point of real interest, but in the special treatment of the cases when the point required is very near to the edge of the rectangle defined by these four points. If these cases are not treated as special cases, there is the propensity to introduce significant rounding errors, as the very small difference between the required point in x and a specific point on the x grid is used in the linear weighting within the interpolation calculation.

The important calculations of the spin-spin correlation function to which the data were fitted are shown in Figure 3.16. In 3.16(a) the full two-dimensional intensity map calculated from the Müller Ansatz is plotted. Since the lower and upper boundaries for the two-spinon continuum are hard-wired in this representation of the spin-spin correlation function, this plot also clearly displays these boundaries. The remarkably accurate description that the Müller Ansatz provides of the spin excitations can be observed in Figure 3.16(b) and Figure 3.16(c). The general shape of the Müller Ansatz excitations is very similar to the other calculations, the largest relative difference being at the upper boundary, where the Müller Ansatz is over an order of magnitude larger than the multi-spinon calculations at $Q = \pi$.

In Figure 3.16(b) the large Lorentzian convoluted with the Hubbard-based calculation is very obvious at the lower boundary, where the spin excitations should have a discontinuous onset. The relatively narrow Gaussian which has been convoluted with the multi-spinon calculations can also be observed. Despite being convoluted with a relatively large Lorentzian, some questionable (but relatively small) features appear in the Hubbard-based calculation in Figure 3.16(b) and Figure 3.16(c) which are clearly observed in the detail in Figure 3.16(b).

Well above the lower boundary of the spinon excitations, the two multi-spinon calculations are almost identical, as we would expect. However, at the lower boundary these two calculations are radically different. In both calculations the data are smoothed via convolution with a Gaussian of width $\frac{\ln N}{2N}$ in both cases, as defined in the same way as in 3.8). This results in energy widths of 0.0150 J and 0.0124 J for the $N = 400$ and $N = 500$ calculations respectively. However, in the $N = 500$ dataset, any intensity that is convoluted below the lower (two-spinon) boundary is simply reflected about the boundary, so that there is no intensity below the boundary. Intensity at ΔE below the boundary will be placed at ΔE above the boundary. Although this clearly makes the intensity profile immediately above the lower boundary far from that calculated, it results in a sharp intensity cut-off, which is identical to the reality of the spinon continuum.

High frequency artifacts in the $N = 400$ multi-spinon calculation can be observed in the $Q = \pi$ cut in Figure 3.16(c) but not in the $N = 500$ calculation, suggesting the calculation is better converged in the $N = 500$ version. Such small perturbations to the intensity profiles are not especially concerning however, as once the calculation is convoluted with the instrumental resolution (as well as the energy integration width for each constant energy cut), such small artifacts are very likely to have been averaged out.

After a significant amount of datafitting had been completed with the versions of the spin-spin correlation function already discussed, we were informed by Caux that he had recently completed an exact calculation of the four-spinon excitations in the 1D S=1/2 antiferromagnet. This very important work was published in the Journal of Statistical Mechanics [9]. This work was discussed previously in Section 3.1.2. The exact two-spinon

+ four-spinon calculation which has been calculated provides a version of the spin-spin correlation function for a 1D $S = 1/2$ Heisenberg system which is only missing 2% of the total spectral weight.

Constant Q cuts through the combined exact two-spinon and four-spinon excitation spectrum are plotted in Figure 3.17. In both Figure 3.17(a) and (b) the close agreement between the multi-spinon calculations and the two-spinon + four-spinon calculation can be observed, which suggests that the missing spectral weight from higher order excitations is indeed negligible. In the detail of Figure 3.17(a), the details around the lower boundary of the spinon continuum can be observed. In this region, the two-spinon + four-spinon calculation shows better agreement to the version of the multi-spinon calculation which was smoothed using a simple Gaussian (smoothing method 1). This makes sense if the two-spinon + four-spinon calculation is truly the most accurate calculation, as in the multi-spinon calculation smoothed via the second method the accuracy of the calculation is compromised in the region immediately above the lower boundary (see Section 3.4.5). The lack of any intensity below the lower boundary in the two-spinon + four-spinon calculation is also clear from this detail.

3.4.6 Fitting the data to other versions of the spinon continuum

After fitting the Müller Ansatz painstakingly in order to concentrate on the formulation of the background, the data were now fitted to the other forms of the spin-spin correlation function at our disposal. Firstly we turn to the fitting of the INS data to the extended Hubbard model calculation of the spin-spin correlation funciton provided by Holger Benthien [67, 68]. The A and J plots are provided in Figure 3.18. Note that the choice of energy cuts is different to that detailed earlier in this chapter, as in later incarnations of the fitting the choice of the energy cuts that were fitted was changed, dramatically increasing the number of cuts fitted. One drawback of this choice is that now there are adjacent constant energy cuts which contain some of the same data, as they integrate over overlapping areas in $(\boldsymbol{Q}, \Delta E)$ space. For example, the constant energy cuts at $E_i = 1088$ meV are now separated by 20 meV, but are integrated over a range of energy ± 25 meV

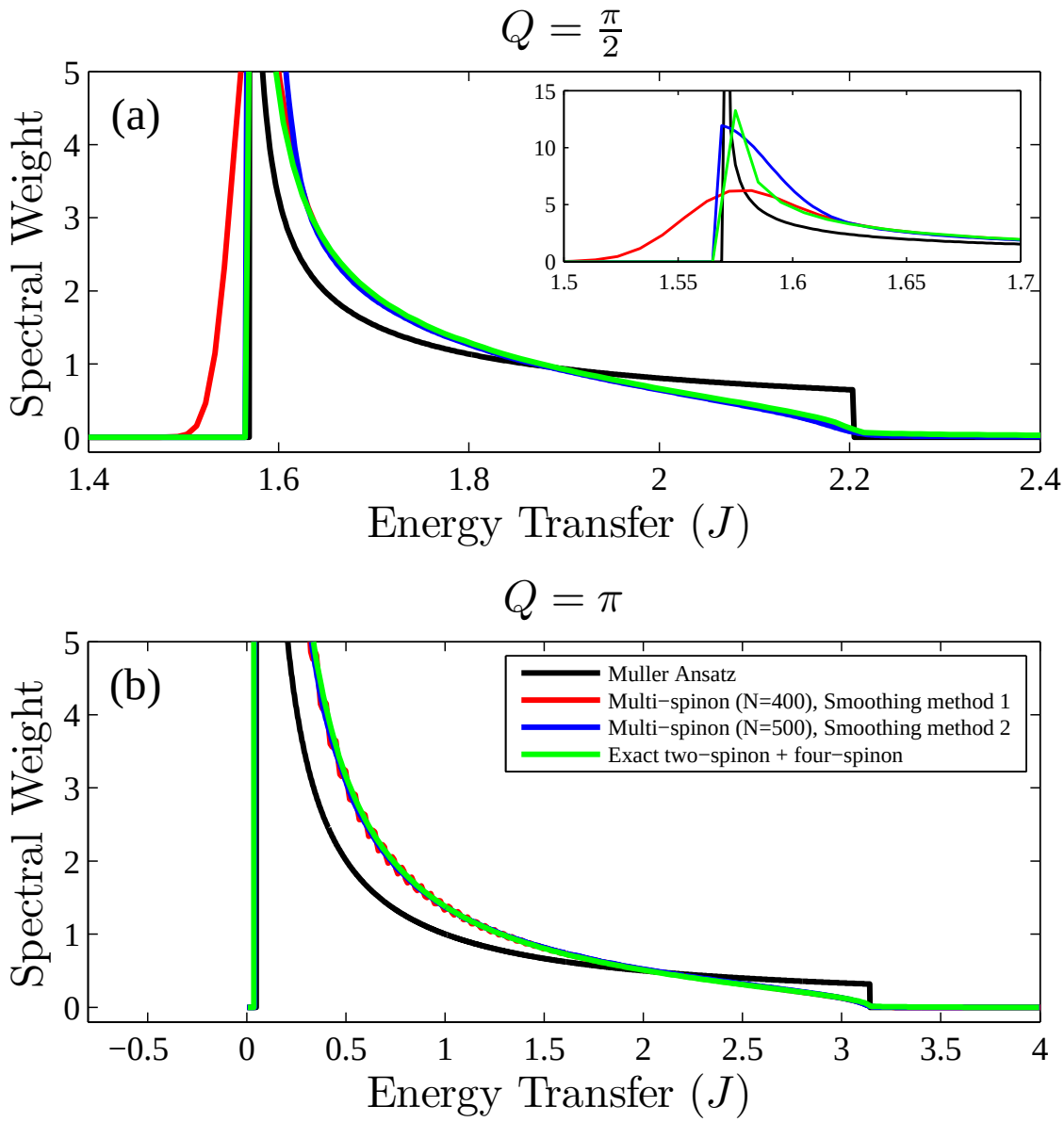

Figure 3.17: Constant Q cuts through the two-spinon + four-spinon calculation, as compared to the earlier multi-spinon calculation and the Müller Ansatz. Cuts plotted in (a) are at $Q = \frac{\pi}{2}$ and in (b) at $Q = \pi$. Please note that the slight discrepancies in the onset of intensity at the lower boundary are a result of differences in the energy binning between the different datasets. The Müller Ansatz was calculated using the same (Q,ΔE) grid as the two-spinon + four-spinon calculation.

about the centre of each cut, so the highest 30 meV of one cut is also used in the lowest 30 meV of the cut which immediately follows. Although this means that the values of the fitted parameters from each cut are correlated with the parameters found from neighbouring cuts, it enables one to see more easily any energy transfer dependence in the fitted parameters.

Both the fitted values and the errors for A and J are extremely erratic at low energy transfer. In particular, for the cut at $E_i = 240$ meV with an energy transfer 60 meV, the value of J is not even within the range of the J axis, whilst its error covers the entire range. Above an energy transfer of about 160 meV, the fitted values are more stable, and consequently the average values of A and J in the figure are calculated from only the fits made on cuts above 160 meV. The poor fitting at low energy transfer is a direct consequence of the large Lorentzian tails of the extended Hubbard model calculation extending well below the lower boundary of the spinon excitations, as it results in A and J being extremely strongly correlated. The discussion is more easily made in relation to the Müller Ansatz, as it has a sharp onset of magnetic intensity at the lower boundary: at low energy transfers, the excitations are well described by a set of very sharp peaks at $Q_k = n + 0.5$ (in r.l.u.), where n is any integer. If J is made larger by the fitting routine, the experimental energy transfer corresponds to a lower energy on the spinon continuum energy scale (in units of J). This serves to increase the intensity of the set of peaks and also make them even narrower. The change in intensity of the peaks can easily be compensated for by decreasing the value of A, but the change in width of the feature makes the choice of A and J unique. However, for the extended Hubbard model calculation, this progressive narrowing of the set of peaks is largely smoothed out as a result of the large Lorentzian smoothing function, meaning that there is often no unique choice for values of A and J.

The other key point that comes out of this analysis is that the intensity scale factor A does not appear to be independent of energy transfer: it appears to gradually decrease at higher energy transfers, going from about 0.42 at 160 meV to about 0.32 at 620 meV. This suggests that perhaps the extended Hubbard model - as well as the Müller Ansatz - is insufficient to describe the data. This is despite the fact that the values of U, V and t used

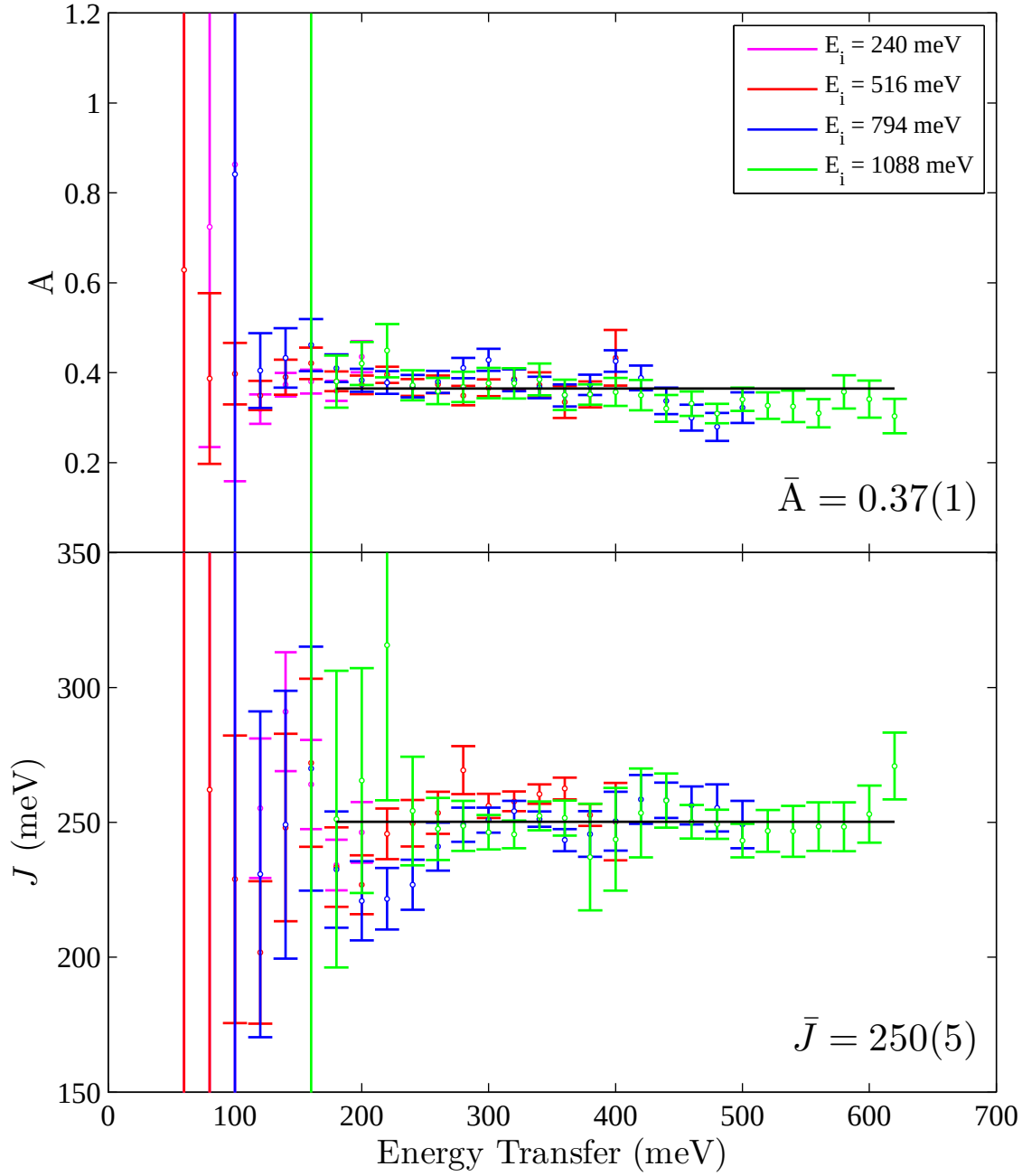

Figure 3.18: A and J plots for fits to the spin-spin correlation function calculated within the extended Hubbard model [68]. The weighted mean values of A and J (calculated from fits only to cuts of energy transfer above 160 meV) are shown and plotted on the graph (black).

in this calculation are close to those found in Sr_2CuO_3 (they are actually the values found experimentally for $SrCuO_2$). For this description of the spin-spin correlation function, there is no range of values for the intensity prefactor A as there is for the Müller Ansatz: it should simply be unity at all energy transfers. However the intensity scale factor A is once again reduced by about a factor of a third, as it was in the fits to the Müller Ansatz.

The A and J plots are plotted in Figure 3.19 for the fitting to three forms of the spinon continuum calculated using the Heisenberg model: 3.19(a) shows the results of fits to the first multi-spinon dataset, which uses a spin chain with 400 sites, 3.19(b) shows the results of fitting to the third dataset of the multi-spinon calculation that Caux sent (which artificially maintained discontinuity of the magnetic intensity at the lower boundary), and 3.19(c) contains the results of the fits to the exact two-spinon + four-spinon calculation. The first point to make about these three sets of datafitting is that although they are clearly consistent (the average values of A and J are well within error of each other) the quality of fit is much poorer at very low energy transfer in 3.19(a). This is due to precisely the same effect observed in the fitting to the extended Hubbard model: the lack of a sharp onset of intensity at the lower boundary of the spinon excitations. So despite the rather obscure manner in which the smoothing has been accomplished at the lower boundary in the data fitted for Figure 3.19(b), it has improved the overall quality of fit to our data in comparison to that shown in 3.19(a) by maintaining the sharp onset of the spinon excitations at the lower boundary. The agreement of theory and experiment is clearly best in 3.19(c), where the errors on the fitted parameters are reasonable at all energy transfers, and practically every value of A and J is within error of the weighted mean average.

In 3.19(a) - (c), both A and J are clearly independent of energy transfer, suggesting that in fact the Heisenberg model is a complete description of the spin excitations in Sr_2CuO_3. This is a surprise, as the idea of spin-charge separation is usually underpinned by the fact that they occupy entirely different energy ranges, but in Sr_2CuO_3 the spin and charge excitations are less than an order of magnitude apart. However, once again the fitted value of the intensity scale factor A is much reduced from its correct value, by again a factor of a third. As for the extended Hubbard model calculation, the intensity scale factor ought

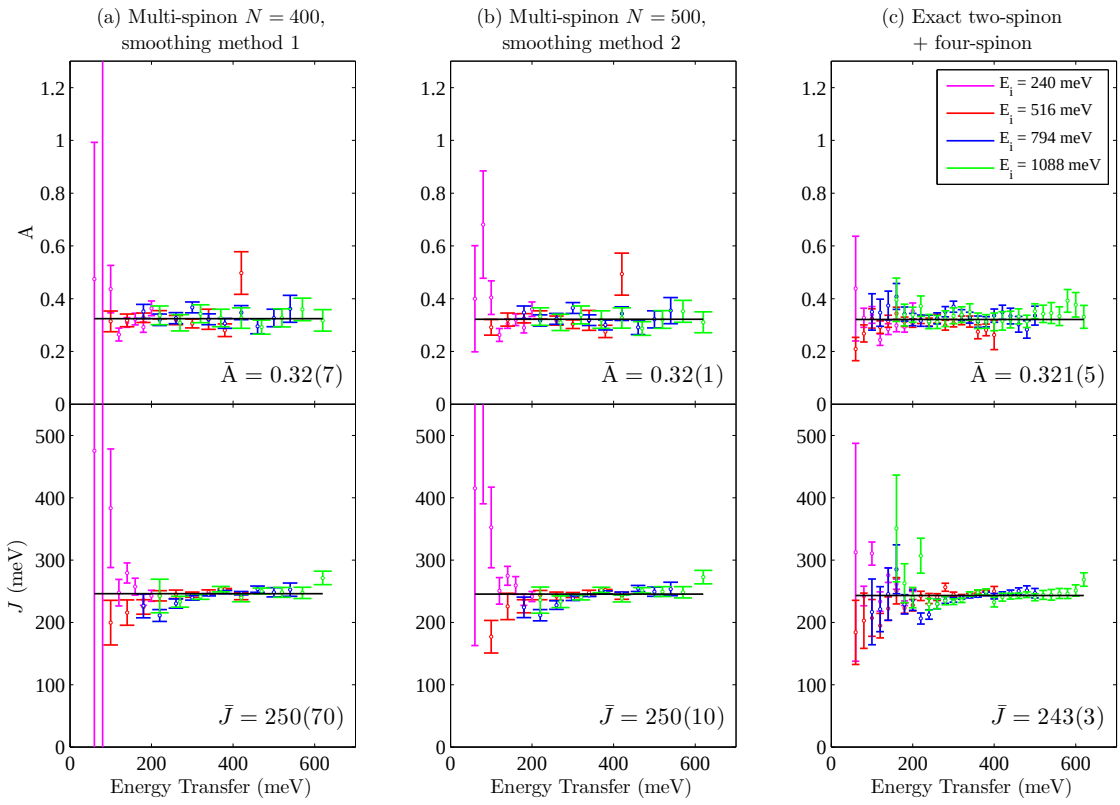

Figure 3.19: A and J plots for fits to three versions of the spinon continuum calculation for the Heisenberg model. The fitted parameters A and J are plotted for the fit to the multi-spinon calculation with 400 sites on the chain using the first smoothing method in (a) [48, 66]. In (b) A and J are plotted for the fit to the multi-spinon continuum now with 500 sites using the second smoothing method. In (c) A and J are presented for the fits to the exact two-spinon + four-spinon calculation. In each plot, the weighted mean value of A and J is shown and plotted on the graph (black).

to be entirely unnecessary to fit, as it should be unity. The problem of missing intensity remained, until some additional work was done by a theoretical group at the Brookhaven National Laboratory, USA, on the magnetic form factor in Sr_2CuO_3.

3.5 The problem of missing intensity: a new magnetic form factor for Sr_2CuO_3

The quality of fit to the exact two-spinon + four-spinon calculation presented in Figure 3.19(c) is impressive, but as discussed, the intensity scale factor A has to be reduced to a third of its true value in order to produce a high quality fit. This missing intensity is not a new effect: a similar reduction in A was observed in a similar study on $SrCuO_2$ when fitted to the Müller Ansatz [10]. Interestingly, other studies on the magnetic excitations on the 2D cuprates (which of course include the high-temperature superconducting cuprates) also report considerable missing intensity. This has been highlighted in a recent paper about INS measurements on two-dimensional superconducting cuprates [69]. One of the many factors that are discussed in this paper is the so-called 'shielding factor': because the electrons have increased freedom to hop from one site to the next in a system such as Sr_2CuO_3, the sites which are now unoccupied or doubly-occupied have no overall spin, so the neutrons do not interact with these sites. This would act to decrease the measured inelastic neutron scattering intensity, as observed.

Here it is instructive to look at the simplified expression that describes the INS cross-section as given to the TobyFit software (see Appendix B). Equation B.12 is repeated here:

$$S_{\text{TobyFit}}(\mathbf{Q}, \Delta E) = (\gamma r_0)^2 |F(\mathbf{Q})|^2 \frac{1}{2\pi} \, 2 \, S^{zz}_{\text{Caux}}(\mathbf{Q}, \Delta E) \tag{3.10}$$

While γ and r_0 are constants, the only other term which could be different in a real system is the magnetic form factor squared $|F(\mathbf{Q})|^2$. The magnetic form factor is the Fourier transform of the magnetic spin density, or alternatively the Fourier transform of

the electron density (but only those electrons which have an overall non-zero moment). So if the magnetic form factor was different to the form factor which had been used throughout the analysis, perhaps this could explain the missing intensity observed. If the magnetic electron density in real space has more weight than anticipated at larger distances from the central Cu^{2+} ion, the corresponding magnetic form factor will have less intensity at higher Q due to the act of the Fourier transform. On a direct neutron spectrometer like MAPS at ISIS, high energy transfer measurements (energy transfers over 100 meV, as all of our most useful data are) correspond to relatively high Q measurements, so they are very sensitive to the magnetic form factor at high Q. However, from the analysis up to this point, the functional dependence of the magnetic form factor seemed to be reasonably accurate, as any change in the magnetic form factor could manifest itself as an additional energy transfer dependence of the fits to the scale factor A and exchange coupling J.

From these considerations, we discussed the possibility of the magnetic form factor being calculated specifically for Sr_2CuO_3 with Wei Ku and his group at Brookhaven National Lab, USA. Ku's group have world-class expertise at using Density Functional Theory to describe both static and dynamic properties of electrons in strongly correlated electron systems. The suspicion was that the magnetic electrons could be further from the central Cu^{2+} ion because of increased covalency in the bonding between the Cu and O in Sr_2CuO_3, resulting in some magnetic moment being transferred nearer to the O^{2-} electronic orbitals.

Chi-Cheng Lee, a member of Wei Ku's group, carried out calculations of the magnetic form factor for Sr_2CuO_3. Lee had used Wannier functions constructed from LDA+U orbitals to calculate the magnetic electron density, and then took the Fourier transform to find the magnetic form factor. Before the Fourier transform had been taken, the real space map of the magnetic electron density showed without doubt that there was now some probability of the magnetic electrons being in the oxygen p orbitals. This extension of the magnetic electron density to larger distances in real space corresponds to a contraction of the magnetic form factor in reciprocal space.

The contraction of the magnetic form factor is observed in Figure 3.20. The black line in Figure 3.20(a) - (c) corresponds to the analytic magnetic form factor, which has been used

in all of the fitting which has been discussed thus far. The red line corresponds to the LDA+U calculation of the magnetic form factor for Sr_2CuO_3. All of cuts used throughout all the fitting were integrated over $-8 \leq Q_h \leq 8$ and plotted from $Q_k = -2$ to $Q_k = 2$ (where the units of Q are reciprocal lattice units). In Figure 3.20(b), it is clear that the analytical version of the magnetic form factor would anticipate a much larger measured magnetic signal, as the integral of the analytical magnetic form factor between $Q_h = 0$ and $Q_h = 8$ is clearly larger than that for the LDA+U calculation (a simple integration from the dataset shows that it is about 1.5 times larger). From Figure 3.20(a) it would also appear that the measured magnetic signal should be relatively large at low Q_k, as the magnetic form factor very quickly drops to half of its total value at $|Q_k| \approx 0.5$r.l.u.

Not only is the magnitude of the LDA+U magnetic form factor much reduced from the analytical form factor over a large range of momentum transfer, but the new calculation also appears to have a good deal more structure in Q. This is logical since the analytical version of the magnetic form factor is simply based on Cu $3d_{x^2-y^2}$ orbitals, whereas the LDA+U magnetic form factor includes effects from additional O p orbitals from neighbouring oxygen sites. Although the structure in the LDA+U magnetic form factor is striking in the Q_k and Q_h directions, in the Q_l direction the two magnetic form factors look relatively similar. This similarity is highlighted in the insert, where the ratio $\frac{|F_{\mathrm{Analytic}}|^2}{|F_{\mathrm{LDA+U}}|^2}$ is plotted. Since the two magnetic form factors are so similar in this direction, the A and J plots already plotted in this chapter *should* still be representative of the energy transfer dependence of the fitted parameters, as the Q_l direction is very highly correlated with energy transfer.

There were many considerations to take into account before the supplied magnetic form factor dataset could be used within TobyFit. The original dataset was provided over a relatively huge range in Q (approximately $\pm 16\text{Å}^{-1}$ in all three directions), and was over 150 Mb in size. The first step was to find what the minimum required Q range was in each direction, in order to use MatLab to create a shorter version of the datafile to be read in TobyFit. By far the easiest way to do this was to utilise the functionality of MSLICE, and project the data onto Q_k (the chain direction), Q_h (in the scattering plane, vertical) and Q_l (along the incident beam direction). From these projections the magnetic form factor

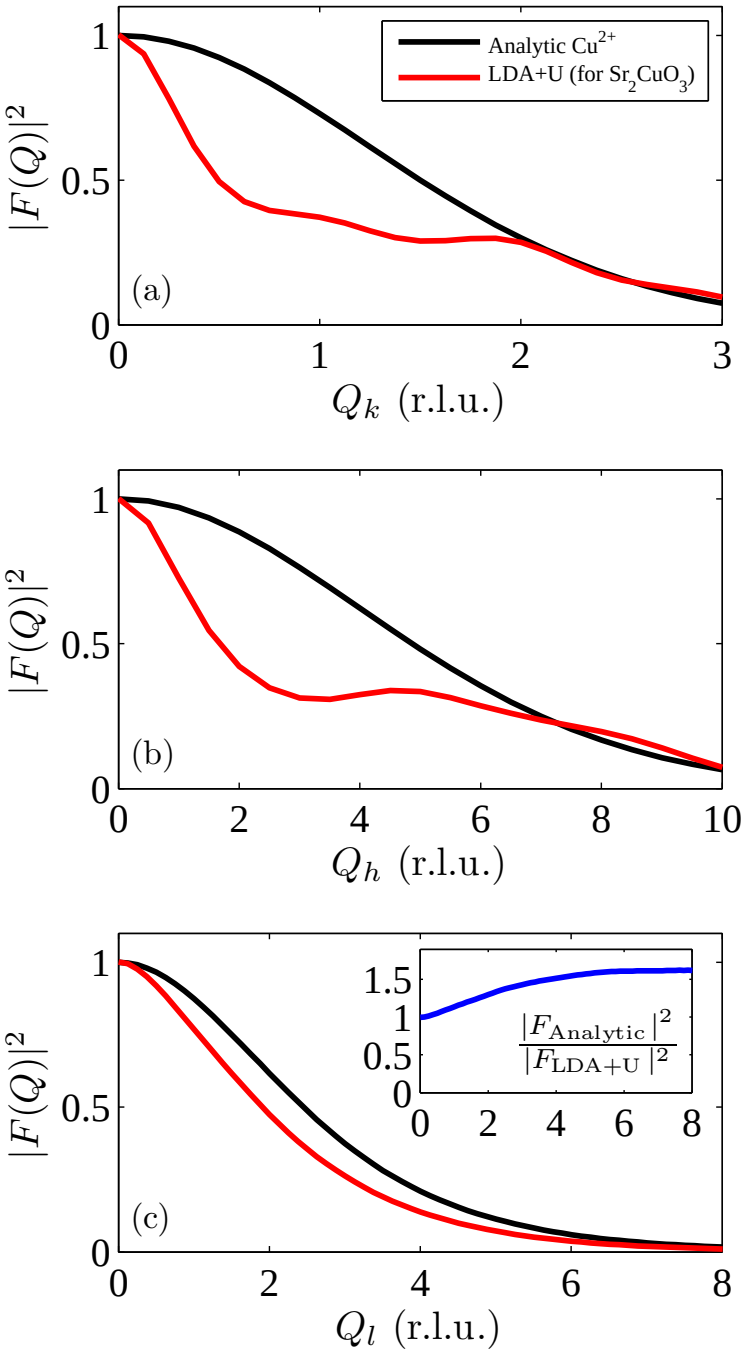

Figure 3.20: Cuts through the analytical ionic magnetic form factor for Cu^{2+} (in black) and the covalent LDA+U magnetic form factor (in red) are plotted in the Q_k (Q_{chain}) direction (a), in the Q_h direction (in the vertical, perpendicular to the incident beam) (b), and in the Q_l direction (in the incident beam direction) (c). The insert in (c) shows the ionic magnetic form factor divided by the LDA+U magnetic form factor in the Q_l direction.

calculation was reduced to the range to 3 r.l.u. in Q_k, 9 r.l.u. in Q_h and 8 r.l.u. in Q_l. The first two of these choices were obvious based on the limits of the constant energy cuts being fitted, but the latter was based on the projections discussed. These Q ranges were then converted into inverse Angstroms (for consistency with the units of the magnetic form factor dataset), and rounded up to the nearest integer number of Angstroms, to reduce the chance still further that the reduced momentum range may not be sufficient for all momenta measured at in the inelastic neutron scattering datasets. Any redundant negative Q values were also removed, as for an orthorhombic structure $(Q_h,Q_k,Q_l) = (-Q_h,-Q_k,-Q_l)$. The resulting datafile produced was just 1 Mb in size.

An initial stumbling block was whether the magnetic form factor provided had already been squared (as it appears in the INS cross-section, see Equation 3.10) or whether it was truly the magnetic form factor. However, both correspondence with our collaborators and comparison with the analytical version of the magnetic form factor eventually confirmed that the dataset was in fact the magnetic form factor squared. Care also had to be taken to ensure that the units of momentum transfer used within TobyFit (reciprocal lattice units) were carefully converted to match with the inverse Angstroms used in the magnetic form factor dataset.

Once these details had been dealt with, the LDA+U magnetic form factor was used together with the exact two-spinon + four-spinon calculation in the latest fit to the data. The corresponding A and J plot is provided in Figure 3.21. With the analytic magnetic form factor presented in Figure 3.19(c), only about 30% of the expected intensity was apparently being measured, but with the LDA+U calculated magnetic form factor now almost 80% of the expected magnetic intensity is being measured, which is at the limit of that which we might expect from inaccuracies in the vanadium normalisation procedure discussed in Section 2.7. However, on the face of it this conclusion could seem suspicious, since the A and J plots really only strongly probe the Q_l dependence of the magnetic form factor, which we knew to be similar to the analytic version of the magnetic form factor. Figures 3.20(a) and (b) show clearly that the strongest discrepancy between the two magnetic form factors is in the Q_k and Q_h directions (within the plane of the Cu $3d_{x^2-y^2}$ orbitals). The fits shown in Figure 3.22 provide crucial evidence that we are also

sensitive to the magnetic form factor in the Q_k direction.

The individual fits to the original constant energy cuts enable one to study the dependence of the magnetic intensity as a function of Q_k. In Figure 3.22 data are presented which has been fitted with both the analytical magnetic form factor (in the left column) and the LDA+U calculated magnetic form factor (right column). The key point here is that although the fit quality is good in both cases, the LDA+U calculation dramatically improves the quality of fit in the region around $Q_k = 0$, where the LDA+U magnetic form factor is large compared to its values at higher Q_k (see Figure 3.20). The poor fit of the INS data near $Q_k = 0$ originally motivated the use of a θ^4 term in the background discussed in Section 3.4.2, but it now appears that the discrepancy was due to the wrong choice of magnetic form factor. The four constant energy cuts presented have not been chosen purely because the difference between the two calculations is maximised, but were deliberately chosen over a wide range of energy transfer and at two different incident energies. The larger than anticipated magnetic intensity at low Q_k can be observed in **all** of the constant energy cuts which have magnetic signal in this area in Q_k.

3.6 Summary

The spinon excitations in Sr_2CuO_3 were measured up to 0.6 eV, and the data were compared to a variety of different forms of the spin-spin correlation function for a 1D $S = 1/2$ antiferromagnetic chain, both in the limit of large intrasite exchange to hopping ratio, U/t (the Heisenberg model), and to Hubbard model calculations for $U/t \approx 7$, which is appropriate for the case of Sr_2CuO_3. The recently calculated two-spinon + four-spinon correlation function for the $U/t \rightarrow \infty$ case gives an excellent description of the data, indicating that there is no large effect on the effective Hamiltonian due to the charge excitations. The success of the Heisenberg picture in the one-dimensional case is in contrast with INS measurements of the spin excitations in the two-dimensional $S = 1/2$ square lattice of La_2CuO_4, where $U/t = 7.3$, in where departures from the $U/t \rightarrow \infty$ prediction were well explained by ring exchange arising in the finite U/t Hubbard model [39]. However, the use of a new form of the Cu^{2+} magnetic form factor calculated especially

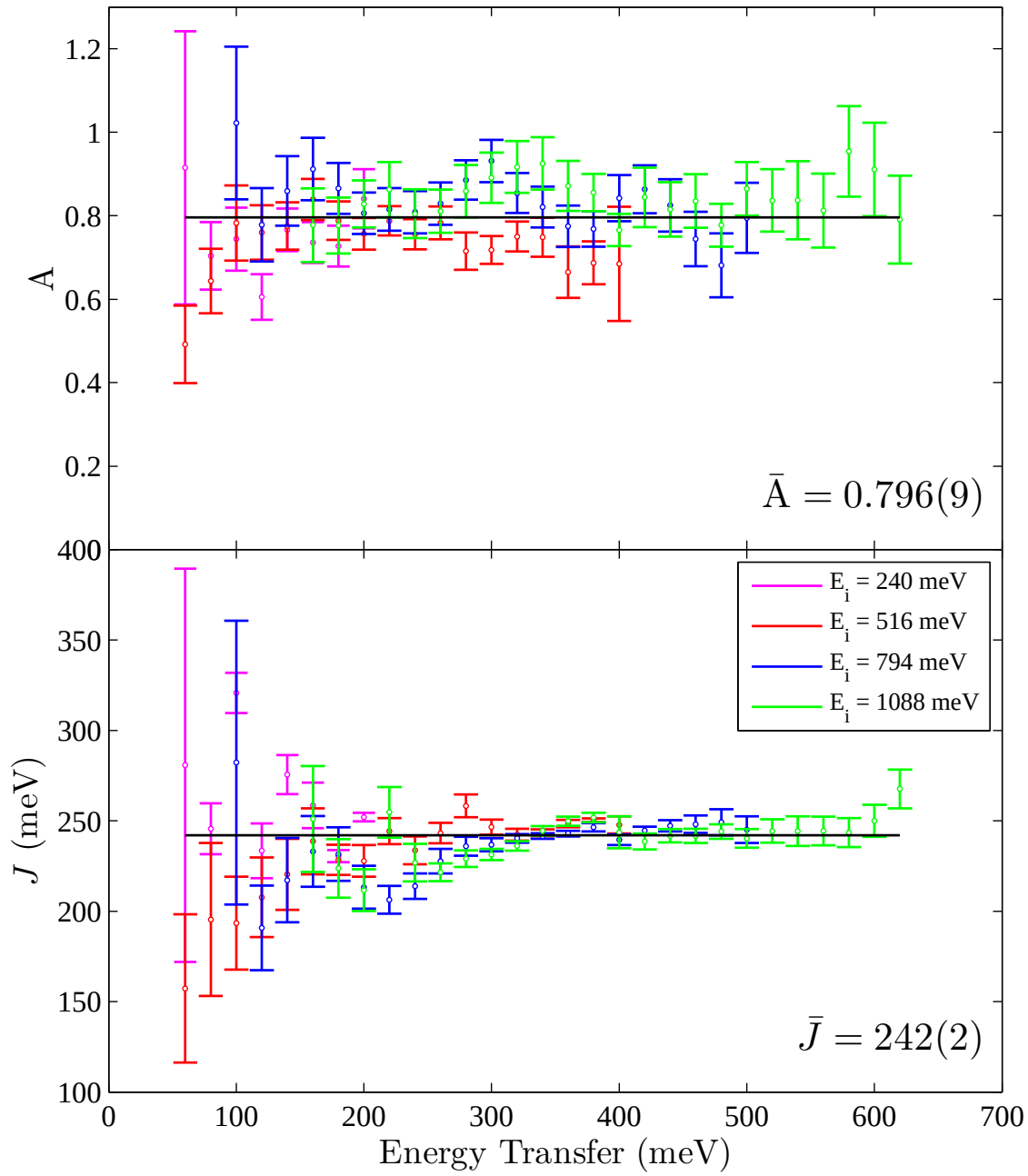

Figure 3.21: A and J plots are presented for the fits to the exact two-spinon + four-spinon calculation, using the LDA+U magnetic form factor for Sr_2CuO_3. For each set of A and J plots, the weighted mean value of A and J is shown and plotted on the graph (black).

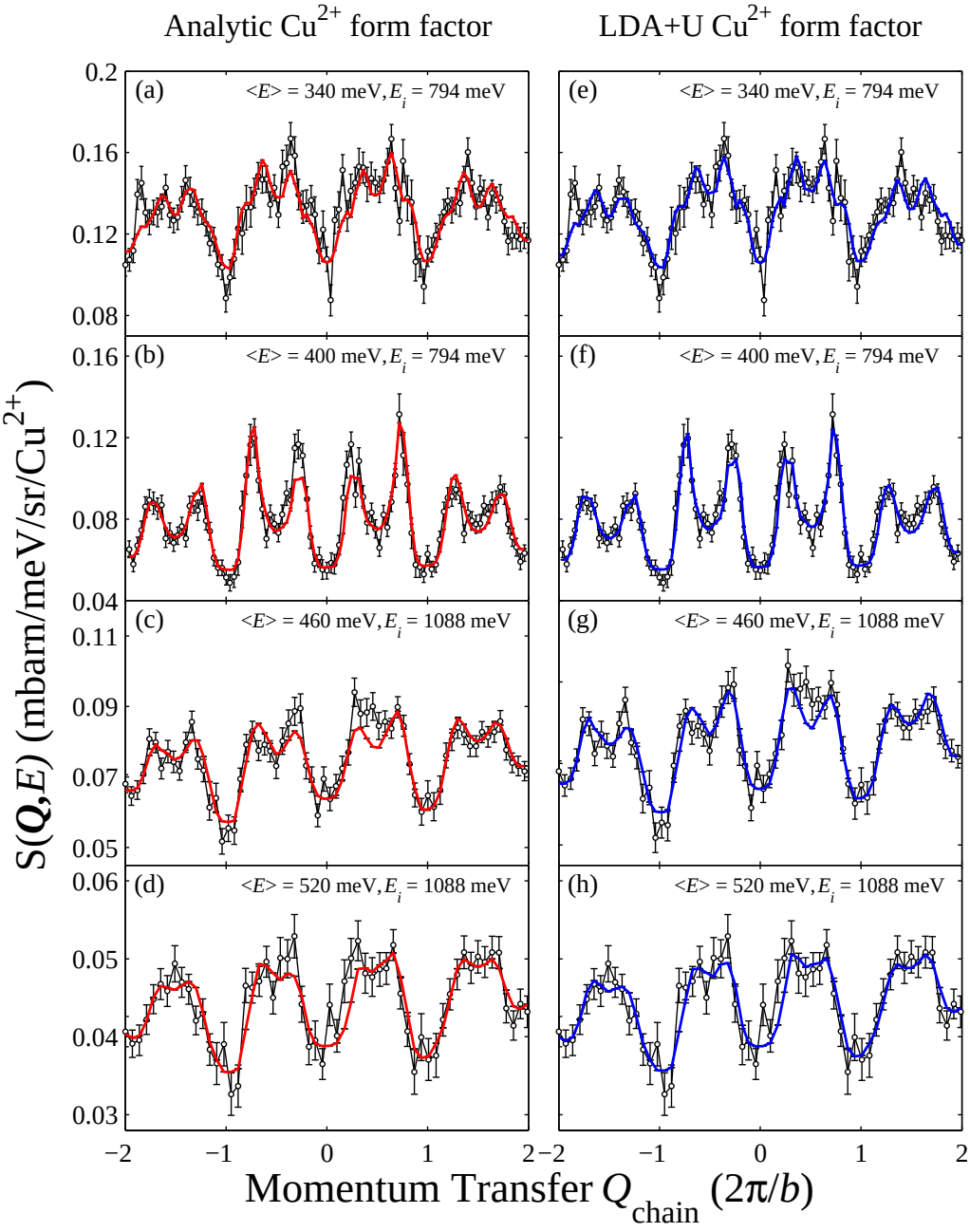

Figure 3.22: Example constant energy cuts through the data plotted as a function of Q_k (Q_{chain}). The full lines are fits to the data using the two-spinon + four-spinon continuum, together with the ionic Cu^{2+} magnetic form factor (left column, (a) - (d)) and the LDA+U magnetic form factor (right column, (e) - (i)). A range of different constant energy cuts from both the $E_i = 794$ meV and $E_i = 1088$ meV datasets are plotted to highlight the independence of the improved quality of fit from incident energy and energy transfer. The better quality of fit using the LDA+U form factor can be seen by comparing horizontally adjacent panels.

for Sr_2CuO_3 provides an explanation for the large discrepancy in the absolute magnitude of the INS intensity measured, as the magnetic form factor is much sharper in Q than normally assumed.

Our data then support the hypothesis that the magnetic electrons are not localised on the copper sites, but are involved in bonding with the adjacent electrons: i.e. the bonding is covalent in character. This is at odds with much of the current research in this area, which supports the picture that the bonding is predominantly ionic. The idea that the bonding may not be wholly ionic is not a new idea, but perhaps has been neglected somewhat in the recent literature. Theoretical calculations for the spin-density of cuprate systems made almost twenty years ago [70, 71] suggested that covalent effects in these systems may be significant, but were felt to be inconsistent with neutron diffraction measurements [72].

Chapter 4

Inelastic X-ray Scattering Study of the Quasi-Two-Dimensional Graphite Intercalated Compounds

4.1 Introduction to superconductivity in the Graphite Intercalated Compounds

Graphite Intercalation Compounds (GICs) have been studied for well over a hundred years [73], thanks in no small part to their wide range of properties. They are formed when two-dimensional arrays of a different chemical species are placed between graphene layers in graphite, usually resulting in an increase in the separation of adjacent graphene layers. This foreign species is called the intercalate. The choice of different intercalates allows the properties of the final GIC to be controlled. The number of free carriers is extremely small for undoped graphite, but the so-called 'Dirac cone' in the band structure of graphite means that if the graphite is doped, the number of free carriers (both electrons or holes) can easily be dramatically increased. So via the choice of intercalate, very sensitive control of the number of free carriers corresponds to very sensitive control of the electronic properties of the GIC.

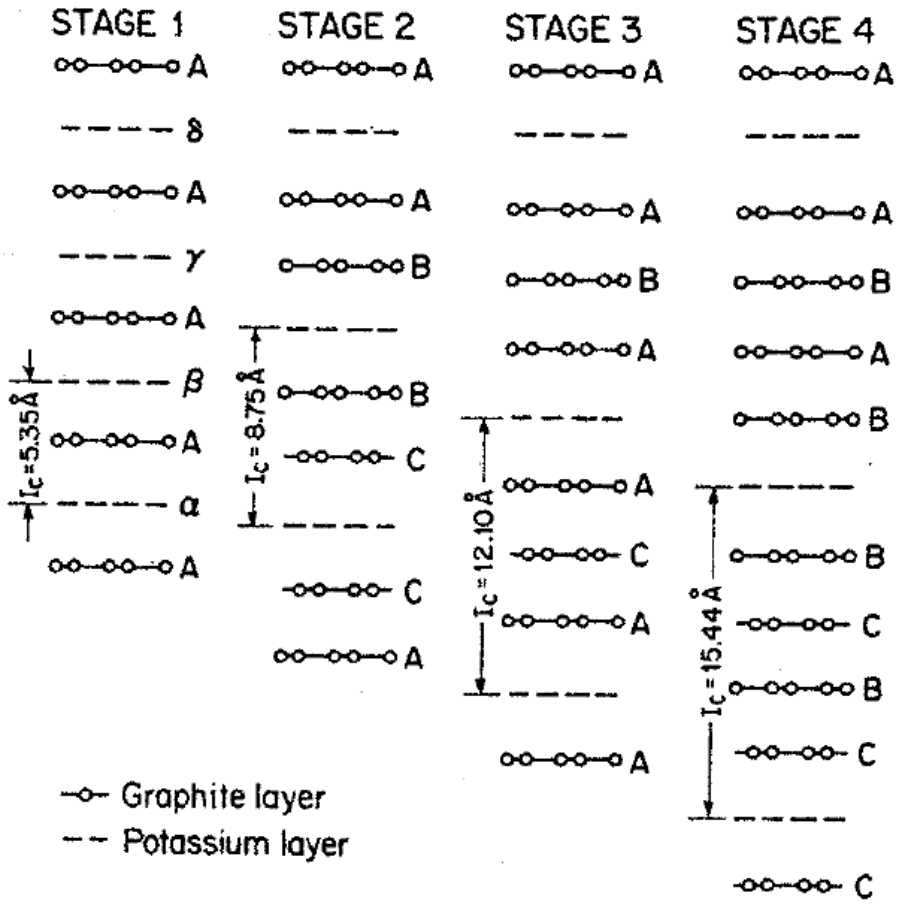

Figure 4.1: Schematic diagram of the staging phenomenon in potassium graphite for stages 1 to 4. The potassium layers are indicated by dashed lines and the graphite layers by solid lines which connect open circles, which show a projection of the carbon atom positions in that layer [73].

GICs display the phenomenon of 'staging': a stage n GIC has n layers of graphene between adjacent intercalant layers. A schematic of the different staging possible in a GIC (potassium graphite) is presented in Figure 4.1. Graphitic layers are normally labelled with Roman letters, and the intercalant layers with Greek letters. The four Greek letters (α, β, γ and δ) used to label the potassium layers in the stage 1 potassium GIC (KC_8) denote that there are four different types of intercalant layer, and the overall structure can therefore be referred to as AαAβAΓAδ. It is noteworthy that in this nomenclature graphite itself has the structure AB, but when an intercalate is formed the graphite often changes its own stacking to AA to accommodate the intercalate.

In the last few decades stage 1 lithium graphite (LiC_6) has become one of the most studied GICs thanks to its widespread usage in lithium-ion batteries as the active part of the anode [74]. The anode is required to be able to absorb and emit lithium ions during charging and discharging respectively. It is ideally suited for this purpose, as the intercalation of lithium into graphite is largely reversible, with little damage caused to the original graphite. Most intercalation compounds do not have this property. More generally, many different alkali metal GICs have been shown to act as catalysts for many different processes in organic chemistry, but unfortunately there is no clear understanding of how this mechanism works [73]. GICs have also been put forward as future hydrogen storage materials in a hydrogen economy, as alkali metal GICs provide a hydrogen storage mechanism where the hydrogen can readily be absorbed into the GIC or removed. Stage 2 alkali metal GICs (e.g. KC_{24}, CsC_{24}) have displayed significant hydrogen gas uptake, up to two molecules of hydrogen gas per alkali metal atom M ($\approx 2H_2/M$) [75].

In recent years, the discovery of superconductivity in the stage 1 GICs YbC_6 and CaC_6 with superconducting critical temperatures (T_c) of 6.5 K and 11.5 K respectively [19], has reinvigorated the research interest in the study of GICs. These superconducting transition temperatures are over an order of magnitude higher than had been previously observed in any other GIC.

The structure of YbC_6 is presented in Figure 4.2, and is similar to many other stage 1 alkali metal GICs (e.g. BaC_6, SrC_6), with AαAβ stacking in the hexagonal space group $P6_3/mmc$ [19, 77]. For YbC_6 the lattice parameters are $a = b = 4.32$ Å and $c = 9.15$ Å[78]. Surprisingly, CaC_6 has a different structure to any other GIC studied, with AαAβAγ stacking in the rhombohedral space group $R\bar{3}m$ ($a = 4.33$ Å and $c = 13.572$ Å) [79]. This structure is shown in Figure 4.3. The $R\bar{3}m$ structure can be described using either a hexagonal or a rhombohedral basis, which allows the use of hexagonal coordinates in CaC_6 for easier comparison with the other GICs. Throughout this work, the directions in reciprocal space are described using the hexagonal basis, despite the fact that the majority of the theoretical groups who have published work on this subject use the rhombohedral basis. The choice here aids comparison with the other GICs, and also simplifies the definition of the out-of-plane direction (perpendicular to the graphene sheets), which in

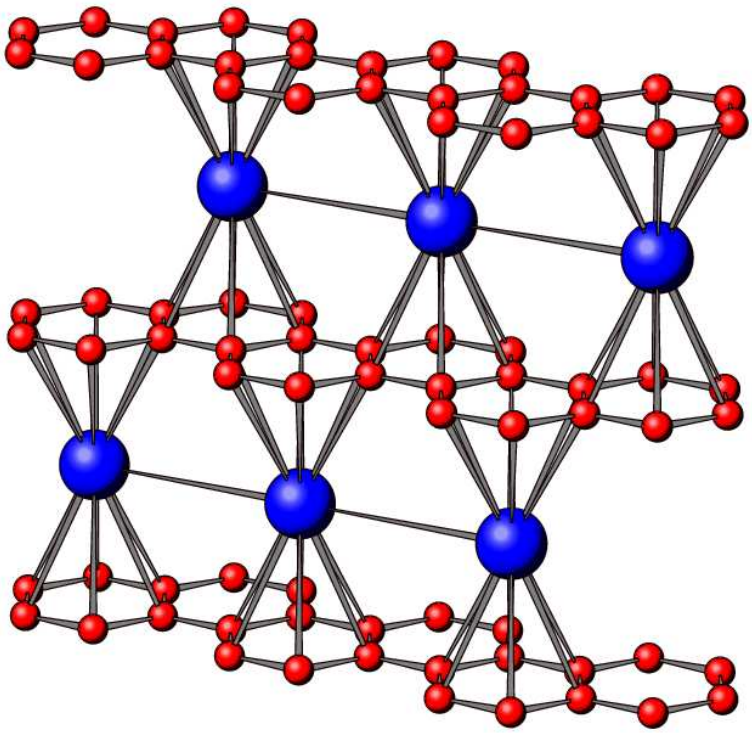

Figure 4.2: The structure of YbC_6, BaC_6 and SrC_6. The space group is $P6_3/mmc$. Carbon atoms are red, intercalant atoms are blue [76].

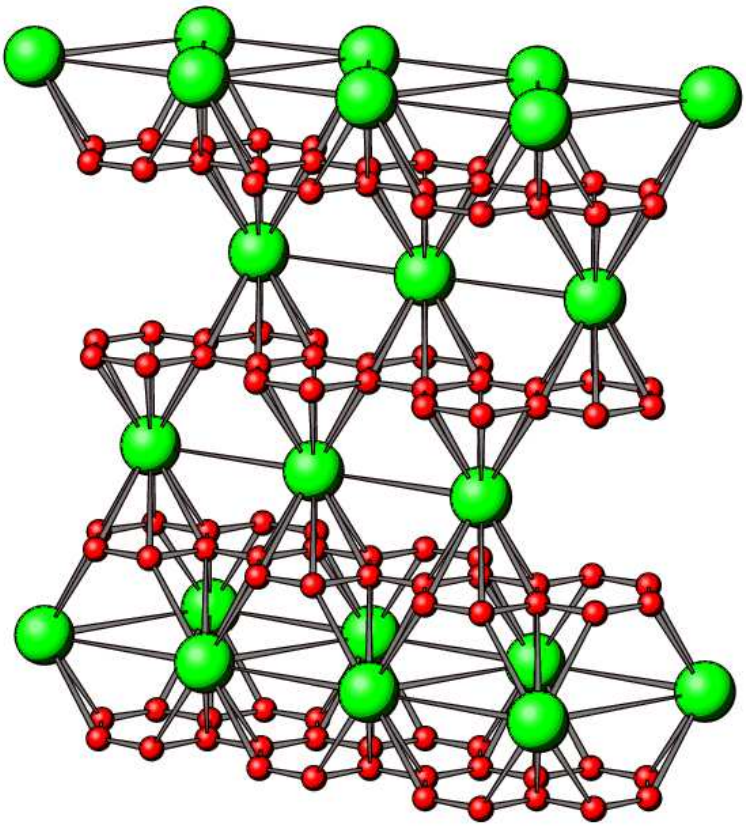

Figure 4.3: Structure of CaC_6. The space group is $R\bar{3}m$. Carbon atoms are red, calcium atoms are green [76].

the hexagonal basis is the (00L) direction but in the rhombohedral basis is the (HHH) direction. The Brillouin zone of CaC_6, with some of its symmetry points labelled, is provided in Figure 4.4. The Γ point is in the centre of the Brillouin zone, and the ΓL direction is equivalent to the (00L) direction.

Immediately after the discovery of superconductivity in YbC_6 and CaC_6 it was suggested that a novel pairing mechanism involving excitons or acoustic plasmons could be responsible for the stability of the superconducting phase [81], due to the empirical observation of superconductivity often coinciding with the electronic occupation of an isotropic, three-dimensional band in CaC_6 (often called the interlayer band). These conclusions were criticised in a subsequent paper by Igor Mazin [82], which put forward a more conventional picture of electron (Cooper) pairs forming via electron-phonon coupling. Based on

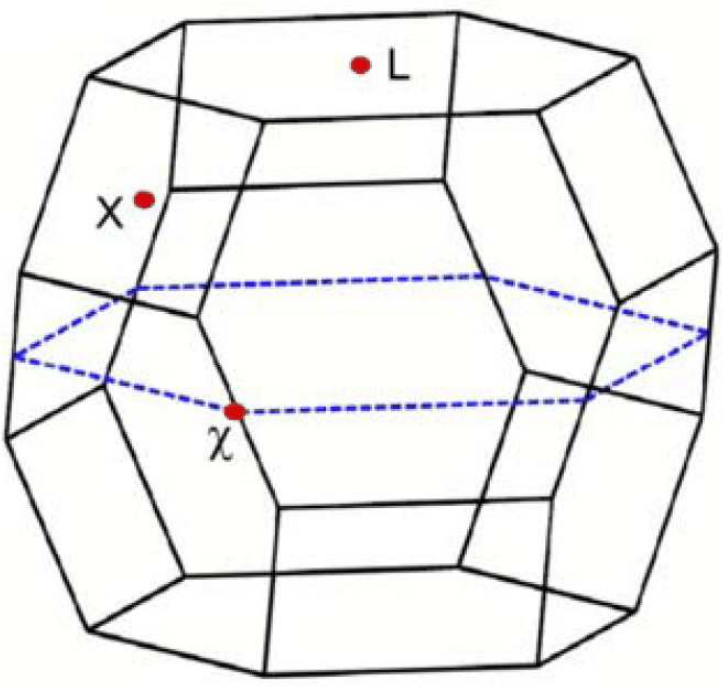

Figure 4.4: Brillouin zone of CaC_6. The X, χ and L points on the edge of the Brillouin zone are labelled [80].

the isotope effect in BCS superconductivity, Mazin was able to make a relatively simple argument to make a prediction for the amount of electron-phonon coupling to intercalant (Yb or Ca) phonons and graphitic (C) phonons. As the isotope effect in the superconducting GICs is still a subject of much debate, it is constructive to work through this early argument by Mazin here.

For an elemental superconductor, the isotope effect is defined as

$$\alpha = -\frac{M}{\Delta M}\frac{\Delta T_c}{T_c} \tag{4.1}$$

where M is the mass of the element and ΔM is the mass difference between the two isotopes. This equation can easily be rearranged to give $T_c \approx M^{-\alpha}$. In the case of an elemental BCS superconductor $\alpha = 0.5$, since in the BCS theory T_c is directly proportional to the energy of the phonon involved in electron-phonon coupling, and a change of the mass at each ionic site corresponds to a renormalisation of the phonon energy by a factor

of $(\frac{(M+\Delta M)}{M})^{-0.5}$. In the case of a superconducting compound however, such as CaC_6, we define partial isotope coefficients for calcium and carbon, namely α_{Ca} and α_C, and Equation 4.1 becomes

$$\alpha_{total} = \alpha_{Ca} + \alpha_C = -\frac{M_{Ca}}{\Delta M_{Ca}}\frac{\Delta T_c}{T_c} - \frac{M_C}{\Delta M_C}\frac{\Delta T_c}{T_c} \tag{4.2}$$

If we assume that the superconductivity is BCS-like ($\alpha = 0.5$) and that all of the electron-phonon coupling comes from the intercalant phonons, we may write that $T_c^{CaC_6} \sim M_{Ca}^{-0.5}$ in CaC_6 and $T_c^{YbC_6} \sim M_{Yb}^{-0.5}$ in YbC_6. Combining these two statements gives

$$\frac{T_c^{CaC_6}}{T_c^{YbC_6}} = \sqrt{\frac{M_{Yb}}{M_{Ca}}} \tag{4.3}$$

From the experimental data, the left hand side of Equation 4.3 is equal to $11.5/6.5 = 1.77$, whereas the right hand side is $\sqrt{173.04/40.078} = 2.08$. The remaining discrepancy can be understood as arising from additional electron-phonon coupling involving graphitic phonons. This argument suggests that 1.77/2.08 (85%) of the electron-phonon coupling arises from coupling to the intercalant phonons in YbC_6 and CaC_6, with just 15% arising from coupling to graphitic phonons.

Subsequent to Mazin's work, Matteo Calandra and Francesco Mauri made calculations using density functional perturbation theory (DFPT) which proposed a complete description of the electron-phonon coupling mechanism in CaC_6 [20]. Both the electronic structure and the phononic structure of CaC_6 were calculated, as well as the electron-phonon coupling constants for calcium and graphitic phonons, with distinction given to phonons which vibrate in the graphite plane and phonons which vibrate perpendicular to the graphite plane. The phonon dispersions calculated are presented in Figure 4.5. They concluded that, contrary to the picture provided by Mazin, the electron-phonon coupling has almost equal contributions from calcium and graphitic phonons, with $\alpha_{Ca} = 0.24$ and $\alpha_C = 0.26$. The primary electron-phonon coupling is said to occur as a result of the Ca-derived part of the Fermi surface interacting with C_z phonon modes (graphitic phonons which vibrate

perpendicular to the graphite plane) and Ca_{xy} phonon modes (calcium phonons which vibrate in the graphite plane).

The Fermi surfaces as calculated by Calandra and Mauri for BaC_6, SrC_6 and CaC_6 are shown in Figure 4.6, drawn within the first Brillouin zone. These calculations were done assuming that all of these materials have the $R\bar{3}$m structure, which is only true for CaC_6. Consequently the true shape of the Brillouin zone is only correct for CaC_6. In these materials the C $2p\sigma$ band electrons do not contribute to the Fermi surface, as this band is entirely filled and well below the Fermi energy. The C $2p\pi$ electrons are largely responsible for the cylindrical parts of the Fermi surface with their major axis perpendicular to the graphene sheets, which are shown in the first two columns in Figure 4.6. The Ca $4s$ and Ca $3d_{z^2}$ electronic states are predominantly to be found in the almost spherical part of the Fermi surface in CaC_6, shown in the third column in Figure 4.6. This Fermi surface can be thought of as forming due to Ca electronic states interacting with the interlayer band in pure graphite (an unoccupied band in graphite which in real space is located between the graphene sheets) [23]. This part of the Fermi surface in CaC_6 is accordingly often called the interlayer band, and it is this part of the Fermi surface which is thought to be primarily involved in the electron-phonon coupling [20]. The Fermi surfaces in the second and third columns in Figure 4.6 intersect.

The measurement of a significant Ca isotope effect in CaC_6 [83] gave further evidence to suggest that phonons were heavily involved in the superconducting mechanism, but the size of the measured Ca isotope effect was the biggest surprise: $\alpha_{\mathrm{Ca}} = 0.53(2)$, which is just over the usual limit for BCS of 0.5. Assuming that the electron-phonon coupling mechanism is indeed BCS-like, the natural conclusion from the measured Ca isotope effect is that there is virtually no electron-phonon coupling to any graphitic phonons, contrary to the DFPT picture [20]. Other explanations include suggestions that either the total isotope effect is actually larger than 0.5, in line with some of the high temperature superconductors, or there are experimental issues which could explain why the isotope effect is found to be so large. Issues of sample purity are the most obvious suggestion, but magnetic impurities can affect the measured isotope effect, as well as anharmonicity in the phonons involved in electron-phonon coupling, which can make the electron-phonon coupling λ strongly

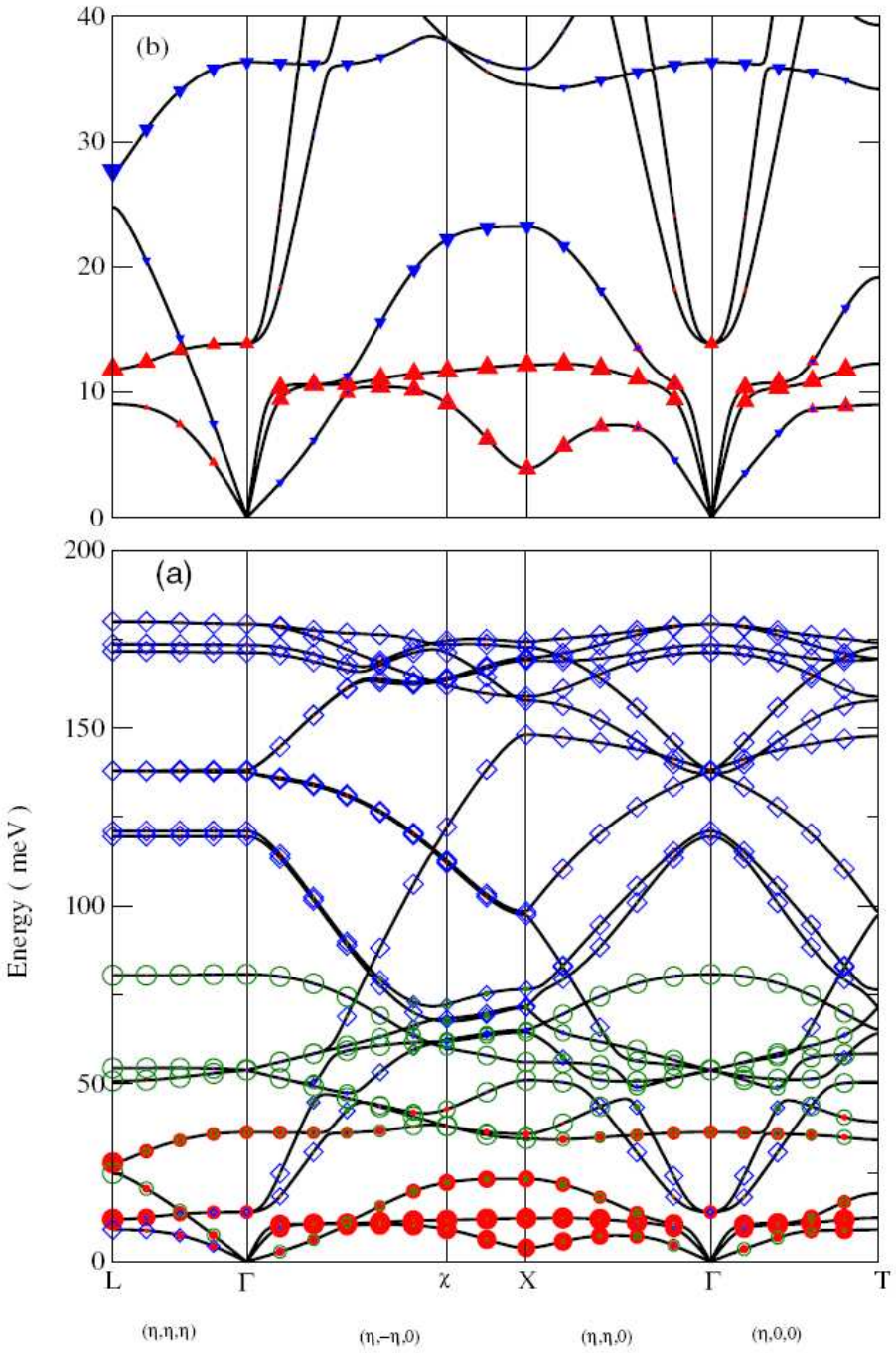

Figure 4.5: (a) Full CaC_6 phonon dispersion as calculated using density functional perturbation theory (DFPT) [20]. The amount of Ca vibration is represented by the size of the ●, of C_z by the size of ○, and of C_{xy} by the size of ◇. (b) CaC_6 phonon dispersion up to 40 meV. The amount of Ca_{xy} vibration is indicated by the size of ▲, and of Ca_z by the size of ▼.

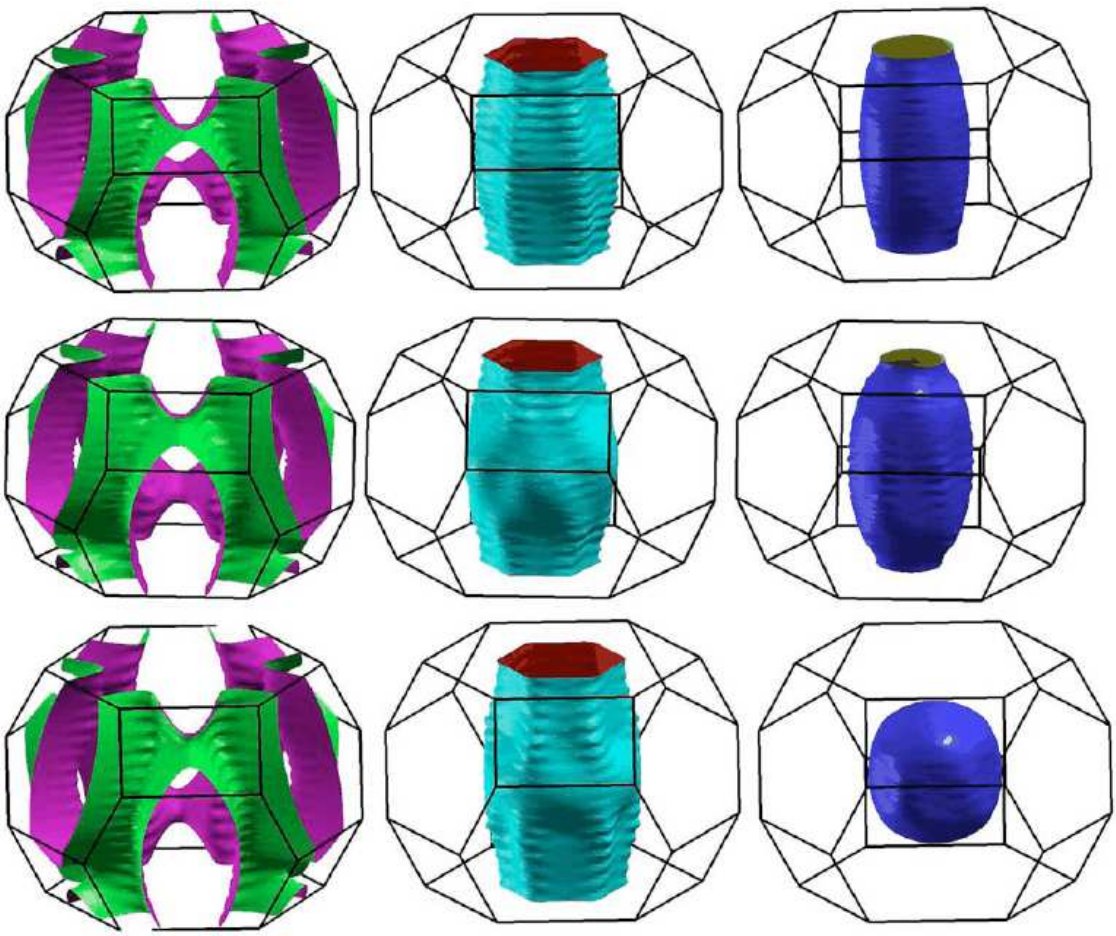

Figure 4.6: DFPT-calculated Fermi surfaces of BaC_6 (first row), SrC_6 (second row) and CaC_6 (third row) [77]. Here the vertical axis is perpendicular to the graphene sheets [77].

dependent on the mass. Clarification on this point could be made by measuring the C isotope effect in CaC_6 using ^{13}C, but as yet no study has been published.

The positive linear dependence of the critical temperature in CaC_6 up to around 8 GPa [84, 85, 86] is also not fully understood. DFPT calculations predict that the T_c should increase with pressure, but non-linearly [77]. The predicted non-linearity in T_c comes from the non-linear softening of an acoustic Ca_{xy} phonon to zero energy transfer, which in turn produces a non-linear increase in the calculated electron-phonon coupling, since electron-phonon coupling is inversely proportional to the phonon energy [77]. The measured positive linear dependence of T_c on pressure is also observed in YbC_6 and SrC_6, which have values of T_c of 6.5 and 1.65 K respectively at ambient pressure [22]. In the case of CaC_6 it was postulated that this behaviour could arise from a continuous staging transition from stage 1 calcium graphite to stage 2 [77]. However, a pressure-dependent X-ray diffraction study of CaC_6 shows that the $R\bar{3}m$ space group is stable up to 13 GPa, but at 8 GPa the system is believed to undergo a order-disorder transition, signified by a sudden increase in the Bragg peak widths measured and a dramatic increase in the measured isothermal compressibility [87]. The order-disorder transition is believed to result from random shifts of the Ca atoms in-plane away from their ambient pressure positions, as any explanation cannot be a result of a change in structure as no change was observed. There still remains no definitive explanation for the peculiar pressure dependence of T_c up to 8 GPa, and this inconsistency between theory and experiment could belie a misunderstanding of the superconducting mechanism.

Since there are still unanswered questions about the superconductivity in GICs, there is clear motivation to look for other correlations that T_c may have with other physical parameters. One parameter which does appear to scale with T_c in the superconducting GICs is the separation of adjacent graphene layers d. The correlation between T_c and d is presented in Figure 4.7. There is an almost exponential decrease of T_c as the layer separation d increases. This observation is also consistent with the pressure dependence of T_c, as the increased pressure acts to decrease the graphene layer separation. In Figure 4.7 this is shown in the case of CaC_6 by plotting an additional point (in grey) which describes the case when CaC_6 is subjected to a pressure of 8 GPa. It has been suggested that

the decreased layer separation promotes an interband interaction between the C $2p\pi$ and interlayer parts of the Fermi surface which intersect (see the second and third columns in Figure 4.6), which in turn increases the amount of electron-phonon coupling possible [22, 88].

In the last two years there have been Angle-Resolved PhotoEmission Spectroscopy (ARPES) studies of both doped graphene systems and GICs [89, 90], which have suggested that the electron-phonon coupling to high-energy ($\approx$ 200 meV) graphitic in-plane phonons is both strong and highly anisotropic. Similar conclusions have also been made based on ARPES measurements on CaC_6 [91]. This observation is in clear disagreement with the DFPT description, as the observed electron-phonon coupling to these modes is sufficient to explain the enhanced T_c without any additional electron-phonon coupling to lower energy modes.

ARPES is primarily used to measure the electronic structure of materials, but in addition is also sensitive to electron-phonon coupling. Electron-phonon coupling manifests itself in ARPES data as a sudden change in the gradient of an electronic band when plotted as a function of energy E and momentum k, since the effective mass $m_{eff} \propto [\frac{d^2E}{d^2k}]^{-1}$. The strength of the electron-phonon coupling λ_k can then be calculated using the equation $\lambda_k = \frac{v_k^0(E_F)}{v_k(E_F)} - 1$, where $v_k^0(E_F)$ and $v_k(E_F)$ are the measured and the bare velocities of the electronic band at the Fermi energy E_F. The bare velocity is the band velocity ($v = \frac{dE}{dk}$) that would be measured if there were no electron-phonon coupling. It is usually estimated by extrapolating from the band structure which is well away from the energy range in which electron-phonon coupling is strongly affecting the observed electronic structure, but as near to E_F as possible.

However, electron-phonon coupling is not a property that can be simply switched off in order to measure the bare velocity, and a recent paper has been published which shows that assuming linearity in the bare bands around the Fermi energy could lead to large over-estimates in the estimate of λ [92]. For these reasons, in two of the papers mentioned (both on GICs: on KC_8 [90] and CaC_6 [91]) the imaginary part of the self-energy has been used to support the arguments for large electron-phonon coupling, a method which does not require knowledge of the bare electronic bands. The CaC_6 study also uses independent

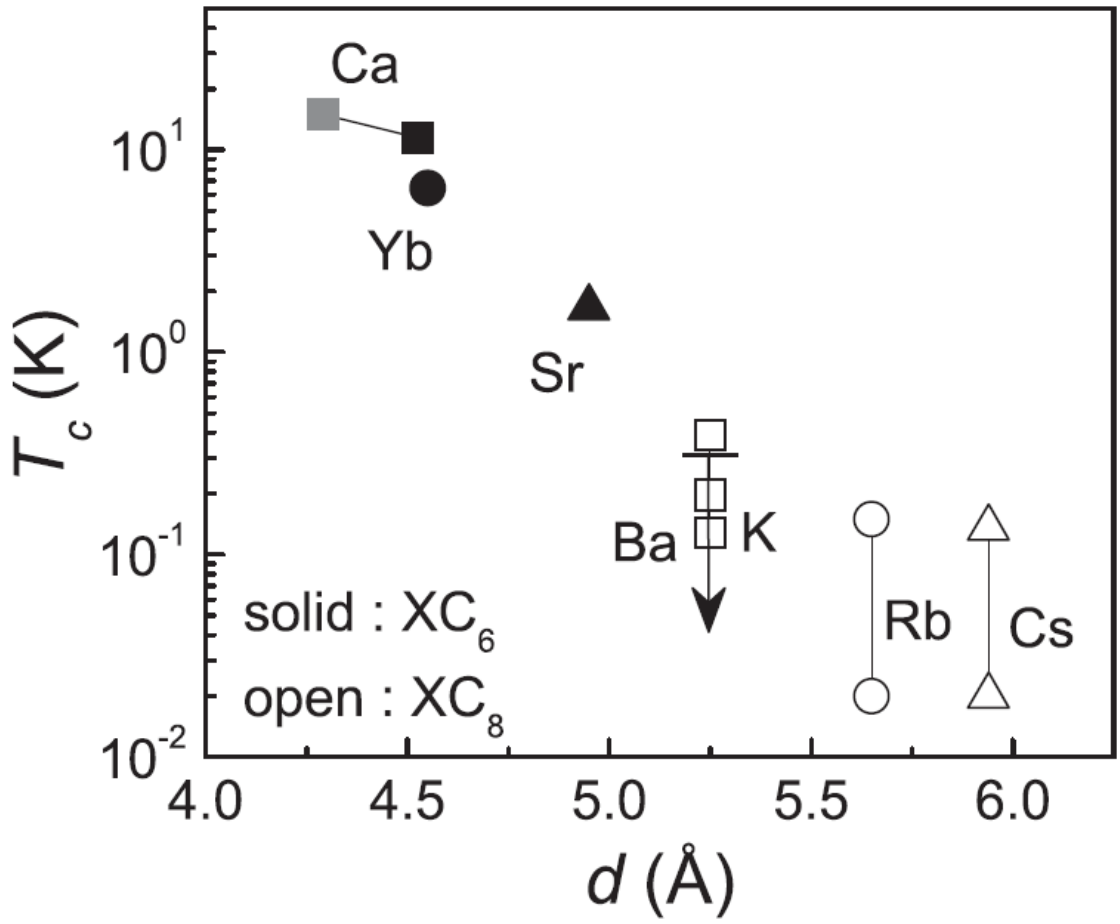

Figure 4.7: T_c as a function of d for CaC_6, YbC_6, SrC_6, BaC_6, KC_8, RbC_8 and CsC_8. For CaC_6, T_c at $P = 8$ GPa is also plotted in grey (d is calculated from the bulk modulus found using by DFPT [85]). An upper limit of T_c for BaC_6 (0.3 K) is labelled with an arrow [22], although this upper limit has been subsequently superseded (now 0.080 K) [21].

calculations of the band structure as a description of the bare electronic structure for an independent estimate of λ [91]. This change in the assumption of the bare bands does reduce the calculated electron-phonon coupling strength, but the strong anisotropy still exists, unlike the measurements done on Ca-doped graphene [92].

These ARPES studies emphasise the large remaining inconsistencies in the understanding of the superconducting GICS and doped graphene systems. Many would argue that the strong anisotropic coupling may come from complexities in the underlying band structure, but with the current descriptions of the band structure for CaC_6 having insufficient curvature to explain the observed behaviour, the problem quite rightly still remains one for much debate.

Since ARPES is a direct way of measuring the band structure and perturbations to the measured band structure can be attributed to coupling to bosons (such as phonons), the obvious further study would be look at the phonons in the superconducting GICs and look for any signs of electron-phonon coupling from the phononic signal. This has been the driving force behind much of the work on GICs in this thesis. In an effort to discover what leads to such enhanced superconducting transition temperatures in CaC_6 and YbC_6, I have worked on three inelastic X-ray scattering (IXS) experiments at Sector 3 at the Advanced Photon Source, Illinois, the first two studying CaC_6 and the third looking at BaC_6, all as a function of temperature.

In an early paper on the superconducting GICs [81], it was suggested that BaC_6 could also have a relatively large T_c, since the interlayer band is occupied. However, later studies have shown that there is no superconducting transition in BaC_6 down to 0.080 K [21]. The DFPT description of superconductivity appears to be at least in approximate agreement with the measured superconducting transition temperatures of BaC_6 and SrC_6, where BaC_6 was predicted to be 0.23 K and SrC_6 is predicted to be 3.03 K and has been measured to be at 1.65 K [22]. The motivation to study both CaC_6 and BaC_6 was to search for any signature of electron-phonon coupling which appeared in CaC_6 but was not present in BaC_6, thereby providing a direct measurement of the difference in the strength of the electron-phonon interaction in these two systems. Electron-phonon coupling in a

phonon study can manifest itself in different ways depending on the system, either by a significant increase in the linewidth of a mode, a direct result of the lifetime of the excitation reducing, or the softening or hardening of a phonon mode. These IXS studies also constitute a direct test of the DFPT description of superconductivity in GICs, as any deviation away from the predicted dispersion could signify an important difference between the theory and reality.

In the past the only method by which phonons could be measured throughout the entire Brillouin zone was inelastic neutron scattering (INS), but in recent years meV resolution has been achieved using IXS at some of the major synchrotrons around the world (ID16 and ID28 at the ESRF in France, Sectors 3 and 30 at the Advanced Photon Source in the USA, and BL35XU at SPring-8 in Japan). This is discussed in detail in Chapter 2. The great advantage that IXS has over INS in the case of studying GICs is that far smaller samples are required for the same statistics.

4.2 Sample preparation of GICs

It is unsurprising that since different GICs can have such dramatically different properties, it is more difficult to prepare samples of one kind of GIC than another kind of GIC. Most GICs present a challenge to prepare, primarily because most are sensitive to oxygen and water and therefore have to be manipulated inside gloveboxes containing helium or argon gas. In particular, it is extremely difficult to prepare high-purity samples of CaC_6 and BaC_6. This difficulty in sample preparation has meant that these materials have resisted much experimental study, and a wealth of experimental research has only been recently performed on these materials, despite these difficulties, due to the wide-spread interest in their superconductivity. In scattering techniques, it is vital that the samples are pure over a significant volume of the sample, as so much of the sample is probed by the X-rays in each measurement. In IXS the samples are required to be pure over a length scale of the order 100 μm in all directions.

One of the main reasons that has made both X-ray and neutron scattering studies of GICs

difficult is the complete lack of large single-crystal samples. This is a direct result of it being impossible to obtain large single crystals of the starting material, graphite. There are many different forms of graphite, which are used in many different contexts. In all the measurements discussed here, we used highly-ordered pyrolytic graphite (HOPG) as our base material. Pyrolytic graphite has some covalent bonding between graphene layers, which helps to strengthen the material against shearing and makes it less brittle. From a crystallographic point of view, HOPG is a rather peculiar material: although in the c direction (normal to the graphene planes) HOPG can be made to have a mosaic as small as 0.5°, within the ab-plane the sample is essentially a powder, as the crystallite size is of the order of 1 μm in the ab-plane. This means that for all of our IXS measurements on GICs with Q in the (00L) direction, we can study the phonons as if the sample is a single crystal. With Q in-plane, we are sensitive to the in-plane phonon density of states, as we are sampling Q in all directions in-plane simultaneously.

The method used to produce all the CaC_6 samples discussed in this Chapter is the alloy method. This method of GIC preparation involves the immersion of a graphite platelet into a Li-Ca alloy at 350°C for ten days [93]. We did this within a stainless steel reactor tube which was hermetically sealed with a Swagelok blank. The parameters to be optimised in the alloy method are the relative concentrations of lithium metal and calcium metal in the alloy (we used 3 parts lithium, 1 part calcium), the temperature at which the alloy is kept and the length of time the graphite is immersed in the alloy. Any one of these parameters, if incorrectly chosen, can hugely reduce the purity of any CaC_6 samples formed [93]. Another parameter that became apparent was the graphite platelet size, both in the ab-plane and in the c direction: too big (over $\approx$ 3 mm in the ab-plane or over $\approx$ 1 mm in the c direction), and there would always be a LiC_6 core inside a CaC_6 shell. By carefully optimising these parameters, the alloy method was able to produce samples with better than 99% purity, considerably better than the sample purities often quoted in the literature of up to 5% impurities [94].

It has been shown that initially (within the first 20 minutes) the lithium is intercalated within the graphite layers, creating lithium graphite of stages 1 to 5 [95]. After about two hours, the lithium arranges itself into the stage 1 lithium graphite, LiC_6, and then over the

course of the next few days, the calcium atoms are preferentially intercalated whilst the lithium is deintercalated. The melting point of calcium is extremely high, so this method circumvents that problem by alloying the calcium with the lithium in order for the calcium atoms to be in the liquid phase. The role of lithium in the sample preparation process is not especially well understood [79]. In addition, BaC_6 can also be prepared with a Li-Ba (3 parts lithium, 1 part barium) alloy in a similar manner to CaC_6, with high sample purity possible [93].

One issue that is raised about the alloy method of making GICs is the question of lithium impurities. Although CaC_6 samples can be made in which the (00L) lithium graphite diffraction peaks are more than two orders of magnitude smaller than the equivalent CaC_6 peaks, this does not remove the possibility that there may be some kind of amorphous lithium impurity, which may be most prevalent at the grain boundaries between different crystallite in the graphite used. This impurity may not give long range order peaks due to the inherent disorder. Currently as yet unpublished inelastic neutron scattering (INS) data of CaC_6 certainly supports the case that there is still a significant amount of lithium in the samples, as lithium is a strong incoherent scatterer of neutrons, which gives rise to a very large incoherent scattering cross-section on top of which phononic signal from CaC_6 is observed. This is another reason why IXS is the preferred option for studying phonons in GICs.

GIC samples are often made using vapour transport, in which an evacuated reactor tube is placed in a furnace, one end containing the metal to be intercalated and the other end containing graphite samples. Each end is maintained at a certain temperature, high enough to vaporise the metal at one end, and not high enough to damage the graphite or the resulting GIC at the other. Through trial and improvement, the best combination of temperatures and length of time in the furnace is found. This method can produce very high-purity samples of many GICS (e.g. KC_8, KC_{24} and LiC_6 can be made this way). For both CaC_6 and BaC_6 however, this method only achieves partial intercalation of the graphite, with the final samples anything between 5% to 50% GIC and the remainder unreacted graphite. Most of the GIC forms at the edges of the original graphite platelet, as the metal vapour enters the graphite between graphene layers.

Although large (greater than 200 μm $\times$ 200 μm $\times$ 200 μm) platelets of pure CaC_6 or BaC_6 cannot be made via the vapour transport method, the sample only needs to be pure in the area which the X-ray beam interacts with. In the case of Sector 3, the beam cross-section used in all our beamtimes was 250 μm (vertical) by 300 μm (horizontal). Whilst the CaC_6 samples made via vapour transport are only intercalated in the ab-plane in the region within 50 μm from the edge, it has proved possible for vapour transport produced samples of BaC_6 to be intercalated up to 1 mm away from the edge of the sample. A photograph of two such samples is presented in Figure 4.8, in which the BaC_6 part of the samples can be observed, with the slight gold colour of the GIC obvious in comparison to the dull silver of the aluminium foil. Since the pure part of the sample was larger than the beam size at Sector 3, this allowed us to use a sample made via the vapour transport method in our beamtime on BaC_6. We were able to support this conclusion with X-ray diffraction done at UCL, which showed that the relative height of the BaC_6 Bragg peaks was maximised when the sample was positioned such that only its edge was illuminated by the incident X-rays. The purity of the BaC_6 sample at the edge was later confirmed by diffraction at Sector 3, showing a region approximately 1 mm $\times$ 1mm in area where only BaC_6 peaks could be observed.

4.3 Mounting CaC_6 and BaC_6 samples for IXS experiments

Due to the sensitivity of CaC_6 and BaC_6 to oxygen and water, the samples had to be somehow isolated from the air during our experiments. In addition to this there must be geometrical access to the sample for the incident and scattered X-rays. The option that we decided upon was to mount the samples prior to each set of beamtime inside a sample can sealed with an indium seal, since this meant that the seal could be verified prior to the start of the IXS experiment, and if necessary replaced. The sample can was then shipped to the US for each experiment. The problem of X-ray beam access was overcome by using a sample can equipped with beryllium windows. Since beryllium has very few electrons ($Z = 4$) and X-rays scatter from electrons, beryllium is essentially transparent to X-rays. The samples were mounted well in advance of each experiment so that the sample purity

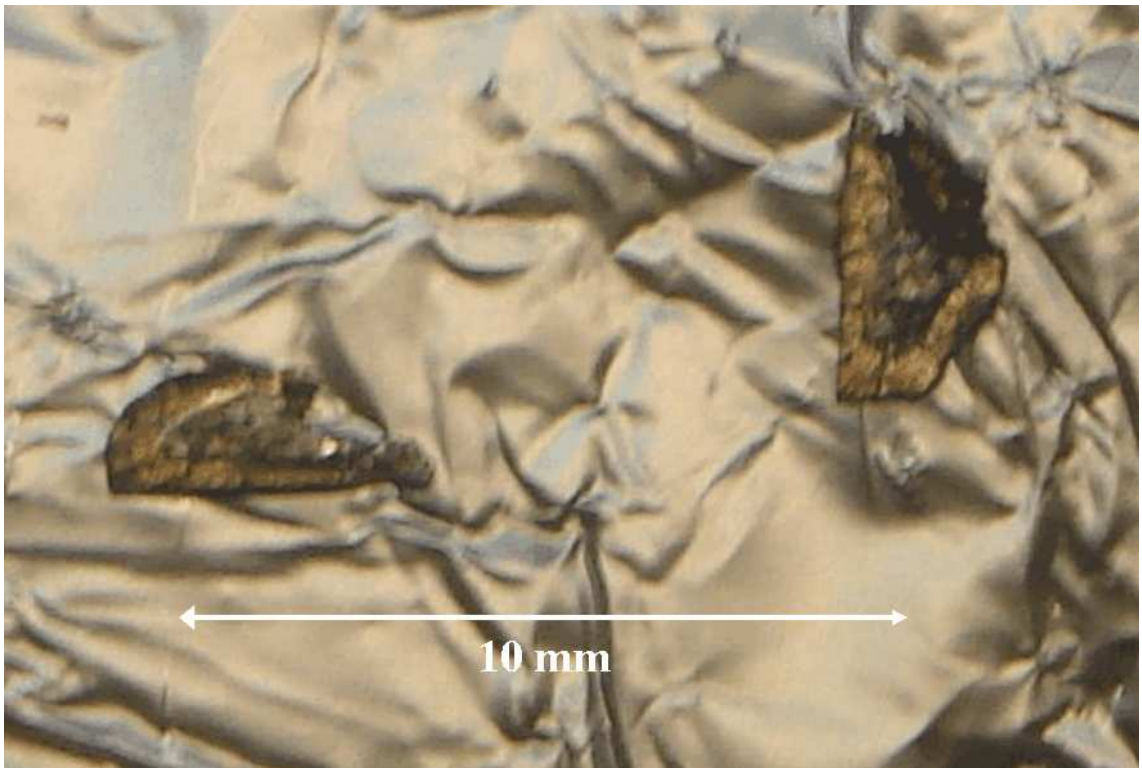

Figure 4.8: Two BaC_6 samples on aluminium foil prior to mounting. The intercalated part of the sample can be seen around the edge of the sample. A length scale is shown to aid the reader.

and the indium seal could be thoroughly checked.

We mounted all of the GIC samples studied as shown in Figure 4.9, by hanging the sample half off a copper peg. This setup allowed both reflection and transmission experiments to be done using the same sample, provided there was sufficient range in the ϕ motor (which has its rotation axis labelled in the Figure). Good thermal contact to the beamline cryogenics was provided by putting the sample in close proximity to the copper peg, which is in physical contact with the copper base.

A consequence of the choice to mount the samples well before beamtimes was that the sample was required to be placed within the can at such a height at which it could be put on the beamline and be at the centre of rotation of the ϕ and χ motors. Ideally the instrument could be made so that these motors sit on adjustable x, y and z stages so that regardless of where the sample is relative to where it has been secured to the goniometer, the sample can be placed on the centre of rotation. Unsurprisingly this is often not the case, as if the sample is easy to manipulate (i.e. not air-sensitive) it can simply be moved to the centre of rotation by hand using optical techniques. At Sector 3 there was some flexibility, but only $\pm$ 2 mm, so the sample needed to be centred precisely so that the very edge of the sample was within that range. The required distances were supplied by Dr Ahmet Alatas at Sector 3, and from my schematic the UCL MAPS workshop provided copper pegs of precisely the right length.

One major issue that was problematic throughout these experiments was the choice of how to secure the GIC samples to the copper plate. The adhesive had to provide reasonable thermal contact, to allow us to make measurements at low temperatures, but also had to be unreactive with the GICs. This latter condition rules out a lot of commonly used adhesives, as many contain water or are based on alcohol, which can react with GIC samples. Before our initial GIC experiment at the Advanced Photon source, we discovered that our chosen adhesive of GE Varnish (chemical name Phenolic Butvar Resin) actually reacted strongly with CaC_6. We then decided to use vacuum grease to mount our samples, as this was readily available and showed no reaction with CaC_6 after two hours in an Argon glovebox. We had initially discounted this adhesive as we were concerned that the samples would

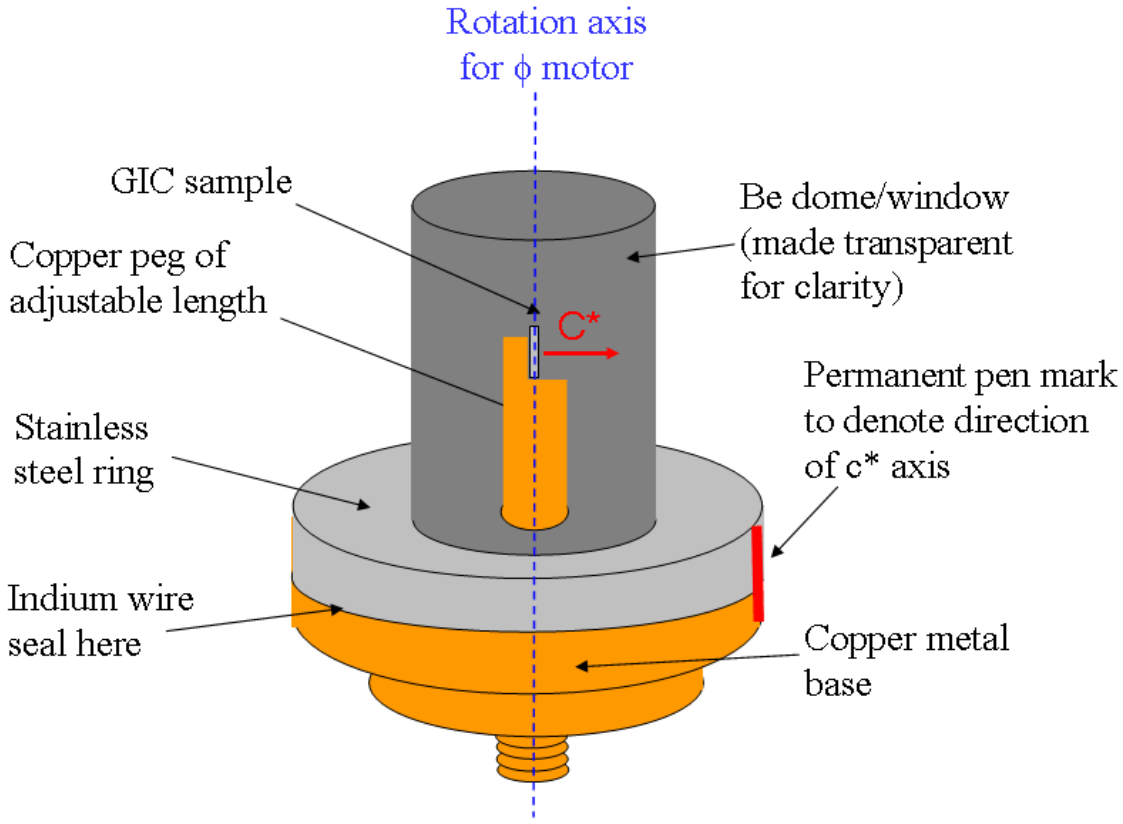

Figure 4.9: A schematic of a generic beryllium can used for IXS experiments.

not be securely fastened to the copper peg, and consequently could be knocked off their mounts in transit. Despite our concerns, this method kept the samples in place for our first set of beamtime, without dramatically affecting the samples.

Prior our second beamtime, some tests were carried out using electrically conductive carbon pads (as used in SEM measurements) to secure the GIC samples to the copper mount. This had the obvious advantage of being far more conductive than the vacuum grease, and only appeared to slightly degrade the GICs on the surface of the sample where it was in immediate contact of the carbon pad. We had concerns that the adhesive may fail at low temperatures, so we tested the adhesive down to 77 K by submerging it in liquid nitrogen, which appeared to make no difference to the adhesive. The manufacturers of the carbon pads claimed that the adhesive worked at liquid helium temperatures, so we felt confident enough to use these pads to mount the sample. However this choice was unfortunate as the CaC_6 sample fell off twice in the same beamtime at Sector 3. In retrospect, I think that a differential between the thermal expansions of CaC_6 and the carbon pad could have caused the problem, causing tensile stress to the bond. Perhaps a more probable reason is that the adhesive became very brittle at low temperatures, and consequently any strain on it (from thermal expansions or even just vibrations) could result in the failure of the bond.

After the carbon pad failed twice, we decided to return to the vacuum grease solution, specifically the use of Apiezon N Grease. This grease is designed to be used down to liquid helium temperatures, and crucially for us did not react with the samples appreciably. This was the adhesive used in the third beamtime at Sector 3, on BaC_6, and proved to be an ideal solution to the problem.

4.4 Purity assessment of CaC_6 and BaC_6 samples

Although the first set of beamtime showed that an indium seal could provide long-term protection to the GIC sample, we had not been able to check by sight how the sample fared after being sealed inside the can, as beryllium metal is not transparent to visible light.

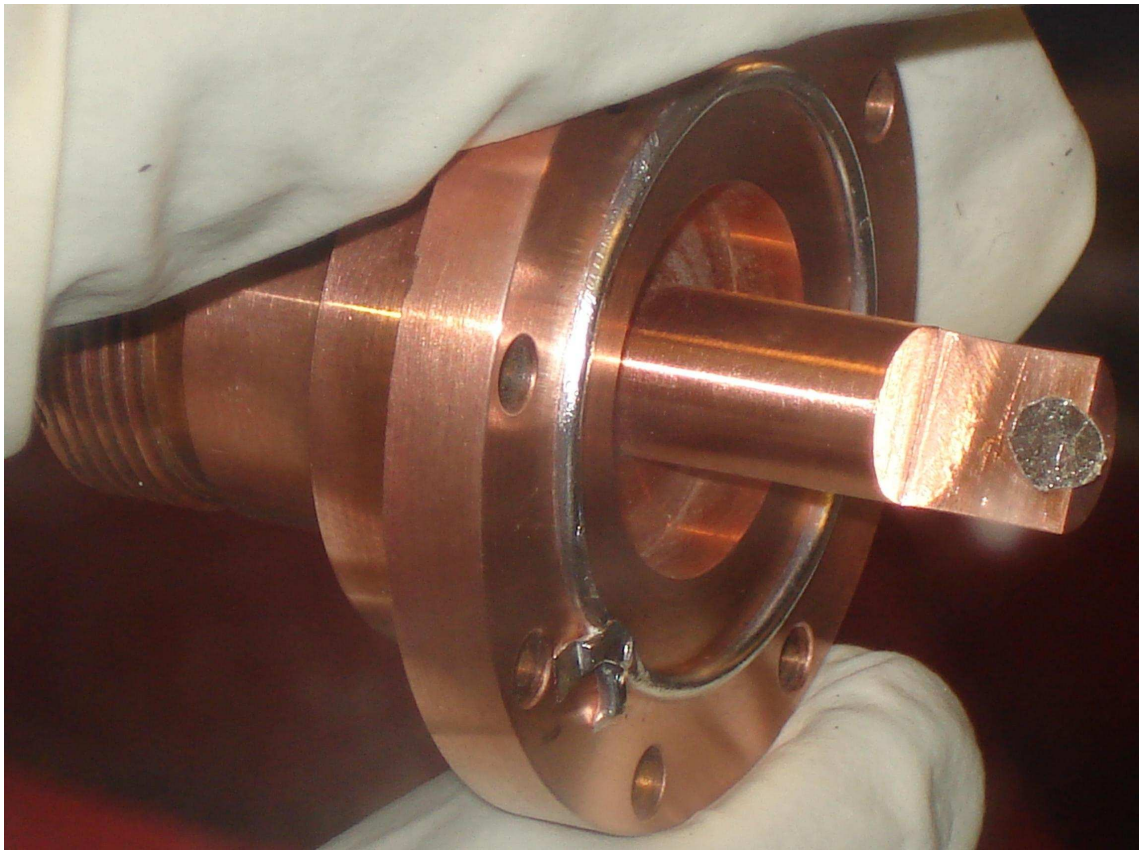

Figure 4.10: An example of a CaC_6 sample mounted for an IXS experiment. In this case GE varnish was used to secure the sample to the copper peg, an adhesive which unfortunately reacted with the samples. This sample subsequently had to be replaced before final mounting.

The sample purity had been confirmed using X-ray diffraction on CaC_6 samples from the same batch (from the same reactor tube) using a lab-based X-ray diffractometer. As the diffractometer had been used with other reactive GIC samples, it already had a sample can used routinely which had Mylar windows and was sealed with an O-ring seal. However this can was not airtight, and consequently the GIC sample which had been measured upon was always left to perish. I decided to improve upon this far from ideal situation by designing an adapter plate which could be secured to the X-ray diffractometer, into which the sample can with beryllium windows could be placed. We could then do X-ray diffraction on the very sample that we were to do our IXS experiment on, allowing us to check both the sample purity and the quality of the indium seal.

A schematic for the adapter plate which was made is presented in Figure 4.11. The adapter plate provides an additional ϕ rotation, as well as additional flexibility in the sample position in the direction of the axis defined by the ϕ rotation. This flexibility allowed the alignment of the sample to be tweaked depending on the distance that the GIC sample had been positioned from the copper baseplate (see Figure 4.9). The use of the adapter plate proved crucial, as one of the CaC_6 samples which we were planning to use for the second beamtime (which appeared to be the best for our purposes due to its thickness) actually had a large LiC_6 core which was not visible from the surface.

In Figure 4.12 diffraction measurements done at University College London on the CaC_6 sample used for the first set of beamtime on CaC_6 are provided. In Figure 4.12(a) I plot diffraction measured 7, 12 and 72 hours after the sample was mounted inside the beryllium can. This diffraction was done on the edge of the CaC_6 platelet measured with Q perpendicular to the graphene sheets (also called the (00L) direction). We were able to isolate the very edge of the sample by using the adapter plate to move the sample almost completely out of the incident X-ray beam. Our diffraction shows that the sample is extremely pure at its edge, with only a small peak associated with LiC_6 appearing at $Q = 1.7\text{Å}^{-1}$. However, this peak is only clearly visible in the scan taken after 7 hours, is weaker after 12 hours and is not visible on the 72 hours. This is strongly indicative that the LiC_6 is preferentially reacting with any water or oxygen which remained in the beryllium can after loading. This observation was not an isolated instance: we saw this

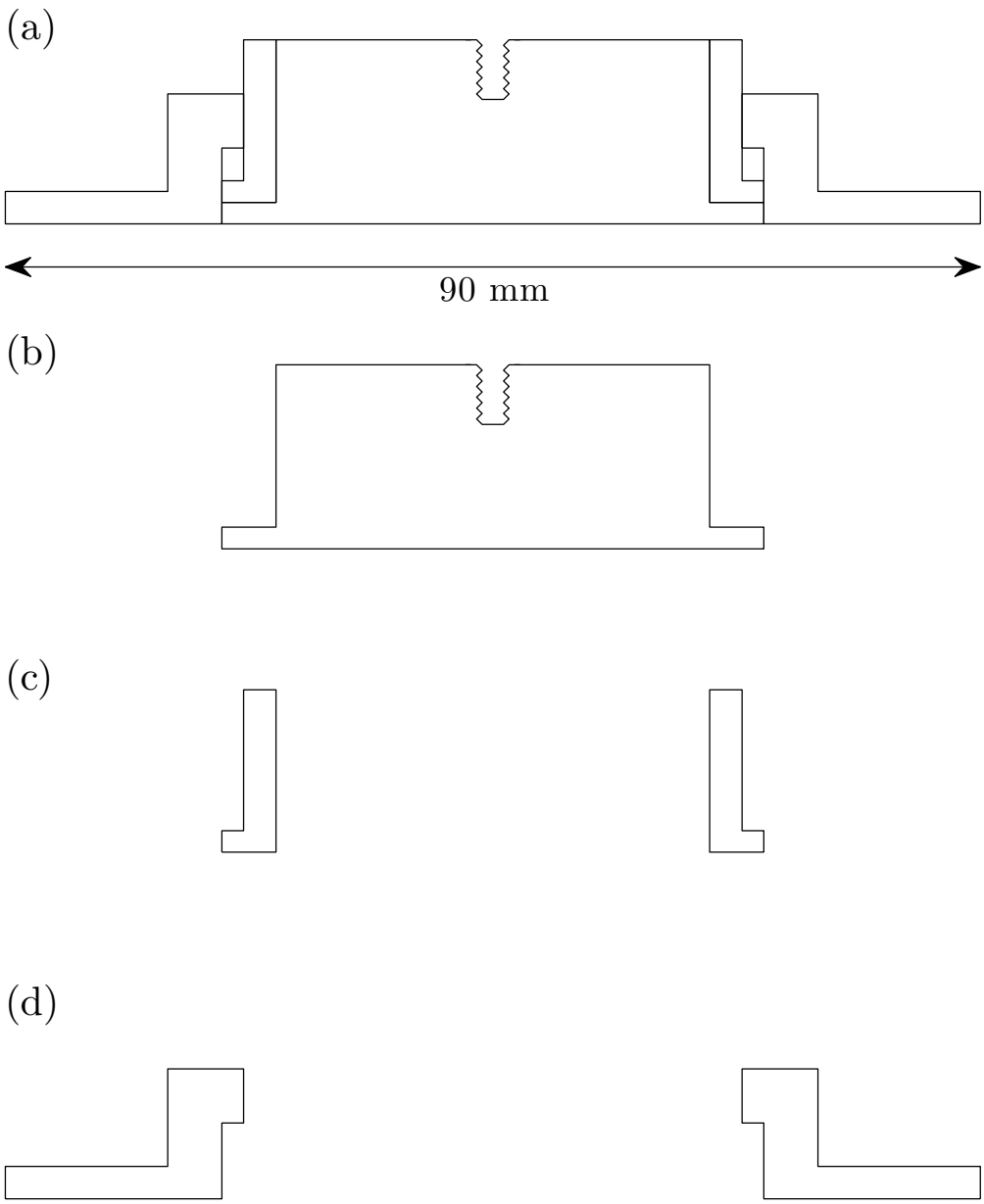

Figure 4.11: A schematic for the adapter plate made to allow X-ray diffraction of sample in-situ within the sample can with beryllium windows. (a) shows the adapter plate constructed out of the three independent parts, which are shown in (b), (c) and (d). Each part had cylindrical symmetry, so in order to describe each part most efficiently, a cross-section was drawn of each part through the axis of rotational symmetry. GS_1 and GS_2 label the positions at which grub screws were placed in the adapter plate in order to fix the relative positions of the three parts.

effect in the CaC_6 sample used in the second beamtime at Sector 3, but in this case the LiC_6 (002) was even weaker initially and within 6 hours became too weak to see on the X-ray set at UCL.

The left inset in Figure 4.12(a) is a scan done in θ at the value of 2θ for the CaC_6 (006) peak. This kind of scan is known as a 'rocking curve', as the sample is rocked (rotated in θ) whilst the incident and outgoing beam are maintained in the same directions. The width of this rocking curve is 3.67(1)°. This width also includes instrumental and sample size effects, but since it is so large we can assume that the majority of the width is a direct result of the sample mosaic. The right inset is a close up on the CaC_6 peak in the main figure. It shows undoubtedly that the sample was reacting with oxygen or water in the can, but the rate of sample deterioration had markedly decreased after 72 hours. We took that as a sign of the seal having worked, as the CaC_6 (and LiC_6) had reacted with the small amount of oxygen or water in the can. This behaviour could also be explained even if the seal was not leak tight, since when CaC_6 oxidises, it creates a protective layer on its surface, stopping any of the sample beneath the surface from breaking down. However, the rate of deterioration of CaC_6 in the beryllium can was much reduced in comparison to when the Mylar windowed sample can was used, suggesting that the seal was good.

4.5 Optimising the thickness of CaC_6 and BaC_6 samples for IXS experiments

Optimisation of the thicknesses of the GIC samples was important, since a balance needs to be found whereby the amount of sample to be probed is maximised, but also there is not too much sample so that almost all of the incident X-rays are attenuated. The beam cross-section used in all our beamtimes at Sector 3 was 250 μm (vertical) by 300 μm (horizontal), so for transmission measurements (where the GIC platelet normal is parallel to the incident beam) the volume over which the sample needs to be pure is 250 μm by 300 μm by approximately twice the attenuation length of the GIC. Usually the sample thickness is chosen to be approximately one attenuation length thick [29], so although

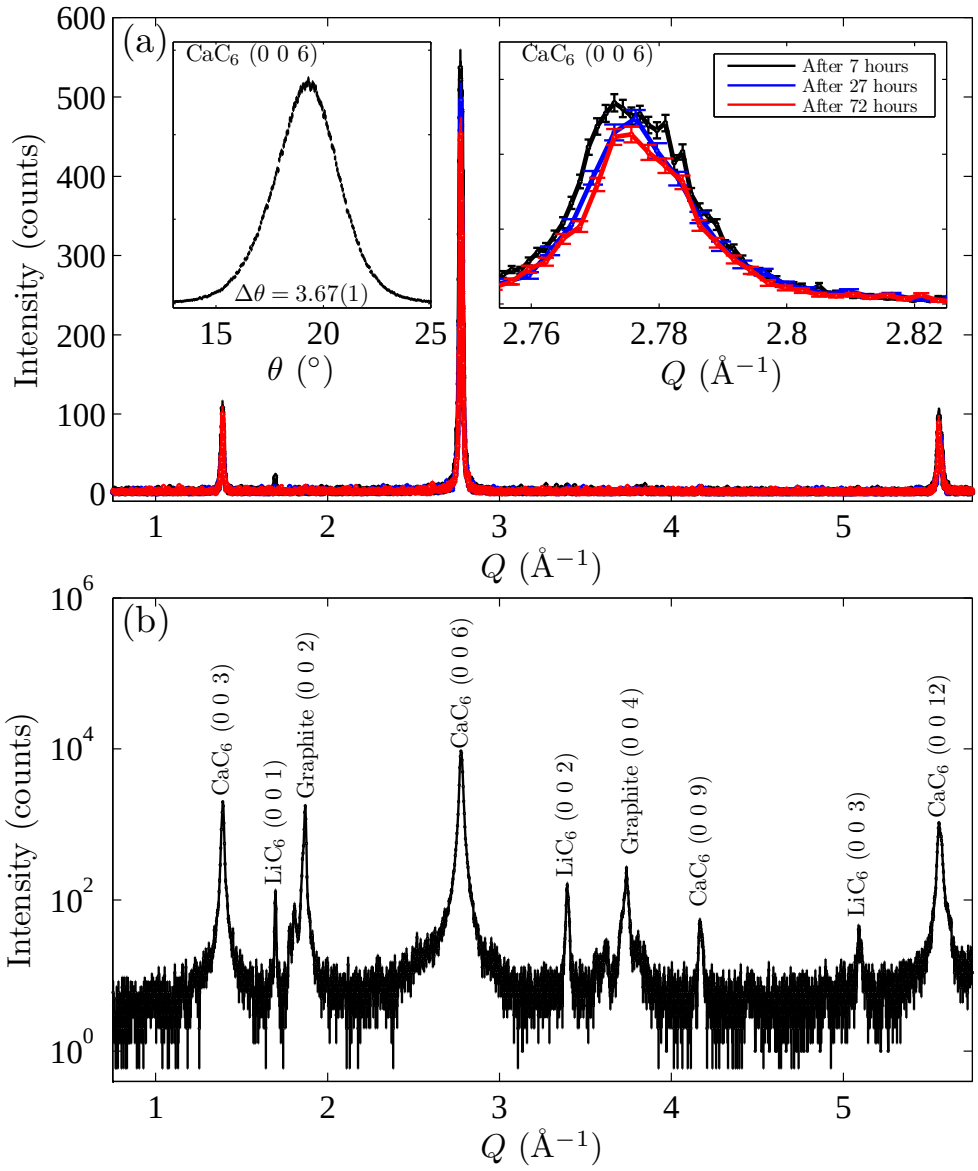

Figure 4.12: Representative diffraction scans done at University College London prior to IXS beamtime on CaC_6. All diffraction was done on the sample used in the first beamtime on CaC_6. In (a) diffraction measured at the edge of the sample is presented, with Q in the (00L) direction. The measurements were made after the sample had been sealed inside a beryllium can for 7, 27 and 72 hours. The three large peaks shown are all CaC_6 derived. The left inset is a rocking curve on the CaC_6 (006) peak, and the right inset is a close-up of the main figure around the CaC_6 (006) peak. (b) is X-ray diffraction from the same sample, but with a larger incident X-ray beam so that all of the sample was being probed. This scan shows the considerable LiC_6 and graphite impurities in the sample, which were not present in the edge of the sample, as shown in (a).

GIC	Chemical formula	Density (g/cm^3)	X-ray attenuation length with sample surface normal parallel to X-rays (cm)
Lithium Graphite	LiC_6	2.206	14.950
Graphite	C	2.261	13.940
Calcium Graphite	CaC_6	2.535	1.024
Barium Graphite	BaC_6	4.128	0.1580

Table 4.1: X-ray attenuation lengths of graphite, LiC_6, CaC_6 and BaC_6 at the incident energy at Sector 3 (21.657 keV). The mass densities of these materials are also provided.

the attenuation factor will be about $e^{-1} = 37\%$, the number of scattering centres is still relatively large. In Table 4.1 I present the attenuation lengths of graphite and some GICs at the incident energy of Sector 3.

Since the samples have to be removed from the Ca-Li alloy and any trace of this impurity alloy has to be removed, the final CaC_6 samples are significantly thinner than the 1 mm thick graphite samples from which they were formed. Our sample in our first set of beamtime was measured to be 0.63(1) mm using a micrometer screw gauge in an Argon glovebox, and in the second we managed to increase the sample thickness slightly to 0.68(1) mm. For our BaC_6 beamtime, we managed to thin the sample to approximately 0.25(1) mm (the attenuation length is 0.16 mm, see Table 4.1), but we decided to not risk attempting to thin the sample further as at this thickness the samples became very brittle and there was a significant risk of the BaC_6 platelet breaking into shards.

4.6 IXS measurement of the phonons in CaC_6 and BaC_6

4.6.1 Collecting the IXS data

Our initial plans for our first set of beamtime at Sector 3 were to try to do a full survey of the phonons in CaC_6 in the out-of-plane direction both below and above the superconducting temperature T_c. Consequently that meant we required the use of some cryogenic equipment. Sector 3 have a Closed-Cycle Refrigerator (CCR) which can provide liquid helium temperatures (≈ 4 K), which can be mounted onto the χ circle. Rather than mount

the CCR from the side, we decided to mount the CCR vertically to minimise any strain effects from the weight of the CCR. This could result in the sample position gradually moving throughout the experiment as the CCR itself gradually strains under the weight.

The first step in our alignment procedure for each beamtime was to find the copper peg edge. This was done by exploiting the straight-through beam, with the necessary attenuation to the incident beam so that the detector is not overloaded. The copper was easily thick enough to attenuate the entire X-ray beam, so this provided a reality check in that the copper peg was where we would expect, and is the size we expect (8 mm in diameter). From this information, we were able to make an determination of where the sample should be. We would ensure that the sample was positioned edge-on to the incident beam, as in this orientation the sample presents its largest thickness to the X-ray beam. A horizontal scan of the sample stage would then be done, revealing a dip in the intensity as the X-ray beam is attenuated by the sample. Horizontal and vertical scans of the sample stage can then reveal the full extent of the sample. An additional advantage of arranging the sample in this orientation to find its position is that the sample only needs to rotated in θ by about five degrees to reach the Bragg condition for the CaC_6 (003) peak. If the sample is not in the centre of rotation of the theta motor, then the sample will precess about the true centre of rotation, possibly moving out of the incident beam. However, if the sample is only being rotated by a small angle, any precession will be minimal and so the (003) diffraction peak should be found relatively easily.

In the first beamtime, a plate which fluoresced when exposed to X-rays was placed immediately after the sample inside the beryllium can. Using this plate we were able to adjust the x, y and z stages to observe the (00L) peaks. We could then make the appropriate adjustments to ϕ and χ to place one of the peaks into one of the analysers. We decided to forgo this step in the alignment for the second beamtime on CaC_6 and for BaC_6, as it was unnecessary, as the large width of the (00L) peaks made them easy to find. We would simply find the sample using the straight-through beam, and then rotate to the correct position in 2θ. We always saw some Bragg intensity at this position, which we could then optimise on using the ϕ and χ motors.

One important choice in any phonon measurement is where best to measure the phonons: i.e in which Brillouin zone can certain phonons be observed most readily. Theoretical simulations of the phonon intensity can provide a guide, but in our case the measurements on CaC_6 and BaC_6 took place prior to any discussion with a theorist working on GICs. We decided to measure at all available Q, as although the IXS cross-section is proportional to Q^2, it is possible for phonons to be very difficult to observe as their symmetry means they are dramatically suppressed in intensity (in an analogous way to systematic absences in diffraction studies).

From Equation 2.3, $Q = \frac{4\pi}{\lambda}\sin\theta$, and the wavelength λ cannot be changed, this means that to get to higher Q, the scattering angle θ must be increased. This can create problems, as the detector arm has to be large (of the order of 5 to 10 m) in order to have sufficient energy resolution, so this large detector arm needs to have sufficient space to rotate. At Sector 3 the maximum 2θ is 17.3° (at which point the box which contains analyser 1 is touching the hutch wall). This meant that the maximum Q we could attain was 3.30 Å^{-1}.

Firstly considering the (00L) phonons in CaC_6 and BaC_6, we find that the Brillouin zone extent from Γ to L is 0.694 and 0.597 Å^{-1} in CaC_6 and BaC_6 respectively. Any Bragg peak defines a Γ point, a vector at which the lattice could be translated onto itself. In CaC_6, the lowest Q Bragg peak in the (00L) direction is the (003), followed by the (006), then the (009) etc. Since the lattice parameter c is 13.572 Å, this means that the Q of this Bragg peak is $3 \times \frac{2\pi}{c} = 1.389$ Å^{-1}. This Q defines the distance from one Γ point to the next, so the distance from Γ to L (from the centre of the Brillouin zone to the edge, as measured in the 00L direction) is half this value ($1.389 \div 2 = 0.694$ Å^{-1}). A similar argument applies for BaC_6, but with the proviso that the (00L) peaks in BaC_6 are the (002), (004), (006) etc.

When Q is near to zero we measure near to the Γ point, so in CaC_6 at Sector 3 we can measure in the first, second and third Brillouin zones (although not completely in the third as we reach the limit in Q of 3.30 Å^{-1}). Since the Brillouin zone in BaC_6 is smaller in extent in the (00L) direction than in CaC_6, in BaC_6 we are also able to measure some dispersion in the fourth Brillouin zone.

One disadvantage of IXS studies of phonons as opposed to INS studies is that it can be extremely difficult to measure the phonon dispersion at Γ. This is because if an intense Bragg peak exists at Γ, the phonon spectrum can be overloaded with additional elastic intensity, making the phonons difficult to observe. This issue is intensified in the case of our GIC samples, as the large mosaic means that special care has to be taken to ensure that the analyser near Γ does not measure too much elastic intensity. This is the reason why our experimental dispersion in CaC_6 (see Figure 4.15) has no points very near to Γ. In BaC_6 the mosaic of the sample was somewhat improved (thanks to the sample being prepared via vapour transport), and as a consequence we were able to measure considerably nearer to Γ.

Initially we tried to measure the (00L) phonons all the way up to 200 meV, as this is just above the highest energy phonons calculated for CaC_6 [20]. However, we saw no observable phonon intensity above 50 meV in either CaC_6 or BaC_6. This was primarily because the phonons above 50 meV are predicted to be entirely due to vibrations of carbon atoms, and the lower electron density of carbon as compared to the intercalant means that the IXS cross-section is dramatically smaller for these carbon modes. In addition there is a $\frac{1}{\Delta E}$ dependence in the IXS phonon cross-section which acts to decrease the intensity of higher energy modes (shown in Equation 2.14 and 2.15). All the phonons measured out-of-plane in CaC_6 and BaC_6 appear to be intercalant in nature, and consequently have a larger IXS cross-section.

4.6.2 Analysing the IXS data

All of the IXS data discussed were fitted within the MatLab MFit package, written by Emmanuel Farhi, Des McMorrow and co-authors. I wrote a routine which simulated the measured IXS spectra with a peak at zero energy to simulate any elastic scattering and peaks at $\pm E_{phonon}$ for the inelastic scattering. The simulated peak intensities at $\pm E_{phonon}$ were calculated using the Stokes and anti-Stokes criteria, where the population of each phonon state (which is proportional to the measured IXS intensity) is assumed to be proportional to the bose factor $(1 - \exp(-\frac{E_{phonon}}{k_B T}))^{-1}$. Due to the complicated

monochromator setup at Sector 3, the lineshape is not a simple Lorentzian, but rather a convolution of a Lorentzian and a Gaussian, known as a Voigt. In order for simplicity (and in addition to speed up datafitting), Sector 3 describe their resolution function as a Pseudovoigt [35], which is an analytical approximation to a Voigt. The PseudoVoigt used is defined in Equation 4.4, centred at $\omega = 0$:

$$I(\omega) = I_0 \left\{ \frac{2\eta}{\pi\Gamma} \left[1 + 4(\frac{\omega}{\Gamma})^2 \right]^{-1} + (1-\eta)\frac{2}{\Gamma} \left(\frac{\ln 2}{\pi} \right)^{\frac{1}{2}} e^{-4\ln 2(\frac{\omega}{\Gamma})^2} \right\} \tag{4.4}$$

where I_0 is a constant of normalisation (which is a fit parameter), Γ is the full width half maximum (FWHM) of the peak, and η is the mixing parameter, and can have any value from 0 to 1. It is a measure of how Lorentzian or Gaussian the Pseudovoigt is (0 defines a Gaussian, 1 defines a Lorentzian). The mixing parameter is usually defined as 0.65 [35] at Sector 3, but can vary depending on the particular set-up of the monochromator for the particular experiment. A check of the resolution of each analyser was done at the beginning of each beamtime, using a standard plexiglass sample. Plexiglass is used as it has a very small coherent phonon IXS cross-section, and so can be used as an ideal measure of the energy resolution of the spectrometer by measuring the elastic linewidth. However, I found that the resolution widths found using these plexiglass scans was consistently larger than that found on the GIC samples in the (00L) direction, and the mixing parameters were also inconsistent. Consequently I disregarded these resolution checks and instead fitted each energy scan on its own merits. This inconsistency could be attributed to the effect of sample mosaicity, although naively this effect would be thought to increase the measured elastic linewidth, not reduce it.

Since the data are necessarily limited in their statistical quality, the issue of over parameterising each 1D dataset can arise. This problem is exasperated by the fact that each peak is defined by four parameters (intensity, position, width and mixing parameter), whereas in many X-ray or neutron disciplines only three parameters are necessary. Usually the resolution checks using the Plexiglass sample provide the mixing parameter to be used for any peak measured with that specific analyser, but that was not satisfactory in our case.

4.6.3 Solving the issue of the inconsistency in repeated runs at Sector 3

During our experiment on BaC_6 at Sector 3 at the APS, we found that certain datasets were not reproducible. In particular, a scan done on a cold day was very different than an equivalent scan done on a somewhat warmer day. *Padd*, the in-house program at Sector 3, designed to add together different spectra measured at the same momentum transfer, applies a scale factor to the energy transfer scale which resulted in the inconsistency. Although the *Padd* program could not be used externally to the APS, access was granted to the Fortran code within it by its authors. I converted this code into MatLab, rewriting the input and output commands so that the MatLab version had the same functionality of *Padd*, as well as tidying up the major part of the code which takes the angular positions of the two monochromators (as well as the temperature of the monochromator and the analysers) and converts that into an energy scale.

In Figure 4.13 a phonon measured in BaC_6 in three datasets (runs 53, 54 and 79) is plotted against three different versions of the energy scale. All of these scans were made using analyser 1 at 3.302 $Å^{-1}$. In Figure 4.13(a) the three datasets are plotted after the energy scale is calculated by my MatLab code using precisely the same settings as *Padd*. The three datasets are shown with the Pseudovoigt fit to the phonon peak. It is clear that the three scans are all inconsistent with each other, and in particular runs 54 and 79 are 1 meV apart (run 54 puts the phonon energy at 25.32(7), whereas run 79 has it at 26.29(7)), almost half of the energy resolution of 2.2 meV. One obvious suspicion to this could be that this inconsistency could be a result of the work done in MatLab in the conversion of *Padd*, so to provide evidence to the contrary the *Padd* output for this Q is also plotted, after convolution with a Gaussian of width 0.8 meV so that it may be plotted as a smooth line for clarity. It is clear that the energy of the phonon according to *Padd* is consistent with my code when it is provided with the same input.

In Figure 4.13(b) the different runs are plotted once the energy scale calculation has been done with my MatLab code, but with the correction for the analyser temperature given the opposite sign. This change in sign is denoted by labelling Figure 4.13(a) as that produced if it is assumed that the thermal expansion of Si α_{Si} is $-2 \times 10^{-6} K^{-1}$ at room

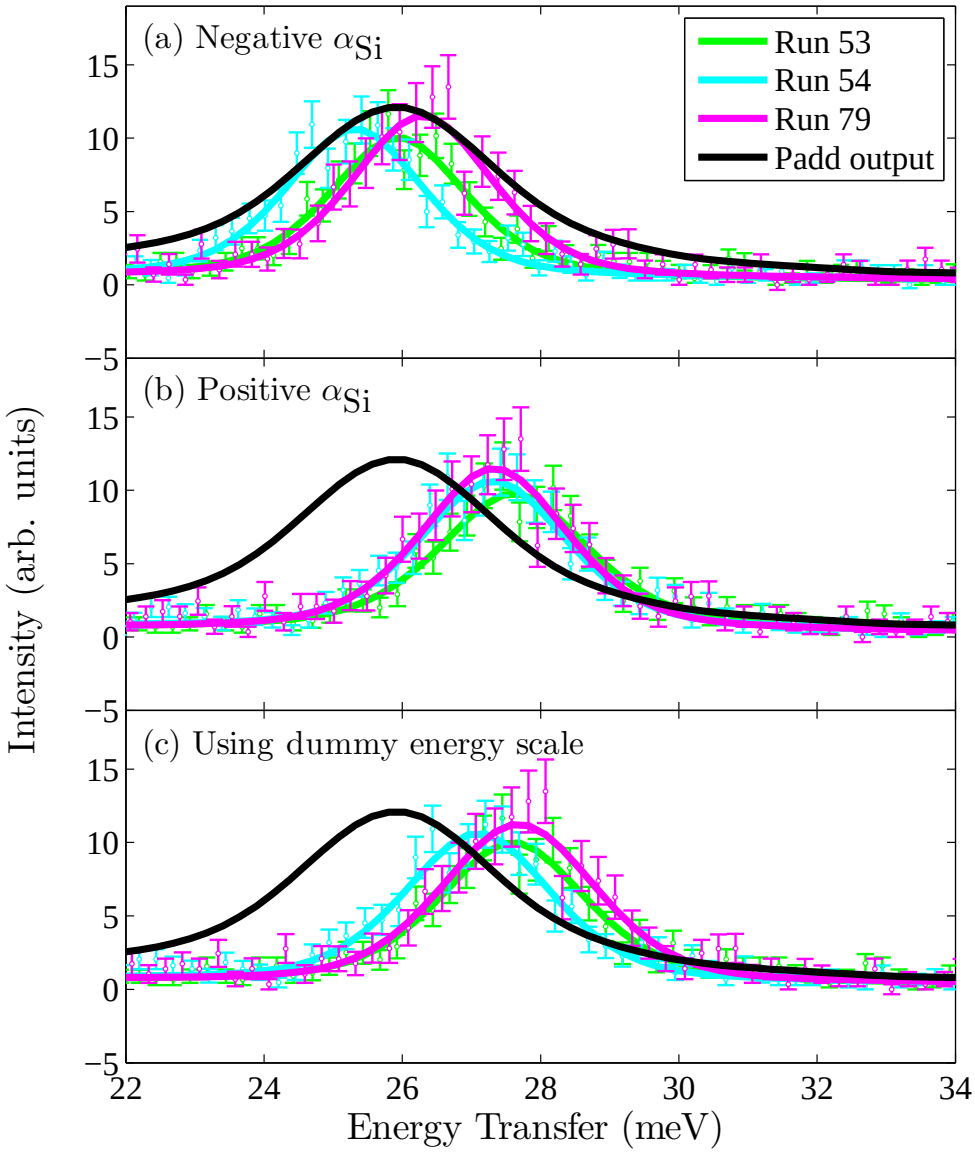

Figure 4.13: Detail from three different runs done on BaC_6 using analyser 1 at Sector 3 at $Q = 3.302$ Å^{-1} in the (00L) direction, concentrating on the highest energy mode observed in this direction. The energy scale in each of the three subfigures has been created in a different way. In (a) the output from *Padd* is simulated by providing my MatLab code with the same input as *Padd* was given originally. In (b) the energy scale is calculated using my code with corrected inputs: in particular the temperature correction due to the thermal expansion coefficient of Si is defined with the opposite sign. In (c) the energy scale used is simply that which is used at the beamline to drive the monochromator, and has no knowledge of the analyser temperature.

temperature, as it was defined in *Padd*. The choice in the placement of this negative sign is arbitrary, but it follows that if $\alpha_{\mathrm{Si}} = -2 \times 10^{-6} K^{-1}$ then the temperature correction done in the original version of *Padd* is correct. However, the thermal expansion of Si at room temperature has been known to be $+2.6 \times 10^{-6}$ K^{-1} for some time [96]. The most accurate values for the thermal expansion of Si around room temperature have been provided by Bergamin et al. [97], and the value contained within is what is now used in my version of *Padd* ($+2.581 \times 10^{-6} K^{-1}$). With the correction to the energy scale in the opposite sense it can be observed that the three runs are now within error of each other (the fitted phonon energies change to 27.61(8), 27.31(7) and 27.33(8)). The smoothed original *Padd* output is also plotted in Figure 4.13(b) for comparison. It is clear that this change in sign of α_{Si} makes a dramatic difference to the phonon energy in this case.

In Figure 4.13(c) the same runs are plotted with the energy scale used at the beamline. This energy scale is calculated purely from the relative angular positions of the two parts of the double monochromator, with no knowledge of the temperature of the analyser. The zero for energy can be reset throughout the experiment, as since it is this measure of the energy transfer which is used to drive the monochromator, it is important that it is at least accurate to 1 or 2 meV during each run. Remarkably, this energy scale seems to be more accurate than the version outputted by the original version of *Padd*. It is noteworthy that the agreement between scans is still inferior to that shown in Figure 4.13(b). The behaviour observed here is also seen in other datasets, but in most cases the variation of the temperature of the analysers was not as large over the whole scan, and consequently the temperature dependent change in the energy scale is not as dramatic.

This behaviour can be explained as follows: at room temperature, if the temperature of the analyser T_{anal} increases by an amount ΔT, to a temperature $T'_{anal} = T_{anal} + \Delta T$, the d-spacing d_{hkl} of the analyser crystal must have also increased since the thermal expansion of Si is positive. We know from Bragg's law that $E_{hkl} \propto \frac{1}{d_{hkl}}$, so the energy E_{hkl} associated with that d-spacing d_{hkl} must have decreased. The energy transferred to the sample is $\Delta E = E_i - E_f$ (Equation 2.1), and the final energy of the scattered X-ray is defined by the analyser crystal, so therefore $E_f = E_{hkl}$ and we find $\Delta E = E_i - E_{hkl}$. As stated, if the temperature of the analyser crystal increases, the energy E_{hkl} decreases, so this means

ΔE must increase. Therefore the result of the analyser rising in temperature should be to stretch the measured energy scale, as observed using my new version of *Padd*, not the compress it as shown in the original version of *Padd*.

In a separate communication, the instrument scientists at Sector 3 have also explained that the first reflection in the double monochromator is from the (4 4 0) in silicon, not the (2 2 0) as has been the case in the standard input file for *Padd*. This mistake resulted in the energy scale being slightly compressed by a factor of 1.018, which although important is unlikely to affect the vast majority of studies done at Sector 3. My version of *Padd* has accordingly been corrected for this mistake.

In many studies, the temperature of the analysers may vary somewhat less than we found in our BaC_6 experiment. For example, the dispersions measured in CaC_6 are largely consistent with the dispersions measured with the original temperature correction. The phonons in CaC_6 are now all slightly hardened, (the maximum energy shift is 1 meV for the highest energy phonon mode in the (00L) direction) but the primary reason for this is due to the mistake in the first reflection in the silicon monochromator (actually the (440), not the (220) as had been used in *Padd*). Throughout all the measurements made at Sector 3 the temperature of the analysers gradually increases, presumably due to heatload from the scattered X-ray beam. This consistency in temperature change is an additional reason why this issue has only come to light now.

4.7 The phonon dispersion in CaC_6 and BaC_6

4.7.1 Out-of-plane (00L) dispersion in CaC_6

In Figure 4.14 all of the energy scans used to find the (00L) phonon dispersion in CaC_6 are presented. At any Q lower than 0.780 $Å^{-1}$ the phonons are too weak due to the Q^2 dependence in the IXS cross-section for phonons, and as discussed, 3.30 $Å^{-1}$ is the maximum Q obtainable at Sector 3. Because of these constraints, all of the measurements take place within the second and third Brillouin zones. It would appear that the highest

energy phonon between 30 and 40 meV (blue in Figure 4.14) is largely suppressed in the third Brillouin zone, consequently it was very important to take as many measurements as possible in the second Brillouin zone in order to find the dispersion of this mode accurately. Conversely, the mode which disperses up to 25 meV (labelled green) is most easily measured at higher Q.

The fitted phonon energies found from the data in Figure 4.14 were then used to plot the dispersion of the phonons within the reduced Brillouin zone scheme. The reduced Q is provided in brackets next to the magnitude of Q in Figure 4.14. This procedure was followed for data collected at 5 K and 50 K. Figure 4.15 presents the resulting phonon dispersion in CaC_6 measured at 5 K, 50 K and 300 K. The error on the fit to the raw data is plotted as an error bar on this plot, to provide an estimate of the accuracy of the fitted energy position. This error is also dependent on the other parameters which define the Pseudovoigt, which are in the vast majority of cases completely free to vary in the fit, and consequently the errors on the energy positions may underestimate the true error. This can happen as the width, or especially the mixing parameter attains a value which is not its 'true' value after fitting (as this value minimises χ^2), and consequently the phonon energy position can be distorted.

Overall the agreement to theory is reasonable, especially in the mode which disperses up to 25 meV (the acoustic Ca_z mode). The character of the higher energy mode which disperses between 30 and 40 meV (the optic Ca_z mode) seems in good agreement with the calculation, but we find it to be 2 meV more energetic than predicted. As a general trend we also find that both of these Ca_z modes are hardened upon cooling (this is especially obvious in the optic Ca_z mode), but there seems to be almost no significant difference between the data measured above and below T_c (5 K and 50 K). The temperature dependence may come from a slight change in the lattice parameters upon cooling, since if we suppose that the 00L lattice parameter c decreases at lower temperatures, the Ca atoms may be more strongly held between the graphene sheets. This would accordingly mean that the energy to excite a phonon which involves vibration of Ca atoms in the 00L direction would increase. However, this change in lattice parameters would of course change the extent of the Brillouin zone, meaning that the reduced Q for each scan should change

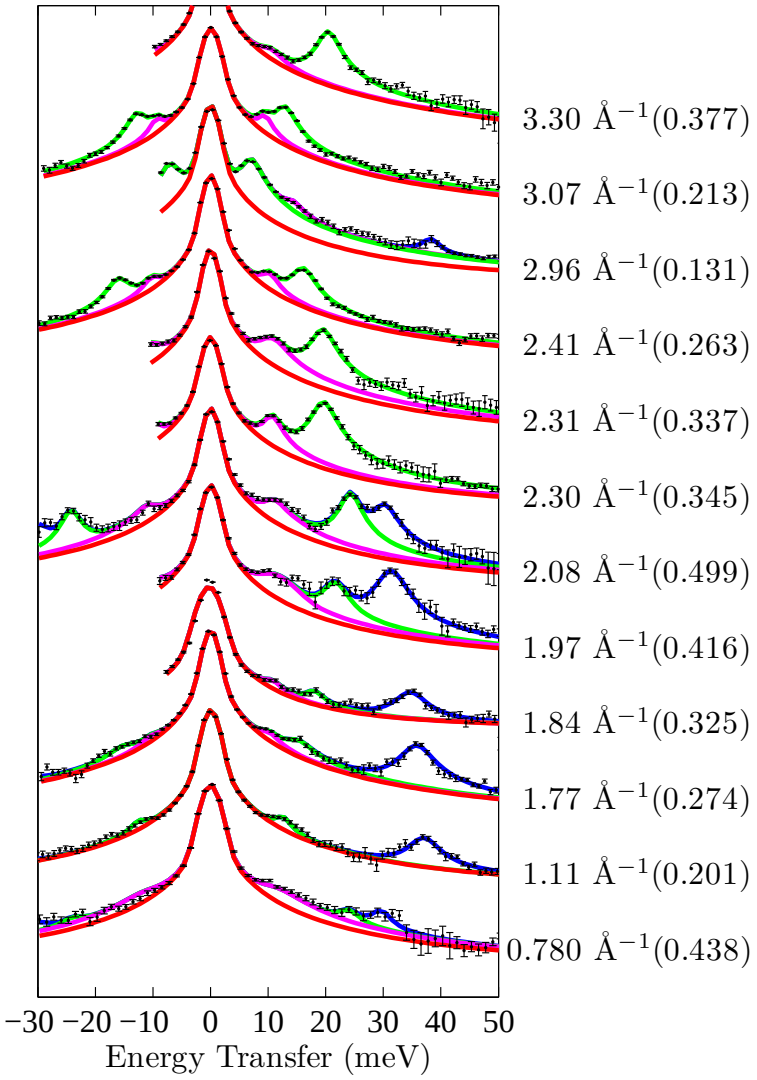

Figure 4.14: All data used to find the (00L) dispersion in CaC_6 at 300 K are presented. The intensity is plotted on a logarithmic scale. Each run is labelled with its Q and its reduced Q in brackets. Both momenta are given in units of 1.39 Å^{-1}. In these units of reduced Q, $\Gamma = 0$ and $L = 0.5$. The fit to each run is also plotted, with the fit to the elastic line plotted in red, and to each phonon plotted in magenta, green and blue.

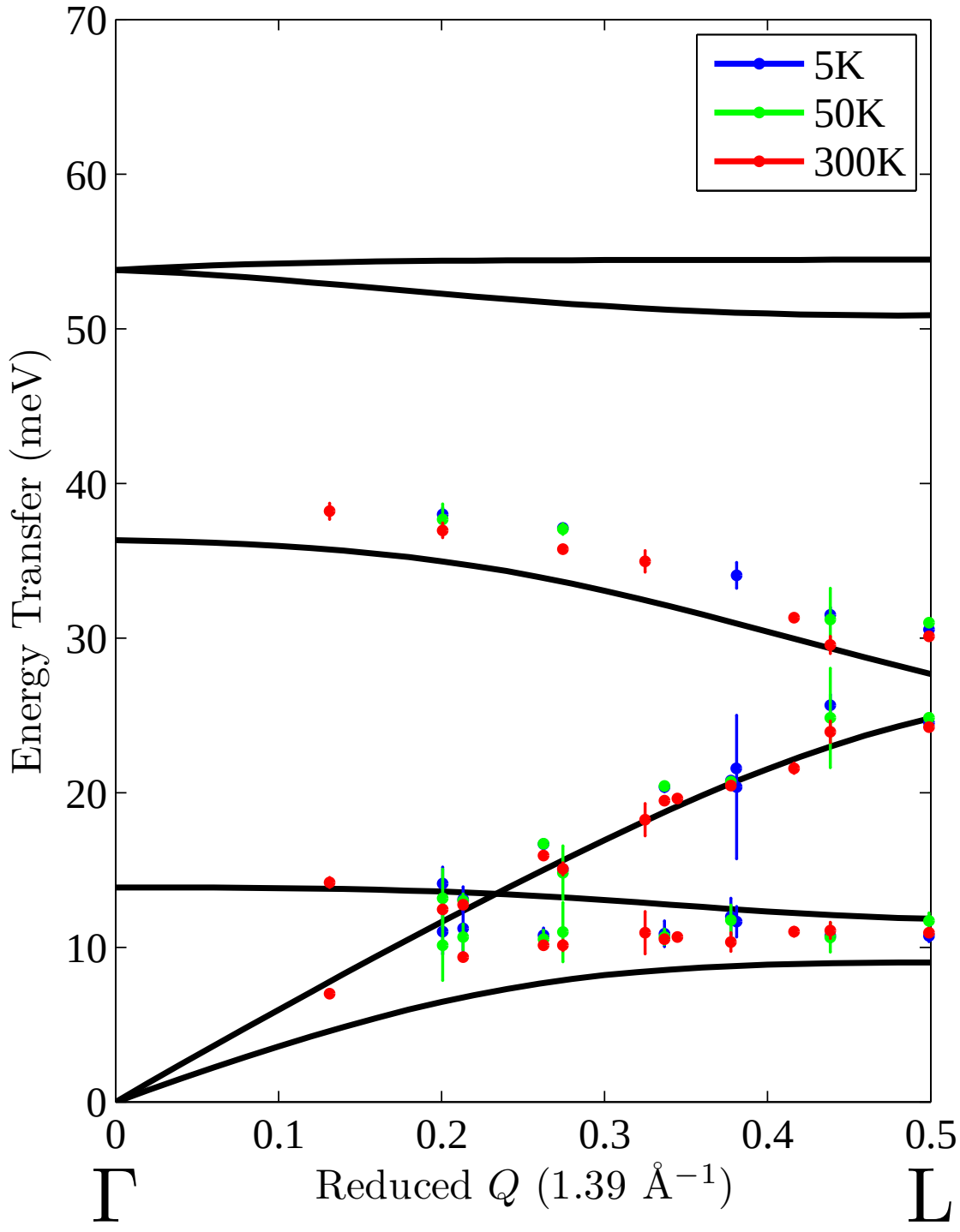

Figure 4.15: Experimental (00L) phonon dispersion in CaC_6 as measured at 5 K (blue), 50 K (green) and 300 K (red). The corresponding theoretical phonon dispersions are plotted in black [20].

slightly. I have not included any such effects in my analysis. If the change in the size of the Brillouin zone was significant, the scans done at high Q should look significantly out of place, as their reduced Q would be badly wrong. No such behaviour can be seen.

The widths of the two Ca_z modes are certainly not resolution limited: the acoustic Ca_z mode has an average fitted FWHM of approximately 3.5 meV, and the optic mode has an average FWHM of 5.2 meV, far larger than the instrumental resolution of 2.2 meV. These large widths are likely to be a result of the large mosaic, and make it extremely difficult to say anything further about linewidth changes due to electron-phonon coupling. We are sensitive to a change in the widths as a function of temperature, but we see no evidence of this in CaC_6.

The clearest discrepancy with theory comes at low energies, where we observe a relatively weak, largely non-dispersive feature at approximately 11 meV (plotted in magenta in Figure 4.14). The two phonon branches which would appear to be the origin of this intensity are in fact predicted to be due to phonons polarised within the ab-plane, and consequently should not be observable in the (00L) direction. Again, the large mosaic could provide an explanation for our observation of these modes, as this means that the momentum Q will be necessarily also measuring the phonon dispersion with some component in-plane. For this reason, in our published account of part of this dataset [80] we used two phonons to fit it at the scan done almost precisely at the L position ($Q = 2.08$ Å^{-1}). However, it is difficult to be clear that there are two definite peaks, and for simplicity I have simply fitted this feature with one peak at all Q.

The width of this feature is difficult to pin down precisely, as it is both relatively weak and in the vicinity of the elastic line, meaning that it is usually sat on a extremely sloping background. However, it is usually found to be between 4-5 meV wide, which is not inconsistent with the widths of the other two modes measured.

One important consideration which comes into the discussion of the mosaic of the sample is the choice of which analyser was used at Sector 3. It is customary at Sector 3 to align θ with analyser 1, the analyser with the highest value of 2θ. This means that the value of θ is as accurate as possible for analyser 1, but is increasingly inaccurate for the scans

done simultaneously with analysers 2, 3 and 4, which are spaced at intervals of 1.73°. So at analyser 4, the value of θ is $(3 \times 1.73°)/2 = 2.60°$ away from where it would be if the sample θ were aligned specifically for analyser 4. If this effect was very pronounced, one would expect that the dispersion at each Q would be heavily dependent on the analyser which was used to measure it. We see no scatter in the measured dispersion which could be ascribed to this effect. If the 11 meV mode in the (00L) direction was a direct result of the mosaic, one would expect it to be heavily dependent on the choice of analyser, with its intensity minimised when analyser 1 was used and maximised when analyser 4 was used. Again, no such behaviour is observed in the data. It would appear then that the choice of analyser is not a key issue.

Since the choice of analyser makes little difference to the observed dispersion, this suggests that the mosaic is not the correct explanation for the observation of the 11 meV mode. It suggests instead that this mode is a real mode with its polarisation factor in the c axis. The next most obvious explanation is that this mode could be due to some kind of impurity, most likely LiC_6, which we know was in the sample used in the first beamtime. However, the part of the sample illuminated in the first CaC_6 beamtime (and the entire sample used in the second beamtime) was found to have no measurable LiC_6 (00L) diffraction peaks. Additional evidence which points to this not being an impurity effect is that the raw data in Figure 4.14 are in fact an amalgamation of different datasets from both the first and second beamtimes, and there is no obvious difference between the two, despite the second sample being of higher purity. In particular, comparing the measurements done at 2.30 $Å^{-1}$ (second beamtime) and 2.31 $Å^{-1}$ (first beamtime) highlights this point very clearly, as the relative intensities of the acoustic Ca_z mode and the 11 meV mode are very similar in the two scans.

Since the 11 meV mode has very little dispersion, it could be suggested that another possible source of the intensity could be a powder impurity. However, the raw dataset measured at 2.96 $Å^{-1}$ gives strong evidence to the contrary. We see that for the only time, the much more intense acoustic C_z mode is now at lower energy than the 11 meV mode, and (albeit only observed at one Q point) the weaker mode has dispersed to higher energies. This is very clear in the dispersion in Figure 4.15. This mode seems to have

similar dispersion to the optic C_{xy} mode predicted in the (00L) direction, but has some out-of-plane component, contrary to calculations.

4.7.2 In-plane (HK0) dispersion in CaC_6

In addition to the measurements done in the (00L) direction, we also did measurements in the ab-plane. As already discussed, the samples are disordered in the ab-plane, so consequently any measurements done purely in the ab-plane essentially provide a quasi-2D phonon density of states measurement. We made extensive measurements within the first Brillouin zone, so that any modes which have cylindrical symmetry about the c axis should be observable. This choice was a significant investment of beamtime, as it necessarily means measuring at low Q, decreasing the IXS phonon cross-section. Any measurements done outside of the first Brillouin zone are extremely difficult to understand, as you are necessarily sampling a large part of the Brillouin zone simultaneously. At some values of Q outside the first Brillouin zone, you may sample one particular part of the Brillouin zone more than other parts of the Brillouin zone, whereas at some Q you may sample the entire Brillouin zone equally. This means that these high-Q scans can contain information about the single crystal dispersion of the sample. However in the case of these GIC samples it is difficult to decipher this information, as it is made more complicated by virtue of the peculiar crystallinity of the graphite samples.

I present the (HK0) IXS scans measured in CaC_6 in Figure 4.16. These five datasets are the summation of over forty different scans, which if done consecutively would take around 3 days of beamtime. Happily the scans at 0.246 $Å^{-1}$, 0.579 $Å^{-1}$ and 0.912 $Å^{-1}$ were done simultaneously using analysers 2, 3 and 4, and the other two scans were also done simultaneously using analysers 3 and 4. Note that the elastic line intensity is dramatically increased in intensity for the 0.246 $Å^{-1}$ dataset: this is due to some intensity leakage from the straight through beam as we were at extremely low Q. It is puzzling that we do not see any intensity from the higher energy C_{xy} branch (magenta in the figure) at $Q = 0.409$ $Å^{-1}$, as it is seen in the two scans which are adjacent in Q. The feature is both weak and broad however, and it possible that the statistics on this scan are insufficient for this

peak to be separated from the background. The peak measured at 76 meV at $Q = 0.246$ Å^{-1} seems abnormally small in width, which is likely due to the poor statistics in this scan above 70 meV. Only one of the ten repeats at this Q had a sufficient energy range to measure this peak. The poor statistics above 70 meV could also provide an explanation for why the measured peak is substantially lower in energy than predicted by theory (see Figure 4.17).

In Figure 4.17 I present the measured phonon dispersion in CaC_6 measured within the first Brillouin zone. Again there appears to be some reasonable agreement between experiment and theory, with the flat acoustic Ca_{xy} predicted at 11 meV by the theory being observed at 12-13 meV. There is no observable temperature dependence here. Similarly, two modes attributed to C_{xy} phonons with high dispersion can also be seen, in agreement with the theory. There is a mode with little dispersion between 35 and 40 meV which we observe out-of-plane but not at all in-plane (despite its weak dispersion over the whole of the Brillouin zone according to theory), as its polarisation is entirely out-of-plane. This observation once again suggests that the mosaic cannot explain the observation of the 11 meV mode out-of-plane, as if the mosaic was sufficiently large to make the Ca_{xy} mode visible out-of-plane, we might expect to see some leakage of Ca_z mode intensity in-plane.

In the scan done at the lowest Q in-plane (only 0.25 Å^{-1}), we also see some intensity at 53 and 76 meV resulting from two C_z modes, which should be suppressed in-plane. However, this scan used analyser 3, which means that the value of θ used was wrong by 1.73°. Since 2θ itself was only 1.29°, this means the true direction of Q was in fact significantly out-of-plane, providing an explanation for why these modes are only observed in these scans.

The acoustic mode which disperses up to approximately 22 meV in the DFPT calculation also appears to be approximately symmetric in-plane, but this mode is due to Ca_z, leading us to suspect it should not be visible in-plane. This logic suggests that we should see this mode at low Q, where a significant component of Q is out-of-plane. At this position the energy of the mode is supposed to be extremely low however, creating the possibility that we are unable to distinguish the mode from the elastic line.

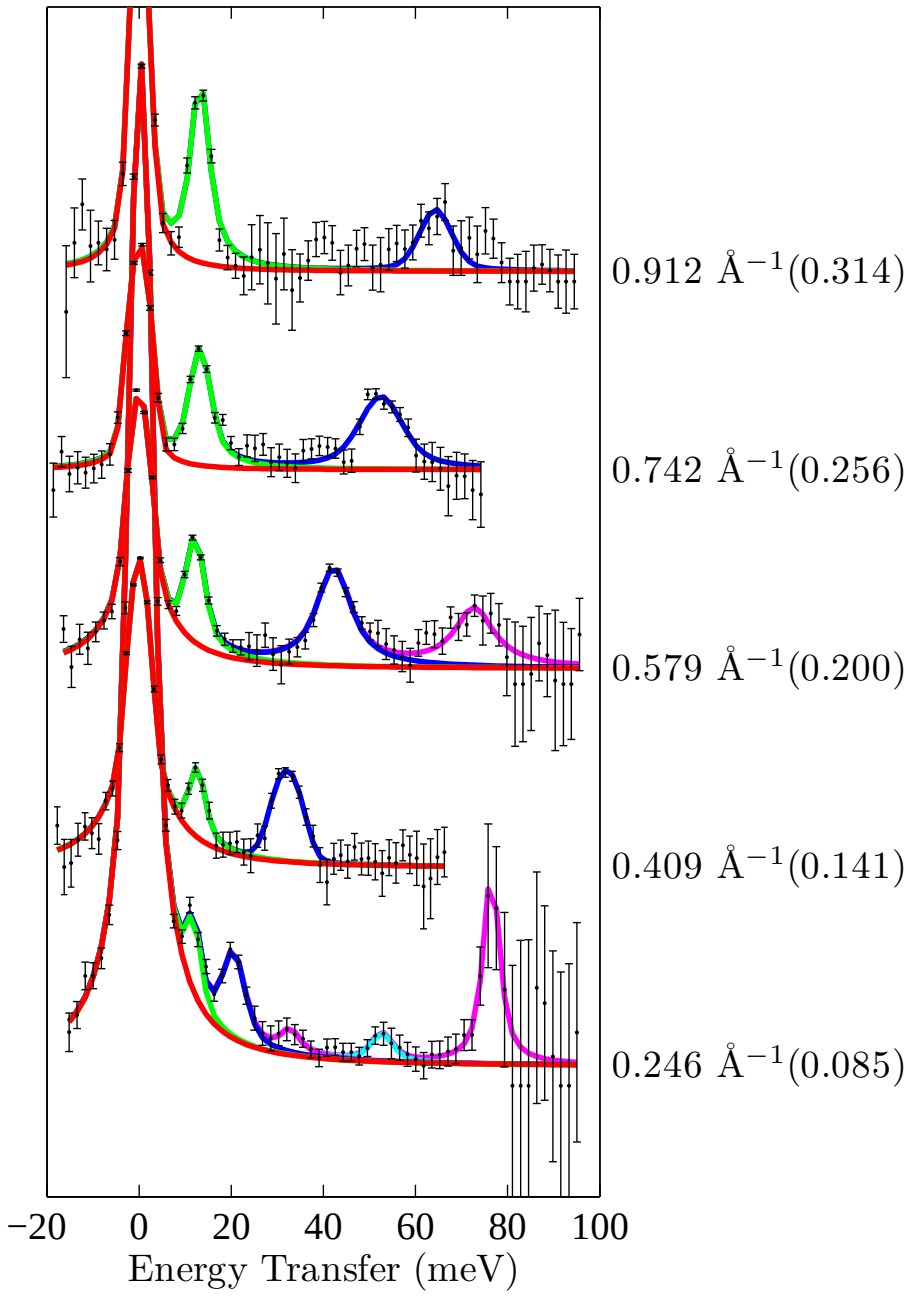

Figure 4.16: All data used to find the HK0 dispersion in CaC_6 at 5 K are presented. The intensity is plotted on a logarithmic scale. Each run is labelled with the Q it was measured at, with the reduced Q provided in brackets in units of 0.34 Å^{-1}. In these units of reduced Q, $\Gamma = 0$ and $\chi = 0.3581$, consistent with the convention used in some of the DFPT calculations [20]. The fit to each run is also plotted, with the fit to the elastic line plotted in red, and to the phonons plotted in magenta, green, blue and cyan.

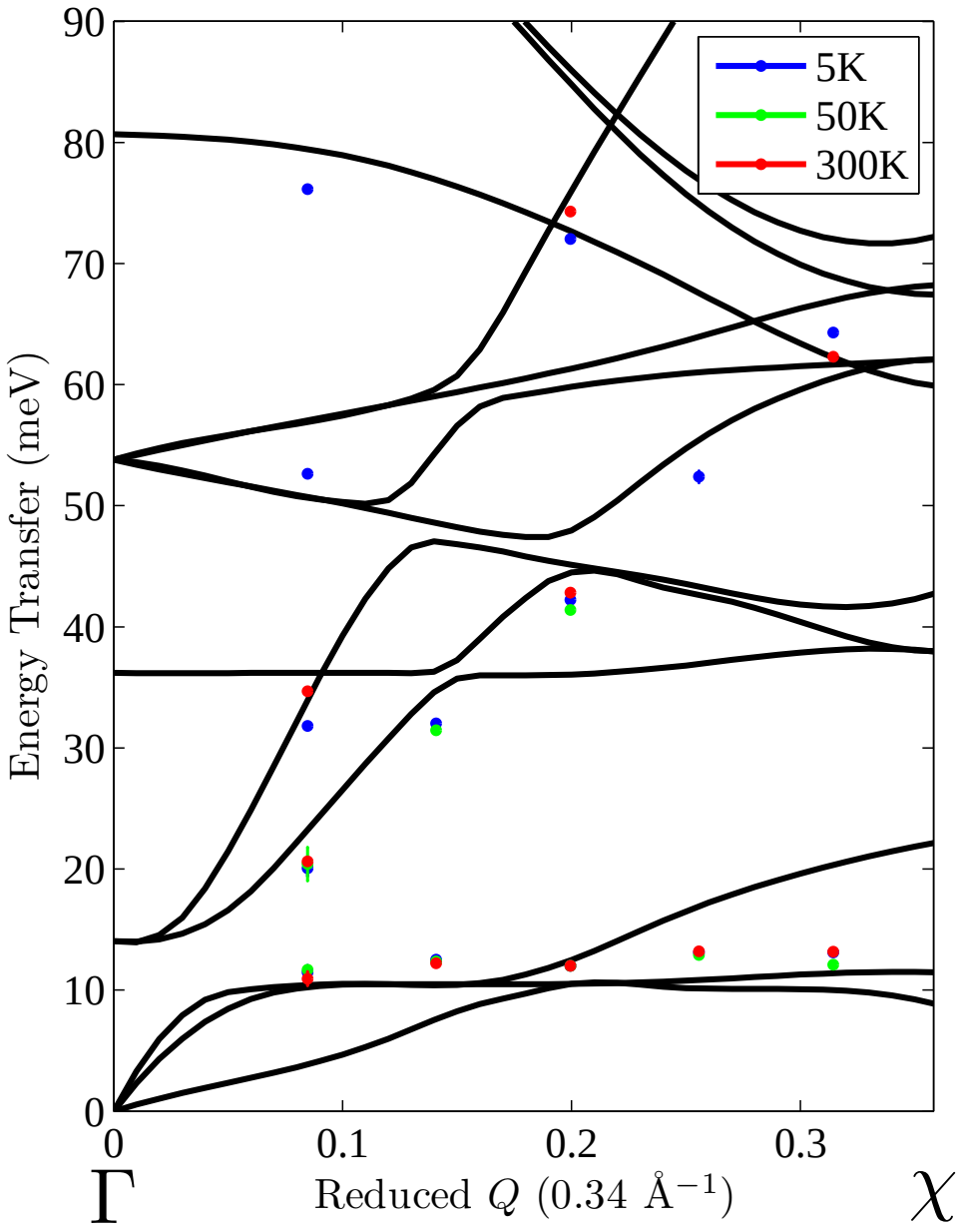

Figure 4.17: Experimental (HK0) phonon dispersion in CaC_6 (in the ab-plane) as measured at 5 K (blue), 50 K (green) and 300 K (red). The corresponding theoretical phonon dispersions are plotted in black [20]. All measurements were made in the first Brillouin zone due to the disordered ab-plane of the sample used.

It is worthy to note that the dispersion presented here is much more extensive than that in the published paper [80]. This is a direct result of the energy scale correction due to the variation of the temperature of the analysers (see Section 4.6.3). Without the temperature correction being correctly implemented, it proved impossible to sum repeated scans together to improve the statistics, as any stretch or compression of the energy scale has an accordingly bigger impact at higher energy transfers.

4.7.3 Out-of-plane (00L) dispersion in BaC_6

In Figure 4.18 I present the measured phonon dispersion in BaC_6 measured in the (00L) direction, along with the theoretical dispersions [77]. Once again we observed two intercalant modes polarised out-of-plane (Ba_z). However it is clear that the consistency with theory is much reduced in comparison to that seen in CaC_6, notably both of these modes are measured at significantly higher energies to that predicted by theory. Near Γ the measured phonon energy for the optic Ba_z mode is over 5 meV higher than theory. The character of the dispersion of the acoustic Ba_z mode seems to be the same as predicted, but whereas the optic mode is predicted to soften towards Γ we observe quite the reverse: the mode is largely dispersionless but appears to harden slightly from about 25.8 meV to 26.6 meV from L to Γ.

This discrepancy may stem from the inaccurate values of the lattice parameters a and c used in the calculation. In the paper [77] that these calculations are taken from, the lattice parameters that were used are equivalent to $a = 4.350$ Å and $c = 10.40$ Å, significantly different to the values of $a = 4.302$ Å and $c = 10.50$ Å, which are established experimentally from X-ray diffraction [98]. In addition, the incorrect space group is used for BaC_6, as $R\bar{3}m$ is used, the space group of CaC_6. However, it is argued that this choice of space group should not make a dramatic difference, as the first and second nearest neighbours are identical in both $R\bar{3}m$ and $P6_3/mmc$ (the space group of BaC_6). Nevertheless, both of these reasons could play some part in this large discrepancy.

It is clear that there is no discernable temperature dependence of the two Ba_z phonons, which is different to the case in CaC_6. It is of interest that this effect only appears

to occur in the GIC with an enhanced superconducting transition, but clearly a more extensive study of other GICs - including YbC_6 - would be necessary to provide sufficient evidence for such a trend.

We once again see unexpected phonon intensity with the same character as that seen in CaC_6, but this mode is shifted to lower energies than seen in CaC_6 (< 10 meV). This makes it extremely difficult at Sector 3 to separate the phononic signal from the elastic line. Clearly in the fits there appears to be a significant amount of temperature dependence of this mode, but this interpretation should be viewed with caution: the intensity of this mode is very weak, and its proximity to the elastic line makes it extremely difficult to fit.

4.7.4 In-plane (HK0) dispersion in BaC_6

The in-plane phonon dispersion is presented in BaC_6 in Figure 4.19. The statistical quality of the in-plane data for BaC_6 is somewhat poorer than in CaC_6, and consequently very weak phononic signal at high energy transfer is impossible to separate from the background. However, the phonon dispersion at lower energies looks similar to that seen in CaC_6: we see the flat Ba_{xy} between 8 and 11 meV, as well as the lower highly dispersive branch (C_{xy} according to theory). The branch appears to turn into two separate features at higher energy transfers, one of which follows the theoretical dispersion very well but the other peak is considerably lower in energy. This effect is likely to stem from some anisotropy in the phonon mode observed, as it appears likely that the mode softens slightly when viewed away from the $\Gamma\chi$ direction.

The lower energy phonon (Ba_{xy}) mode near to Γ could not be fitted reliably, as in this region the mode softens sufficiently to make it extremely difficult to separate from the elastic line. This is an effect which is also seen in the (00L) direction. The dispersion of the mode appears to follow just one of the three theoretically calculated modes which are almost degenerate at about 10 meV, as it appreciably disperses to lower energies towards the edge of the Brillouin zone.

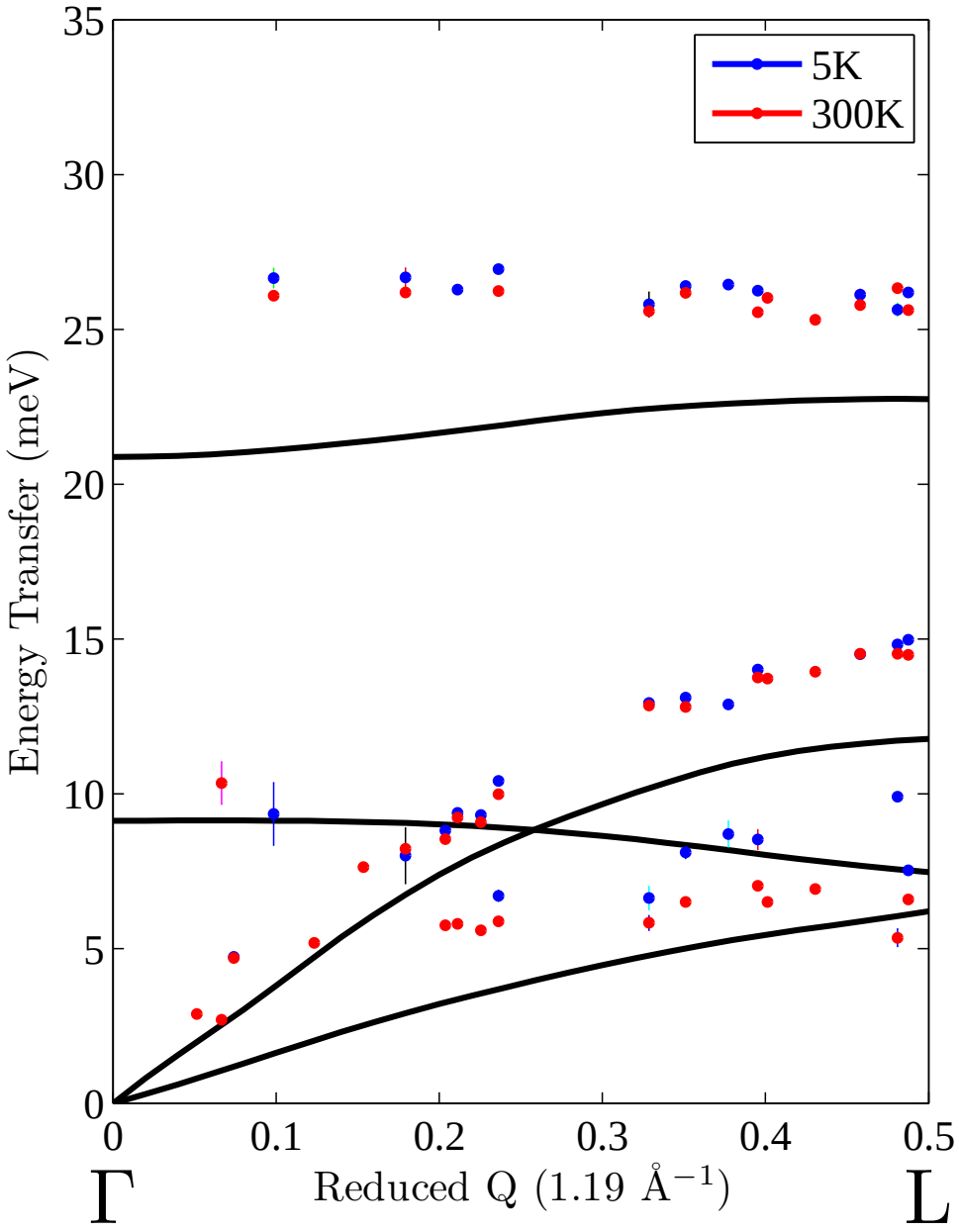

Figure 4.18: Experimental (00L) phonon dispersion in BaC_6 as measured at 5 K (blue) and 300 K (red). The corresponding theoretical phonon dispersions are plotted in black [77].

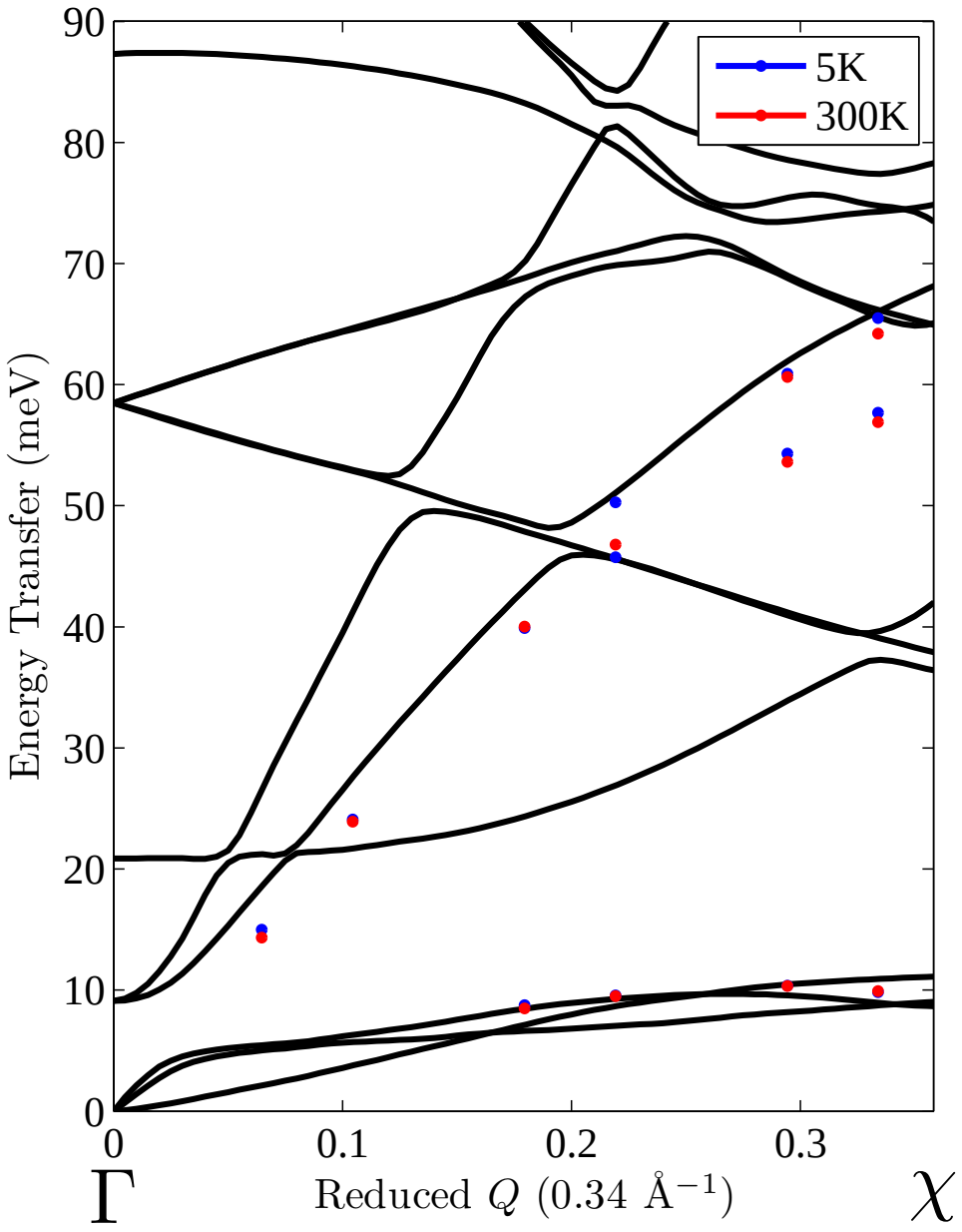

Figure 4.19: Experimental (HK0) phonon dispersion in BaC_6 as measured at 5 K (blue) and 300 K (red). All measurements were made in the first Brillouin zone due to the disordered ab-plane of the sample. The black lines are the theoretically calculated phonon dispersions from Γ to χ [77].

4.7.5 Quantifying the effect of the mosaic in BaC_6

Following correspondence with Matteo Calandra, access to his calculations for BaC_6 was granted. This includes software which can simulate IXS phonon spectra. In addition, for datasets which have an in-plane component, it automatically takes account of the crystallinity of the samples by calculating the phonon dispersion at specific points around a ring within in the ab-plane in reciprocal space, and then taking a simple average of the results.

Two very simple MatLab routines have been written which provide a means to quantifying both the issues of mosaic and the issue of which analyser is being used (for all scans the value of θ is set for analyser 1). The first of these takes two inputs: firstly the magnitude of Q at which the analyser of interest is being positioned and secondly the amount (in degrees) that the angle θ is aligned incorrectly for the sample. The routine then outputs the component of Q which is along the direction intended and then the component of Q which is now perpendicular to the intended direction. By using this code at different offsets to the true value of θ, a set of values of Q can be used within the calculations provided by Calandra. This set of calculations can then be used as a basis for taking into account any mosaic effects, by using the appropriate weighting of the calculations. The second MatLab routine is very similar to the first, but instead it takes as an input the Q which is put into analyser 1 and then calculates the components of Q in analyser 2, 3 or 4 (depending on the input). This allows the effect of the choice of analyser to be accounted for.

Simulations of the expected IXS intensity are provided in Figure 4.20. The experimental IXS data are shown plotted against three different version of the simulated intensity. This figure highlights the large difference between theory and experiment as regards the specific phonon energies of the two Ba_z modes, as the discrepancy between experiment and theory is huge in all three cases. What does seem to be consistent with the data is the ratio of the intensities of the two phonon peaks. Please note that this specific dataset has been chosen because analyser 1 was being used, and so any issues with the choice of analyser are nullified. This dataset also represents the highest Q measured at, so the statistical

quality of this dataset is especially high.

The widths of the phonons have been set to the instrumental width at Sector 3 (2.2 meV), but the code provided can only produce a Lorentzian lineshape, so this is what is plotted. The intensity of the phonons has been scaled for easy comparison with the dataset, and has been added to the fit to the elastic line found from the dataset, hence the perfect agreement at zero energy transfer. The black line in the figure is the simulated intensity assuming the sample is a perfect single-crystal of vanishingly small mosaic. It is clear that this simulation cannot explain any of the intensity consistently observed out-of-plane between 5 and 10 meV, as the modes which are predicted to exist in this region are not allowed by the polarisation factor.

The green and cyan lines are simulations produced by combining 11 simulations done within Calandra's code, using the MatLab routine discussed above. These 11 simulations include the black line, and 10 more calculations for when the direction Q is 1, 2 ... 10° away from the expected direction. For the green line, these simulations were weighted using a normalised Gaussian of FWHM of 5.4°. This width has been found directly from a fit to a ϕ scan done at during our beamtime at Sector 3. The cyan line adds the 11 simulations up simply (remembering to double the contributions from all of the simulations other than the one at 0° to take into account the mosaic spread in both the positive and negative directions of θ) with no special weighting for each simulation. This latter simulation is clearly a severe over-estimate of the mosaic, but is provided for comparison.

The realistic model of the simulated phonon intensity, using a mosaic spread of FWHM of 5.4°, appears to have minimal effect on the simulated intensity. Even in the extreme case of the mosaic, where the mosaic is 20°, no appreciable intensity between 5 and 10 meV can be found. In fact, in this extreme case the phonon peaks become significantly asymmetric, which is at odds with the dataset which shows peaks with little asymmetry. These calculations also debunk any notion that the considerable discrepancy between theory and experiment can be simply assigned to the large mosaic spread, as the phonon energies are changed by a maximum of 2 meV even when the mosaic spread is made 20°. It is important to note though that this scan was done at a reduced Q of 0.24 (units of 1.19

$Å^{-1}$), where the gradient of both the modes in question is relatively small. Consequently any effect from the mosaic spread is likely to be less than if the mode was dispersing more quickly. It is easy to imagine a situation where the acoustic Ba_z mode dispersion near Γ could be notably different to that naively found assuming a small mosaic, since the mode disperses quickly in this region.

4.8 Summary of the IXS data of CaC_6 and BaC_6

The dispersions of the low-energy phonons in CaC_6 and BaC_6 have been found using meV-resolution inelastic X-ray scattering. The CaC_6 data presented have already been published [80], although the quality of the data presented here are significantly improved thanks to the work done on the temperature correction of the analysers at Sector 3 (discussed in Section 4.6.3).

In CaC_6, reasonable agreement with the DFPT dispersions is found [20], although there is a consistently observed small hardening of the out-of-plane Ca_z phonons as the temperature is decreased (see Figure 4.14) which is not present in the equivalent Ba_z phonons in BaC_6. In BaC_6 the agreement of the experimental and DFPT-calculated phonon dispersions [77] is far poorer, which could be due to the incorrect choice of space group and lattice parameters as discussed earlier.

There is also evidence in both the CaC_6 and BaC_6 datasets for an additional phonon mode which has defied most explanations, such as being derived from an impurity or a by-product of the significant mosaic spread of these samples. In particular, any LiC_6 impurity in the samples, which could provide an explanation of this feature in the CaC_6 samples made via the alloy method, cannot explain the appearance of this mode in the BaC_6 data, as the sample used was made via the vapour transport method, with no lithium involved at any stage. The energy of the mode at the L point in the Brillouin zone decreases with intercalant mass (decreasing from $\approx$ 11.5 meV in CaC_6 to $\approx$ 7.5 meV in BaC_6), which suggests that this phonon is intercalant in nature. This hypothesis is also supported by the observation in Figures 4.15 and 4.18 that this mode has a similar energy to the two

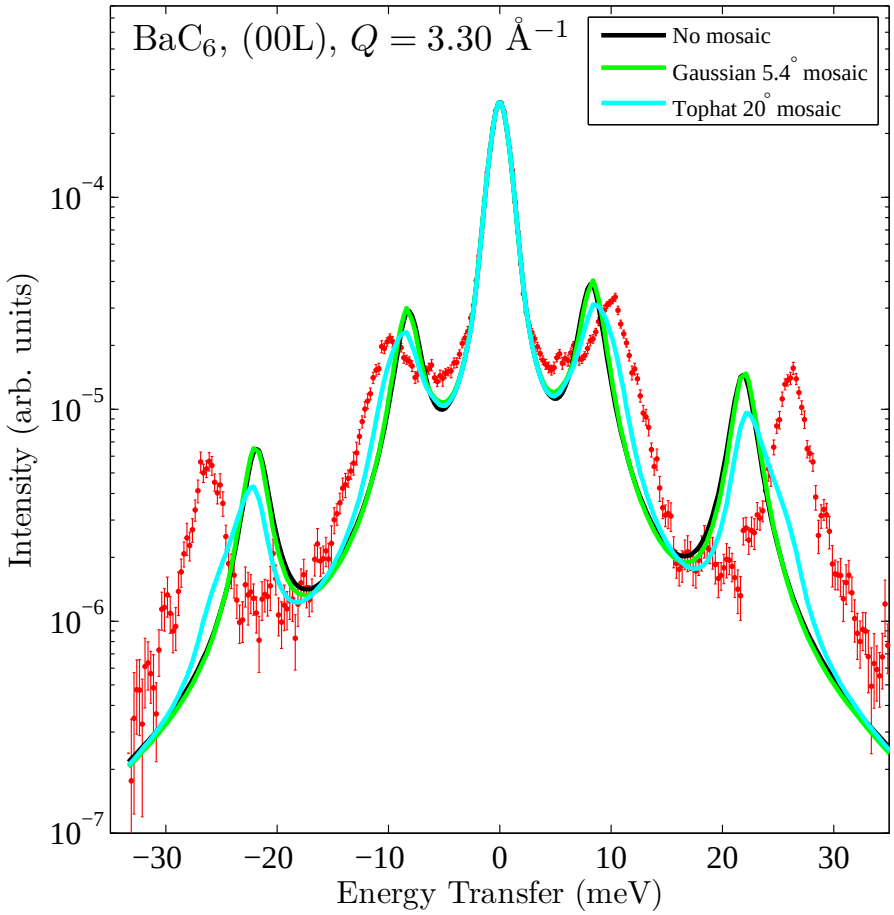

Figure 4.20: IXS data from BaC_6 at 300 K at $Q = 33.0$ Å^{-1} in the (00L) direction measured using analyser 1, with various versions of the simulated IXS spectrum overplotted. The black line is the simulated intensity assuming the sample has zero mosaic and is a perfect single crystal. Green is the simulated intensity assuming a Gaussian mosaic of FWHM of 5.4°, a mosaic based on the width of a χ scan done on the BaC_6 (004) peak, and the cyan line is the simulated intensity assuming that the mosaic is a top-hat function of FWHM 20°.

predicted I_{xy} modes (I = intercalant), which should not be measured in the (00L) direction due to their polarisation.

To summarise, the good consistency between theory and experiment in the phonons of CaC_6 provides additional - if indirect - supporting evidence for the DFPT description of the superconductivity in this material. In contrast, the dramatic inconsistency between theory and experiment for the BaC_6 phonons strongly motivates further theoretical study on this material, especially to ascertain whether the discrepancy can be attributed simply to inaccuracies in the structure used in the DFPT calculation. No temperature dependent signal of electron-phonon coupling is observed in either GIC, although since no superconducting transition in BaC_6 has been observed down to 0.080 K [21] significant electron-phonon coupling in BaC_6 may not be expected. Since there is no clear picture of how pronounced the effect of electron-phonon coupling may be on the phonons in CaC_6, any such effects may be too small to observe with the energy and momentum resolution available at Sector 3 at the APS.

Chapter 5

Conclusions and future plans

The two major strands discussed in this thesis have been successful, with the inelastic neutron scattering study of Sr_2CuO_3 providing one of the most detailed studies of the spin excitations of a 1D $S = \frac{1}{2}$ antiferromagnet ever performed, and also the inelastic X-ray studies of CaC_6 and BaC_6, the phonon excitations of which had never been measured before by X-rays or neutrons. A summary of the importance of these two projects is presented, together with a discussion of future plans for the publication of our work on Sr_2CuO_3, and a description of additional recent inelastic studies of GICs (both with X-rays and neutrons) that I have been involved in.

5.1 INS measurements of the 1D $S = 1/2$ spin chain Sr_2CuO_3

My work on Sr_2CuO_3 discussed in this thesis has culminated in the writing of a paper, which has been submitted onto the arXiv, the archive for electronic preprints of scientific papers [99]. In this paper, the argument put forward follows the argument given in Chapter 3, in that we find the magnetic form factor used normally to describe the Cu^{2+} ion is woefully inadequate, and if a magnetic form factor is used which takes account of the itinerancy of the system the agreement of theory and experiment is much improved. We feel that this discovery is of great significance to a huge area of current research, as it may

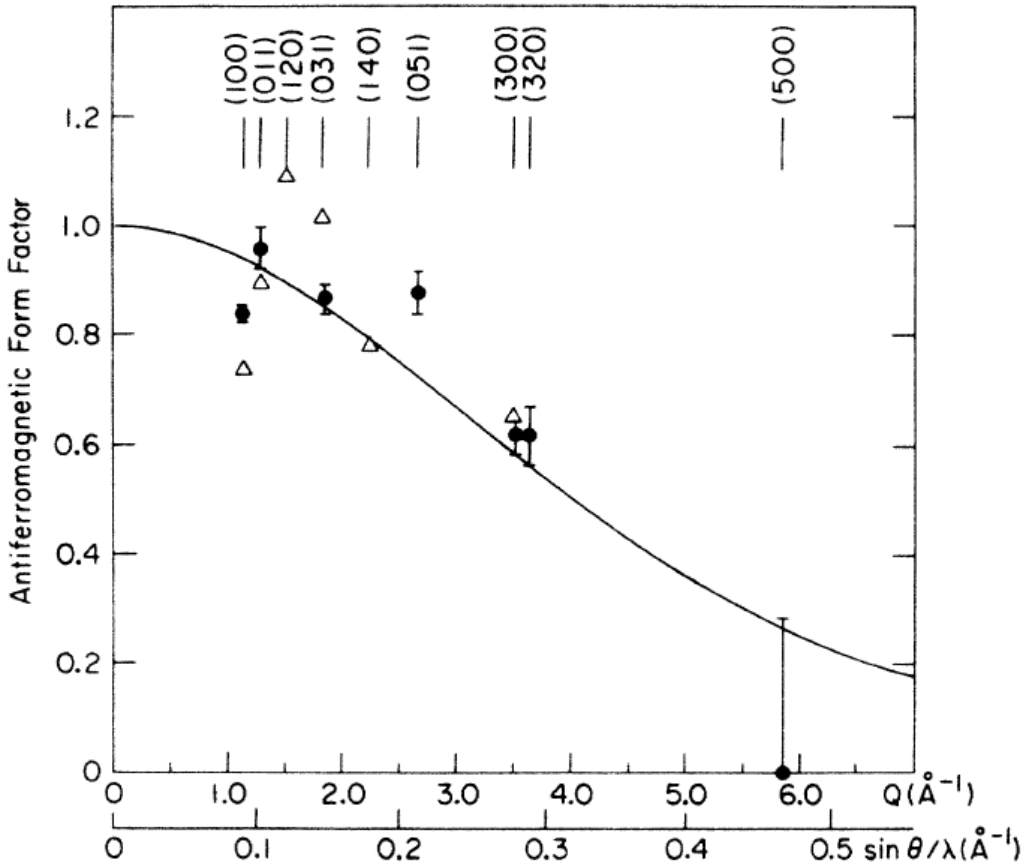

Figure 5.1: The antiferromagnetic form factor in La_2CuO_4 plotted as a function of Q [72]. The black filled circles were found from neutron diffraction [72], the open triangles are based on band-structure calculations for the similar compound $ScCuO_4$ [100] (after rescaling by a factor of 0.77), and the solid line is the ionic magnetic form factor for Cu^{2+} [31].

not just be the Cu^{2+} magnetic form factor which can be significantly affected by covalency. In fact our work shows that INS measurements can provide a very accurate measurement of the magnetic form factor (provided the spin-spin correlation function is known well), and deviations from the analytical ionic form of the magnetic form factors [31] should be considered more frequently in the future by the inelastic scattering community.

To highlight the implications of this discovery on other related compounds, in Figure 5.1 some theoretical and experimental values for the magnetic form factor in the parent high-T_c compound La_2CuO_4 are provided [72]. Note that there is very little information about

the magnetic form factor beyond 4 $Å^{-1}$, and the only data point which has been measured using neutron diffraction (at about 5.8 $Å^{-1}$) suggests that the magnetic form factor may be significantly lower than predicted by the analytical form factor. This is once again consistent with the covalent picture of the cuprates that we put forward.

We are currently working on an improved version of the paper currently on the arXiv, which will entail additional work on the figures. As the technique of magnetic inelastic neutron scattering is relatively complicated, this can mean that scientists that are not in the field may find the results of this work somewhat unclear and esoteric. It is up to us as the authors to make our study as clear as possible, and to do that we are moving forward with new ideas about how to present our data.

One possibility for a new figure is to present three-dimensional plots of the data, with axes Q_{chain}, Energy Transfer, and Intensity. The real data could then be plotted within the first two Brillouin zones, alongside two similar plots of the simulated intensity as it would be with (a) the ionic Cu^{2+} magnetic form factor, and (b) using the LDA+U calculated magnetic form factor. These latter two plots would be made assuming that no intensity scale factor was required in each case. This would highlight how much more intense the magnetic intensity is predicted to be using the ionic magnetic form factor, as it would be about three times as intense. The figure currently in the paper (Figure 3.22 in this thesis) compares both of these simulations with the data after both simulations have been rescaled by the fitted intensity scale factor, which takes emphasis away from the huge disparity between the predicted scale factor (unity) and the fitted value (0.321) for the ionic magnetic form factor.

In the future we also plan to write an additional paper which will discuss the Sr_2CuO_3 data in greater depth, which will include additional information which is reported in this thesis. This paper will also present the $SrCuO_2$ data collected on the MAPS spectrometer prior to my PhD which was reported in Physical Review Letters [10], but now fitted with the use of a covalent magnetic form factor for $SrCuO_2$, in an analogous way to the analysis presented here. Since the reduction in intensity observed with the ionic form of the magnetic form factor was similar in $SrCuO_2$ to that reported here, we expect to

be able to show consistency between these two independent datasets. In order for this analysis to be done most effectively, new ascii file scripts will be prepared for the fitting program TobyFit based upon the ones already in place for Sr_2CuO_3. These scripts will be written in turn by MatLab scripts into which the input details can be placed for the fitting, dramatically speeding up the refitting of the data.

5.2 Studying the phonons in GICs: a continuing project

There has already been noticeable success in the work on phonon excitations in GICs, the publication of a Physical Review B (Rapid Communication) paper being the highlight so far [80]. The analysis reported in this thesis on CaC_6 is based on precisely the same datasets published in this paper, but since the issue of correcting for the temperature of the analysers at Sector 3 has now been remedied (see Section 4.6.3), the quality of the data is now dramatically improved, resulting in the capability for more conclusions to be drawn out of those datasets. We plan to publish a paper shortly based on the work presented here, comparing both the CaC_6 and BaC_6 datasets, which will highlight the issue of the puzzling mode which appears at about 11 meV in CaC_6 and even lower in BaC_6. At this stage it is difficult to suggest further experiments which may shed more light on this phenomenon, as there is so much uncertainty as to its origin. There are already two extensive datasets for both CaC_6 and BaC_6 which concentrate in this region with an energy resolution of 2.2 meV, which is comparable to the best resolution that can be achieved at any meV-resolution inelastic X-ray scattering instrument.

Subsequent to these two studies of CaC_6 and BaC_6 I have continued to be involved in many more studies of GICs. There has been a third set of beamtime at Sector 3 on CaC_6, but this time on a different kind of GIC sample with different crystallinity. In this thesis the GIC samples discussed had been based on HOPG samples, where the in-plane structure is powder-like, but in this beamtime the CaC_6 sample used had a mosaic of around 1° within the plane, but a mosaic of about 10° to 15° out-of-plane. This change of crystallinity results from the type of graphite which is used as the starting material, as instead of HOPG being used, these new samples use Madagascan natural flake graphite.

Before intercalation the samples have a small mosaic in the c direction, but the process of intercalation dramatically reduces the crystallinity in this direction. Regardless, the small mosaic in-plane opens up the possibility of studying the phonons in-plane in far more detail with these new samples, in comparison to the in-plane density-of-states that can be studied with HOPG-based samples.

These natural flake graphite based samples provide other problems in comparison to the HOPG samples, as their average thickness is approximately 0.1 mm thick, and the crystallites within the 1 mm^2 sized platelets (prior to intercalation) are thought to only be approximately 100 μm $\times$ 200 μm in size [101]. In addition, the alloy method for producing CaC_6 samples cannot be easily used on natural flake graphite based samples, as this method leaves a layer of Li-Ca alloy on the surface of the sample, and the brittleness of the natural flake graphite means that any attempt to mechanically remove this layer results in the sample breaking up into shards. The vapour transport method of producing CaC_6 was used, but resulted in only about 40% intercalation of the graphite, primarily around the edge of the sample (in a similar way to the BaC_6 sample discussed in this thesis).

Prior to this subsequent Sector 3 beamtime, there had been no opportunity to do X-ray diffraction with a focused incident beam (around 50 $\times$ 50μm), so we had hoped that we might be able to isolate a CaC_6 crystallite at the very edge of the sample with the incident beam (which is 250 μm by 300 μm). We found that although we were able to successfully isolate the CaC_6 peaks from the graphite peaks, regardless of where the incident X-ray beam was positioned on the sample, there was Bragg scattering from multiple CaC_6 crystallites within the plane. This issue was dealt with by optimising the translational motor positions as much as possible on one specific crystallite, but this took no account of any procession of the sample about the χ or ϕ centres of rotation. As a consequence we were very likely to be sensitive to multiple crystallites during our energy scans. Some subtle differences could be observed between scans measured in the ΓX direction and the $\Gamma\chi$ direction, but considering the above discussion it was deemed very difficult to make more of this observation.

To overcome this difficulty, we applied for beamtime at meV-resolution instruments which

have additional focusing on the incident X-ray beam, which allow IXS measurements to be taken with a beam with dimensions of about 50 μm by 50 μm. The idea was that the smaller beamsize would then allow us to isolate a single crystallite and make a detailed survey of the phonons in-plane. We applied for beamtime at HERIXS Sector-30 at the APS, which had only just been formally commissioned at the time, and also at ID28 at the ESRF. Both proposals were accepted after one resubmission, and so we decided to study CaC_6 at ID28 and YbC_6 at HERIXS, primarily because the improved cross-section for the intercalant phonons in YbC_6 would help to counter the fact that the incident flux at HERIXS with a energy resolution of 1.5 meV is almost an order of magnitude lower than that at ID28 with a resolution of 3 meV. The energy resolution at ID28 can be made comparable to that at HERIXS, with a drop in incident flux which makes the two beamlines comparable. With such small samples, the priority is placed on maximising the phonon intensities.

Prior to the CaC_6 beamtime at ID28, consultation with the ID28 instrument scientist Dr Michael Krisch led to an additional two days of beamtime being allocated to us. This was so that the natural flake graphite based CaC_6 samples could be characterised sufficiently by X-ray diffraction, to maximise the effectiveness of the IXS beamtime. This additional sample characterisation time led to the realisation that the geometry of the measurement needed to be changed. In all in-plane measurements up to this point, the platelet sample had been orientated so that its c axis was close to being parallel to the incident X-rays (the large face of the sample facing the incident X-rays). However, in-plane measurements can also be done with the sample c axis near to perpendicular to the incident X-rays (the platelet is edge on to the incident X-rays). In both cases the momentum transfer Q can be arranged to lie completely in-plane. All the X-ray diffraction done in these additional two days was done in the former, face-on orientation. Even with a much smaller incident X-ray beam (50 μm $\times$ 30 μm) than that used at Sector 3, multiple Bragg peaks were observed from all parts of the sample, in common with the previous observation. With the use of a position sensitive detector (PSD), it was also clear that some of the crystallites could be observed at all positions on the sample. The only possible explanation for this behaviour was that the crystallites must be very small in the c direction, but very large in-plane.

Consequently we would only be able to isolate a single-crystal if we measured the sample in the edge-on geometry so that we could isolate a single crystallite.

Preparing and mounting CaC_6 samples for ID28 presented new challenges, as the χ motor at ID28 only has freedom to move $\pm 10^\circ$. This meant that there was no way in which phonons could be measured in both the ΓX and $\Gamma\chi$ with the same sample (barring a remount). In previous studies of natural flake graphite at ID28 [101, 102], different graphite samples had been prepared in two different orientations: one with the c axis in the vertical (for in-plane studies: ID28 has a horizontal scattering geometry) and the other with the c axis 30° from the vertical. Similarly in CaC_6, the $\Gamma\chi$ direction is entirely in-plane whereas the ΓX direction is 30° from the plane. Since we wished to study phonons in both directions, but a simple remount of the sample could not be done because of the air-sensitivity of CaC_6, we mounted the multiple samples in different geometries within one beryllium can. The sample mount is presented in Figure 5.2. We could then switch between different samples by use of a translation stage, which had freedom of ± 10 mm. We mounted two samples in the geometry appropriate for the $\Gamma\chi$ direction, and two for the $\Gamma\chi$ direction. This redundancy was introduced as the CaC_6 samples vary dramatically in purity, so we would align both samples in the same orientation and then pick one with higher purity. This sample holder also had to be exactly compatible with the beryllium window to be used, so that the indium seal could be made successfully.

The careful preparation for the ID28 beamtime paid dividends, as we were able to measure at a variety of different positions in the $\Gamma\chi$ direction, as well as in similar directions in-plane. Because of the large ($> 10^\circ$) mosaic of the sample in the c direction, it was extremely difficult to isolate the CaC_6 from the graphite impurity in the ΓX direction. This could perhaps be done with the use of a more accurate PSD at ID28, as the current incarnation does not have a specified position that it takes up when it is put in position, so all the scattering angles that are calculated from it have to be treated with some suspicion.

A subset of the data collected in-plane is provided in Figure 5.3. This is a selection of energy scans made at various fixed momenta, plotted with a simulated IXS profile for CaC_6 [103]. These scans were chosen as each energy scan was made at a different point

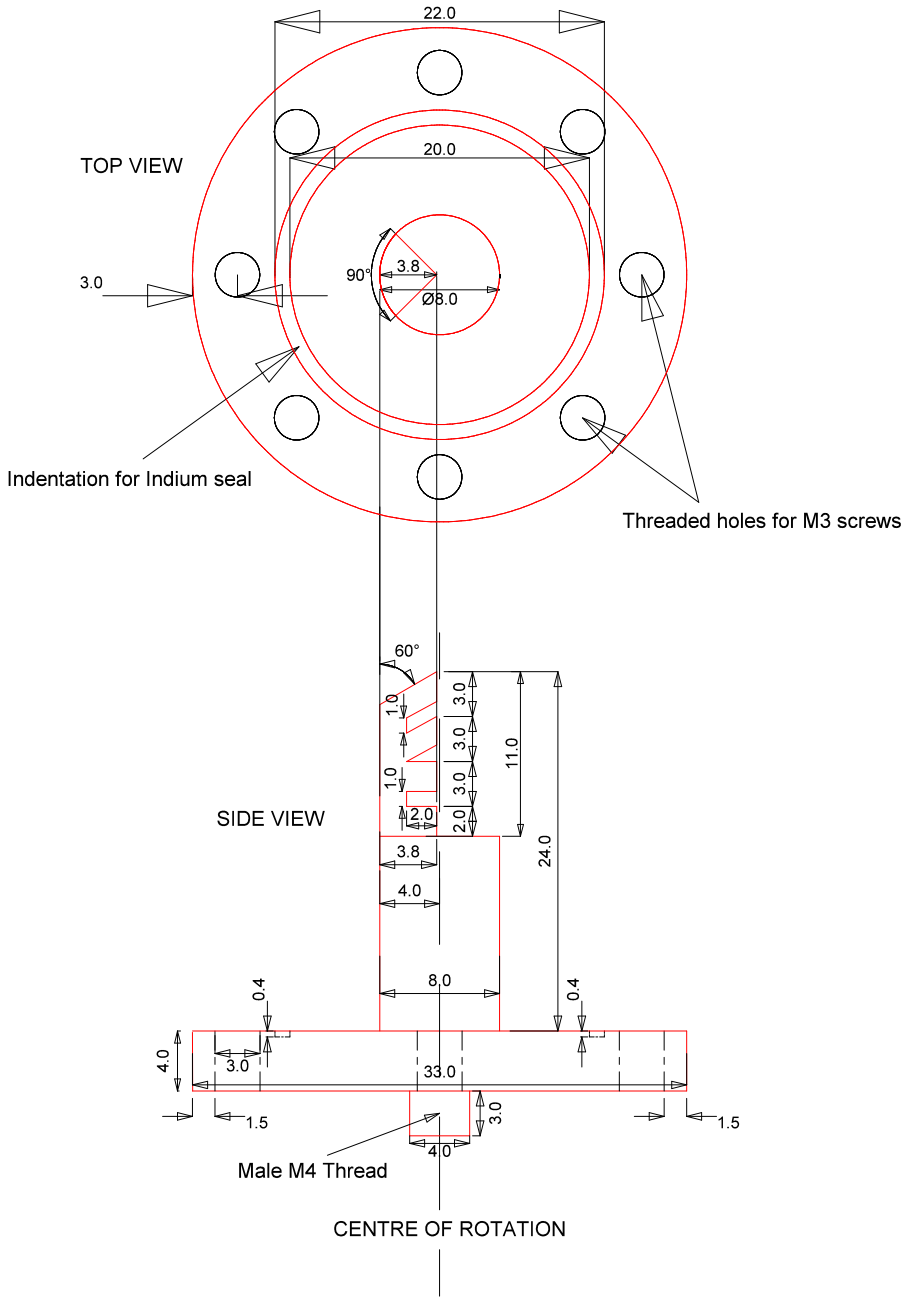

Figure 5.2: Sample holder designed for inelastic X-ray scattering experiment on natural flake graphite based CaC_6 sample at ID28 at the ESRF. The sample holder is drawn in red, while all measurements are in black. Four samples were mounted, on the upper surfaces of the 'teeth' of the copper peg. The sample being studied was changed by translating the sample can by approximately 3 mm in the vertical, with all the samples positioned within 1 cm of each other.

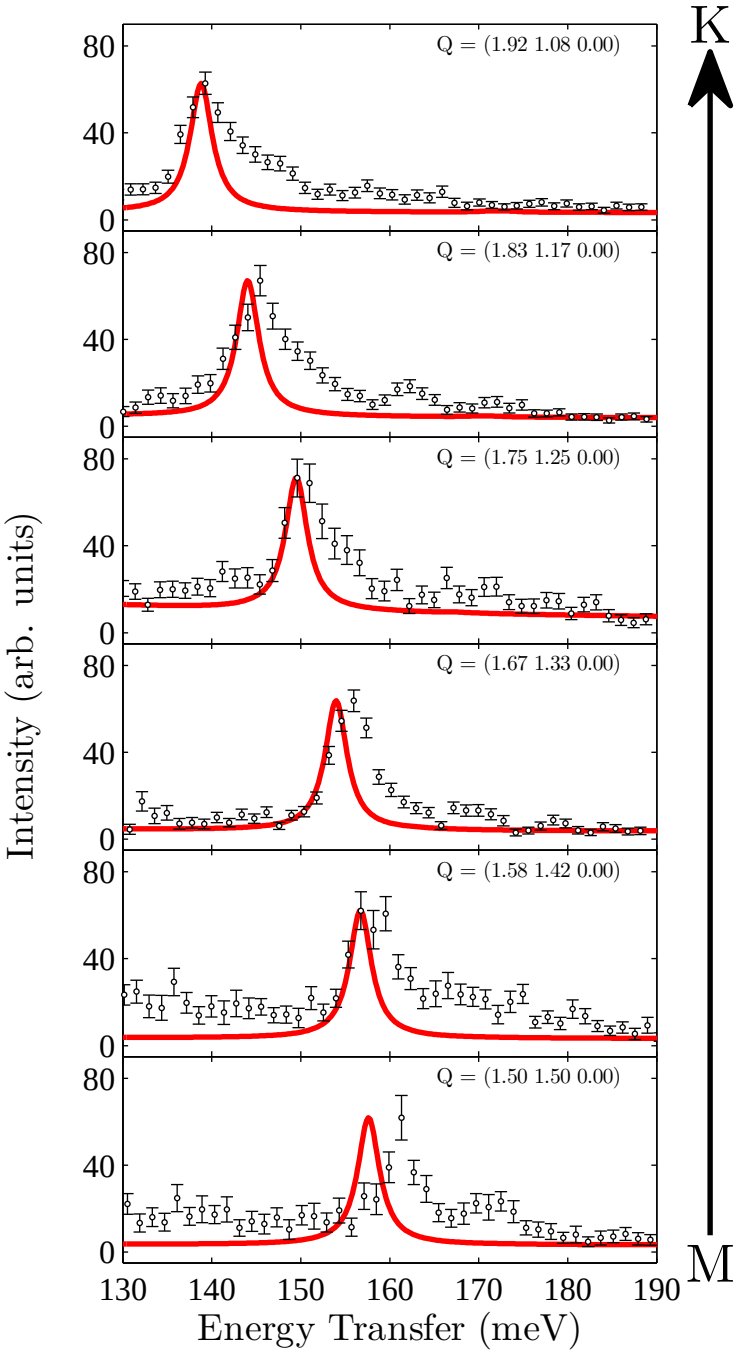

Figure 5.3: (a) Raw inelastic x-ray scattering data (black) measured at ID28 on CaC_6, measured parallel to the graphene sheets. Each dataset is labelled with its reduced Q and plotted with the appropriate DFPT-based calculation (red) of the expected phonon intensity [103].

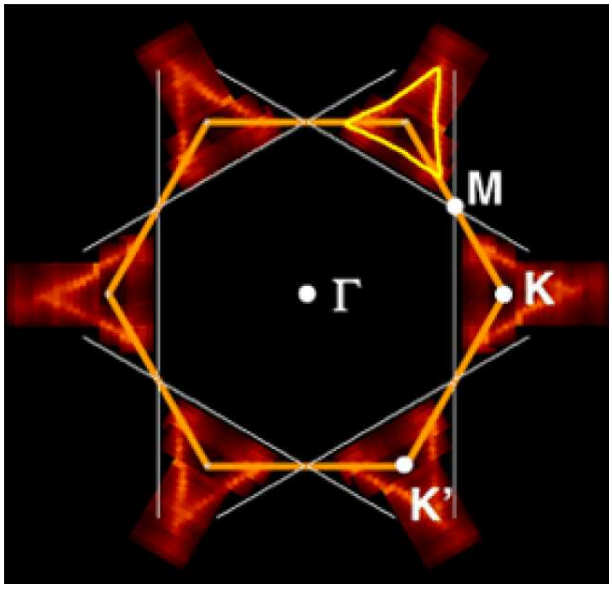

Figure 5.4: ARPES measurement of the Fermi surface in CaC_6 [91].

along the M-K line as labelled within the graphite Brillouin zone. In Figure 5.4 the measured Fermi surface of CaC_6 as measured by ARPES is presented [91]. From the ARPES measurements electron-phonon coupling is expected to occur around the corners of the 'triangles' of the Fermi surface, one of which lies on the M-K line. There is a strong suggestion of broadening of the measured phonon at $\approx$ 145 meV in the Q = (1.83 1.17 0) scan, which could be a direct result of this phonon coupling to the electronic p* band. The analysis of this dataset is still a work in progress, so at this stage it would be rather naive to make any large-scale statements about what this could mean. However, there is no doubt that there is a significant deviation of the data from the theory, and that more work still needs to be done to fully understand the phonons in CaC_6.

My involvement in a recent Sector 30 beamtime (in February 2009) on YbC_6 was peripheral, but the sample holder for which the schematic was provided in Figure 5.2 was used once again. The sample was prepared once again by vapour transport (in the case of YbC_6 there is no choice in sample preparation method, as there is no equivalent alloy method as there is in CaC_6). A detailed study of the in-plane intercalant phonons was done in this beamtime, and the data are currently being analysed by Dr Mary Upton of the APS in tandem with my analysis of the ID28 CaC_6 data. The YbC_6 dataset has the advantage of

improved energy resolution (1.5 meV as opposed to 3 meV in the CaC_6 ID28 data), which will aid the study of the low-energy Yb_{xy} modes which are likely to be extremely low in energy due to the large intercalant mass.

As well as these inelastic X-ray scattering studies, we have also had inelastic neutron scattering beamtime on CaC_6 at IN1 at the ILL neutron reactor source. In order to produce the necessary 4 g of sample, the CaC_6 samples were made using the alloy method with large HOPG platelets. The motivation for this study was to take advantage of the relatively large neutron scattering length of C as compared to Ca, as b_C is 6.65 fm and b_{Ca} is 4.70. Ignoring any effects from the Fourier transform of the electronic density for X-ray scattering, the scattering power for X-rays is proportional to Z^2, where Z is the proton number of the element. Z^2 for C is 36, whereas Z^2 for Ca is 400. Consequently as discussed, X-rays are far more sensitive to excitations involving calcium than neutrons are. Note that in both cases the phonon cross-section is also affected by a factor of $\frac{1}{M_{element}}$, which increases the cross-section from C phonons relative to Ca vibrations.

An inelastic neutron scattering scan done at IN1 at the ILL is presented in Figure 5.5. This scan was counted over the course of a day in total. All of the data sit on a huge background which is peaked at zero energy transfer. This background is very likely to come from disordered lithium in the sample, as lithium has a large incoherent neutron cross-section. Phonon intensities can be observed at 38, 55 and 77 meV, and can be ascribed to a Ca_z mode and two C_z modes respectively. The direction of Q is given above the figure in reciprocal lattice units, and is predominantly out-of-plane. With Q purely out-of-plane the phonon intensities were much smaller, so the choice was made to sample a powder ring of momenta in-plane in order to increase the phonon cross-section. To move forward with the analysis of this INS data, we require CaC_6 phonon calculations to be made which take into account the large mosaic of the combined sample that we used. The combined sample in this experiment had a mosaic of about 8°, so mosaic effects should be maximised.

The third set of IXS beamtime at Sector 3 on CaC_6 (which was ultimately used as an attempt to look at the phonons in a 'single crystal' of CaC_6, discussed earlier) was initially

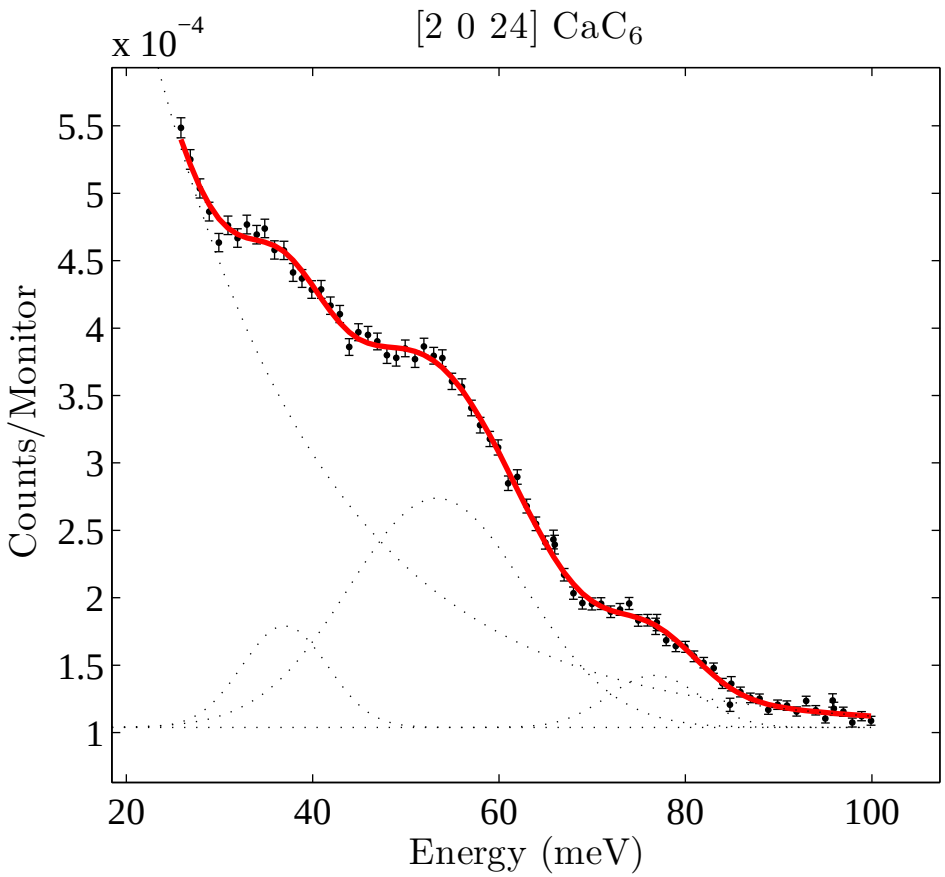

Figure 5.5: Inelastic neutron scattering data measured at IN1 at the ILL. The Q measured at (2 0 24) is described in reciprocal lattice units in CaC_6, where $a^* = 1.45$ Å^{-1} and $c^* = 0.463$ Å^{-1}. This figure is provided courtesy of Mark Dean, of Cambridge University.

planned to be a study of the phonons as a function of applied pressure, in collaboration with Dr Viktor Struzhkin and Dr Alex Goncharov, of the Carnegie/DOE Alliance Center in Washington, DC. The study of the phonons in CaC_6 and YbC_6 under pressure is highly pertinent, because of the peculiar strong positive dependence of T_c on pressure which remains unexplained within the DFPT description (discussed in Section 4.1). It is possible that one of the in-plane phonon modes heavily involved in the electron-phonon coupling softens considerably with pressure, increasing the strength of the electron-phonon coupling and increasing T_c. However, many unfortunate issues related to pressure cell preparation and temperamental gloveboxes meant that we were unable to successfully mount any samples in the pressure cells provided without significant sample deterioration.

In the future there are plans to continue the study of the phonons in the superconducting GICs, now as a function of pressure. In my future role as a postdoctoral researcher at ID28, I plan to learn the practical skills required to do successful IXS experiments at high pressures. A proposed low temperature study of the phonons in CaC_6 has already been submitted for beamtime at ID28, as we will now be more sensitive to any temperature dependence of the in-plane phonons thanks to the new single crystal CaC_6 samples. We have also been awarded beamtime at Sector 30 at the APS, in which it is likely that the study of the phonons in YbC_6 will be continued, perhaps in the (00L) direction.

Appendix A

Constant energy cuts through the INS data of Sr_2CuO_3

In this appendix details are provided of the constant energy transfer cuts which were used to fit the INS data of Sr_2CuO_3 in TobyFit. These cuts were fitted independently, and the fit parameters found from each fit were plotted as a function of the energy transfer. This provided a check of the global fit to the dataset, as independence of the fitted parameters from energ transfer would indicate a high level of agreement between experiment and theory.

E_i (meV)	$<\epsilon>$ (meV)	ϵ Integration Width (meV)	Q_h Integration Limits (r.l.u.)	Q_k Limits (r.l.u.)	Q_k Bin Width (r.l.u.)
240	60 80 100	10	-8→8	-2→2	0.010
	120 140				0.015
	160 180 200				0.020

Table A.1: Details of the cuts measured with $E_i = 240$ meV.

E_i (meV)	$<\epsilon>$ (meV)	ϵ Integration Width (meV)	Q_h Integration Limits (r.l.u.)	Q_k Limits (r.l.u.)	Q_k Bin Width (r.l.u.)
516	100 140				0.030
	180 220 260 300				0.040
	340 380 420				0.050

Table A.2: Details of the cuts measured with $E_i = 516$ meV.

E_i (meV)	$<\epsilon>$ (meV)	ϵ Integration Width (meV)	Q_h Integration Limits (r.l.u.)	Q_k Limits (r.l.u.)	Q_k Bin Width (r.l.u.)
794	180 220 260	40	-8→8	-2→2	0.05
	300 340 380				0.04
	420				0.05
	460 480				0.06
	500				0.07
	540				0.08

Table A.3: Details of the cuts measured with $E_i = 794$ meV.

E_i (meV)	$<\epsilon>$ (meV)	ϵ Integration Width (meV)	Q_h Integration Limits (r.l.u.)	Q_k Limits (r.l.u.)	Q_k Bin Width (r.l.u.)
1088	220 270 320 370 420	50	-8→8	-2→2	0.05
	470				0.06
	520				0.07
	570				0.08
	620				0.09

Table A.4: Details of the cuts measured with $E_i = 1088$ meV.

Appendix B

Details of the normalisation of INS data of Sr_2CuO_3

B.1 Inelastic neutron scattering cross-section definitions

Throughout the following the definition of the differential cross section for magnetic scattering by unpolarised neutrons from the book 'Neutron Scattering with a Triple-Axis Spectrometer' [33] is used. These equations correspond to equations (2.65) and (2.66) in this book:

$$\frac{d^2\sigma}{d\Omega_f dE_f} = \frac{N}{\hbar}\frac{k_f}{k_i}(\gamma r_0)^2 \left(\frac{g}{2}\right)^2 |F(\mathbf{Q})|^2 \sum_{\alpha\beta}(\delta_{\alpha\beta} - \hat{Q}_\alpha \hat{Q}_\beta) S^{\alpha\beta}(\mathbf{Q},\omega) \tag{B.1}$$

Where $S^{\alpha\beta}(\mathbf{Q},\omega)$, the dynamical spin-spin structure factor, is defined as:

$$S^{\alpha\beta}(\mathbf{Q},\omega) = \frac{1}{2\pi}\int_{-\infty}^{\infty} dt\; e^{i\omega t} \sum_l e^{i\mathbf{Q}\cdot\mathbf{r}_l} \langle S_0^\alpha(0) S_l^\beta(t)\rangle \tag{B.2}$$

Caux et al. [48] define the dynamical spin-spin structure factor on a finite lattice as:

$$S^{a\bar{a}}_{\text{Caux}}(q,\omega) = \frac{1}{N}\sum_{j,j'=1}^{N} e^{-iq(j-j')}\int_{-\infty}^{\infty} dt\; e^{i\omega t}\langle S^{a}_{j}(t)S^{\bar{a}}_{j'}(0)\rangle \tag{B.3}$$

Since there are two sums in (B.3) in j and j' which are done over all lattice sites N, the dynamical spin-spin structure factor has to be divided by N in order to remove repeated terms in the dynamical spin-spin structure factor. This suggests that

$$S^{a\bar{a}}_{\text{Caux}}(\mathbf{Q},\omega) = 2\pi S^{\alpha\beta}(\mathbf{Q},\omega) \tag{B.4}$$

We can justify equation (B.4) more definitively using a spin sum-rule known for magnetic inelastic neutron scattering [33]:

$$\frac{(2\pi)^3}{3v_0}S(S+1)\delta_{\alpha\beta} = \int_{-\infty}^{\infty} d\omega \int_{BZ} d\mathbf{Q}\; S^{\alpha\beta}(\mathbf{Q},\omega) \tag{B.5}$$

At zero temperature, there would be no spectral weight below $\omega = 0$, as the system has no energy to transfer to the neutron. This means that the lower energy integral limit can be set to zero in this special case. Also, in one-dimension, the volume of the Brillouin Zone $\frac{(2\pi)^3}{v_0}$ is simply the reciprocal lattice parameter in the chain direction (in our unit cell, $b^* = \frac{2\pi}{b}$).

$$\frac{1}{3}S(S+1)\delta_{\alpha\beta} = \int_{0}^{\infty} d\omega\; \frac{1}{b^*}\int_{0}^{b^*} d\mathbf{Q}\; S^{\alpha\beta}(\mathbf{Q},\omega) \tag{B.6}$$

Substituting $\tilde{\mathbf{Q}} = b\mathbf{Q}$ gives

$$\frac{1}{3}S(S+1)\delta_{\alpha\beta} = \int_{0}^{\infty} d\omega\; \frac{1}{2\pi}\int_{0}^{2\pi} d\tilde{\mathbf{Q}}\; S^{\alpha\beta}(\tilde{\mathbf{Q}},\omega) \tag{B.7}$$

Substituting in $S^{\alpha\beta}_{\text{Caux}}$ using (B.4) and since $S = \frac{1}{2}$ we find

$$\frac{1}{4} = \int_0^\infty d\omega \, \frac{1}{2\pi} \int_0^{2\pi} d\tilde{\mathbf{Q}} \, \frac{1}{2\pi} S^{\alpha\alpha}_{\text{Caux}}(\tilde{\mathbf{Q}}, \omega) \tag{B.8}$$

Which precisely matches the total integrated intensity sum-rule given by Caux in a recent paper [9].

B.2 INS cross-section in TobyFit

TobyFit requires $S_{\text{TobyFit}}(\mathbf{Q}, \omega)$ to be put into the parameter labelled `weight` in the sub-routine `sqw_broad.for` as

$$\frac{d^2\sigma}{d\Omega dE'} = \frac{N}{\hbar} \frac{k_f}{k_i} S_{\text{TobyFit}}(\mathbf{Q}, \omega) \tag{B.9}$$

From (B.1), (B.4) and (B.9) we have for $S_{\text{TobyFit}}(\mathbf{Q}, \omega)$

$$S_{\text{TobyFit}}(\mathbf{Q}, \omega) = (\gamma r_0)^2 \left(\frac{g}{2}\right)^2 |F(\mathbf{Q})|^2 \sum_{\alpha\beta} (\delta_{\alpha\beta} - \hat{Q}_\alpha \hat{Q}_\beta) \frac{1}{2\pi} S^{\alpha\beta}_{\text{Caux}}(\mathbf{Q}, \omega) \tag{B.10}$$

Let us take each of the terms in (B.10) in turn. Firstly, the constant term $(\gamma r_0)^2$ can be easily found with reference to the NIST website to be close to 289.6 mbarns. This constant is labelled `sigma_mag` in `sqw_broad.for`. We have taken $g = 2$, so the second term cancels to 1. The magnetic form factor $|F(\mathbf{Q})|^2$ for a Cu^{2+} ion is that measured in neutron scattering work on $YBa_2Cu_3O_{6.15}$ [104], and is defined in the function `amff_cu3d` within `sqw_broad.for`.

Since there is no long range order in a one-dimensional antiferromagnet, we know that when $\alpha \neq \beta$, $S^{\alpha\beta}_{\text{Caux}}(\mathbf{Q}, \omega) = 0$. We can therefore express (B.10) as

$$S_{\mathrm{TobyFit}}(\mathbf{Q},\omega) = (\gamma r_0)^2 |F(\mathbf{Q})|^2 \frac{1}{2\pi} \sum_{\alpha} ((1-\hat{Q}_x^2) S^{xx}_{\mathrm{Caux}}(\mathbf{Q},\omega) + (1-\hat{Q}_y^2) S^{yy}_{\mathrm{Caux}}(\mathbf{Q},\omega) + (1-\hat{Q}_z^2) S^{zz}_{\mathrm{Caux}}(\mathbf{Q},\omega)) \tag{B.11}$$

Since $S^{xx}_{\mathrm{Caux}}(\mathbf{Q},\omega) = S^{yy}_{\mathrm{Caux}}(\mathbf{Q},\omega) = S^{zz}_{\mathrm{Caux}}(\mathbf{Q},\omega)$, and also because $\hat{Q}_x^2 + \hat{Q}_y^2 + \hat{Q}_z^2 = 1$:

$$S_{\mathrm{TobyFit}}(\mathbf{Q},\omega) = (\gamma r_0)^2 |F(\mathbf{Q})|^2 \frac{1}{2\pi}\ 2\ S^{zz}_{\mathrm{Caux}}(\mathbf{Q},\omega) \tag{B.12}$$

Equation(B.12) shows how the parameter `weight` is defined in `sqw_broad.for` when fitting the two-spinon continuum plus the four-spinon continuum. Please note that the multi-spinon continuum calculations were provided by Caux as $S^{+-}_{\mathrm{Caux}}(\mathbf{Q},\omega)$, which is related to $S^{zz}_{\mathrm{Caux}}(\mathbf{Q},\omega)$ by $S^{+-}_{\mathrm{Caux}}(\mathbf{Q},\omega) = 2\ S^{zz}_{\mathrm{Caux}}(\mathbf{Q},\omega)$.

Appendix C

X-ray and neutron reflectivity of magnetic thin films

In this appendix the study of the structure of three different magnetic thin films is presented. Firstly an introduction to magnetic thin films and their application in spintronics is provided, and then the nominal structure of the films studied is given. Representative neutron and X-ray reflectivity data are then provided, together with a summary of the current status of the project and plans for the future.

C.1 Reflectivity and its application to spintronics

A hugely topical area in materials research is the design and production of prototypes for future electronic devices. Such devices often take advantage of low-dimensionality, especially in the use of two-dimensional epitaxially grown thin films. One branch of special interest is the idea of spintronics: using electron spins to encode information in binary (the two possible spin states denoting 1 and 0) [105] [4]. For this to be possible, components which can polarise an unpolarised electron current must be found which are commercially viable to mass-produce. Some devices made of thin-film manganites have been synthesised that theoretically should have a spin-filter polarisation of over 80%, but have found to

drastically underperform [106]. Many possible reasons for this have been provided in the literature, most of which centre on the local magnetisation within the device being very different to that predicted. In order to understand the magnetic structure of these films, neutron and X-ray reflectometry experiments were conducted on three different thin-film manganites.

X-ray reflectivity has been extensively used for the last fifty years to study the structure of surfaces and thin-film layers. The mathematical formulism that allows us to simulate the expected reflectivity profiles uses a recursive formular first put forward by Parratt in 1954 [107]. X-ray reflectivity is sensitive to the average electron density as a function of depth into the film. This quantity is also called the electron density profile of the film. This not only provides us with the atomic density of the film as a function of depth, and therefore the thicknesses of different layers which make up the thin film, but gives unique information about the interfaces between the different layers. In an analogous way, neutron reflectivity probes the neutron scattering length profile normal to the surface of the material. The added advantage of neutrons is that their intrinsic magnetic moment also allows us to probe the magnetisation profile.

In recent years there has been a huge amount of research activity concerning the production and characterisation of possible spintronic devices: that is, prototypes for future information processing which would utilise the spin states of the electrons [105] [4]. This effort has led to devices which are now commonplace, such as the read heads in hard disk drives, which take advantage of the giant magnetoresistance (GMR) effect. At present there are many exciting theoretical ideas concerning the realisation of spintronics, many of which concern themselves with the production of spintronic components, such as transistors and logic gates. To bridge the gap between theory and experiment, magnetic materials with the potential to be used in spintronic devices need to be fully characterised by experiments.

One spintronic phenomenon that has been the subject of much work is spin-polarised electron tunnelling through a thin insulating barrier. This effect could be used as part of tunnelling magnetoresistive (TMR) devices. The way this is usually achieved in devices

is to place two ferromagnetic metallic (FMM) layers together, separated by a thin non-magnetic insulating layer for the spin-polarised current to tunnel through. The resistivity of the device is much greater if the magnetisations in the two FMM layers are anti-parallel. The thin separating layer also decouples the two FMM layers, so that if the coercivity of one of the layers is very small, the magnetisation in that layer can be controlled with a small magnetic field without affecting the magnetisation in the other layer. Therefore the device has resistivity which is extremely sensitive to the applied field, an effect which is maximised by using half metals such as $La_{0.7}Sr_{0.3}MnO_3$ (LSMO) for the two FMM layers [108] [109].

An alternative, but much less studied TMR junction is a non-magnetic electrode separated by a thin (just a few nanometres) ferromagnetic insulating (FMI) layer from the pinned FMM layer. The potential barrier for tunnelling is higher for electrons with spins anti-parallel to the magnetisation of the insulator. In this case the FMI layer acts as both tunnel barrier and source of spin polarised electrons. A particularly novel combination of layers recently investigated [106] is to use $BiMnO_3$ (BMO) as the ferromagnetic insulator in conjunction with $La_{0.7}Sr_{0.3}MnO_3$ (LSMO), a fully spin-polarised ferromagnetic metal. The novelty lies in the fact that $BiMnO_3$ is a rare example of a multiferroic ferromagnet [110]: the ferroelectric polarisation is coupled to the ferromagnetism, which opens up the possibility of altering the magnetisation using an applied electric field in devices and thereby, for example, non-volatile electric write, spintronic read, MRAM.

Despite the fact that LSMO is a fully spin polarised ferromagnet for $T \ll T_C$ 350K, and BMO is ferromagnetic for $T \ll T_C = 105K$, the performance of these junctions at very low temperatures is far from ideal. In a study of a BMO(3.5nm)—STO(1nm)—LSMO film [3], the spin filter was measured to be 22% at 3K, well below the predicted 88%. More recently, a similar film using $La_{0.1}Bi_{0.9}MnO_3$ (LBMO) instead of BMO produced a spin filter polarisation of 35% [111]: an improvement, but still much reduced from the maximal value if the LBMO and LSMO layers are perfectly magnetised anti-parallel to one another. Explanations include remanent magnetisation in the LBMO well below the saturation value, or reduction of magnetisation at the LBMO—STO interface. A systematic study of the structure and magnetisation profile of these films is necessary in order for the current

limitations in spin-filtering efficiency to be fully understood. I was involved in neutron and X-ray reflectometry measurements to study the magnetic structure of three magnetic thin films. Two of the thin-films were monolayers of $La_{0.7}Ca_{0.3}MnO_3$ (LCMO) on two different substrates, and the final film was a bilayer thin-film of $La_{0.7}Sr_{0.3}MnO_3$ (LSMO) and $BiMnO_3$ (BMO).

C.2 Composition of the thin-films studied

The three thin film samples studied were grown by the Device Materials Group at the University of Cambridge, part of the Department of Material Science. The films were grown using by pulsed laser deposition. All of the neutron reflectivity measurements were made on the CRISP instrument at ISIS, the neutron spallation source based at the Rutherford Appleton Laboratory. The corresponding X-ray measurements were made on the XMAS instrument, based at the bending magnet cource BM28 at the European Synchrotron Research Facility (ESRF). Two of the thin-films were monolayers of the manganite $La_{0.7}Ca_{0.3}MnO_3$(LCMO): one had a layer thickness of approximately 600 Å and was grown on $NdGaO_3$ (NGO) (hereafter this film is referred to as the NGO-LCMO film), and the other with a layer thickness of approximately 700 Å on $SrTiO_3$ (STO) (the STO-LCMO film). These approximate layer thicknesses were determined by small angle x-ray diffraction at a laboratory X-ray source by Dr Wilma Eerenstein of Cambridge University.

The other film was a bilayer structure of $La_{0.7}Sr_{0.3}MnO_3$ (LSMO) and $BiMnO_3$ (BMO), with respective layer thicknesses of 45Å and 250Å on a NGO substrate (the NGO-LSMO-BMO film). As discussed, similar films with a LSMO-BMO bilayer have been made with an electron spin polarisation of 22% [106]. The neutron reflectivity measurements on the STO-LCMO and NGO-LCMO films were done prior to the start of my PhD, but previous data analysis had revealed puzzling features of the data. The reflectivity fringes appeared to have the correct periodicity, corresponding to the thickness of the monolayer, but the size and character of the fringes seemed to be markedly decreased in comparison to simulations. Since it has been suggested that the magnetism at the interfaces between different layers in thin-films could be responsible for the poor efficiency of these prototype

spintronic devices, we felt that this same effect could also be responsible for the strange appearance of the neutron reflectivity. Accordingly we decided that in order to progress with fitting this data, a new reflectivity data fitting program should be written that would allow us to vary the magnetic smoothing length scale from one layer to the next, independent of the structural smoothing length scale.

C.3 PrettyPolly: a new X-ray and neutron reflectivity fitting program

The new program that has been written for fitting neutron and X-ray reflectivity data, PrettyPolly, is based on the program called Polly, written by Dr Sean Langridge, who is one of the instrument scientists at CRISP. Both Polly and PrettyPolly follow the representation of the reflectivity calculation as put forward by Blundell and Bland in 1993 [112]. PrettyPolly carries out all the necessary computation within Fortran 95, which in turn is controlled using the command line in MatLab. The computation is done in Fortran to improve the speed of reflectivity calculations, since the formula for calculating the reflectivity profiles is recursive, and scales with the number of layers in the thin film being simulated, it is computationally expensive. In the stand-alone version of Polly, the user interface contains many bugs, including an extremely annoying propensity to crash whenever the window containing the plotted reflectivity is resized. Of course, PrettyPolly also includes extra functionality, the most major being:

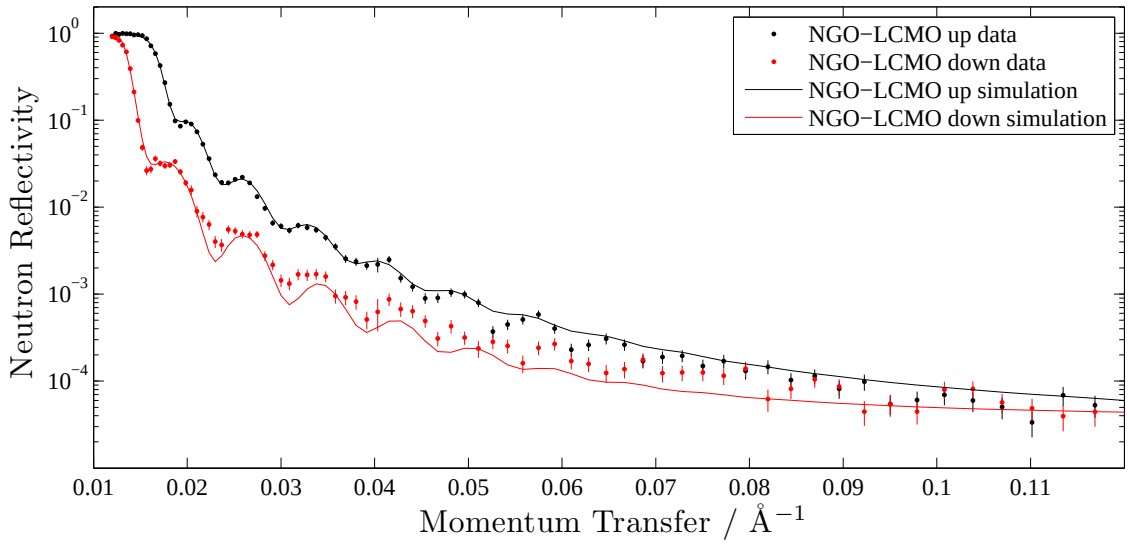

Figure C.1: Measured neutron reflectivity and fit for the NGO-LCMO film at 10K. The experiment was conducted on the CRISP reflectometer at ISIS.

- The ability to independently change the smoothing length scale of the layer density, scattering length density, magnetisation magnitude, magnetisation direction and absorption through any interface in the thin film. This functionality can also be altered so that rather than smoothing the magnetisation magnitude and direction, the smoothing length scales can be applied to the two components of the magnetisation in-plane that the neutrons are sensitive to.
- The ability to set another, unrelated, length scale on the variation of the total film thickness (in the case that the layer does not have uniform thickness, we requires some length scale over which the thickness is allowed to vary).
- The program does not simply use one function to change the value of a parameter from one layer to the next: there are currently three different possible choices of smoothing functions. These are the error function, the hyperbolic sine function and a simple linear function.

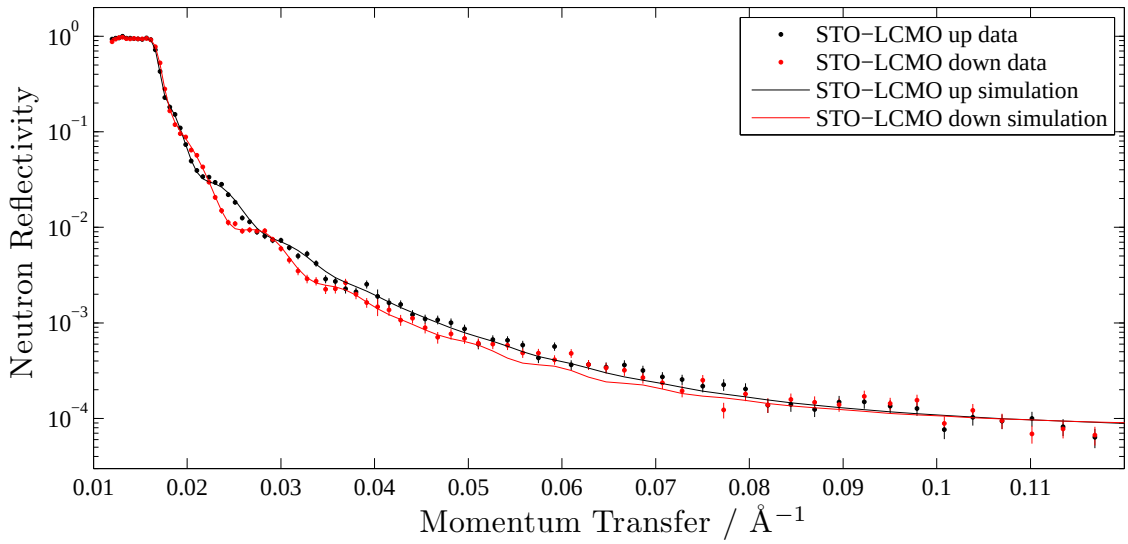

Figure C.2: Measured neutron reflectivity and fit for the STO-LCMO film at 10K. The experiment was done on the CRISP reflectometer at ISIS.

C.4 Neutron reflectometry experiments

As a result of the increased functionality of PrettyPolly, we found that the difficulties in fitting the original neutron reflectivity data from the two LCMO films could be remedied by allowing the thickness of the LCMO films to vary over about 10% of their total thickness. This huge variation in thickness could result from the substrate being slightly tilted when the film is grown, or perhaps, depending on the geometry of the vacuum chamber used in pulsed laser deposition, the film thickness could be humped, with the maximum thickness found in the centre of the film. From fitting this data in PrettyPolly, the thickness of the LCMO film on a NGO substrate was found to be 690Å $\pm$ 140Å, with a magnetisation of $3.78\mu_B \pm 0.06\mu_B$, at 10 K, and the thickness of the LCMO film on a STO substrate to be 740Å $\pm$ 160Åwith a magnetisation of $4.4\mu_B \pm 0.1\mu_B$ at 10 K. Due to the huge variation in thickness over the area of the sample illuminated by neutrons, any subtlety in the interfacial magnetisation is essentially averaged out, so any length scale over which the magnetisation is judged to change across an interface is very difficult to justify with this data.

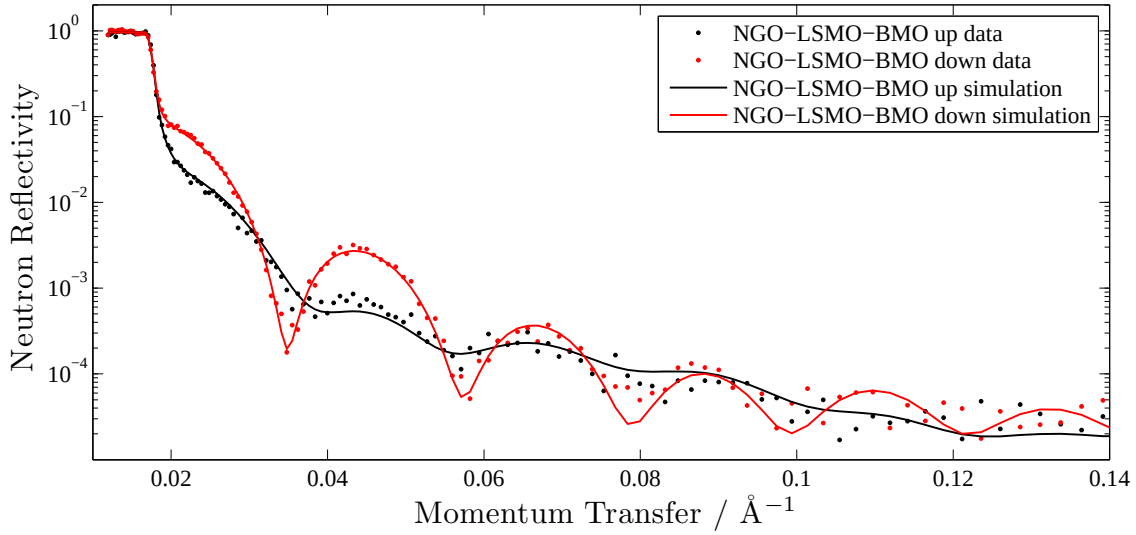

Figure C.3: Measured neutron reflectivity and fit for the BMO-LSMO film at 5K in a magnetic field of 4400 Oe. The experiment was conducted on the CRISP reflectometer at ISIS.

Analysis of the neutron reflectivity of the BMO-LSMO film suggested that the layer thicknesses were far better defined than in the LCMO films, but there are still complications: the neutron scattering length multiplied by the density in the BMO layer and the LSMO layer are remarkably similar. This lack of contrast makes it very difficult to know precisely where the physical interface between these two layers are. The data do show a clear inconsistency with the measurements done at Cambridge using small-angle X-ray scattering (in which the thickness of the BMO layer was found to be $45\text{Å} \pm 2\text{Å}$and the thickness of the LSMO layer was $260\text{Å} \pm 10\text{Å}$), as we are still very sensitive to the total thickness of the two layers. The total thickness of the two layers measured using neutron reflectivity is much smaller than anticipated. We find that the total film thickness is $280\text{Å} \pm 5\text{Å}$, and at 5 K the magnetisations in the LSMO layer and the BMO layer are $2.50\text{Å} \pm 0.03\mu_B$ and $0.5\text{Å} \pm 0.06\mu_B$ respectively.

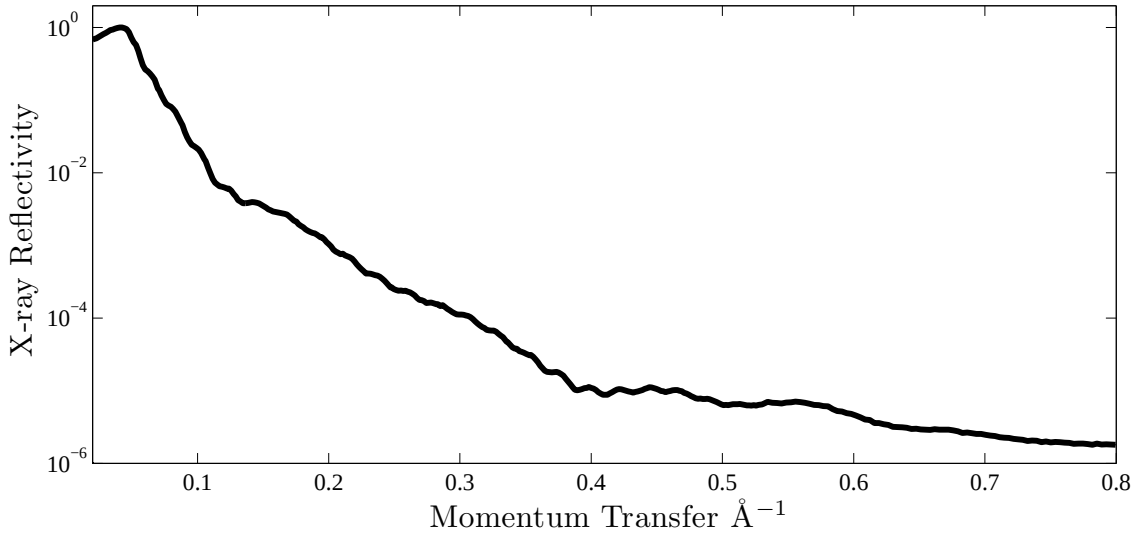

Figure C.4: Measured X-ray reflectivity of the BMO-LSMO film at ambient temperature and pressure. The experiment was done at XMAS at BM28 at the ESRF.

C.5 X-ray reflectometry experiments

We have conducted room temperature X-ray reflectivity measurements on these three films, so that we may get independent measurements on the structure. Because of the thickness variation we saw in the neutron data on the LCMO films, we decided to measure the reflectivity of the films on several strips along its surface. This allowed us to confirm the variation in film thickness that we had already suspected. We used a monochromatic incident X-ray beam at 10.0 keV, so to probe different momenta the sample and detector angle are altered. This means that the actual amount of the film being sampled varies as a function of sample angle, or theta. This has resulted in difficulties in the analysis of the data, as essentially the 'average' sample is changing as a function of theta. This problem was bypassed by CRISP, as there are no moving parts: the range in Q is provided by a white neutron beam being used, providing a range of wavelengths that are measured in any one measurement.

The analysis of these recent X-ray reflectivity measurements has been very problematic, in fact even the BMO-LSMO data have so far proved difficult to fit. I believe that this may be due to significant variation of the density of the BMO and LSMO layers, as there does

appear to be periodicity on a length scale unexpected from either the initial work done at Cambridge or our neutron reflectivity data taken at ISIS. The X-ray measurements were somewhat blighted by instrumental problems for the majority of the five days scheduled, resulting in all of our usuable data coming out of the last 36 hours of beamtime. For the first 3 and a half days of the experiment, we were aligned on the very edge of the X-ray beam, meaning that any minute change in the beam position resulted in huge changes in intensity (of the order 200% to 300%). During this early part of the experiment, significant background issues made all of our data meaningless, and the current problem with my fitting may, unfortunately, be a result of this problem never being satisfactorally resolved.

To move forward with this project, what is currently needed is reliable X-ray data from the bilayer film of $La_{0.7}Sr_{0.3}MnO_3$ (LSMO) and $BiMnO_3$ (BMO). Our measurements have shown that the two monolayer films of $La_{0.7}Ca_{0.3}MnO_3$(LCMO) are of poor quality, as the thickness of the LCMO layers varies by about 10% over its entire surface. However, the Cambridge group which whom we collaborate has continued to make magnetic thin films, often utilising multiferroics, and is one of the foremost groups in the world. The local high-quality of the majority of these films is not in doubt, as it has been shown in recent publications [113], but for our purposes in neutron reflectivity we require uniformity on a relatively huge scale (centimetres, rather than microns) to make neutron reflectivity counting times feasible.

In the future it would be interesting to study other similar thin films, perhaps with the multiferroic layer composed of $BiTiO_3$ rather than $BiMnO_3$, as studied in a paper by the collaborating group at Cambridge [113]. I believe that a study of multiple samples, consisting of the same compounds but with different layer thicknesses, would be an esecially fruitful line of enquiry, as this will then isolate the effect of the thickness of the layers from any other concerns about the samples. Clearly all future studies will also require that the sample homogeneity is confirmed by measuring the X-ray reflectivity at different points on the sample surface. It would make sense (if possible to schedule) to do X-ray measurements on these samples prior to doing a neutron experiment, as the X-ray experiment can provide confirmation that the sample is of sufficient quality for neutrons to be useful. X-ray reflectivity can be achieved on a lab-based X-ray set, so ideally the

first reality check would be to check the first few fringes using such a set-up, as time at a synchrotron is at a premium. This would also act as a test of the homogeneity, as the X-ray beamsize on a rotating anode set-up is usually on the scale of 0.5 mm $\times$ 0.5 mm, with a significant divergence.

The key element I have discussed in the study of thin films by scattering techniques is that the sample quality is quickly determined, so that as little time as possible is wasted in the study of poor quality samples. I believe that the best way in which this problem is avoided is to introduce more overlap between the people who make the samples and the people who do the reflectivity experiments. An ideal situation would be for the sample grower to be able to immediately do a lab-based X-ray reflectometry measurement on the sample as soon as the sample is made, as part of the multiple tests of samples that must occur. Then, if the sample grower is not directly involved in the large-scale facility reflectivity measurements, the people who do these experiments should be closely involved in the sample testing prior to the beamtime. This would facilitate improved efficiency during the reflectivity experiments, as the experimenters will know more about the samples and therefore would be more likely to spot any problems early.

Bibliography

[1] Edited by D. Baeriswyl and L. Degiorgi. *Strong interactions in low dimensions*. Springer, (2004).

[2] P. M. Chaikin and T . C. Lubensky. *Principles of condensed matter physics*. Cambridge University Press, (2000).

[3] P. Gegenwart, Q. Si and F. Steglich. *Nature Physics* **4**, 186–197 (2008).

[4] S. A. Wolf, D. D. Awschalom, R. A. Buhrman, J. M. Daughton, S. von Molna, M. L. Roukes, A. Y. Chtchelkanova, D. M. Treger. *Science* **294**, 1488–1495 (2001).

[5] T. M. Rice. *Physica B* **241–243**, 5–12 (1998).

[6] H. Bethe. *Zeitschrift für Physik* **71**, 205 (1931).

[7] J. Des Cloizeaux and J. J. Pearson. *Physical Review* **128**, 2131–2135 (1962).

[8] G. Müller, H. Thomas, H. Beck and J. C. Bonner. *Physical Review B* **24**, 1429–1467 (1981).

[9] J.-S. Caux and R. Hagemans. *Journal of Statistical Mechanics: Theory and Experiment* , P12013 (2006).

[10] I. A. Zaliznyak, H.Woo, T.G. Perring, C. L. Broholm, C. D. Frost and H. Takagi. *Physics Review Letters* **93**, 087202 (2004).

[11] B. Lake, D. A. Tennant, C. D. Frost and S. E. Nagler. *Nature Materials* **4**, 329–334 (2005).

[12] Y. Yanase, T. Jujo, T. Nomura, H. Ikeda, T. Hotta, K. Yamada. *Physics Reports* **387**, 1–149 (2003).

[13] S. R. Julian and M. R. Norman. *Nature* **447**, 537–539 (2007).

[14] J. Bardeen, L. N. Cooper and J. R. Schrieffer. *Physical Review* **106**, 162–164 (1957).

[15] C. W. Chu, P. H. Hor, R. L. Meng, L. Gao, Z. J. Huang, and Y. Q. Wang. *Physical Review Letters* **58**, 405–407 (1987).

[16] R. J. Cava, R. B. van Dover, B. Batlogg, and E. A. Rietman. *Physical Review Letters* **58**, 408 (1987).

[17] J. Nagamatsu, N. Nakagawa, T. Muranaka, Y. Zenitani and J. Akimitsu. *Nature* **410**, 63–64 (2001).

[18] H. J. Choi, D. Roundy, H. Sun, M. L. Cohen and S. G. Louie. *Nature* **418**, 758–760 (2002).

[19] T. E. Weller, M. Ellerby, S. S. Saxena, R. P. Smith and N. T. Skipper. *Nature Physics* **1**, 39–41 (2005).

[20] M. Calandra and F. Mauri. *Physical Review Letters* **95**, 237002 (2005).

[21] S. Nakamae, A. Gauzzi, F. Ladieu, D. L'Hôte, N. Eméry, C. Hérold, J.F. Marêché, P. Lagrange, G. Loupias. *Solid State Communications* **145**, 493–496 (2008).

[22] J. S. Kim, L. Boeri, J. R. OBrien, F. S. Razavi, and R. K. Kremer. *Physical Review Letters* **99**, 027001 (2007).

[23] A. Sanna, G. Profeta, A. Floris, A. Marini, E. K. U. Gross and S. Massidda. *Physical Review B* **75**, 020511 (2007).

[24] W. L. Bragg. *Proceedings of the Cambridge Philosophical Society* **17**, 43–57 (1913).

[25] J. D. Watson and F. H. C. Crick. *Nature* **171**, 737–738 (1953).

[26] S. K Sinha. *Journal of Physics: Condensed Matter* **13**, 7511–7523 (2001).

[27] J. Als–Nielsen and D. F. McMorrow. *Elements of Modern X-ray Physics*. John Wiley and Sons, Ltd, (2001).

[28] S. W. Lovesey. *Theory of neutron scattering from condensed matter*. Oxford University Press, (1984).

[29] M. Krisch and F. Sette. *Light Scattering in Solid IX*, Volume 108 of *Topics in Applied Physics*, Chapter entitled Inelastic X-ray Scattering from Phonons, 317–370. Springer-Verlag Berlin Heidelberg, (2007).

[30] G. L. Squires. *Introduction to the theory of thermal neutron scattering*. Dover, (1996).

[31] *Neutron Data Booklet*: *Second Edition*, Edited by A.-J. Dianoux and G. Lander, Institut Laue-Langevin, (2003).

[32] P. Pattison. Presentation at the 'Practical Cource in Diffraction Methods', held at the Ecole Polytechnique Fédérale de Lausanne (EPFL), (2009).

[33] G. Shirane, S. M. Shapiro, and J. M. Tranquada. *Neutron Scattering with a Triple-Axis Spectrometer*. Cambridge University Press, (2002).

[34] T. S. Toellner. *Hyperfine Interactions* **125**, 3–28 (2000).

[35] H. Sinn, E. E. Alp, A. Alatas, J. Barraza, G. Bortel, E. Burkel, D. Shu, W. Sturhahn, J. P. Sutter, T. S. Toellner and J. Zhao. *Nuclear Instruments and Methods in Physics Research A* **467-468**, 1545–1548 (2001).

[36] T.G. Perring. *Frontiers of Neutron Scattering*, Chapter entitled Neutron scattering (mostly) from low dimensional magnetic systems. World Scientific, (2000).

[37] T. G. Perring. *High Energy Magnetic Excitations in Hexagonal Cobalt*. PhD thesis, University Of Cambridge, (1991).

[38] H. M. Rønnow, D. F. McMorrow, R. Coldea, and A. Harrison, I. D. Youngson, T. G. Perring, G. Aeppli, O. Syljuåsen, K. Lefmann and C. Rischel. *Phys. Rev. Lett.* **87**, 037202 (2001).

[39] R. Coldea, S. M. Hayden, G. Aeppli, T. G. Perring, C. D. Frost, T. E. Mason, S.-W. Cheong and Z. Fisk. *Physical Review Letters* **86**, 5377–5380 (2001).

[40] D. A. Tennant, R. A. Cowley, S. E. Nagler and A. M. Tsvelik. *Physical Review B* **52**, 13368–13380 (1995).

[41] P. Bourges, L. P. Regnault, Y. Sidis, J. Bossy, P. Burlet, C. Vettier, J. Y. Henry, and M. Couach. *Journal of Low Temperature Physics* **105**, 377–382 (1996).

[42] J. M. Tranquada, B. J. Sternlieb, J. D. Axe, Y. Nakamura and S. Uchida. *Nature* **375**, 561–563 (1995).

[43] P. W. Anderson. *Physical Review* **86**, 694–701 (1952).

[44] S. Maekawa and T. Tohyama. *Reports on Progress in Physics* **64**, 383–428 (2001).

[45] S. J. Blundell. *Magnetism in Condensed Matter*. Oxford University Press, (2001).

[46] T. Yamada. *Progress of Theoretical Physics* **41**, 880–890 (1969).

[47] A. H. Bougourzi, M. Couture and M. Kacir. *Physical Review B* **54**, R12669 (1996).

[48] J.-S. Caux, R. Hagemans and J.-M. Maillet. *Journal of Statistical Mechanics: Theory and Experiment* , P09003 (2005).

[49] S. E. Nagler, D. A. Tennant, R. A. Cowley, T. G. Perring, and S. K. Satija. *Physical Review B* **44**, 12361–12368 (1991).

[50] D. A. Tennant, T. G. Perring, R. A. Cowley and S. E. Nagler. *Physical Review Letters* **70**, 4003–4006 (1993).

[51] Y. Endoh, G. Shirane, R. J. Birgeneau, P. M. Richards and S. L. Holt. *Physical Review Letters* **32**, 170–173 (1974).

[52] F. C. Zhang and T. M. Rice. *Physical Review B* **37**, 3759–3761 (1988).

[53] T. Ami, M.K. Crawford, R. L. Harlow, Z. R. Wang, D. C. Johnston, Q. Huang, R.W. Erwin. *Physical Review B* **51**, 5994–6001 (1995).

[54] S. K. Satija, J. D. Axe, G. Shirane, H. Yoshizawa, and K. Hirakawa. *Physical Review B* **21**, 2001–2007 (1980).

[55] A. V. Sologubenko, E. Felder, K. Gianno, H. R. Ott, A. Vietkine and A. Revcolevschi. *Physical Review B* **62**, R6108–R6111 (2000).

[56] T. Ogasawara, M. Ashida, N. Motoyama, H. Eisaki, S. Uchida, Y. Tokura, H. Ghosh, A. Shukla, S. Mazumdar, and M. Kuwata-Gonokami. *Physical Review Letters* **85**, 2204–2207 (2000).

[57] N. Motoyama, H. Eisaki and S. Uchida. *Physical Review Letters* **76**, 3212–3215 (1996).

[58] H. Fujisawa, T. Yokoya, T. Takahashi, S. Miyasaka, M. Kibune, and H. Takagi. *Physical Review B* **59**, 7358–7361 (1999).

[59] T. E. Kidd, T. Valla, P. D. Johnson, K. W. Kim, G. D. Gu and C. C. Homes. *Physical Review B* **77**, 054503 (2008).

[60] H. Suzuura, H. Yasuhara, A. Furusaki, N. Nagaosa, and Y. Tokura. *Physical Review Letters* **76**, 2579–2582 (1996).

[61] R. Neudert, S.-L. Drechsler, J. Málek, H. Rosner, M. Kielwein, Z. Hu, M. Knupfer, M. S. Golden, J. Fink, N. Nücker, M. Merz, S. Schuppler, N. Motoyama, H. Eisaki, S. Uchida, M. Domke and G. Kaindl. *Physical Review B* **62**, 10 752–10765 (2000).

[62] M. J. Bhaseen, F. H. L. Essler and A. Grage. *Physical Review B* **71**, 020405(R) (2005).

[63] R. Coldea, $MSLICE$, (2001).

[64] G. Müller. *Physical Review B* **26**, 1311–1320 (1982).

[65] Y.-J. Kim, J. P. Hill, H. Benthien, F. H. L. Essler, E. Jeckelmann, H. S. Choi, T. W. Noh, N. Motoyama, K. M. Kojima, S. Uchida, D. Casa and T. Gog. *Physical Review Letters* **92**, 137402 (2004).

[66] J.-S. Caux and J. M. Maillet. *Physical Review Letters* **95**, 077201 (2005).

[67] H. Benthien, F. Gebhard and E. Jeckelmann. *Physical Review Letters* **92**, 256401 (2004).

[68] H. Benthien. *Dynamical Properties of Quasi One-Dimensional Correlated Electron Systems*. PhD thesis, Philipps-Universität Marburg, (2005).

[69] J. Lorenzana, G. Seibold and R. Coldea. *Physical Review B* **72**, 224511 (2005).

[70] T. A. Kaplan, D. Mahanti and H. Chang. *Physical Review Letters* **45**, 2565–2568 (1992).

[71] S. D. Mahanti, T. A. Kaplan, H. Chang, and J. F. Hanison. *Journal of Applied Physics* **73**, 6105–6107 (1993).

[72] T. Freltoft, G. Shirane, S. Mitsuda, J. P. Remeika and A. S. Cooper. *Physical Review B* **37**, 137–142 (1988).

[73] M. S. Dresselhaus and G. Dresselhaus. *Advances in Physics* **51**, 1 (2002).

[74] J.-M. Tarascon and M. Armand. *Nature* **414**, 359–367 (2001).

[75] A. Lovell, F. Fernandez-Alonso, N. T. Skipper, K. Refson, S. M. Bennington and Stewart F. Parker. *Physical Review Letters* **101**, 126101 (2008).

[76] W. Kraus and G. Nolze, $PowderCell\ for\ Windows : Version$ 2.4, (2000).

[77] M. Calandra and F. Mauri. *Physical Review B* **74**, 094507 (2006).

[78] M. El Makrini, D. Guérard, P. Lagrange, A. Hérold. *Physica B* **99**, 481–485 (1980).

[79] N. Emery, C. Hérold, M. dAstuto, V. Garcia, Ch. Bellin, J. F. Marêché, P. Lagrange, and G. Loupias. *Physical Review Letters* **95**, 087003 (2005).

[80] M. H. Upton, A. C. Walters, C. A. Howard, K. C. Rahnejat, M. Ellerby, J. P. Hill, D. F. McMorrow, A. Alatas, B. M. Leu and W. Ku. *Physical Review B* **76**, 220501(R) (2007).

[81] G. Csányi, P. B. Littlewood, A. H. Nevidomskyy, C. J. Pickard and B. D. Simons. *Nature Physics* **1**, 42–45 (2005).

[82] I. I. Mazin. *Physical Review Letters* **95**, 227001 (2005).

[83] D. G. Hinks, D. Rosenmann, H. Claus, M.S. Bailey and J. D. Jorgenson. *Physical Review B* **75**, 014509 (2007).

[84] R. P. Smith, A. Kusmartseva, Y. T. C. Ko, S. S. Saxena, A. Akrap, L. Forr, M. Laad, T. E. Weller, M. Ellerby, and N. T. Skipper. *Physical Review B* **74**, 024505 (2006).

[85] J. S. Kim, L. Boeri, R. K. Kremer and F. S. Razavi. *Physical Review B* **74**, 214513 (2006).

[86] A. Gauzzi, S. Takashima, N. Takeshita, C. Terakura, H. Takagi, N. Emery, C. Hérold, P. Lagrange and G. Loupias. *Physical Review Letters* **98**, 067002 (2007).

[87] A. Gauzzi, N. Bendiab, M. d'Astuto, B. Canny, M. Calandra, F. Mauri, G. Loupias, N. Emery, C. Hérold, P. Lagrange, M. Hanfland and M. Mezouar. *Physical Review B* **78**, 064506 (2008).

[88] L. Boeri, G. B. Bachelet, M. Giantomassi and O. K. Andersen. *Physical Review B* **76**, 064510 (2007).

[89] J. L. McChesney, A. Bostwick, T. Ohta, K. V. Emtsev, T. Seyller, K. Horn and E. Rotenberg. , arXiv:0705.3264v1 (2007).

[90] A. Grüneis, C. Attaccalite, A. Rubio, D. Vyalikh, S.L. Molodtsov, J. Fink, R. Follath, W. Eberhardt, B. Büchner and T. Pichler. , arXiv:0808.1613v2 (2008).

[91] T. Valla, J. Camacho, Z-H. Pan, A. V. Fedorov, A. C. Walters, C. A. Howard and M. Ellerby. *Physical Review Letters* **102**, 107007 (2009).

[92] C.-H. Park, F. Giustino, J. L. McChesney, A. Bostwick, T. Ohta, E. Rotenberg, M. L. Cohen and S. G. Louie. *Physical Review B* **77**, 113410 (2008).

[93] S. Pruvost, C. Hérold, A. Hérold, and P. Lagrange. *Carbon* **42**, 1825–1831 (2004).

[94] J. S. Kim, R. K. Kremer, L. Boeri and F. S. Razavi. *Physical Review Letters* **96**, 217002 (2006).

[95] N. Emery, C. Hérold, P. Lagrange. *Journal of Solid State Chemistry* **178**, 2947–2952 (2005).

[96] K. G. Lyon, G. L. Salinger and C. A. Swenson. *Journal of Applied Physics* **48**, 865–868 (1977).

[97] A. Bergamin, G. Cavagnero, G. Mana and G. Zosi. *The European Physical Journal B* **9**, 225–232 (1999).

[98] D. Guerard, M.Chaabouni, P.Lagrange, M.El Makrini and A. Hérold. *Carbon* **18**, 257–264 (1980).

[99] A. C. Walters, T. G. Perring, J.-S. Caux, A. T. Savici, G. D. Gu, C.-C. Lee, W. Ku, I. A. Zaliznyak. , arXiv:0812.5007 (2008).

[100] T. C. Leung, X. W. Wang and B. N. Harmon. *Physical Review B* **37**, 284–388 (1988).

[101] J. Maultzsch, S. Reich, C. Thomsen, H. Requardt and P. Ordejón. *Physical Review Letters* **92**, 075501 (2004).

[102] M. Mohr, J. Maultzsch, E. Dobardzic, S. Reich, I. Milosevic, M. Damnjanovic, A. Bosak, M. Krisch and C. Thomsen. *Physical Review B* **76**, 035439 (2007).

[103] Private communication, M. Calandra. (2008).

[104] S. Shamoto, M. Sato, J. M. Tranquada, B. J. Sternlieb and G. Shirane. *Physical Review B* **48**, 13817–13825 (1993).

[105] G. A. Prinz. *Science* **282**, 1660–1663 (1998).

[106] M. Gajek, M. Bibes, A. Barthélémy, K. Bouzehouane, S. Fusil, M. Varela, J. Fontcuberta and A. Fert. *Physics Review B* **72**, 020406 (2005).

[107] L. G. Parratt. *Physical Review* **95**, 359–369 (1954).

[108] Y. Lu, X. W. Li, G. Q. Gong, G. Xiao, A. Gupta, P. Lecoeur, J. Z. Sun, Y. Y. Wang and V. P. Dravid. *Physical Review B* **54**, R8357–R8360 (1996).

[109] M. Viret, M. Drouet, J. Nassar, J. P. Contour, C. Fermon and A. Fert. *EuroPhysics Letters* **39**, 545–549 (1997).

[110] H. Chiba, T. Atou and Y. Syono. *Journal of Solid State Chemistry* **132**, 139–143 (1997).

[111] M. Gajek, M. Bibes, S. Fusil, K. Bouzehouane, J. Fontcuberta, A. Barthelemy and A. Fert. *Nature Materials* **6**, 296–302 (2007).

[112] S. J. Blundell and J. A. C. Bland. *Journal of Magnetism and Magnetic Materials* **121**, 185–188 (1993).

[113] W. Eerenstein, M. Wiora, J. L. Prieto, J. F. Scott and N. D. Mathur. *Nature Materials* **6**, 348–351 (2007).